

AD-A073 114

GENERAL DYNAMICS CORP FORT WORTH TX FORT WORTH DIV
THE CRITICALITY OF ENGINE EXHAUST SIMULATIONS ON VSTOL MODEL-ME--ETC(U)
JUL 79 J R LUMMUS

F/G 20/4

N00014-78-C-0384

UNCLASSIFIED

ONR-CR212-255-1F

NL

1 OF 3
AD
A073 114



1 OF 3

AD

A073114



NATIONAL BUREAU OF STANDARDS
PHOTODUPLICATION SERVICE

LEVEL *11*

12
B.S.

REPORT ONR-CR212-255-1F

A073114



D'D'D'
FORM
NO 217
R
REPLY
C

THE CRITICALITY OF
ENGINE EXHAUST SIMULATIONS ON
VSTOL MODEL - MEASURED GROUND EFFECTS

J. R. Lummus, P.E.

GENERAL DYNAMICS
Fort Worth Division

Contract N00014-78-C-0384
ONR Task 212-255

AUGUST 1979

FINAL REPORT

79 08 21 1159

DDC FILE COPY



PREPARED FOR THE

OFFICE OF NAVAL RESEARCH 800 N. QUINCY ST. ARLINGTON VA 22217

This document contains Technical Data considered to be a research under NDA 1-225.1(d) and 200 H.R. 1000-7, and is not a "research" required to be released under the Freedom of Information Act.

SECURITY CLASSIFICATION OF THIS PAGE (When Data Entered)

DD FORM 1473 EDITION OF 1 NOV 65 IS OBSOLETE

SECURITY CLASSIFICATION OF THIS PAGE (When Data Entered)

402 709

UNCLASSIFIED

SECURITY CLASSIFICATION OF THIS PAGE(When Data Entered)

20. ABSTRACT (Continued)

blocking surface more characteristic of a real aircraft planform) were studied.

Nozzle exit turbulent intensities and pressure distributions were determined by exit surveys with a Kulite subminiature pressure transducer and a total pressure probe. Screens of varying grid size and plates with varying hole patterns were used to achieve variations in turbulent intensity and pressure distributions (respectively) that are characteristic of real aircraft turbojet and turbofan engines at representative nozzle pressure ratios ranging from 1.5 to 2.4.

It was determined that turbulence can be changed by increasing the screen grid size, varying the pressure distribution, or decreasing the nozzle pressure ratio.

Total-pressure rake surveys in the fountains formed under these blocking surfaces indicate that, in all cases, increasing the nozzle turbulence decreases the strength of the fountain by increasing the turbulence and, hence, the entrainment of air away from the fountain by powerful radial ground jets that are formed by the impacting free jets on the ground plane.

Although the magnitude of change was highly configuration dependent, increasing the turbulence intensity in all cases resulted in significantly more-unfavorable ground effects.

For planforms characteristic of real aircraft, varying the turbulence from turbojet to turbofan engine levels with relatively high bypass ratios (or fans) results in an equivalent 10% lift or thrust loss which is on the order of the payload of the aircraft. Therefore, if the effects of nozzle exit conditions of the engines expected for use on VSTOL airplanes are not considered, costly errors in airplane sizing will result.

Accession For	
NTIS GRA&I	<input checked="checked" type="checkbox"/>
DDC TAB	<input type="checkbox"/>
Unannounced	<input type="checkbox"/>
Justification	
By _____	
Distribution/	
Availability Codes	
Dist.	Avail and/or special
A	

UNCLASSIFIED

SECURITY CLASSIFICATION OF THIS PAGE(When Data Entered)

ABSTRACT

↙ This experimental investigation demonstrated the criticality of performing accurate full-scale engine exhaust simulations during model-measured VSTOL ground effects testing. The effects of varying the nozzle exit turbulence, total pressure distributions, and nozzle pressure ratio on the net and component ground-induced forces for two-, three-, and four-nozzle configurations with large blocking surfaces (as well as a smaller, cruciform two-nozzle blocking surface more characteristic of a real aircraft planform) were studied. ←

○ Nozzle exit turbulent intensities and pressure distributions were determined by exit surveys with a Kulite subminiature pressure transducer and a total pressure probe. Screens of varying grid size and plates with varying hole patterns were used to achieve variations in turbulent intensity and pressure distributions (respectively) that are characteristic of real aircraft turbojet and turbofan engines at representative nozzle pressure ratios ranging from 1.5 to 2.4.

○ It was determined that turbulence can be changed by increasing the screen grid size, varying the pressure distribution, or decreasing the nozzle pressure ratio.

Total-pressure rake surveys in the fountains formed under these blocking surfaces indicate that, in all cases, increasing the nozzle turbulence decreases the strength of the fountain by increasing the turbulence and, hence, the entrainment of air away from the fountain by powerful radial ground jets that are formed by the impacting free jets on the ground plane.

Although the magnitude of change was highly configuration dependent, increasing the turbulence intensity in all cases resulted in significantly more-unfavorable ground effects.

For planforms characteristic of real aircraft, varying the turbulence from turbojet to turbofan engine levels with relatively high bypass ratios (or fans) results in an equivalent 10% lift or thrust loss which is on the order of the payload of the aircraft. Therefore, if the effects of nozzle exit conditions of the engines expected for use on VSTOL airplanes are not considered, costly errors in airplane sizing will result.

FOREWORD

This investigation into the criticality of engine exhaust simulations in VSTOL model-measured ground effects was sponsored by the Office of Naval Research under Contract No. N00014-78-C-0384 and executed by the Fort Worth Division of General Dynamics Corporation. The contracted activity spans the period from July 15, 1978, to August 14, 1979. This research activity was monitored and guided by Dr. Robert E. Whitehead of ONR. The program was managed by Mr. C. W. Smith. Mr. J. R. Lummus, who acted as principal investigator, managed the testing, conducted the data analysis, and wrote the final report.

TABLE OF CONTENTS

<u>Section</u>		<u>Page</u>
	List of Figures	viii
	List of Tables	xxi
	Nomenclature	xxii
1	INTRODUCTION	1
	1.1 Background and Related Research	3
	1.2 Objectives	15
2	EXPERIMENTAL INVESTIGATION	16
	2.1 Experimental Equipment	16
	2.1.1 Test Set-up	16
	2.1.2 Model Description	21
	2.1.3 Support Hardware	28
	2.2 Test Procedure	29
	2.2.1 Nozzle-Calibration Testing	29
	2.2.2 Induced-Loads Testing	40
	2.2.3 Fountain-Survey Testing	43
	2.3 Instrumentation	46
	2.4 Data Accuracy	54
	2.4.1 Turbulence Measurement	54
	2.4.2 Thrust and Induced-Loads	57
	Measurement	

TABLE OF CONTENTS (Continued)

<u>Section</u>	<u>Page</u>
2.4.3 Model Altitude Measurement	57
2.4.4 Fountain Rake Measurements	60
3 RESULTS	62
3.1 Nozzle-Calibration Testing	62
3.2 Induced-Loads Testing	70
3.2.1 Effects on Net Induced Forces	73
3.2.2 Effects on Component Forces	91
3.3 Fountain Survey Testing	95
3.3.1 Fountain Core Force	95
3.3.2 Fountain Interference	103
4 CONCLUSIONS	106
REFERENCES	111
APPENDIX A: NOZZLE CALIBRATION SURVEY	114
APPENDIX B: INDUCED FORCE MEASUREMENTS	143
APPENDIX C: FOUNTAIN DYNAMIC PRESSURE CHARACTERISTICS	155

LIST OF FIGURES

<u>Figure</u>	<u>Title</u>	<u>Page</u>
1	Flowfields Near a Hovering VSTOL Aircraft	2
2	Previous Analytical Prediction Methods Optimistically Predict the Net-Induced Lift Force and Fountain Force	5
3	The Fountain Blocks the Flow of Gas to the Ground Jet	9
4	The Decay of the Centerline Velocity in a Variety of Free Jet Flows	11
5	Suckdown Variation with Nozzle Velocity Profile	11
6	Jet Centerline Decay vs Nozzle Pressure Ratio	13
7	Discrepancy in VAK-191B Model and Flight Test Ground Effects	14
8	General Dynamics Fort Worth Division's Ground Effects Hover Test Facility	17
9	Initial Experimental Equipment Test Set-Up	18
10	Experimental Test Set-Up after Hardware Modification	20
11	A Multi-Purpose Ground Effects Model Was Used	22
12	Selected Plenum Outlets Were Used to Provide Desired Nozzle Spacings	23

LIST OF FIGURES (Continued)

<u>Figure</u>	<u>Title</u>	<u>Page</u>
13	Large Research and Cruciform Blocking Surface	26
14	Schematic Diagram of Nozzle Calibration Testing	30
15	The Choking Plate, Screens S_1 and S_2 and Pressure Profile Plates P_1 and P_2 Provided the Desired Nozzle Exit Turbulence and Total Pressure Distributions	33
16	Nozzle Exit Total Pressure Distributions Characteristic of Turbojet and Turbofan Engines Were Obtained with the Baseline Nozzle and Plates P_1 and P_2	36
17	Co-Ordinate System for Fountain Surveys	45
18	Schematic Diagram of the Turbulence Intensity Measurement System	48
19	A Kulite/Total Pressure Probe Was Used to Survey the Nozzle Exit	49
20	A Pressure and Temperature Rake Was Used to Survey the Flow	53
21	Frequency Response Characteristics for the AD 2033 True RMS Meter	56
22	Error in Induced Loads and Thrust Measurements	58

LIST OF FIGURES (Continued)

<u>Figure</u>	<u>Title</u>	<u>Page</u>
23	Altitude Positioning Error of the Ground Board Potentiometer	59
24	The Variation of Turbulent Intensity With NPR for Screens and Plates	66
25	Effects of Turbulence Screens on Net-Induced Force, $\Delta L/F_j$, for Two-Nozzle Configuration - Referenced to Turbulent Intensity	78
26	Real Aircraft Engine Turbulence Levels Cause Large Changes in Ground Effects for Aircraft and Research Type Blocking Surfaces	79
27	Effects of Pressure Profile Plates on Net- Induced Force, $\Delta L/F_j$, for Two-Nozzle Configura- tion - Referenced to Turbulent Intensity	82
28	Effects of Turbulence Screens and Pressure Pro- file Plates on Net-Induced Force, $\Delta L/F_j$, for Three-Nozzle and Four-Nozzle Configurations - Referenced to Turbulent Intensity	83
29	Variation of $\Delta L/F_j$ with $P_{T_{MAX}}$ (Required) for the Two-Nozzle Configuration	85
30	Effect of Varying Nozzle Exit Turbulence with Screens on Net-Induced Force for Two-Nozzle Case	87

LIST OF FIGURES (Continued)

<u>Figure</u>	<u>Title</u>	<u>Page</u>
31	Effect of Varying NPR on Net-Induced Force for Two-Nozzle Case	87
32	Effect of Varying Turbulence with Screens on Net-Induced Forces, $\Delta L/F_j$, for Two-Nozzle Configuration - Referenced to Turbulent Eddy Size	88
33	Effect of Varying Turbulence with Screens on Net-Induced Forces, $\Delta L/F_j$, for Four-Nozzle Configuration - Referenced to Turbulent Eddy Size	89
34	Effect of Nozzle Exit Pressure Ratio and Turbulence Scale on Pure Suckdown	96
35	Effect of Eddy Size on Pure Suckdown	97
36	Effect of Nozzle Pressure Ratio on Pure Suckdown	98
37	Effect of Varying Nozzle Turbulence (Screens) and Pressure Distribution on Fountain Core Force	101
38	Increasing Nozzle Turbulence or Varying the Nozzle Pressure Distribution Degrades Foun- tain Interference, $\Delta L_{FI}/F_j$	104

LIST OF FIGURES (Continued)

<u>Figure</u>	<u>Title</u>	<u>Page</u>
A-1	Exit Pressure Surveys for the N_3^2 Baseline Nozzle at NPR = 1.503	115
A-2	Exit Pressure Surveys for the N_3^2 Baseline Nozzle at NPR = 1.551	116
A-3	Exit Pressure Surveys for the N_3^2 Baseline Nozzle at NPR = 1.924	117
A-4	Exit Pressure Surveys for the N_3^2 Baseline Nozzle at NPR = 1.958	118
A-5	Exit Pressure Surveys for the N_3^2 Baseline Nozzle at NPR = 2.096	119
A-6	Exit Pressure Surveys for the N_3^2 Baseline Nozzle at NPR = 2.276	120
A-7	Exit Pressure Surveys for the N_3^2 Nozzle with Screen S_1 at NPR = 1.517	121
A-8	Exit Pressure Surveys for the N_3^2 Nozzle with Screen S_1 at NPR = 1.531	122
A-9	Exit Pressure Surveys for the N_3^2 Nozzle with Screen S_1 at NPR = 1.931	123
A-10	Exit Pressure Surveys for the N_3^2 Nozzle with Screen S_1 at NPR = 2.317	124

LIST OF FIGURES (Continued)

<u>Figure</u>	<u>Title</u>	<u>Page</u>
A-11	Exit Pressure Surveys for the N_3^2 Nozzle with Screen S_1 at NPR = 2.321	125
A-12	Exit Pressure Surveys for the N_3^2 Nozzle with Screen S_2 at NPR = 1.552	126
A-13	Exit Pressure Surveys for the N_3^2 Nozzle with Screen S_2 at NPR = 1.655	127
A-14	Exit Pressure Surveys for the N_3^2 Nozzle with Screen S_2 at NPR = 1.958	128
A-15	Exit Pressure Surveys for the N_3^2 Nozzle with Screen S_2 at NPR = 1.986	129
A-16	Exit Pressure Surveys for the N_3^2 Nozzle with Screen S_2 at NPR = 2.041	130
A-17	Exit Pressure Surveys for the N_3^2 Nozzle with Screen S_2 at NPR = 2.317	131
A-18	Exit Pressure Surveys for the N_3^2 Nozzle with Screen S_2 at NPR = 2.372	132
A-19	Exit Pressure Surveys for the N_3^2 Nozzle with Pressure Plate P_1 at NPR = 1.551	133
A-20	Exit Pressure Surveys for the N_3^2 Nozzle with Pressure Plate P_1 at NPR = 1.972	134

LIST OF FIGURES (Continued)

<u>Figure</u>	<u>Title</u>	<u>Page</u>
A-21	Exit Pressure Surveys for the N_3^2 Nozzle with Pressure Plate P_1 at NPR = 2.310	135
A-22	Exit Pressure Surveys for the N_3^2 Nozzle with Pressure Plate P_2 at NPR = 1.520	136
A-23	Exit Pressure Surveys for the N_3^2 Nozzle with Pressure Plate P_2 at NPR = 1.510	137
A-24	Exit Pressure Surveys for the N_3^2 Nozzle with Pressure Plate P_2 at NPR = 1.990	138
A-25	Exit Pressure Surveys for the N_3^2 Nozzle with Pressure Plate P_2 at NPR = 2.420	139
A-26	Exit Pressure Surveys for the N_{13}^2 Baseline Nozzle at NPR = 1.897	140
A-27	Exit Pressure Surveys for the N_{11}^1 Nozzle with Screen S_2 at NPR = 2.062	141
A-28	Exit Pressure Surveys for the N_2^1 Nozzle with Screen S_2 at NPR = 2.010	142
B-1	Effect of Varying NPR and Model Altitude on $\Delta L/F_j$ for Baseline Two-Nozzle Configuration	144
B-2	Effect of Turbulence Screens on $\Delta L/F_j$ for Two- Nozzle Configuration, N_3^2 N_{13}^2 P_{13} , at NPR = 1.5	145

LIST OF FIGURES (Continued)

<u>Figure</u>	<u>Title</u>	<u>Page</u>
B-3	Effect of Turbulence Screens on $\Delta L/F_j$ for Two-Nozzle Configuration, $N_3^2 N_{13}^2 P_{13}$, at NPR = 2.0	146
B-4	Effect of Turbulence Screens on $\Delta L/F_j$ for Two-Nozzle Configuration, $N_3^2 N_{13}^2 P_{13}$, at NPR = 2.4	147
B-5	Effect of Pressure Profile Plates on $\Delta L/F_j$ for Two-Nozzle Configuration, $N_3^2 N_{13}^2 P_{13}$, at NPR = 1.5	148
B-6	Effect of Pressure Profile Plates on $\Delta L/F_j$ for Two-Nozzle Configuration, $N_3^2 N_{13}^2 P_{13}$, at NPR = 2.0	149
B-7	Effect of Pressure Profile Plates on $\Delta L/F_j$ for Two-Nozzle Configuration, $N_3^2 N_{13}^2 P_{13}$, at NPR = 2.4	150
B-8	Effect of Turbulence Screens on $\Delta L/F_j$ for Three-Nozzle Configuration, $N_3^1 N_{10}^1 N_{11}^1 P_{31}$, at NPR = 2.0	151
B-9	Effect of Turbulence Screens on $\Delta L/F_j$ for Four-Nozzle Configuration, $N_8^1 N_9^1 N_{10}^1 N_{11}^1 P_{41}$, at NPR = 2.0	152

LIST OF FIGURES (Continued)

<u>Figure</u>	<u>Title</u>	<u>Page</u>
B-10	Effect of Pressure Profile Plates on $\Delta L/F_j$ for Four-Nozzle Configuration, $N_8^1 N_9^1 N_{10}^1 N_{11}^1 P_{41}$, at NPR = 2.0	153
B-11	Effect of Turbulence Screens and Pressure Profile Plates on Pure Suckdown	154
C-1	Dynamic Pressure Profiles for Baseline Four-Nozzle Configuration at NPR = 2.0, D = 1.31 in, H/D = 8.0, Z/D = 7.0	156
C-2	Dynamic Pressure Profiles for Baseline Four-Nozzle Configuration at NPR = 2.0, D = 1.31 in, H/D = 8.0, Z/D = 5.5	157
C-3	Dynamic Pressure Profiles for Baseline Four-Nozzle Configuration at NPR = 2.0, D = 1.31 in, H/D = 8.0, Z/D = 3.5	158
C-4	Dynamic Pressure Profiles for Baseline Four-Nozzle Configuration at NPR = 2.0, D = 1.31 in, H/D = 5.0, Z/D = 3.7	159
C-5	Dynamic Pressure Profiles for Baseline Four-Nozzle Configuration at NPR = 2.0, D = 1.31 in, H/D = 5.0, Z/D = 2.5	160

LIST OF FIGURES (Continued)

<u>Figure</u>	<u>Title</u>	<u>Page</u>
C-6	Dynamic Pressure Profiles for Baseline Four-Nozzle Configuration at NPR = 2.0, D = 1.31 in, H/D = 5.0, Z/D = 1.5	161
C-7	Dynamic Pressure Profiles for Four-Nozzle Configuration with S ₂ Screens at NPR = 2.0, H/D = 8.0, Z/D = 6.7	162
C-8	Dynamic Pressure Profiles for Four-Nozzle Configuration with S ₂ Screens at NPR = 2.0, H/D = 8.0, Z/D = 3.5	163
C-9	Dynamic Pressure Profiles for Four-Nozzle Configuration with S ₂ Screens at NPR = 2.0, H/D = 8.0, Z/D = 5.5	164
C-10	Dynamic Pressure Profiles for Four-Nozzle Configuration with S ₂ Screens at NPR = 2.0, H/D = 5.0, Z/D = 3.5	165
C-11	Dynamic Pressure Profiles for Four-Nozzle Configuration with S ₂ Screens at NPR = 2.0, H/D = 5.0, Z/D = 2.5	166
C-12	Dynamic Pressure Profiles for Four-Nozzle Configuration with S ₂ Screens at NPR = 2.0, H/D = 5.0, Z/D = 1.5	167

LIST OF FIGURES (Continued)

<u>Figure</u>	<u>Title</u>	<u>Page</u>
C-13	Dynamic Pressure Profiles for Four-Nozzle Configuration with P_2 Pressure Profile Plates at NPR = 2.0, H/D = 8.0, Z/D = 6.7	168
C-14	Dynamic Pressure Profiles for Four-Nozzle Configuration with P_2 Pressure Profile Plates at NPR = 2.0, H/D = 8.0, Z/D = 5.5	169
C-15	Dynamic Pressure Profiles for Four-Nozzle Configuration with P_2 Pressure Profile Plates at NPR = 2.0, H/D = 8.0, Z/D = 3.5	170
C-16	Dynamic Pressure Profiles for Four-Nozzle Configuration with P_2 Pressure Profile Plates at NPR = 2.0, H/D = 5.0, Z/D = 2.5	171
C-17	Dynamic Pressure Profiles for Baseline Two- Nozzle Configuration at NPR = 2.0, H/D = 8.0, Z/D = 5.5	172
C-18	Dynamic Pressure Profiles for Baseline Two- Nozzle Configuration at NPR = 2.0, H/D = 8.0, Z/D = 3.5	173
C-19	Dynamic Pressure Profiles for Baseline Two- Nozzle Configuration at NPR = 2.0, H/D = 8.0, Z/D = 1.5	174

LIST OF FIGURES (Continued)

<u>Figure</u>	<u>Title</u>	<u>Page</u>
C-20	Dynamic Pressure Profiles for Baseline Two- Nozzle Configuration at NPR = 2.0, H/D = 3.5, Z/D = 2.1	175
C-21	Dynamic Pressure Profiles for Baseline Two- Nozzle Configuration at NPR = 2.0, H/D = 3.5, Z/D = 1.25	176
C-22	Dynamic Pressure Profiles for Baseline Two- Nozzle Configuration at NPR = 2.0, H/D = 2.5, Z/D = 1.1	177
C-23	Dynamic Pressure Profiles for Two-Nozzle Con- figuration with S ₂ Screens at NPR = 2.0, H/D = 8.0, Z/D = 5.5	178
C-24	Dynamic Pressure Profiles for Two-Nozzle Con- figuration with S ₂ Screens at NPR = 2.0, H/D = 8.0, Z/D = 3.5	179
C-25	Dynamic Pressure Profiles for Two-Nozzle Con- figuration with S ₂ Screens at NPR = 2.0, H/D = 8.0, Z/D = 1.5	180
C-26	Dynamic Pressure Profiles for Two-Nozzle Con- figuration with S ₂ Screens at NPR = 2.0, H/D = 3.5, Z/D = 2.1	181

LIST OF FIGURES (Continued)

<u>Figure</u>	<u>Title</u>	<u>Page</u>
C-27	Dynamic Pressure Profiles for Two-Nozzle Configuration with S_2 Screens at NPR = 2.0, H/D = 3.5, Z/D = 1.25	182
C-28	Dynamic Pressure Profiles for Two-Nozzle Configuration with S_2 Screens at NPR = 2.0, H/D = 3.5, Z/D = 1.10	183

LIST OF TABLES

<u>Table</u>	<u>Title</u>	<u>Page</u>
2-1	Summary of Nozzle Exit Surveys Conducted	37
2-2	Plenum Pressure, Corrected Mass Flow, and Corrected Thrust Required for a Given NPR with Each Nozzle-Configuration/Exit Device Combination	41
2-3	Summary of Fountain Survey Cases	44
2-4	Operating Response Characteristics of the CQ-080-25 Kulite Transducer	51
3-1	Turbulent Intensity, I , vs NPR for Screens and Plates	65
3-2	Estimated Large-Scale Eddy Sizes and Asso- ciated Frequencies for Screens	71
3-3	Net-Induced Force Test Matrix	74
3-4	Effects of Nozzle Exit Variables on Net- Induced Force, $\Delta L/F_j$	76
3-5	Maximum Effect of Varying Nozzle Exit Con- ditions on Component Forces	92

NOMENCLATURE

A	Area used in fountain integration	in. ²
D,d	Nozzle-exit diameter	in.
\bar{D}	Angular mean diameter (Ref. 20)	in.
d_f	Distance from one of two jets to the fountain on a line perpendicular to the fountain	in.
δ	Ratio of Barometric pressure (psi) to standard day barometric pressure (14.7 psi)	-
ϵ	Largest physical dimension for turbulence generation; grid size for screens in this experiment	in.
ϵ_e	Average size of turbulent energy-containing eddies of consequence (Kolmogorof, Ref. 15)	in.
F	Force vector used in fountain integration	lbf
F_j	Total isolated thrust of all jet nozzles for single- or multiple-jet configurations	lbf
f	Frequency	hz

NOMENCLATURE (Continued)

γ_F	Fountain flow angularity from vertical in the XZ plane, positive to the rear of the model	deg
H,h	Height of the blocking surface above the ground surface	in.
I	Turbulent intensity (based on Kulite pressure measurements in this study)	-
K_e	Wave number (Ref. 15)	
ΔL	Total induced lift on the blocking sur- face, equal to the sum of the fountain and suckdown components	lbf
ΔL_F	Total incremental effect of the fountain on the induced lift, equal to the sum of the fountain core and fountain interfer- ence components	lbf
ΔL_{FC}	Lift of the fountain core obtained from integrations of the rake pressure data	lbf
ΔL_{FI}	Fountain interference lift	lbf
ΔL_j	Pure suckdown obtained with single nozzle	lbf
\dot{m}	Mass flow per unit area obtained from the rake measurements	$\text{lb}_m/\text{in.}^2 \text{ sec}$

NOMENCLATURE (Continued)

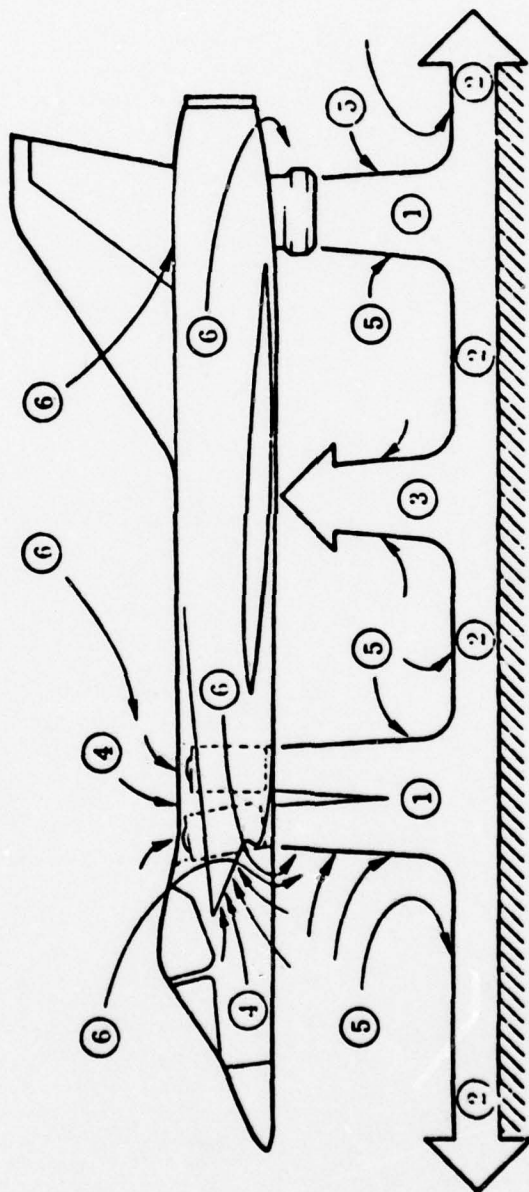
\dot{m}_F	Total mass flow through an X-Y plane cut through the fountain	lb _m /sec
N_j^i	Nozzle designation where j = Location on the plenum (see Figure 11) i = 1, nozzle diameter = 1.32 in. i = 2, nozzle diameter = 1.41 in.	-
NPR	Nozzle Pressure Ratio	-
P_k	Blocking surface designation where k indicates plate used (see Figure 12)	-
P_{PL}	Plenum pressure	psi
P_{TOTAL}	Total pressure	psi
P_{TP}		
P_1, P_2	Pressure distribution plates (see Figure 14)	-
Q_F	Dynamic pressure in the fountain	psi
Q_{FV}	Vertical component of the fountain dynamic pressure	psi
ρ	Density	slugs/ft ³
S	Strouhal number	-

NOMENCLATURE (Continued)

S_1	Turbulence screen with element size = 0.125 in. (see Figure 14)	-
S_2	Turbulence screen with element size = 0.240 in. (see Figure 14)	-
T	Temperature	$^{\circ}\text{F}$
θ, θ_T	Ratio of temp ($^{\circ}\text{F}$) to standard day temp (59°F)	-
θ_F	Fountain flow angularity from vertical in the YZ plane, positive to the right (as viewed from the pilot's position)	deg
W, W_a	Nozzle weight flow	lbs/sec
X	Distance from the centroid of the nozzle configuration perpendicular to the rake path	in.
Y	Distance from the centroid of the nozzle configuration along the rake path	in.
Z	Distance above the ground plane	in.

1. INTRODUCTION

When a VSTOL aircraft operates near the ground, the high-velocity jets exhausting below the aircraft react with the ground and airframe (Figure 1) to produce propulsion-induced aerodynamic forces and moments which must be determined for accurate propulsion and control system sizing and, hence, accurate aircraft sizing. Accurate prediction of these induced aerodynamic forces is critical to VSTOL aircraft design because they can represent significant changes in the thrust required for VTOL operations, resulting in large increases in required takeoff gross weight and, ultimately, in large cost increases to accomplish the mission requirements. Research with free jets and recent flight test experience with full-scale aircraft indicate that nozzle exit conditions influence the magnitude of these induced forces. Therefore, to improve the accuracy of current prediction methodologies and to gain physical understanding of the flow mechanisms involved, an experimental investigation was conducted to determine the criticality of full-scale engine-nozzle exit conditions (nozzle exit turbulence, total pressure distribution, and pressure ratio over the ranges expected for full scale aircraft engines) on the propulsion-induced



1 EXHAUST FLOW (FREE JET)

2 GROUND JET

3 FOUNTAIN JET

4 ENGINE INLET FLOW

5 & 6 ENTRAINED AMBIENT AIR

Figure 1 Flowfields Near a Hovering VSTOL Aircraft

aerodynamic forces. This investigation was limited to the case of hover in still air (no crosswind, no forward speed) with zero pitch, yaw, and roll angle.

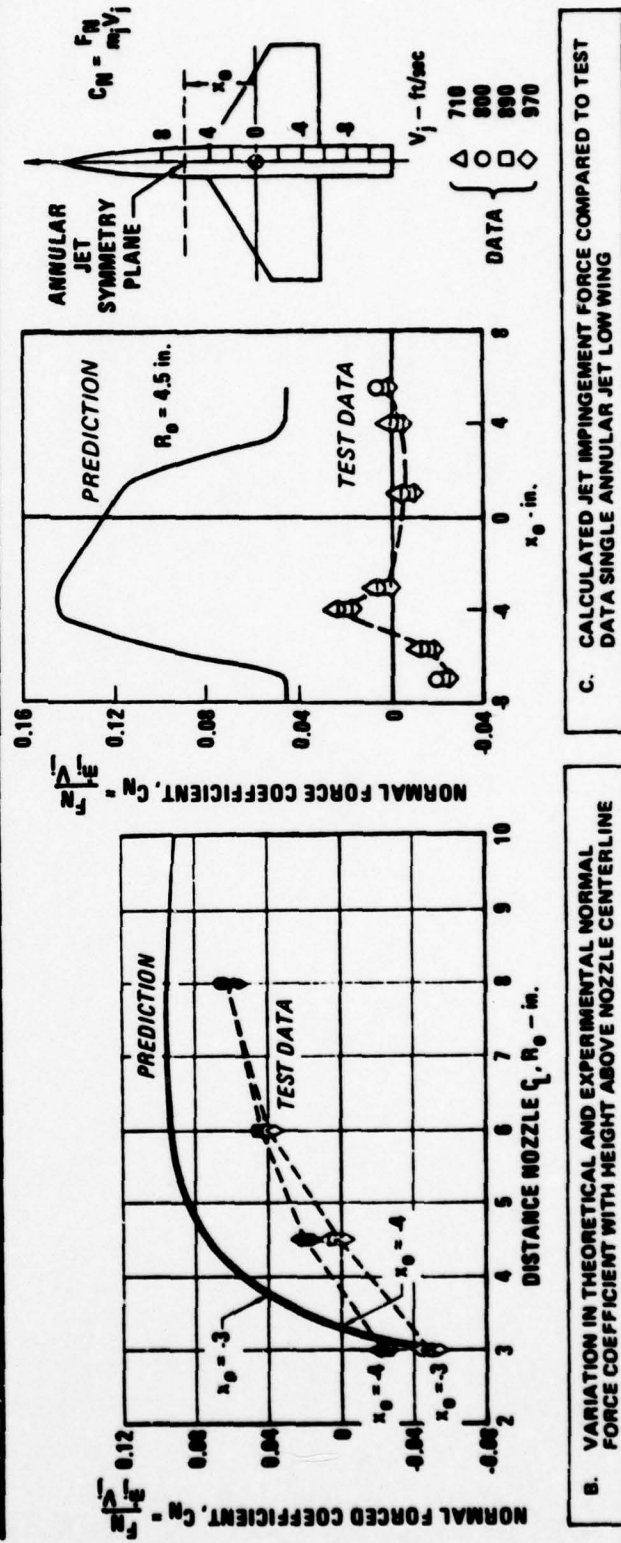
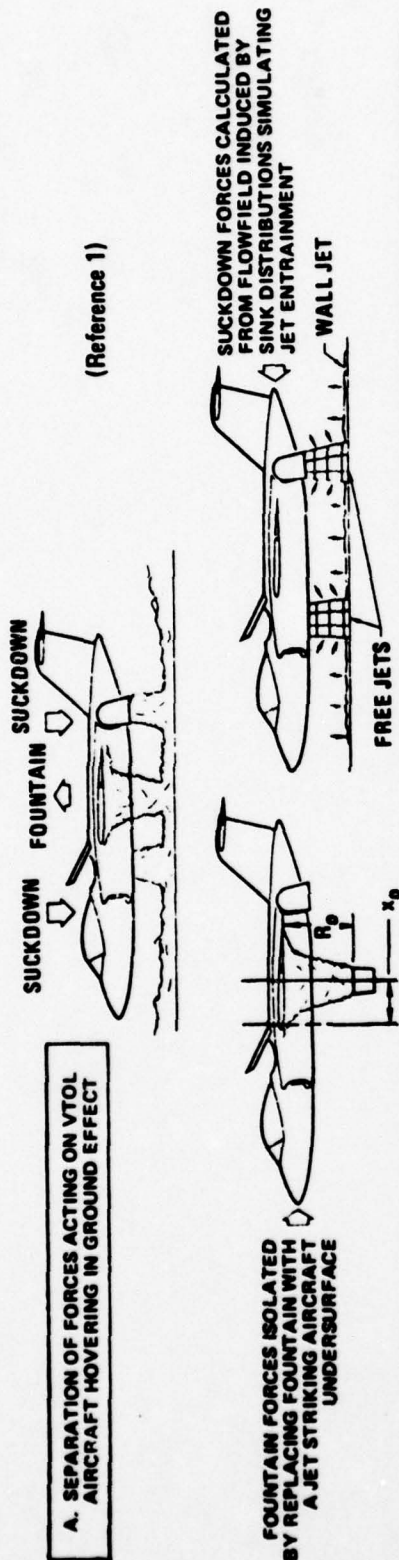
1.1 Background and Related Research

The net-induced normal force on the aircraft (primarily produced by flow regions 1, 2, 3, and 5 in Figure 1) is the summation of two oppositely directed forces, suckdown and fountain. Suckdown, ΔL_j , is a negative force (lift loss) produced by suction pressures on the underside of the aircraft created by large quantities of air entrained by the turbulent exhaust and ground jets below the aircraft. The fountain occurs when two or more engine exhaust jets impinge normally on the ground plane and the resulting radially expanding ground jets meet to form a vertical upflow region or fountain. This fountain induces a positive force, ΔL_F , (lift enhancing) to the airframe that sometimes cancels or exceeds the negative suckdown force.

Previous analytical methods (References 1 and 2) predict net-induced lift losses that are too optimistic (Figure 2). The prediction error results partly from an assumption that the effects of the various flow regions illustrated in Figure 1 may be superimposed, that is, they do not react

with each other and therefore the suckdown and fountain forces can be independently predicted without regard to any mutual interference effects. This assumption had a large effect on the way the flowfield was modeled in Reference 1 for example, where the suckdown forces were calculated from flowfields induced by potential flow sink distributions to simulate the free and wall (ground jet) entrainment while fountain forces were isolated by replacing the fountain with a jet striking the aircraft undersurface. The importance of adding empirical corrections to the potential theory to account for the prevalent viscous flow and real interference effects are apparent when the predicted fountain jet and net-induced forces are compared with the experimental data as shown in Figure 2. It appears that an empirical prediction approach is required because the flowfield is simply too complicated to be adequately predicted by strictly theoretical means.

General Dynamics has been involved in developing an empirically based prediction methodology for these induced forces for several years (References 3, 4, 5). Karemaa (Reference 4) determined that the net fountain force (net induced force minus pure suckdown, both experimentally ob-



tained as described in Section 2.2) is made up of a fountain core force, ΔL_{FC} , which produces a positive lift on the blocking surface, and a fountain interference component, ΔL_{FI} , which produces either a positive or a negative lift caused by the interaction of the fountain, the blocking surface, and the entrainment process. For a two-nozzle configuration with a large rectangular blocking surface, Karemaa postulated that the fountain interacts with the blocking surface and the entrainment flow to produce a pressure field under the blocking surface that is different from the one that would exist if the fountain were not present. This interference term accounted for the error of previous prediction methodologies. Karemaa formulated a relationship to describe how these non-dimensionalized component forces make up the net induced force measured with the typical ground-effects research model:

$$\frac{\Delta L}{F_j} = \frac{\Delta L_j}{F_j} + \frac{\Delta L_{FC}}{F_j} + \frac{\Delta L_{FI}}{F_j} \quad (1)$$

The superposition assumption was therefore considered invalid, but more evidence and understanding of this fountain interference term was required.

This led to a series of experiments, conducted by General Dynamics and supported by the Office of Naval Research, to

investigate the characteristics of the fountain flow formed beneath large research-type blocking surfaces with two-, three-, and four-nozzle configurations (Reference 5). This research was also aimed at determining more about the interaction of the fountain with the entrained air and blocking surface and at quantifying the subsequent fountain interference force. Dynamic pressures in the fountain were measured with a total-pressure rake and integrated to determine the fountain core force and the mass flow entrainment characteristics of the fountains studied.

The net induced force and the pure suckdown component, measured in the manner described in Section 2, were obtained for each nozzle configuration; the interference force was then determined by Equation 1. The results conclusively proved the existence of a fountain interference component for large blocking surfaces. The interference component was found to be as large or larger than the fountain core force for the large blocking surfaces tested. Therefore, analytical prediction methods and experimental efforts that only consider the fountain core will overlook a major fraction of the fountain contribution. The fountain interference was also found to be a function of nozzle configuration, producing large lift losses with the two-nozzle cases and

aerodynamic forces. This investigation was limited to the case of hover in still air (no crosswind, no forward speed) with zero pitch, yaw, and roll angle.

1.1 Background and Related Research

The net-induced normal force on the aircraft (primarily produced by flow regions 1, 2, 3, and 5 in Figure 1) is the summation of two oppositely directed forces, suckdown and fountain. Suckdown, ΔL_j , is a negative force (lift loss) produced by suction pressures on the underside of the aircraft created by large quantities of air entrained by the turbulent exhaust and ground jets below the aircraft. The fountain occurs when two or more engine exhaust jets impinge normally on the ground plane and the resulting radially expanding ground jets meet to form a vertical upflow region or fountain. This fountain induces a positive force, ΔL_F , (lift enhancing) to the airframe that sometimes cancels or exceeds the negative suckdown force.

Previous analytical methods (References 1 and 2) predict net-induced lift losses that are too optimistic (Figure 2). The prediction error results partly from an assumption that the effects of the various flow regions illustrated in Figure 1 may be superimposed, that is, they do not react

large lift gains with the stronger-fountain four-nozzle configuration. In fact, the positive net induced force measured for the four-nozzle case was found to be due primarily to the positive fountain interference component and not to the fountain core force as had been thought before this research. The integrated rake measurements showed that a very weak fountain was formed with the two-nozzle cases and that usually dissipated before reaching the blocking surface, thus contributing no net positive fountain core lifting force to the blocking surface. The fountain dissipation was found to be due to air being entrained away from the weak fountains by the powerful radial ground jets - at a diminishing rate with increasing height in the fountain, as described in the following excerpt from Reference 5:

As the fountain rises from the ground plane, the two-nozzle fountains lose large amounts of mass and entrain some ambient air for a net loss in mass. The three-nozzle fountain also loses mass, while the four-nozzle fountain gains mass

Karemaa and Smith (Reference 6) explain that fountain interference is probably a result of the fountain itself acting as a blocking surface that reduces the rate of entrainment of ambient air by the ground jets (Figure 3); the fountain blocks one path available for a single jet to en-

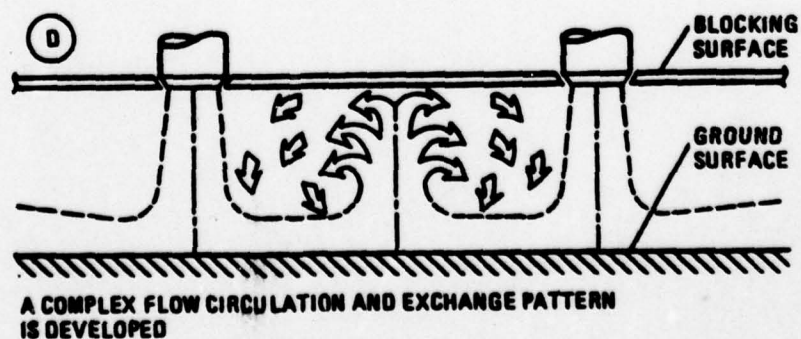
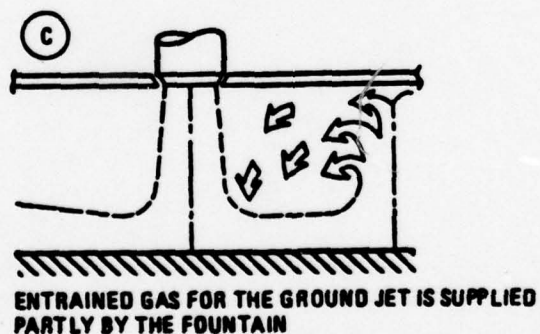
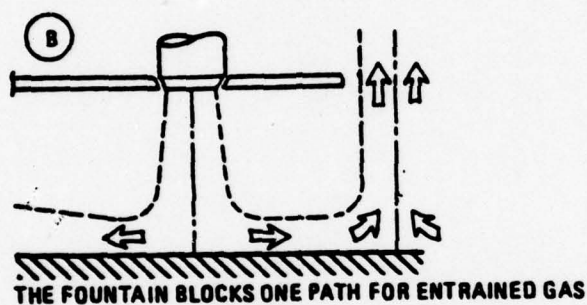
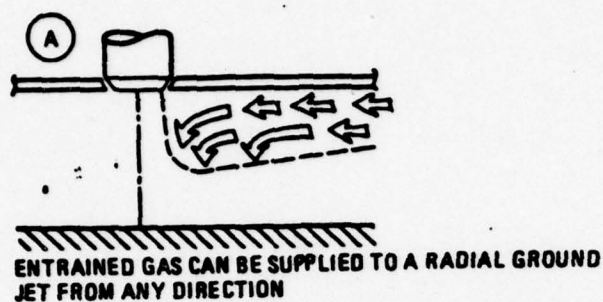


Figure 3 The Fountain Blocks the Flow of Gas to the Ground Jet

train gas into the ground jet (Sketch B) so that air is entrained away from the fountain and into the ground jet (Sketch C). Air was found to be more easily entrained away from the weak fountain of the two-nozzle case into the ground jet. The three-nozzle fountain, which is somewhat stronger than the two-nozzle fountain, had less air entrained away and actually produced a positive fountain core force. The four-nozzle fountain was found to be much stronger than either the two- or three-nozzle fountains and actually entrained air into the fountain. A strong positive fountain core force and positive interference was produced. The authors noted that the mechanism of the positive fountain interference was and still is unknown and requires a more detailed definition of the flowfield.

It is apparent that the entrainment mechanism is responsible for much of the ground effects with VSTOL aircraft. Comparisons of the measured free-jet centerline decay by several experimenters (Reference 7) show considerably different spreading rates near the nozzle exit for axisymmetric free jets (Figure 4), but to date no systematic work has been done to explain the source of the difference. However, Kuhlman and Warcup (Reference 8) have demonstrated that al-

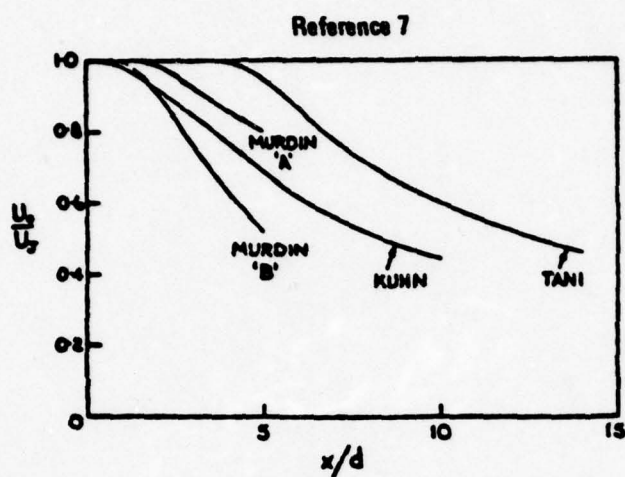


Figure 4 The Decay of the Centerline Velocity in a Variety of Free Jet Flows

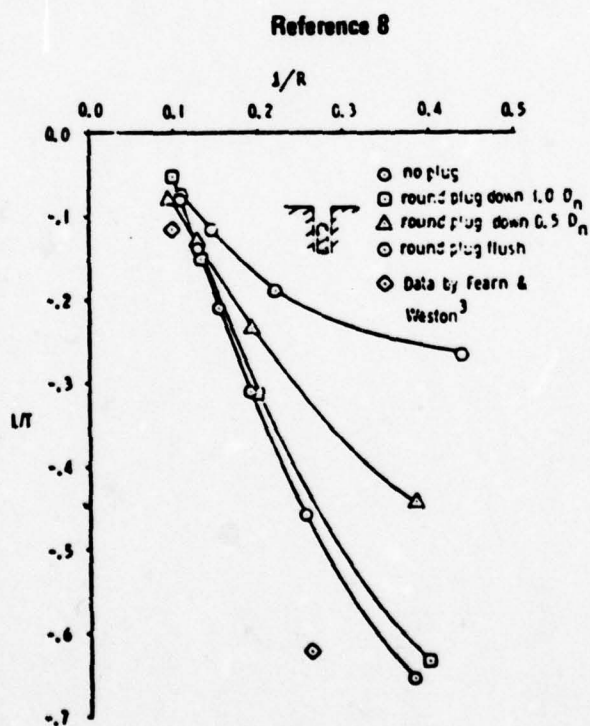


Figure 5 Suckdown Variation with Nozzle Velocity Profile

tering the exit velocity profile of an axisymmetric jet can alter its spreading rate (Figure 5) and produce a large change in the induced loading on the blocking surface plate through which the free jet exits. Varying the nozzle pressure ratio is another means of obtaining different spreading rates with a free jet, as shown by Gentry and Margason (Reference 9) and reproduced as Figure 6; they also established a correlation between jet spreading rate and ground effects measured on a model. Since the turbulent structure of axisymmetric jets does not become self preserving until some 80 jet exhaust diameters downstream of the nozzle exit, as demonstrated by Wygnanski and Fielder (Reference 10), nozzle exit conditions are expected to have a significant effect on the flowfield around a VSTOL airplane at altitudes where the ground effects are important, these altitudes being usually much less than 80 nozzle exhaust diameters.

In the course of the VAK 191B VSTOL aircraft development and evaluation program (Reference 11) flight tests produced quite different results than did model tests in VTOL measured ground effects (Figure 7). It is reported in Reference 11 that the difference is believed to lie in the failure to simulate the full-scale engine-nozzle exit conditions in the model tests.

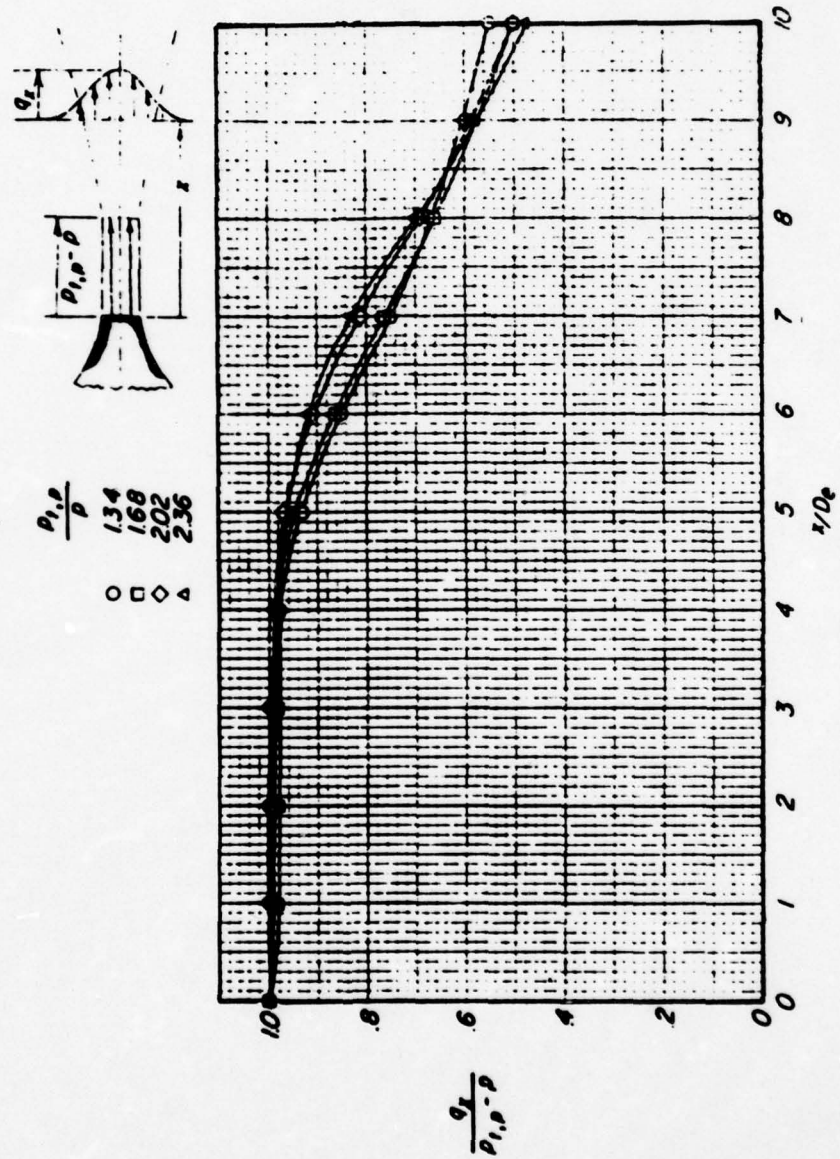


Figure 6 Jet Centerline Decay Vs Nozzle Pressure Ratio

H = HEIGHT
b = WING SPAN

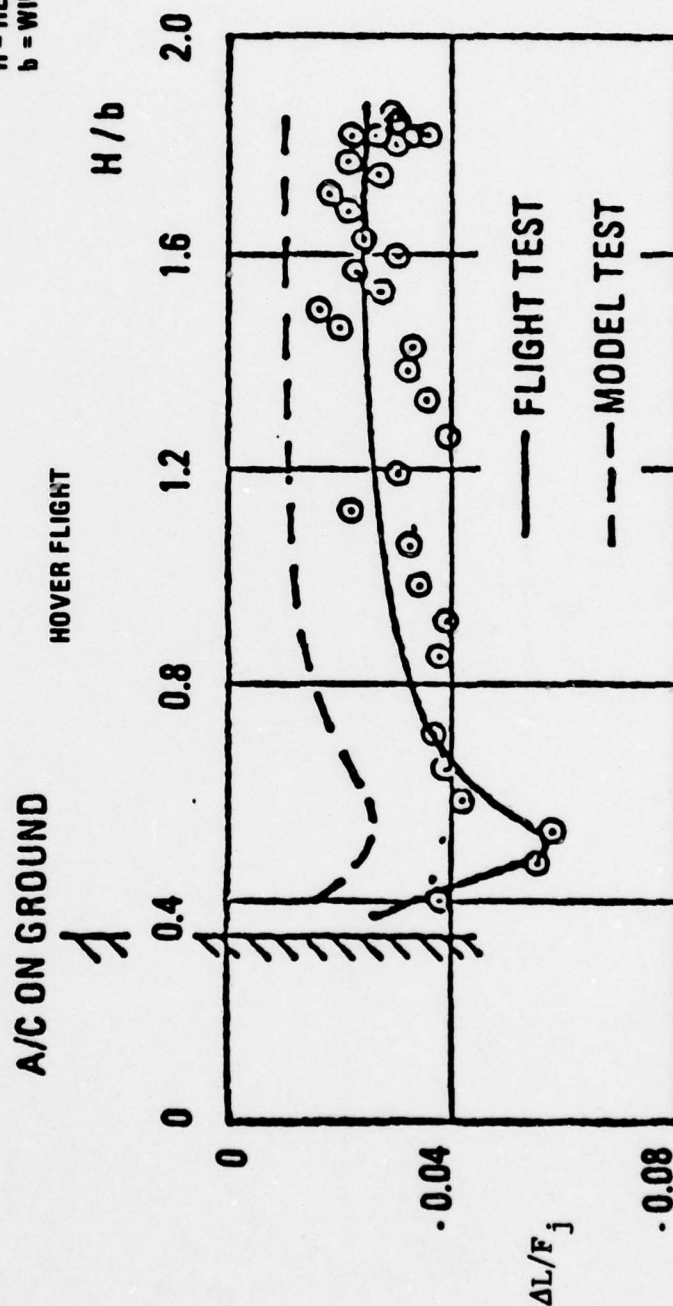


Figure 7 Discrepancy in VAK-191B Model & Flight Test Ground Effects (Reference 11)

1.2 Objectives

It is apparent from the research described above that nozzle exit conditions do affect the VSTOL-related flowfield and that these engine exhaust conditions should be modeled accurately so that model-measured ground-induced forces can be extrapolated to those of full-scale vehicles. In order to determine the criticality of these engine exhaust simulations, an experimental investigation was conducted on the effects of varying the nozzle exit turbulence, total pressure distribution, and nozzle pressure ratio on the ground-induced forces for two-, three-, and four-nozzle configuration models with large flat-plate blocking surfaces. The nozzle configurations and blocking surfaces were the same ones used in an earlier investigation of fountain characteristics and temperature effects (Reference 5). Since the ultimate objectives of this research are the development of prediction techniques and an understanding of the physical flow phenomena, the effects of varying the nozzle exit conditions on the component forces described in Equation (1) as well as on the net-induced force had to be determined.

2. EXPERIMENTAL INVESTIGATION

The experimental investigation was conducted at the General Dynamics Fort Worth Division's Ground Effects Hover Test Facility (Figure 8). Testing consisted of three phases - a nozzle calibration phase, in which variations in nozzle exit conditions were determined; an induced-loads phase, in which the net and component induced forces produced by variations in model configuration (number of nozzles and blocking surface planform shape), model altitude, and nozzle exit conditions were measured; and, finally, a fountain survey phase, in which the fountain flowfield characteristics were investigated. As noted earlier, the experiments were limited to a simulation of hover (no forward speed) with zero crosswind and at zero pitch, roll, and yaw angle. Unlike the work reported in Reference 5, nozzle exit temperature was not a variable in this study and was maintained at approximately 80°F.

2.1 Experimental Equipment

2.1.1 Test Setup

The initial test setup is shown in Figure 9. High-pressure air was supplied to two plenums by a large-volume

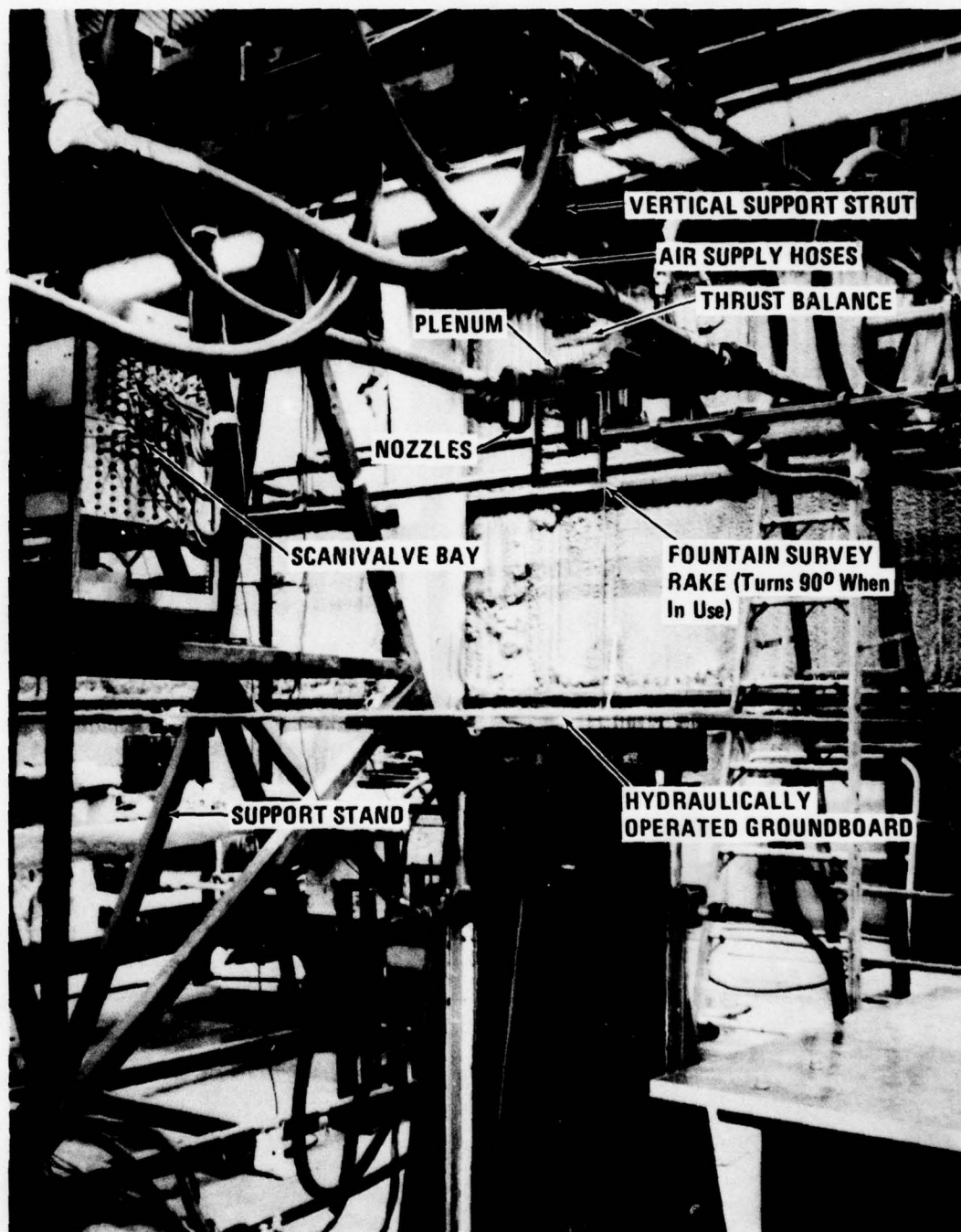


Figure 8 General Dynamics Fort Worth Division's Ground Effects Hover Test Facility

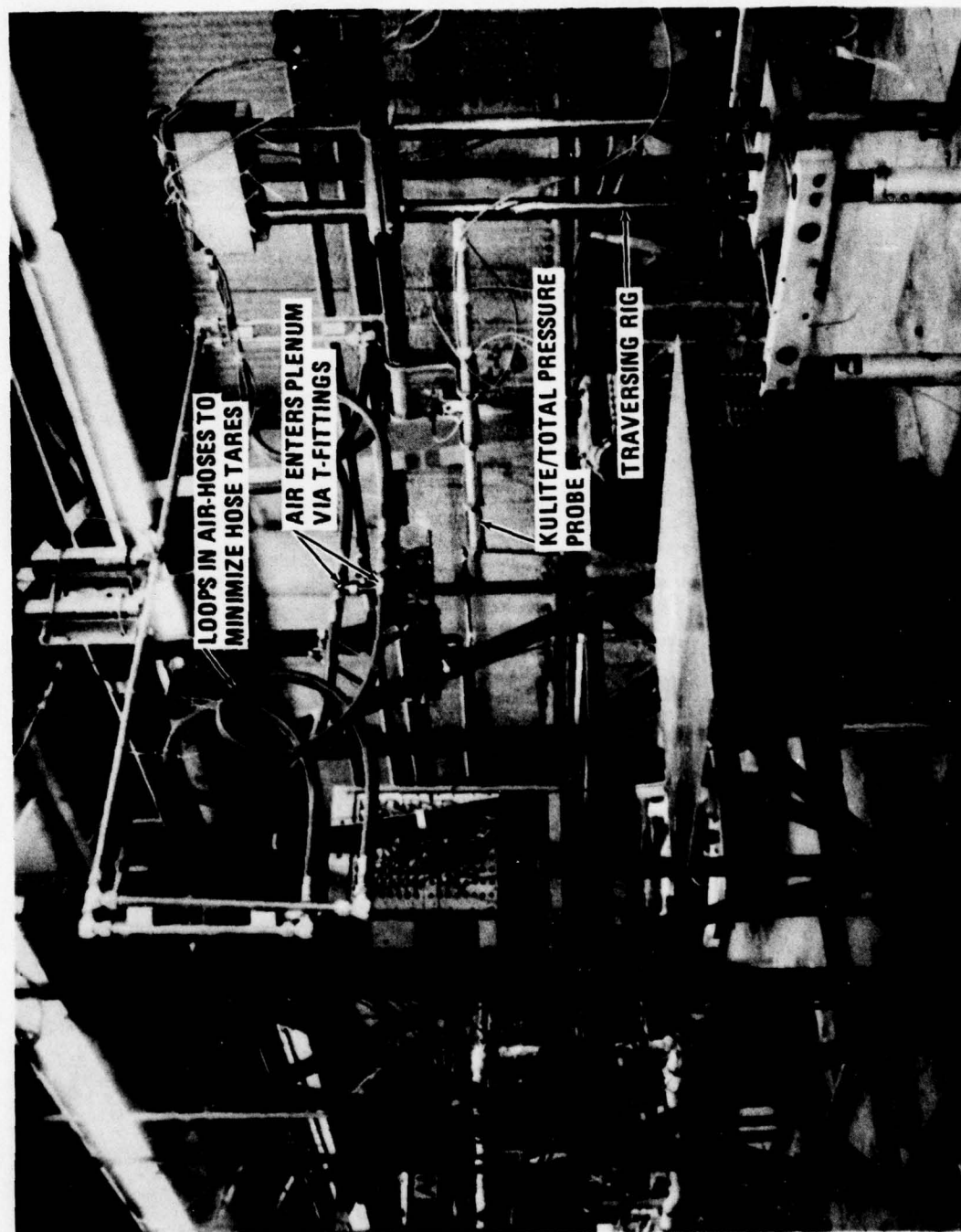


Figure 9 Initial Experimental Equipment Test Set-Up

dedicated compressor through four 3/4-inch-inside-diameter flexible hoses connected to T-fittings on the top of the plenums. The choking plates used with the model in previous experiments (References 4 and 5) were again employed to insure uniform plenum flow to the nozzles. Early in the nozzle calibration phase, the air compressor failed, requiring a new air supply system.

Increasing the sizes of the air supply lines to the plenums, changing the entry points for the air into the plenums, and replacing the choking plates allowed use of the plant compressed-air supply system. Details of these hardware modifications are noted below. The key elements of the revised test setup are shown in Figures 8 and 10. This plenum/air supply arrangement was maintained through the remainder of testing. Checks were made to insure that the nozzle flow characteristics observed before the compressor failure could be repeated with the new plenum/air-supply arrangement, thus eliminating the need to rerun data obtained before the compressor failure.

A key feature of this type of ground effects testing is the desire to isolate the thrust produced by the nozzles and the propulsion-induced loads on the blocking surface.



Figure 10 Experimental Test Set-Up after Hardware Modification

This isolation was accomplished by making the blocking surface metric with the lower induced-loads-measuring five-component strain-gage balance (located between the blocking surface and the plenum) and by keeping the thrust-producing system (plenums and nozzles) nonmetric to this balance. The thrust forces were measured (with the blocking surface removed) by the upper five-component strain-gage balance, which is connected to the vertical support strut.

2.1.2 Model Description

The model is composed of the plenum assembly, associated nozzle hardware, and flat-plate blocking-surfaces. A general arrangement of the model is provided in Figure 11.

The plenum assembly is composed of a forward and aft plenum with 15 possible nozzle locations (nine forward, six aft). The plenums are machined from a single piece of steel with the bottom surface welded into place. Three sides of each plenum contain 2-inch-diameter holes to allow for the installation of various nozzles. The selected nozzle locations for the two-, three-, and four-nozzle configuration studied in this investigation are shown in Figure 12. Cover plates are provided for the non-blowing positions.

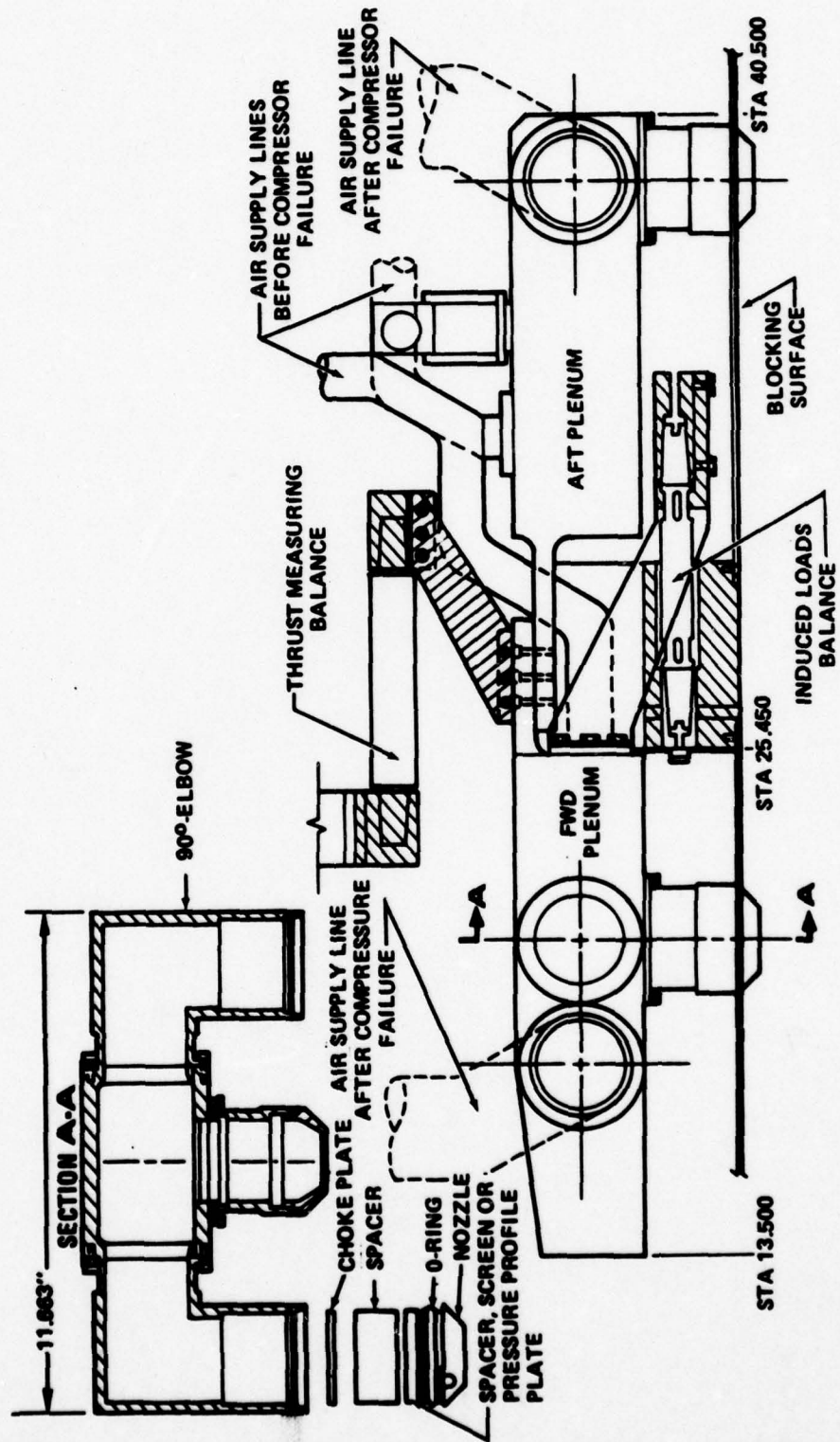


Figure 11 A Multi-Purpose Ground Effects Model Was Used

The high pressure air supply system used for the major portion of this investigation (shop/plant compressed-air supply system) necessitated modifications to the plenums to achieve the desired nozzle pressure range (1.5 to 2.4) with the multiple-nozzle configurations. The plenums were modified to bring the high-pressure air into the sides of the plenums at nozzle locations 6, 7, 14, and 15 via four flexible 1.5-inch-diameter rubber hoses connected to fittings welded to the cover plates; in previous experiments, the air entered the aft end of the forward plenum and the top of the aft plenum (Figure 11). A maximum plenum pressure of 95 psig was required for some nozzle arrangements. The maximum, normalized weight flow condition through one plenum was 1.27 pounds per second as determined by individual-plenum venturi flow meters located upstream of the flexible hoses.

The nozzle assemblies, shown in Figure 11, are composed of either a straight or a 90-degree elbow barrel (depending on nozzle configuration), a choking plate, a spacer (which was replaced with the devices for varying the nozzle turbulence or pressure profile), and the nozzle itself. The high-pressure plant air-supply utilized required a new choking plate with a rectangular grid and

with more porosity than previously used so as to reduce pressure losses and achieve the desired range of flow parameters (see Section 2.2, Figure 15).

The new choking plate, used alone as the baseline nozzle configuration, was located well upstream of the nozzle convergence. It was always present with the other devices for varying nozzle conditions to maintain uniform plenum flow. These other devices were located just upstream of the convergence nozzle section. The 30-degree conical, half angle, convergent nozzles screwed into the barrel assembly to hold the internal pieces in place. Two nozzle exit diameters were tested, 1.42 inches for the two-nozzle cases and 1.32 inches for the three- and four-nozzle cases.

The blocking-surface models are shown in Figure 13. The large rectangular two- and four-nozzle as well as the triangular three-nozzle blocking surfaces were the ones employed in the Reference 4 and 5 tests. (Note that sections of these plates may be removed or mounted off the balance to allow testing with one nozzle to determine the pure suckdown component, as described in Section 2.2.2.) In addition, a new cruciform plate with the same two-nozzle spacing was studied briefly because it is more characteristic of the

planform shapes of real aircraft than the other large research-type blocking surfaces. All of these flat-plate blocking surface models are made of aluminum and have sharp 90-degree edges.

For consistency with previous investigations utilizing this hardware (References 4 and 5), the applicable nomenclature rationale is noted as follows. The blocking surface models are noted as P with subscript 13 for the two-nozzle rectangular configuration, 31 for the three-nozzle triangular configuration, and 41 for the four-nozzle rectangular configuration. All nozzles are designated by subscripts for location and by superscripts for size. The location subscript is keyed in Figure 12 and designates the nozzle location on the plenum chambers. The superscript refers to the nozzle diameter (1 = 1.32 in., 2 = 1.41 in.). A complete test configuration $N_3^1 N_{10}^1 N_{11}^1 P_{31}$ would mean a three-nozzle arrangement with 1.32-inch-diameter nozzles located at points 3, 10, and 11. The triangular three-nozzle blocking surface would be mounted on the induced-loads balance.

2.1.3 Support Hardware

The support hardware consists of the model support stand to which the model is mounted, the hydraulically driven ground board-table, and the traversing rig.

The support stand (Figure 8) is a massive, welded-steel, rectangular beam structure that rigidly supports the model over the ground board. The stand is bolted to the concrete floor to assure rigidity. It also serves as support for the scanivalve bays servicing the model instrumentation as discussed in Section 2.3.

The hydraulically driven ground-board table provided the desired variation in model altitude. An 8-foot-square reinforced aluminum plate assembly mounted on top of the small table surface shown in Figure 8 served as the ground board for this experiment. The table was either manually or computer operated to vary ground height positioning over a range of height-to-nozzle-diameter (h/D) ratios of from 2.5 to 10.

The traversing rig, shown in Figure 9, was used to survey the nozzle exit flow with the Kulite/total pressure probe and the fountain flow with the cone-probe total-pressure rake (both devices are described in Section 2.3).

The rig provides longitudinal, lateral, and vertical displacement probe positioning by use of a screw/drive motor combination. A braking circuit was incorporated in the drive motors to prevent "coasting" after the positioning power signal ended, thereby improving probe-positioning accuracy. The rig was rigidly mounted to a sturdy support table to further insure positioning accuracy.

2.2 Test Procedure

2.2.1 Nozzle Calibration Testing

Initially the model plenums were attached to the upper five-component strain-gage balance, which was in turn mounted to the vertical support strut and support stand. Flexible air hoses, with loops to minimize tares, supplied the high-pressure air to the plenums. With all exit passages from the plenum blocked by cover plates, the air hoses were pressurized to obtain the hose tare forces on the thrust balance. Check loads were also made to insure that thrust could be measured through the whole data acquisition system to the desired accuracies with the hoses pressurized.

A schematic diagram of the nozzle calibration testing is presented in Figure 14. With the N_3^2 baseline nozzle

BASELINE NOZZLE FOR 2, 3, 4, NOZZLE CONFIGURATIONS

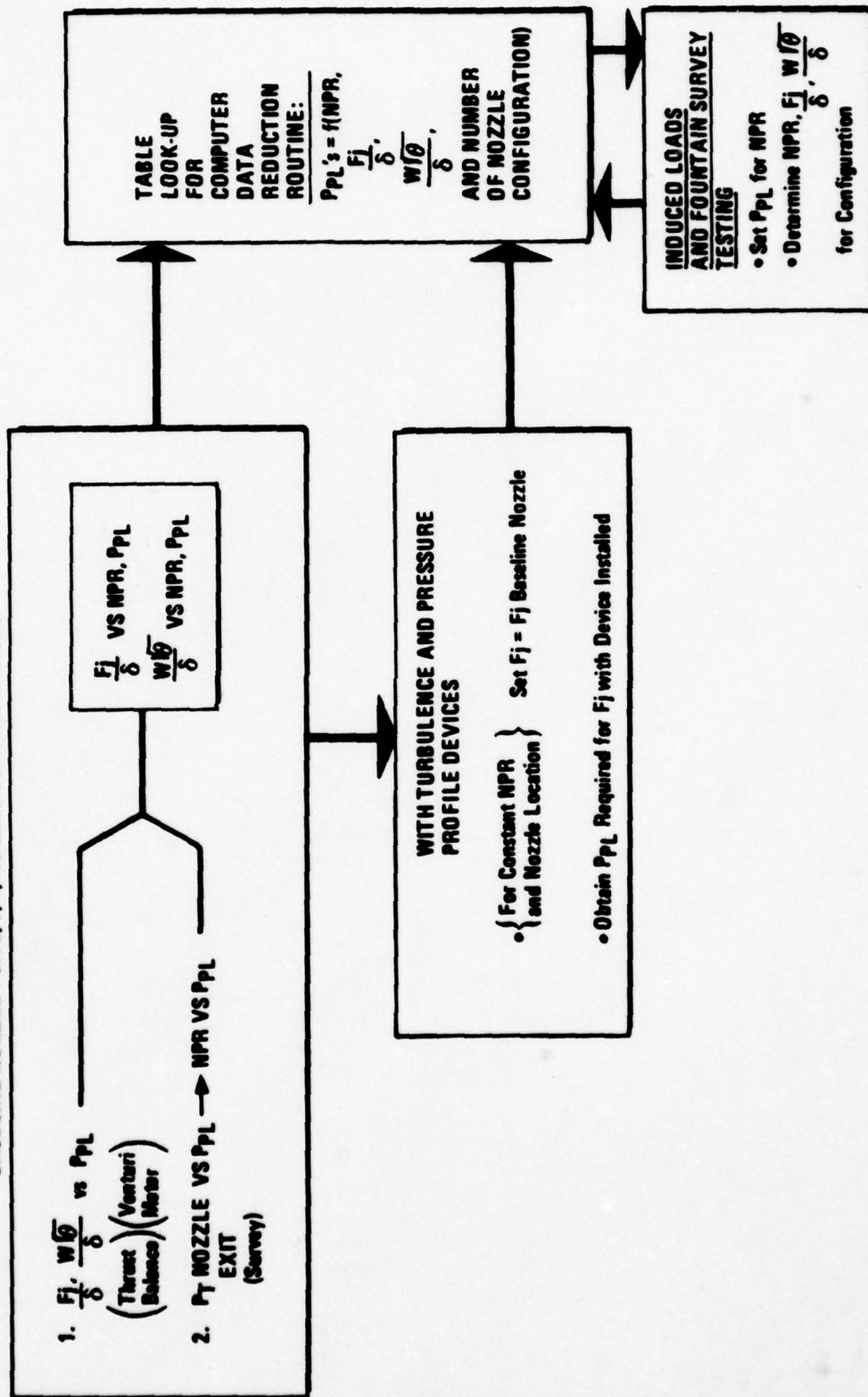


Figure 14 Schematic Diagram of Nozzle Calibration Testing

installed (on the forward plenum), plenum pressure, P_{PL} , was varied to determine corresponding variations in venturi-measured corrected airflow to the plenum, $\frac{W \sqrt{\theta}}{\delta}$, and corrected balance measured thrust, F_j/δ . The N_3^2 baseline nozzle exit was then surveyed at various plenum pressures with a Kulite/total-pressure probe to determine the nozzle exit turbulence and total-pressure distribution. Each nozzle exit survey required two traverses of the nozzle exit 90-degrees apart. During the survey, the Kulite/total-probe instrumentation reached a maximum displacement of 0.1 inch from the nozzle exit plane at $NPR = 2.4$; obviously some nominal displacement was required to prevent instrumentation damage due to impact with the model as a result of model/probe vibrations. However, the probe boom was more flexible than desired, resulting in probe displacement from the nozzle exit plane that varied slightly during exit surveys. This displacement was a function of the amount of probe boom extended into the nozzle flow, producing an aerodynamic drag force and the subsequent displacement. The exact displacement is unknown but is considered to have a negligible effect on the overall results of this investigation.

The nozzle pressure ratio, NPR, is defined as the area-weighted average total pressure measured across the nozzle exit plane (with the total probe described above) divided by the static ambient pressure. (The area-weighted average total pressure was computed over the inner 80% of the nozzle diameter ($r/D \pm 0.4$, Appendix A Figures) due to lateral and longitudinal deflections of the total-pressure probe caused by the very high shear layers near the nozzle edge.) The plenum pressure and corrected airflow required to achieve the desired nozzle pressure ratio and subsequent nozzle thrust were thus determined.

In order that the desired variations in nozzle turbulence and total-pressure distribution could be obtained over the ranges expected for full-scale aircraft engines (see Section 3), the nozzle exit was surveyed with a variety of screen and plate devices located just upstream of the convergent nozzle section (Figure 15). The thrust was held constant (for a given NPR) for the baseline nozzle and with the turbulence screens and pressure plates in place. The nozzle exit surveys were performed at nominal NPRs of 1.5, 2.0, and 2.4.

The plenum pressure was adjusted until the desired baseline nozzle thrust was measured on the thrust balance

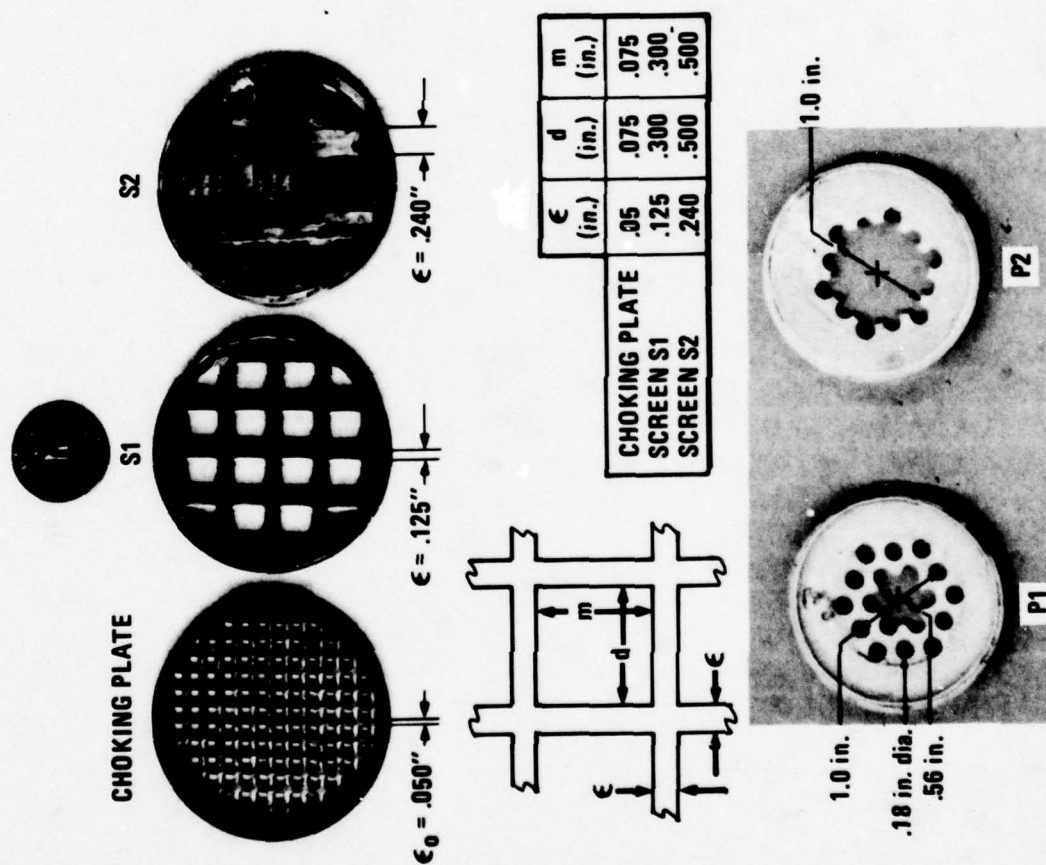


Figure 15 The Choking Plate, Screens S1 and S2 and Pressure Profile Plates P1 and P2 Provided the Desired Nozzle Exit Turbulence and Total Pressure Distributions

at the desired NPR. This allowed the nozzle exit surveys to be obtained at the same NPRs as were used in the induced-loads and fountain-survey testing phases. Ultimately, then, the objective of relating nozzle exit conditions to the induced loads and to what was occurring in the flowfield could be realized.

The nozzle exit surveys yielded a measure of turbulence in terms of a turbulent intensity, I , defined as the area-weighted average RMS value of the fluctuating total pressure across the nozzle exit as determined by a high-response subminiature Kulite transducer (see Section 2.3) divided by the area-weighted average total pressure (gage) across the nozzle exit as determined by the total pressure probe. (The turbulent intensity was also defined over the inner 80% of the nozzle diameter because of the difficulty in measuring the total pressure near the nozzle edge as noted above.) The accuracy of measuring the turbulent intensity with the Kulite transducer will be discussed in Section 2.4.1.

The devices selected for varying the nozzle exit conditions are shown in Figure 15. Screens of varying mesh size were used to achieve variations in nozzle exit turbulence while maintaining a virtually uniform total-pressure distribution. The choking plate on the left is shown for

comparison. Exit total-pressure distributions representative of turbofan engines with varying bypass ratios were obtained with pressure profile plates P_1 and P_2 (Figure 16); the baseline nozzle's "top hat" pressure distribution is representative of a turbojet engine.

NPR is a somewhat arbitrary term when applied to non-uniform exit pressure profiles like those produced by P_1 and P_2 . Therefore, the NPRs for the non-uniform profiles were taken as those measured on the baseline "top hat" profiles when the thrust produced by the non-uniform profiles matched that of the baseline. The screens S_1 and S_2 produced virtually uniform profiles so that no analogous difficulty was present.

After the compressor failure occurred, the hardware modifications described above were accomplished to allow use of the new air supply system. Repeat exit surveys and thrust calibrations at an NPR of 2.0 for the baseline nozzle N_3^2 and with turbulence screen S_2 installed showed good nozzle-condition repeatability; therefore the nozzle calibrations were continued. Table 2-1 summarizes the nozzle exit survey cases.

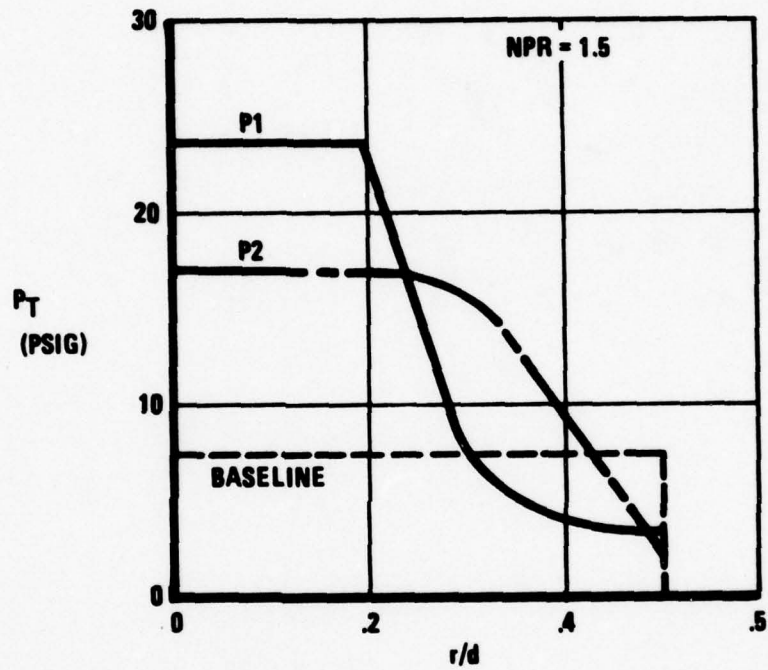


Figure 16 Nozzle Exit Total Pressure Distributions Characteristic of Turbojet and Turbofan Engines Were Obtained with the Baseline Nozzle and Plates P_1 and P_2

Table 2-1 SUMMARY OF NOZZLE EXIT SURVEYS CONDUCTED

CONFIGURATION	NPR	DIRECTLY APPLICABLE CONFIGURATION
N_3^2	1.5, 2.0, 2.4	2 NOZZLE
$N_3^2 + S1$	1.5, 2.0, 2.4	2 NOZZLE
$N_3^2 + S2$	1.5, 2.0, 2.4	2 NOZZLE
$N_3^2 + P1$	1.5, 2.0, 2.4	2 NOZZLE
$N_3^2 + P2$	1.5, 2.0, 2.4	2 NOZZLE
N_{13}^2	—, 2.0, —	2 NOZZLE
$N_{11}^1 + S2$	—, 2.0, —	3 AND 4 NOZZLE
$N_9^1 + S2$	—, 2.0, —	4 NOZZLE

Nozzle calibration testing was minimized through the use of several rather involved but justifiable assumptions:

1. Since the nozzle exit surveys showed good agreement between the forward and aft plenum cases for the two-nozzle baseline case (i.e., N_3^2 and N_{13}^2) at an NPR of 2.0, the forward and aft nozzle exit conditions were assumed equal at other NPRs and with S_1 , S_2 , P_1 , and P_2 devices installed. Therefore, nozzle exit surveys for the aft plenum, two-nozzle case, N_{13}^2 , were required only at an NPR of 2.0.
2. Nozzle diameter was also assumed to have no effect on the nozzle exit surveys; therefore, for constant NPR, the turbulent intensity and total-pressure distributions (including variations with screens and plate) obtained with the 1.42-inch-diameter N_3^2 nozzle (used for the two-nozzle configuration) were assumed equal to those of the 1.32-inch-diameter N_3^1 nozzle (used for the three-nozzle configuration). Justification for this assumption is provided in the discussion of assumption 3.

3. Finally, it was assumed that, when two nozzles are symmetrically located on the same plenum (as in the cases of the aft plenum for the three-nozzle configuration with N_{10}^1 and N_{11}^1 , and for both the forward and aft plenums on the four-nozzle configurations, with N_8^1 , N_9^1 , and N_{10}^1 , N_{11}^1 , respectively), nozzle exit surveys are required on only one side of each plenum. Therefore, surveys were made of N_9^1 and N_{11}^1 , representing the forward and aft plenums, respectively (screen S_2 was installed in both cases). These surveys were made with both nozzles operating on the plenum of interest. (Air was supplied only to the plenum being investigated in all cases described.) At an NPR of 2.0, the turbulent intensities agreed so well with those of the larger nozzle, N_3^2 (with S_2 installed), that the variations due to changing screens and plates were assumed to be the same for the larger nozzle positioned for the four-nozzle configuration as obtained for the smaller nozzle, N_3^2 , positioned for the two-nozzle configuration. Since the induced loads were to be measured only at an NPR of 2.0 for the three- and four-nozzle

configurations, exit surveys were limited to an NPR of 2.0 for these cases.

Forward and aft plenum pressures were then varied independently for each remaining nozzle-configuration/exit-device combination to determine the corresponding changes in F_j/δ and $\frac{W}{\delta} \sqrt{\theta}$. These variations allowed the thrust and corresponding plenum pressure required for a desired NPR to be determined for each of the nozzle-configuration/exit-device combinations. The results of these variations, summarized in Table 2-2, formed the basis for setting the nozzle flow conditions for a given NPR, nozzle configuration, and nozzle device in the induced-loads and fountain-survey testing phase.

2.2.2 Induced-Loads Testing

The net induced lift force, ΔL , on the blocking-surface model planforms was measured directly with the five-component strain-gage induced-loads balance while configuration, nozzle exit flow parameters, and model altitude were varied.

The two-nozzle configuration was tested at NPRs of 1.5, 2.0, and 2.4; three- and four-nozzle configurations were tested at an NPR of 2.0. The turbulence screens and pressure

Table 2-2 PLENUM PRESSURE, CORRECTED MASS FLOW, AND CORRECT THRUST REQUIRED FOR A GIVEN NPR WITH EACH NOZZLE-CONFIGURATION/EXIT DEVICE COMBINATION

FORWARD PLENUM TABLE

NOZZLE CONFIG	N_3^2 NOZZLE				N_3^1 NOZZLE				$N_8^1 N_9^1$ NOZZLES			
	$\frac{P_{PL}}{\delta}$	$\frac{F_j}{\delta}$	$\frac{W_a \sqrt{\theta_T}}{\delta}$	NPR	$\frac{P_{PL}}{\delta}$	$\frac{F_j}{\delta}$	$\frac{W_a \sqrt{\theta_T}}{\delta}$	NPR	$\frac{P_{PL}}{\delta}$	$\frac{F_j}{\delta}$	$\frac{W_a \sqrt{\theta_T}}{\delta}$	NPR
BASIC	33.0	16.0	.67	1.5	31.0	15.6	.64	1.5	31.1	30.3	1.20	1.5
	49.0	33.5	1.04	2.0	43.6	29.0	.922	2.0	44.5	57.0	1.72	2.0
	60.0	45.0	1.27	2.4	53.3	40.0	1.138	2.4				
BASIC + P1	47.6	16.0	.61	1.5	68.8	29.0	.88	2.0	58.3	45.0	1.42	1.8
	60.9	22.5	.76	1.7	73.7	32.5	.955	2.1	67.5	57.0	1.66	2.0
	75.8	33.5	.99	2.0								
	91.3	45.0	1.18	2.4								
BASIC + P2	34.8	16.0	.60	1.5	50.0	29.0	.872	2.0	43.4	45.0	1.09	1.8
	50.3	28.0	.89	1.83	53.8	32.5	.94	2.1	50.5	57.0	1.69	2.0
	55.5	33.5	.98	2.0								
	67.6	45.0	1.20	2.4								
BASIC + S1	34.0	16.0	.68	1.5	31.7	15.6	.652	1.5	44.9	55.0	1.75	1.8
	50.9	33.5	1.05	2.0	45.0	29.0	.905	2.0	45.9	57.0	1.80	2.0
	61.3	45.0	1.26	2.4								
BASIC + S2	37.5	16.0	.66	1.5	50.2	29.0	.89	2.0	43.8	45.0	1.54	1.8
	38.3	16.6	.68	1.51	51.3	30.0	.90	2.0	50.2	57.0	1.78	2.0
	56.5	33.5	1.14	2.0								
	68.8	45.0	1.27	2.4								

Table 2-2 PLENUM PRESSURE, CORRECTED MASS FLOW, AND CORRECT THRUST REQUIRED FOR A GIVEN NPR WITH EACH NOZZLE-CONFIGURATION/EXIT DEVICE COMBINATION (Cont'd)

AFT PLENUM TABLE

NOZZLE CONFIG	N_{13}^2 NOZZLE				$N_{10}^1 N_{11}^1$ NOZZLES			
	$\frac{P_{PL}}{\delta}$	$\frac{F_j}{\delta}$	$\frac{W_a \sqrt{\theta_T}}{\delta}$	NPR	$\frac{P_{PL}}{\delta}$	$\frac{F_j}{\delta}$	$\frac{W_a \sqrt{\theta_T}}{\delta}$	NPR
BASIC	34.5	16.5	.687	1.5	37.3	46.7	1.590	1.8
	49.5	32.3	1.015	2.0	42.8	57.8	1.818	2.0
	60.5	44.0	1.241	2.4				
BASIC + P1	50.3	16.5	.635	1.5	65.0	52.6	1.635	1.9
	63.7	23.0	.770	1.7	67.5	57.8	1.750	2.0
	78.6	32.3	.955	2.0				
	95.0	44.0	1.145	2.4				
BASIC + P2	36.5	16.5	.600	1.5	49.0	55.0	1.595	2.0
	56.6	32.3	.940	2.0	50.0	57.8	1.650	2.0
	59.3	34.5	.985	2.1				
	69.5	44.0	1.185	2.4				
BASIC + S1	35.8	16.5	.695	1.5	40.0	46.7	1.595	1.8
	39.0	19.3	.750	1.8	45.1	57.8	1.815	2.0
	51.8	32.3	1.015	2.0				
	63.5	44.0	1.246	2.4				
BASIC + S2	39.3	16.5	.695	1.5	48.6	54.0	1.636	1.9
	56.7	32.3	1.015	2.0	50.2	57.8	1.710	2.0
	69.7	44.0	1.250	2.4				

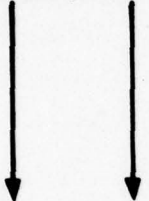
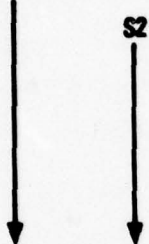
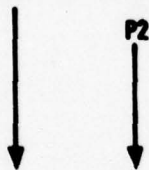
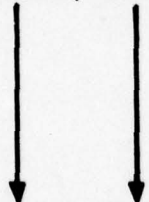
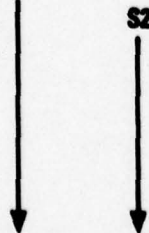
distribution plates were tested with the two- and four-nozzle configurations; only screen variations were tested with the three-nozzle configuration.

To determine the effects of varying nozzle-exit conditions on the pure suckdown component of the net induced force, one half of the two-nozzle plate was removed and the nozzle with the metric half of the plate was operated; induced loads were measured on the metric half plate with the turbulence screens and pressure profile plates installed and with variations in model altitude. In all cases model altitude was varied over h/D values from 2.5 to 10.0 .

2.2.3 Fountain-Survey Testing

The cone-probe rake, described in Section 2.3, was used to survey the fountains formed with the two- and four-nozzle configurations at an NPR of 2.0 to ascertain the effects on the fountain of the turbulence and pressure profile devices. The cases studied are summarized in Table 2-3; the coordinate system employed is defined in Figure 17. (The appropriate distance measurements are dimensionalized by the nozzle diameter, D .) For a given model altitude, h/D , the survey rake was placed at a desired height above the ground plane, Z/D , and traversed along the Y axis

Table 2-3 SUMMARY OF FOUNTAIN SURVEY CASES

CONFIGURATION	h/D	z/D	FIGURE
4 NOZZLE, BASELINE 	8.0	7.0	C-1
		5.5	C-2
		3.5	C-3
	5.0	3.7	C-4
		2.7	C-5
		1.5	C-6
	8.0	6.7	C-7
		5.5	C-8
		3.5	C-9
	5.0	3.5	C-10
		2.5	C-11
		1.5	C-12
	8.0	6.7	C-13
		5.5	C-14
		3.5	C-15
	5.0	2.5	C-16
2 NOZZLE, BASELINE 	8.0	5.5	C-17
		3.5	C-18
		1.5	C-19
		3.5	C-20
		1.3	C-21
		1.1	C-22
	8.0	5.5	C-23
		3.5	C-24
		1.5	C-25
		3.5	C-26
		1.3	C-27
		1.1	C-28

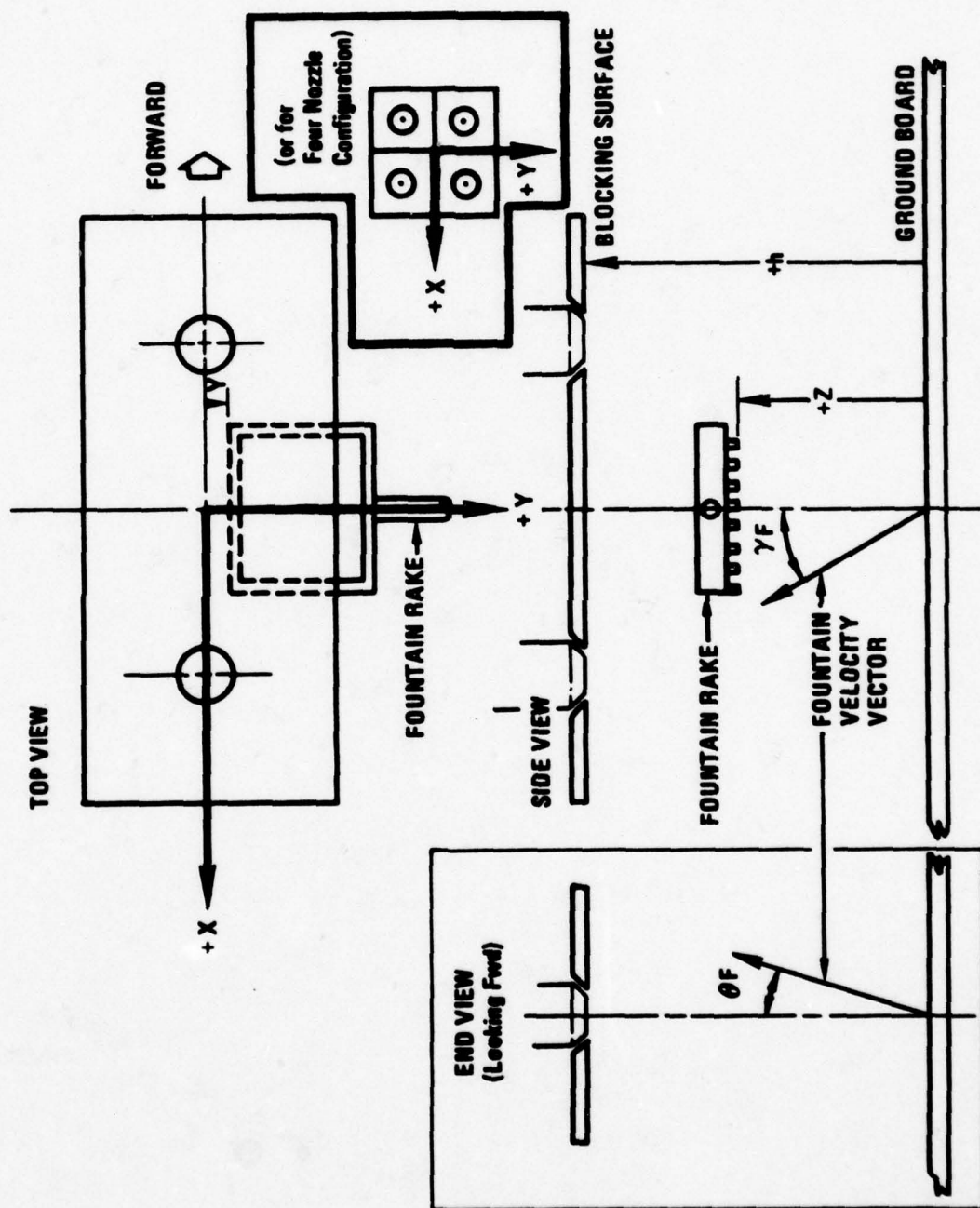


Figure 17 Co-Ordinate System for Fountain Surveys

(centerline between fore and aft nozzles where the fountain center is expected). The Y-traverses were begun slightly past center (negative Ys) and extended until the fountain flow became unmeasurable (approached zero). Seventy pressure readings on the rake were recorded at each Y/D location in the traverse. Traverses of up to three Z/D locations were made for a given model altitude.

2.3 Instrumentation

The instrumentation used in this investigation may be divided into five functional categories: (1) airflow monitoring, (2) nozzle exit survey, (3) thrust measurement, (4) induced loads measurement, and (5) fountain survey.

(1) Airflow monitoring instrumentation consisted of two venturi flow meters used to independently monitor the airflow to the forward and aft plenums and plenum static pressure taps and thermocouples (one of each per plenum located in the body of each plenum). The thermocouples were used for monitoring airflow temperature to the plenums; no total temperature drop was assumed through the nozzles for calculating isentropic nozzle exit flow characteristics.

(2) Nozzle exit survey instrumentation consisted of the turbulence and total-pressure measurement systems. The turbulence intensity measurement system shown schematically

in Figure 18 consisted of two subsystems, one for turbulence and one for total pressure. The turbulence subsystem consisted of a very sensitive Kulite subminiature pressure transducer that provided an analog signal of the fluctuating total pressure (25 psi maximum) in the nozzle flow to an Analog Device true RMS voltmeter, Model AD2033, which determined continuous RMS values of the signal. This continuous RMS signal was in turn sampled by the high-speed data acquisition system at an adequate rate and period determined experimentally as the minimum rate and period at which no measurable change in the averaged RMS value occurred for the highest screen-produced turbulence case, S_2 . This rate and period turned out to be 500 samples/second for 1 second. The Kulite transducer, Model No. XCQL-14-093, was mounted on the forward support of the Kulite/total-pressure-probe boom, as shown in Figures 9 and 19. Five of these Kulite transducers were calibrated statically (DC levels only) before testing by determining the variation of pressure on the transducer face with output voltage over the maximum allowable range of pressures (± 25 psi); the variations were found to be very linear. These calibration curves became part of the data reduction procedure for determining the RMS value of the fluctuating total pressure associated with the nozzle

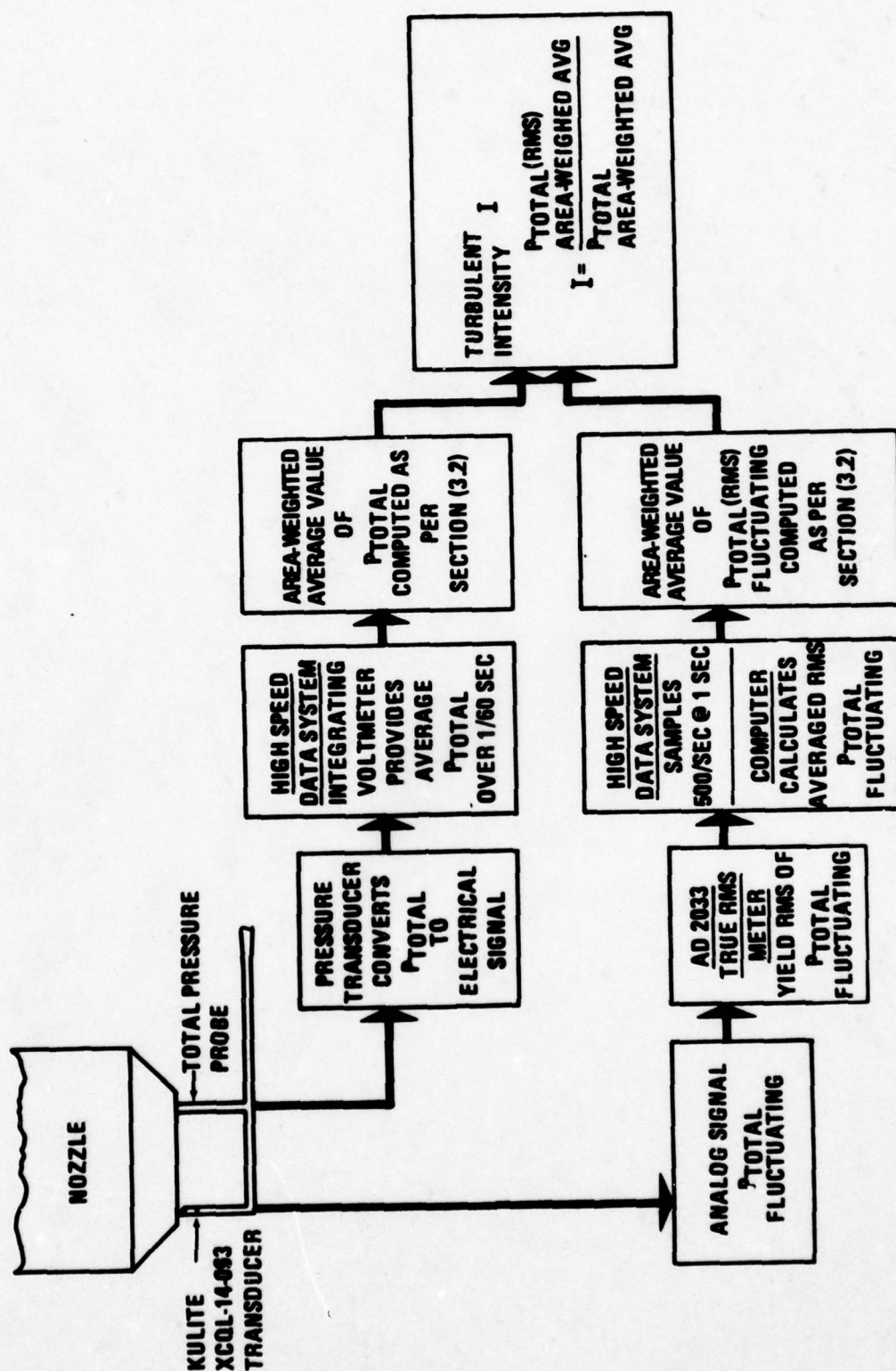


Figure 18 Schematic Diagram of the Turbulence Intensity Measurement System

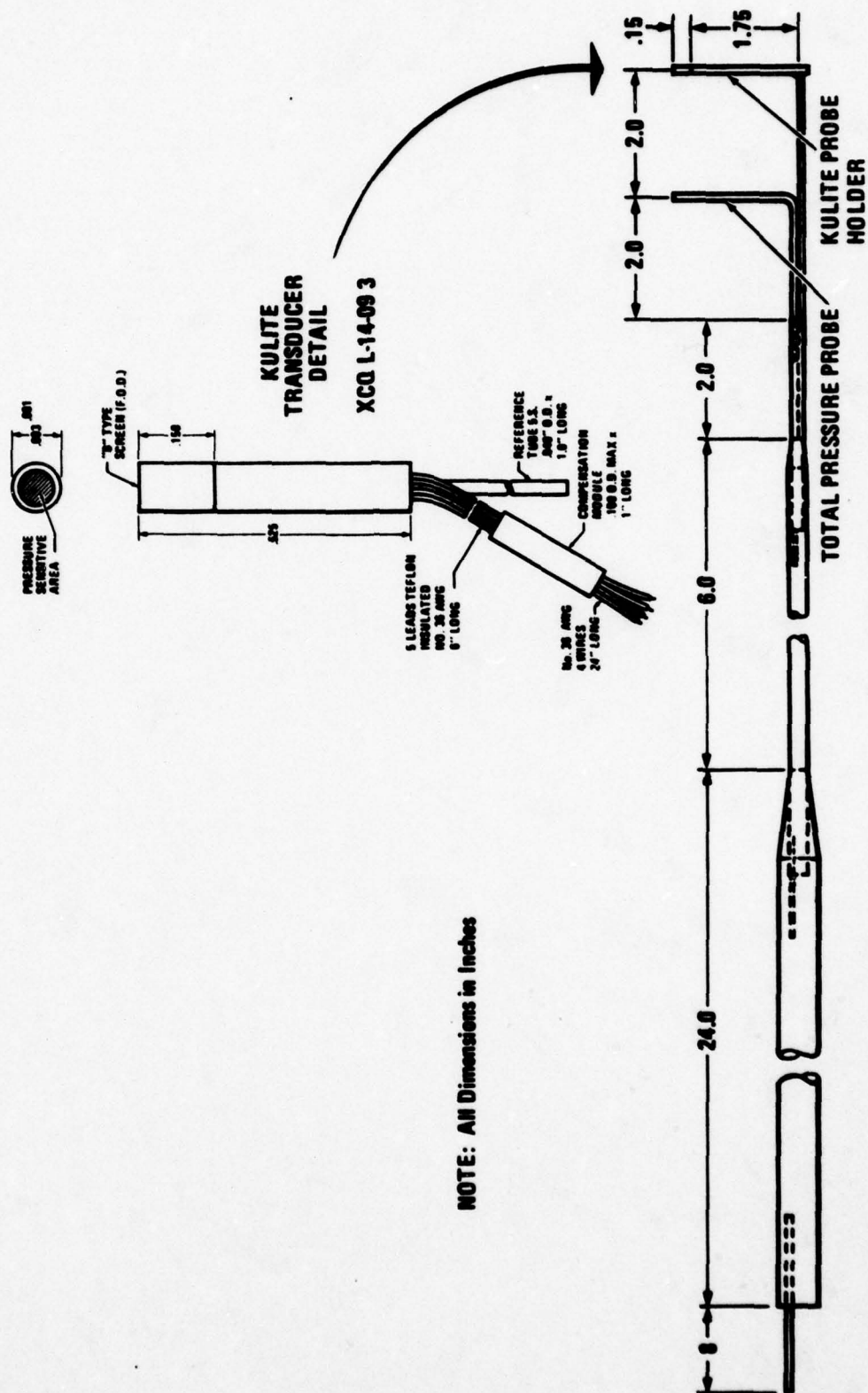


Figure 19 A Kulite/Total Pressure Probe Was Used to Survey the Nozzle Exit

turbulence. Only one transducer was required throughout the testing. The XCQL-14-093 Kulite model is essentially a model CQ-080-25 with a longer barrel and an FOD protective screen over the 0.08-inch-diameter, pressure-sensitive, silicone transducer face, which increases the total transducer outside diameter to 0.093 inch. The operating response characteristics are reported by the manufacturer to be identical to that of the CQ-080-25 (see Table 2-4). The frequency response characteristics of this Kulite transducer are related to the accuracy of the turbulence measurements obtained in this experiment, as described in Section 2.4.

The total pressure measurement subsystem consisted of the total pressure probe on the Kulite/total probe, which was connected to a Data Sensors Inc. Model PB415-B9 \pm 40 psid pressure transducer. This pressure transducer provided a continuous electrical signal which, when integrated over 1/60 second by an integrating voltmeter, provided an average total pressure (psig) value for a given probe location. This value was divided into the Kulite-measured fluctuating pressure to obtain the turbulent intensity, I.

(3) and (4) Thrust and induced-loads measurements were made on identical 5-component-strain-gage, moment-type

Table 2-4 OPERATING RESPONSE CHARACTERISTICS OF THE CQ-080-25 KULITE TRANSDUCER

Rated Pressure	25 psi
Maximum Pressure	50 psi
Output-Nominal at Rated Pressure	65 mV
Bridge Excitation	5 V Nom (7.5V Max) (AC or DC)
Bridge Impedance	750 Ω (Nom.)
Zero Balance	\pm 3% FS max.
Combined Non-Linearity and Hysteresis	\pm 0.75% FS max.
Repeatability	0.15%
Compensated Temperature Range	80°F To 180°F
Operating Temperature Range	65°F To 250°F
Change of Sensitivity With Temperature	\pm 1.5%/100°F
Change of No-Load Output with Temperature	+0.5% FS/100°F (max.)
Natural Frequency (Approximate)	230kHz
Acceleration Sensitivity Perpendicular Transverse	.0002%FS/g .00004%FS/g

balances designated as GD 1000A1 and A2; these balances are capable of measuring maximum moment loadings up to 650 inch pounds at a 30,000-psi stress.

(5) Fountain survey measurements were made with the same flow-field survey rake used in the Reference 5 tests. This rake, shown in Figure 20, has 13 chromel/alumel thermocouples (not used in this investigation) and 14 cone pressure probes. Each of the cone probes has four pressure orifices on the conical surface and one total-pressure port in the nose. Data obtained with the cone probes were used to determine local total pressure and local flow direction.

The cone-probe pressures were sampled with five scanivalves. All five of the pressure orifices on one of the 14 probes were read simultaneously (one per scanivalve); the scanivalves then cycled to the next probe. The interval between probe readings (five pressure orifices) was approximately 1 second; thus, about 14 seconds were required to take data from all of the rake's probes.

Since the cone probes are not accurate for determining flow direction when the flow angles exceed about 40 degrees, constraints were placed in the test data reduction to eliminate the data when the indicated flow angles, θ_F or

γ_F , were greater than 42 degrees (based on rake calibrations) or when the total pressure probe on the nose of the cone probe indicated a pressure less than static ambient.

The scanivalves, which sampled the cone-probe data, were each equipped with a Druck Ltd. differential pressure transducer, Model PDCR22, with a range of ± 2.5 psia and with a Recording Devices Model SCSG/075 signal conditioner.

2.4 Data Accuracy

Accuracies were estimated for the turbulence, thrust and induced loads, model altitude, and fountain rake measurements. These measurements are considered sufficiently accurate to justify the conclusions presented in Section 4.0.

2.4.1 Turbulence Measurement

The error in turbulent intensity measurement due to the non-linear frequency response characteristics of the Kulite transducer is reported by the manufacturer to be less than 3% for the turbulence frequency range of this experiment (< 50 kHz) provided the turbulence characteristic length (eddy size) is greater than the diameter of the Kulite transducer face (0.08 in); as this characteristic length approaches the size of the transducer face, the error increases. Since the turbulence screen S_1 and S_2 and the pressure-profile

plates P_1 and P_2 used in this experiment all have characteristic lengths larger than the transducer face, the error in turbulent intensity measurement for these cases is considered negligible ($< 10\%$). For the baseline nozzle case (with choking plate), the eddy characteristic length is probably somewhat smaller than the transducer face diameter and a significant error may be produced (with indicated readings too low). However, since the turbulence intensities are low for the baseline nozzle case ($< 10\%$), large percentage errors in their measurement have little effect on the conclusions of this experiment. (See Section 3 for a discussion of turbulence eddy size and related frequencies.)

The error due to the frequency response characteristics of the true RMS meter used in measuring the turbulence is seen (Figure 21) to be less than 10.5% at the worst case (50 kHz with baseline nozzle and corresponding low turbulence level). Therefore, the RMS meter is sufficiently accurate to cause no effect on the conclusions of this experiment.

Also, as noted above, the sampling rate was fast enough and for a long enough duration to ensure that, in the turbulence frequency ranges of interest (< 50 kHz), the total

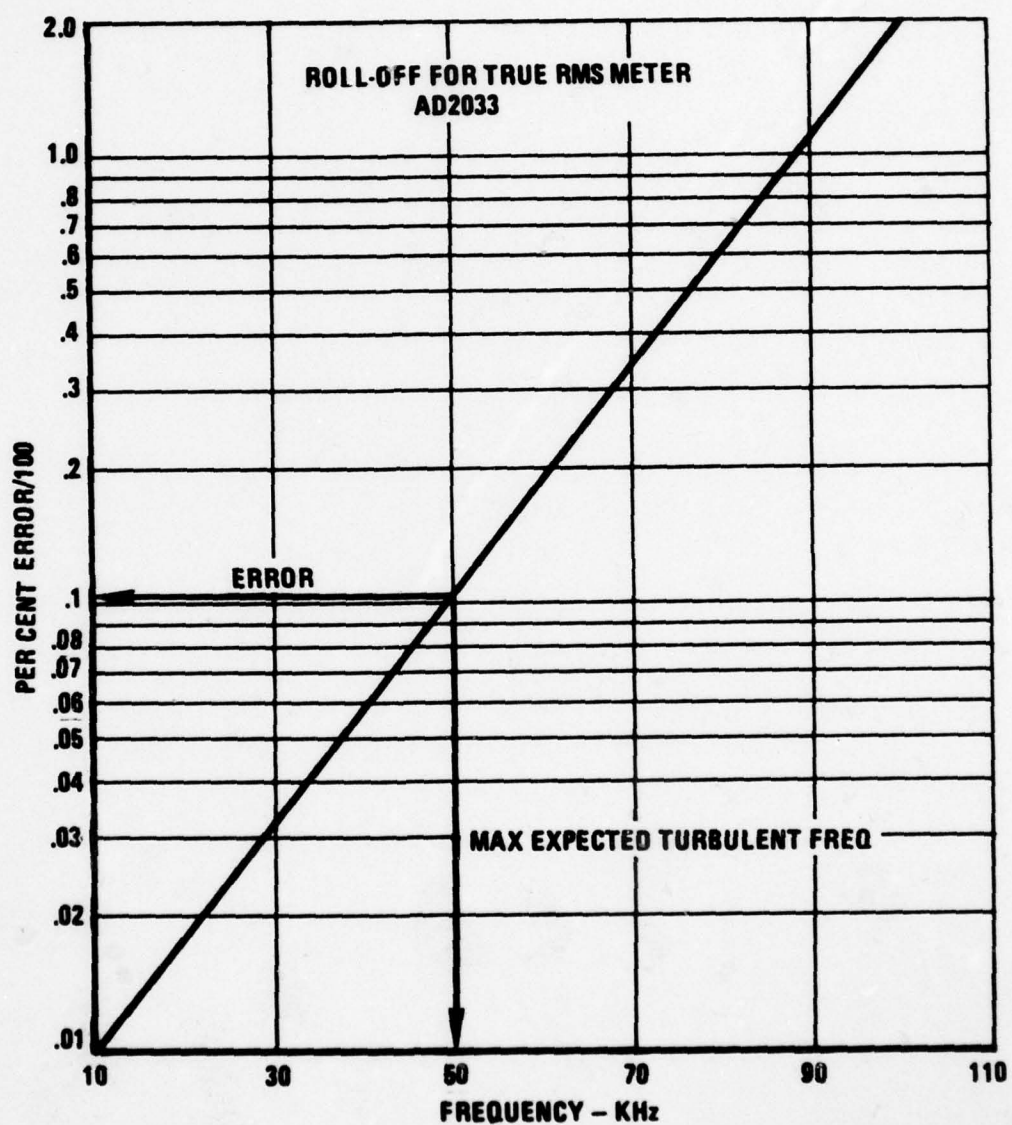


Figure 21 Frequency Response Characteristics for the AD 2033 True RMS Meter

turbulence-measurement-system error was insignificant in terms of the objectives of this experiment. The total-probe bending near the nozzle edge did not introduce error into the calculated turbulent intensities because the outboard 10% radius was not used in calculating the area-weighted average RMS or total-pressure values.

The measurement accuracy of the Data Sensors pressure transducer used with the total pressure probe was $\pm .4$ psid.

The traversing rig positioning accuracy was ± 0.04 inch.

2.4.2 Thrust and Induced-Loads Measurement

Checkloadings indicated errors in the thrust and induced loads balance measurements (as shown in Figure 22) which result in net induced normal force readings $(\frac{\Delta L}{F_j})$ with up to a + 0.8% error (worst case).

2.4.3 Model Altitude Measurement

The error, $\Delta h/D$ in the altitude position indicated by the ground board potentiometer is shown in Figure 23. Since $h/D_s < 2.5$ were not tested in this experiment, the corrections to the indicated readings were considered negligible and are not included in the data presented in this report;

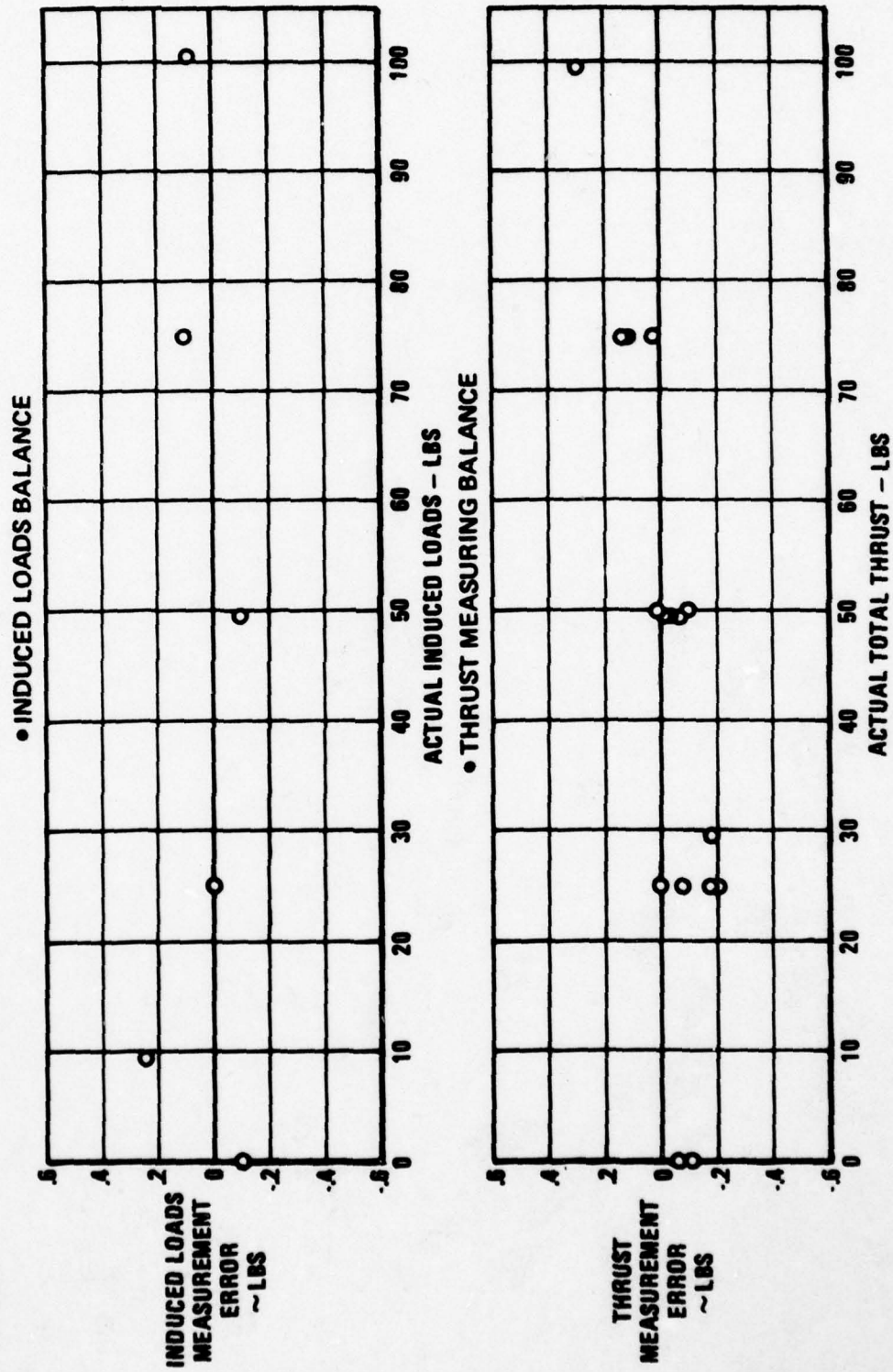


Figure 22 Error in Induced Loads and Thrust Measurement

ALTITUDE POSITIONING ERROR

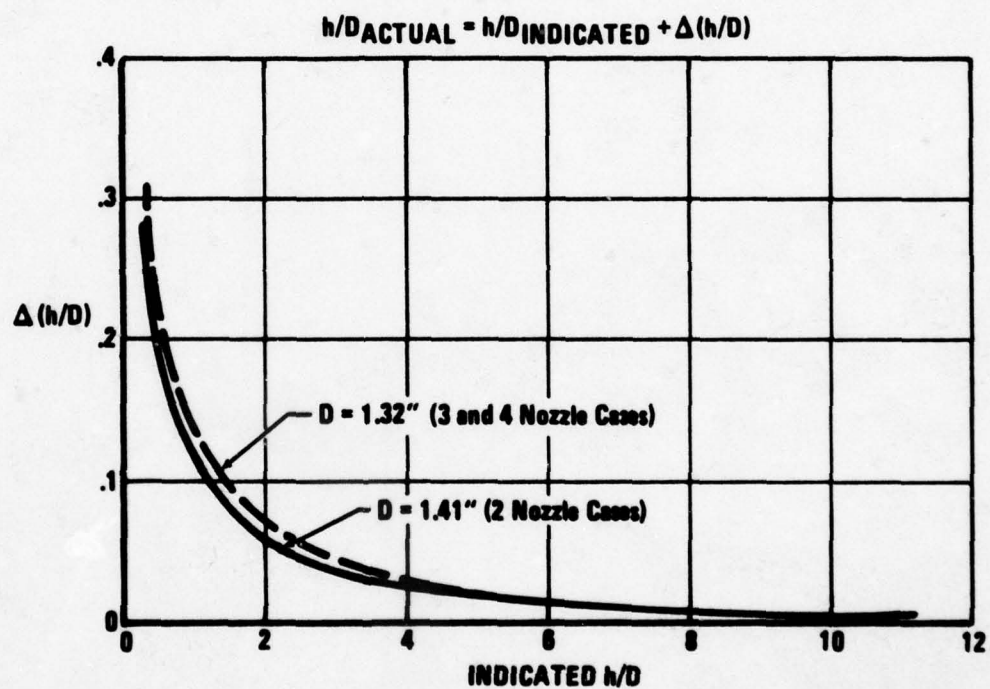


Figure 23 Altitude Positioning Error of the Ground Board Potentiometer

the maximum correction to the data presented in this report is + .057 for the three- and four-nozzle configurations at an h/D of 2.5.

2.4.4 Fountain Rake Measurements

The pressure transducers used for measuring the rake-pressure had a $\pm 0.06\%$ accuracy over the ± 2.5 -psia pressure range. These transducers are considered the most accurate transducers commercially available.

The same traversing-rig positioning accuracy of ± 0.04 inch was present in the fountain rake measurements as noted for the nozzle calibration testing.

Some unknown error is introduced into the fountain survey measurements as a result of making the readings over a finite 14-second time interval. If the fountain flow is itself highly turbulent, as has been reported in Reference 12, there is certainly some question about the validity of using a steady-state flow-type device like a pressure rake to make accurate measurements in a highly unsteady flowfield. However, it should be recalled that the objective of this investigation was to study trends and to quantify results within the scope of the contracted effort. In future investigations, other means of quantifying the fountain flow-

field and its changes with nozzle exit conditions might be considered.

3. RESULTS

The experimental results and analysis of the nozzle calibration, induced loads, and fountain survey testing will demonstrate, for the nozzle/planform configurations tested, the criticality of nozzle exhaust simulation on the net induced forces as well as the component forces and will provide an indication of the mechanism of the associated flow phenomena.

3.1 Nozzle-Calibration Testing

Appendix A contains the nozzle-exit fluctuating and corresponding total pressure survey results for each nozzle/device combination described in Section 2.2.

Although the X and Y traverses show reasonable agreement in most cases, they do not agree perfectly. Therefore, the following averaging procedure was used to determine the turbulent intensity. The area-weighted average RMS pressure was determined from the X-traverse using the RMS distribution obtained from the nozzle centerline to $+0.4r/D$ and then repeated for the X-traverse RMS distribution obtained from the nozzle centerline to $-0.4r/D$. This process was then repeated for the Y-traverse distribution (from centerline to $+0.4r/D$ and then to $-0.4r/D$). These four

values were then arithmetically averaged to obtain the area-weighted average RMS pressure. The same process was performed for the total pressure surveys. Finally, the turbulent intensity was calculated as the ratio of the area-weighted average RMS pressure to the total pressure determined in this manner. This process collapsed the data scatter in the X and Y traverses to provide a more meaningful turbulent intensity value.

The baseline nozzle configuration, N_3^2 , exhibits the classic "top hat" turbojet-type uniform total-pressure distribution, with a correspondingly low RMS fluctuating pressure level also uniform across the nozzle exit except near the nozzle edges where the large shears occur between the jet and the still, ambient air (Figures A-1 through A-6). The total and RMS pressures increase with increasing NPR; but the total pressure increases at a faster rate, producing a decreasing turbulent intensity with increasing NPR.

Screens S_1 and S_2 (Figures A-7 through A-18) produce increased RMS fluctuating pressures and total pressures with N_3^2 at a given NPR while maintaining virtually uniform total pressure distributions. The screens also produce variations with NPR similar to those described above


for the baseline nozzle.

Total-pressure distributions characteristic of turbofan engines with varying bypass ratios were obtained with pressure profile plates P_1 and P_2 installed in nozzle N_3^2 (Figures A-19 through A-22). Figure 15 above shows a comparison of the nozzle exit total-pressure distribution obtained at an NPR of 1.5 with the baseline nozzle and with pressure profile plates P_1 and P_2 installed. Corresponding increases in fluctuating RMS pressure were also measured with P_1 and P_2 installed; similar trends to the baseline-nozzle case were also noted for variations in NPR (see Appendix A).

The variations in turbulent intensity with NPR calculated from these surveys are summarized in Table 3-1 for each of the nozzle/device combinations. These results are shown in plotted form in Figure 24.

The turbulent intensity variations and the total pressure surveys presented in Figure 24 and in Appendix A show that the ranges of nozzle-exit turbulent intensity and pressure profiles expected for real aircraft engines were successfully covered. Rolls Royce has reported (Reference 13) turbulent intensity measurements, I_{velocity} , of full-scale turbojet (Olympus 593) and turbofan (RB211) engines

Table 3-1 TURBULENT INTENSITY, I VS NPR FOR SCREENS AND PLATES

NOZZLE CONFIGURATION	DEVICE	I~%	NPR	FIG. NO.
N_3^2 	BASELINE	7.24	1.503	A-1
		5.87	1.551	A-2
		5.08	1.924	A-3
		2.39	1.958	A-4 ¹
		4.26	2.096	A-5
		4.58	2.276	A-6
	S1	17.48	1.517	A-7
		17.47	1.531	A-8
		14.00	1.931	A-9
		11.83	2.317	A-10
		12.73	2.321	A-11
		18.86	1.552	A-12
	S2	17.75	1.855	A-13
		16.14	1.958	A-14
		17.57	1.986	A-15
		15.91	2.041	A-16 ¹
		14.66	2.317	A-17
		16.05	2.372	A-18
	P1	29.17	1.551	A-19
		25.40	1.972	A-20
	P2	21.83	2.310	A-21
		18.99	1.520	A-22
	BASELINE	21.55	1.510	A-23
		15.88	1.990	A-24
		14.96	2.420	A-25
		3.80	1.897	A-26 ¹
		15.24	2.062	A-27 ¹
		16.83	2.010	A-28 ¹
N_{13}^2 N_{11}^1 (with N_{10}^1) (Aft Plenum) N_9^1 (with N_8^1) (Forward Plenum)				

¹ Data Taken After Hardware Modification to Test with Plant-Air System

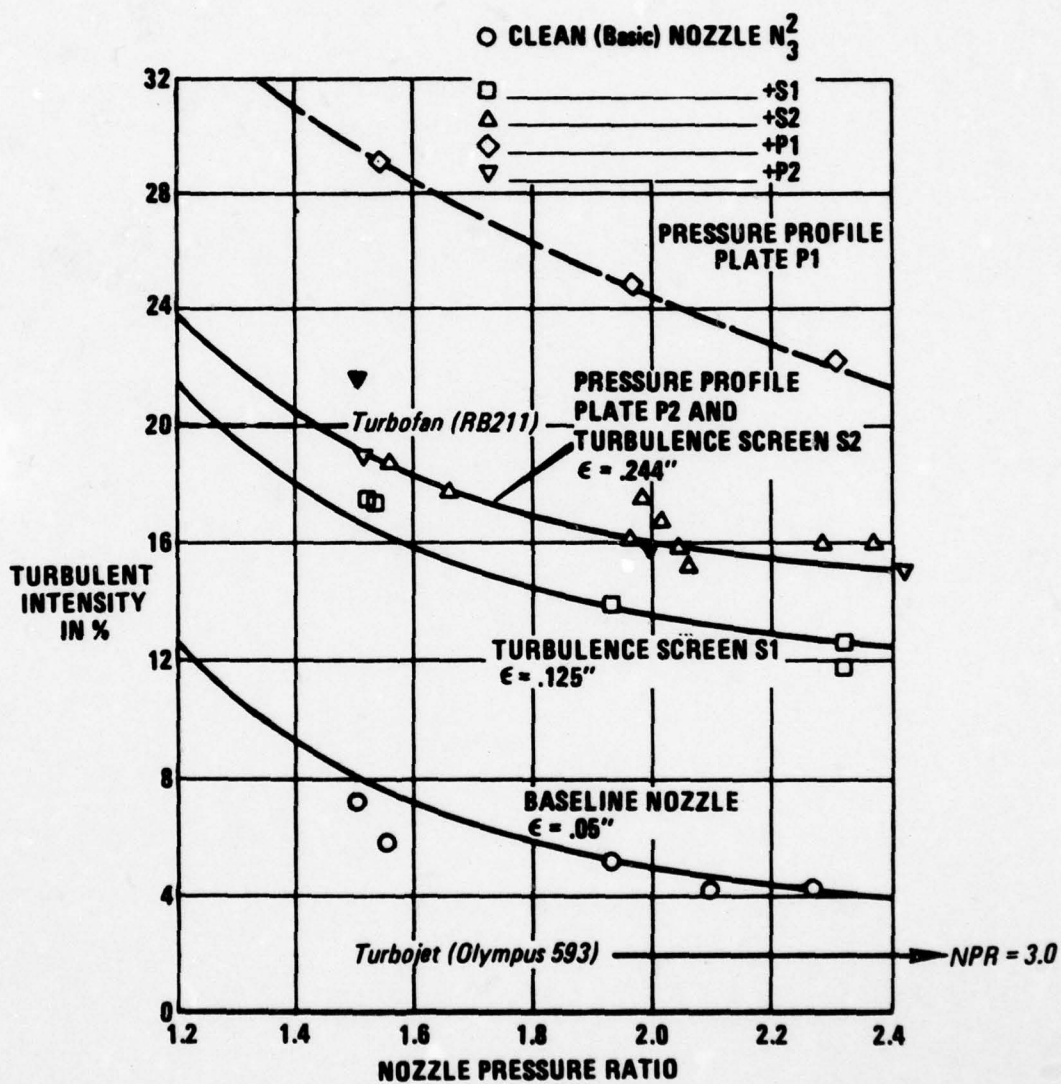


Figure 24 The Variation of Turbulent Intensity with NPR for Screens and Plates

measured with a laser velocimeter that yields equivalent "pressure" turbulence intensities (I_{pressure} equivalent to $(I_{\text{velocity}})^2$), comparable to the Kulite measurements, of 1% to 2% for the turbojet and 1% in the core regions and up to 20% in the fan region for the turbofan engine. Lockheed has made similar laser velocimeter measurements of the flowfield exiting from the nose lift-fan in a large-scale model (70%) of the McDonnell-Douglas Model 260 Type A Navy VSTOL aircraft (Reference 14); these measurements showed equivalent I_{pressure} values of 25%. Therefore, the choice of screens and pressure profile plates in this test was guided by a desire to cover the range of nozzle exit turbulent intensity, I_{pressure} , up to 25% while varying the total pressure distribution to simulate both turbojet and turbofan engines.

In Figure 24 it is demonstrated that turbulent intensity can be changed in three ways: (1), by changing the base level with the screens while maintaining a uniform total-pressure distribution, (2) by distorting the total-pressure distribution with the plate devices, and (3) by changing the nozzle pressure ratio. It is also shown in Figure 24 that, within the accuracy of the data, the same variation in turbulent intensity with nozzle pressure

ratio occurs at all screen grid sizes (including the choking plate of the baseline nozzle case, see Figure 14).

The P_2 pressure profile plate also exhibits this same decreasing variation in turbulent intensity with increasing NPR demonstrated by the turbulence screens. The P_1 pressure plate, however, exhibits a slightly different variation of I with NPR but the trend is certainly the same as with the screens and P_2 .

Increasing the screen grid size increases the turbulent intensity. The turbulence produced by the screen grid can be characterized by the large-scale eddy size, ϵ_e (after Kolmogorof, Reference 15) associated with the turbulence at the NPR. The large-scale eddy size is proportional to the largest physical dimension causing the turbulence, which in the case of the screens is taken as the width of the bars making up the screen grid, ϵ ; ϵ is 0.05 inch for the choking plate of the baseline nozzle case, 0.125 inch for S_1 , and 0.240 inch for S_2 .

Kolmogorof's argument for a characteristic turbulent large-scale eddy size leads to an estimate of the large-scale eddy size and the associated frequencies produced by the baseline nozzle and screens. He suggests that if the Reynolds number (based on the characteristic length producing

the turbulence, i.e., the screen grid size in this case is sufficiently high (say $> 1 \times 10^3$ which is true for all tested grid sizes and NPR's), there are wave numbers, K_e , such that the turbulence is statistically in equilibrium,

$$\text{where the wave number } K_e = \frac{2 \pi f}{U} \quad (2)$$

and f = frequency of the large-scale eddies characterizing the turbulence,

and U = constant velocity that is large compared with the turbulent perturbation velocity, u' ; U = nozzle exit velocity in this case).

If the turbulence is in statistical equilibrium, then the average size of the energy-containing eddies of consequence is $\epsilon_e = 1/K_e$ (Reference 15) and therefore, the eddy size is

$$\epsilon_e = \frac{U}{2 \pi f} \quad (3)$$

Also if the Reynolds number is high enough ($> 1 \times 10^3$), the Strouhal number, S ,

$$\text{where } S = \frac{fD}{U}, \quad (4)$$

is constant. If D is taken as the grid size of the screens producing the eddies, ϵ , then Equations 3 and 4 yield

$$\epsilon_e = \frac{\epsilon}{2 \pi S} \quad (5)$$

which allows an estimate of the turbulent large-scale eddy size provided a suitable experimentally determined value of S is available. In Reference 16 and 17 it is indicated

AD-A073 114

GENERAL DYNAMICS CORP FORT WORTH TX FORT WORTH DIV
THE CRITICALITY OF ENGINE EXHAUST SIMULATIONS ON VSTOL MODEL-ME--ETC(U)
JUL 79 J R LUMMUS

F/G 20/4

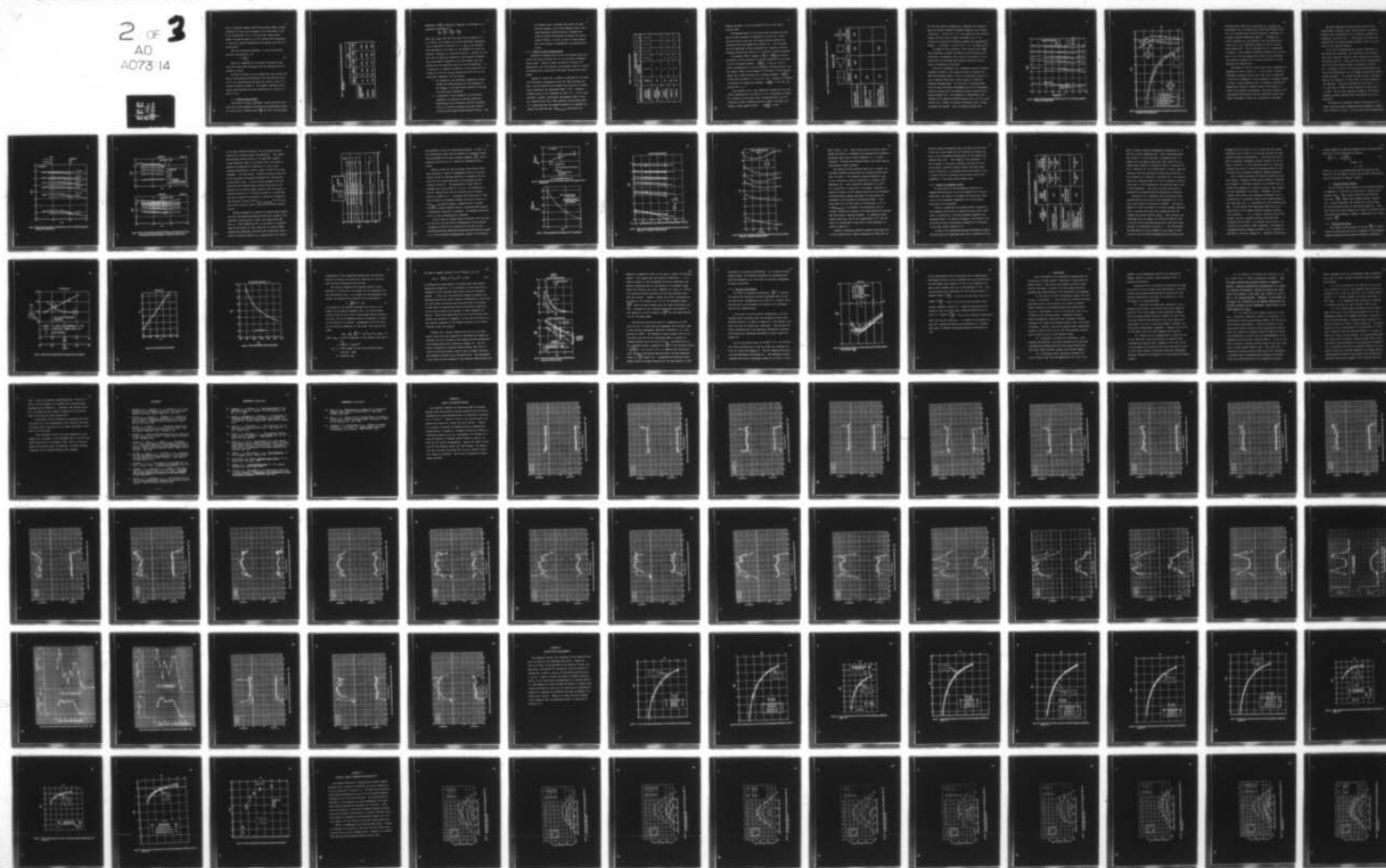
N00014-78-C-0384

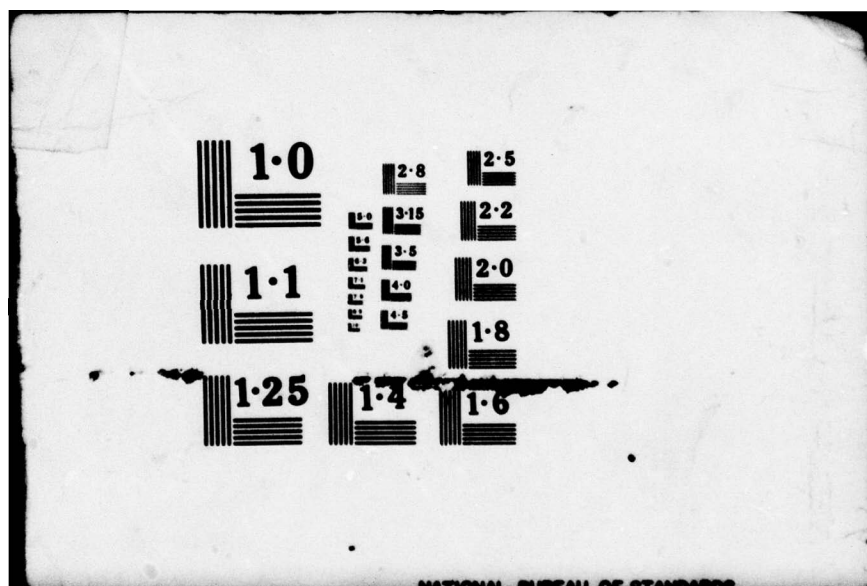
UNCLASSIFIED

ONR-CR212-255-1F

NL

2 OF 3
AD
A073 114





that at Reynolds numbers $> 1 \times 10^3$, the Strouhal number becomes constant for flows past cylinders (0.21) and plates (0.18). To be conservative, an $S = 0.21$ was used, which yields higher frequencies since it is not certain which experimental case more closely approximates the present case with the screen grids.

Then the associated frequency, f , can be calculated directly from Equation 3 as

$$f = \frac{U}{2 \pi \epsilon_e} \quad (6)$$

Table 3-2 summarizes the estimated large-scale eddy sizes and associated frequencies for the choking plate and screens S_1 and S_2 .

The data in Figure 22 also demonstrate that varying the nozzle total-pressure distribution from the baseline turbojet to the turbofan-type profiles with plates P_1 and P_2 increases turbulent intensity. The highest turbulent intensities were measured with the profile plate P_1 (29% at an NPR of 1.55).

3.2 Induced-Loads Testing

Variations of nozzle turbulence, nozzle pressure ratio, and nozzle total-pressure distributions do measurably affect not only the net induced forces ($\frac{\Delta L}{F_j}$) but also the individual

**Table 3-2 ESTIMATED LARGE-SCALE EDDY SIZES AND ASSOCIATED FREQUENCIES
FOR SCREENS**

	ϵ (INCHES)	S	ϵ_g (INCHES)	$f \sim \frac{1}{(\text{SEC})}$		
				NPR = 1.5 $\frac{\text{ft}}{\text{SEC}}$ U = 830	NPR = 2.0 $\frac{\text{ft}}{\text{SEC}}$ U = 1138	NPR = 2.4 $\frac{\text{ft}}{\text{SEC}}$ U = 1138
BASELINE NOZZLE WITH CHOKING PLATE	.05	.21	.0379	41,832	57,355	57,355
SCREEN S₁	.125	.21	.0947	16,732	22,940	22,940
SCREEN S₂	.240	.21	.118	8,715	11,949	11,949

components of $\frac{\Delta L}{F_j}$ as defined in Equation 1 by Karemaa et al (repeated from Section 1).

$$\frac{\Delta L}{F_j} = \frac{\Delta L_j}{F_j} + \frac{\Delta L_{FC}}{F_j} + \frac{\Delta L_{FI}}{F_j} \quad (1)$$

where ΔL_j equals the lift loss due to pure suckdown (i.e., no fountain jets present) and can be determined experimentally as described in Section 2.2.2. ΔL_{FC} is the bouyant force produced by the impact of the fountain jet upon the planform, and ΔL_{FI} is a correction factor to account for the fact that the physical presence of the fountain interferes with entrainment of ambient air by the exhaust flow and ground jets and therefore alters the pure suckdown ΔL_j . It is important to examine the effects of the nozzle-exit conditions not only on the net induced force but also on the individual components for two reasons:

1. The changes in the individual components provide insight and understanding into the mechanism of the changes in the flow field produced by varying the nozzle-exit conditions.
2. A definition of the changes on the individual components is required to develop predictive methodology for an arbitrary aircraft configuration or to correct configuration model results for full-scale engine nozzle exhaust effects. The

net induced force ,although often small for many aircraft designs, can be the algebraic sum of very large oppositely directed forces (suckdown and fountain forces) and failure to correct for nozzle exhaust effects on either or both of these components could result in significant net-induced-force errors.

3.2.1 Effects on Net Induced Forces

Appendix B contains plots of the net-induced-force variations with model altitude for all of the nozzle configurations tested. Table 3-3 shows the matrix of nozzle configurations, exit flow devices, and pressure ratios for which net-induced-force variations with model altitude were determined.

Figure B-1 shows that, as NPR is increased for the baseline two-nozzle configuration with the large blocking surface, the net induced force becomes more positive as choked-nozzle conditions are approached ($\text{NPR} = 1.89$), reaching a constant level at all altitudes for $\text{NPR} > 2.0$. In all cases (baseline, screens, and plates) the maximum effect on the net induced forces due to NPR variation occurs before $\text{NPR} = 2.0$, indicating that the reduced variation in turbulent intensity with NPR for $\text{NPR} > \text{NPR}_{\text{critical}}$ tracks with the

Table 3-3 NET-INDUCED FORCE TEST MATRIX

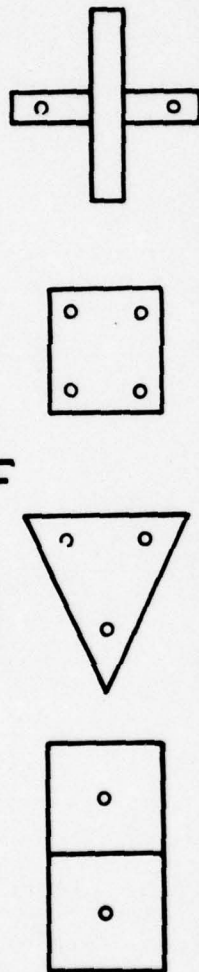
CONFIGURATION	TURBULENCE DEVICE					
	NPR	BASELINE (Choking Plate)	S1	S2	P1	P2
2 NOZZLES (Rectangular Blocking Surface)	1.5	X	X	X	X	X
	2.0	X	X	X	X	X
	2.4	X	X	X	X	X
2 NOZZLES (Cruciform Blocking Surface)	2.0	X	-	X	-	-
1 NOZZLE (Pure-Suckdown)	2.0	X	X	X	X	X
3 NOZZLES	2.0	X	X	X	-	-
4 NOZZLES	2.0	X	X	X	X	X

reduced variation in the net-induced forces at the super-critical NPRs.

The maximum effect of the nozzle-exit variables observed from the data presented in Appendix B for the two-, three-, and four-nozzle cases with the large blocking surfaces are discussed below and summarized in Table 3-4. Also included are the significant results obtained for a smaller cruciform blocking surface more typical of a realistic aircraft planform.

The maximum effect (change in $\frac{\Delta L}{F_j}$ or $\Delta\left[\frac{\Delta L}{F_j}\right]$) of nozzle turbulence with the screens on the net induced force was found to be an increased suckdown ($\Delta\left[\frac{\Delta L}{F_j}\right] = -0.08$) for the two-nozzle configuration with the rectangular blocking surface over the range of NPRs tested (Figures B-2 through B-4). The maximum effect due to NPR variation was a reduced suckdown ($\Delta\left[\frac{\Delta L}{F_j}\right] = +0.04$) (from an NPR of 1.5 to one of 2.4). Varying the pressure distribution increased the suckdown ($\Delta\left[\frac{\Delta L}{F_j}\right] = -0.05$) near the ground ($h/D = 2.5$).

The variation due to the turbulence screens for the three-nozzle configuration at an NPR of 2.0 is illustrated in Figure B-8. Unlike the two nozzle case, the maximum effect of the turbulence screen variation occurs at higher altitudes, producing a large negative effect ($\Delta\left[\frac{\Delta L}{F_j}\right] = -0.032$).

Table 3.4 EFFECTS OF NOZZLE EXIT VARIABLES ON NET-INDUCED FORCE, $\Delta L/F_j$ CHANGE IN $\frac{\Delta L}{F_j}$ 

	2 NOZZLE	3 NOZZLE	4 NOZZLE	CRUCIFORM
TURBULENCE (with Screens S1 & S2)	-.078	-.032	-.021	-.072
NOZZLE PRESSURE RATIO (from 1.5 to 2.4)	+.04	—	—	—
NOZZLE TOTAL PRESSURE PROFILE (with Plates P1 & P2)	-.05	—	-.024	—

For the four nozzle configuration, changing the turbulence with the screens produced a maximum change at low altitudes ($\Delta[\Delta L/F_j] = -.021$ at $h/D = 2.5$, see Figure B-9) but similar changes are also seen at higher altitudes ($h/D = 7.0$).

Varying the pressure distribution produces the same maximum change ($\Delta[\Delta L/F_j] = -0.024$ at $h/D = 7.0$, see Figure B-10).

In Figure 25 the variation of net induced force ($\frac{\Delta L}{F_j}$) with turbulence (screens) and NPR for the two-nozzle configuration is displayed; this curve is also typical of the trends that are obtained with pressure distribution and nozzle configuration variations.

Since the rectangular and triangular research blocking surfaces of Figure 13 are large and seem to dominate the flow field beneath them, it was of considerable interest to test a smaller plate that is more typical of realistic airplane configurations. To this end, a cruciform plate with the same two-nozzle arrangement as for the rectangular plate was tested with the baseline nozzles and with the S_2 screens (Figure 26). The suckdown is considerably less because of the smaller blocking surface size, but it is also evident that, unlike the larger rectangular plate, strong fountains are present. This is probably because the

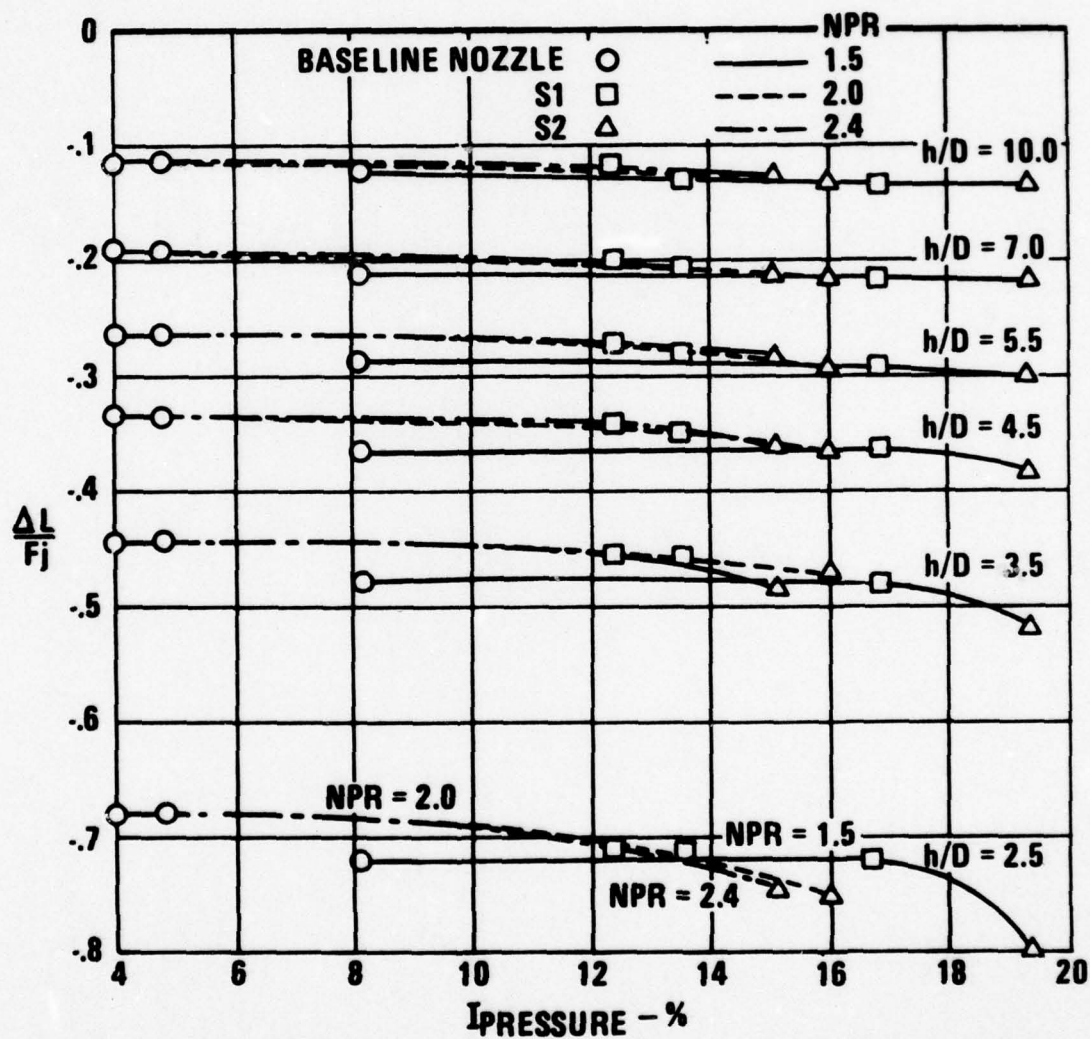


Figure 25 Effects of Turbulence Screens on Net-Induced Force, $\Delta L/F_j$, for Two-Nozzle Configuration - Referenced to Turbulent Intensity

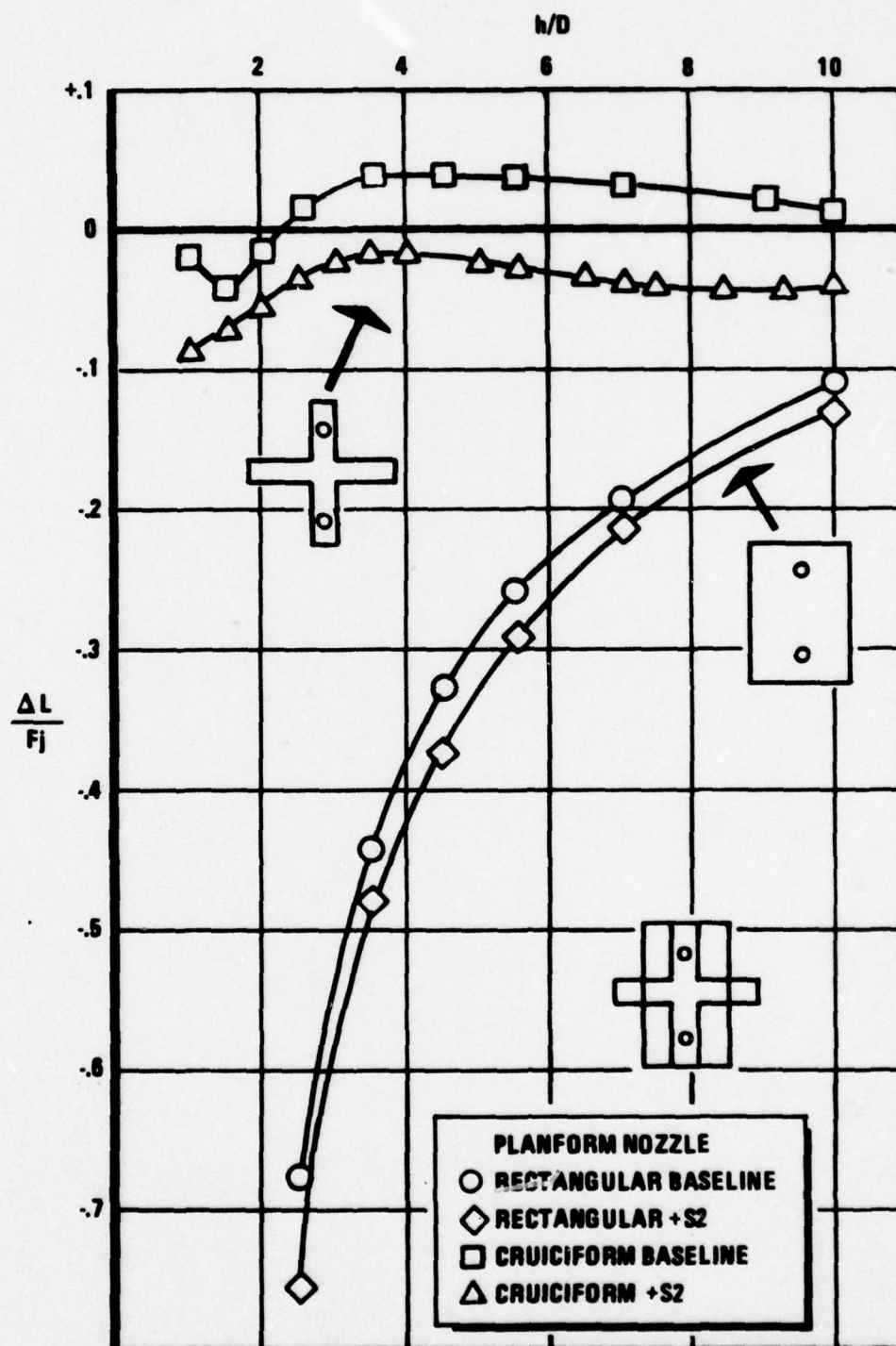


Figure 26 Real Aircraft Engine Turbulence Levels Cause Large Changes in Ground Effects for Aircraft and Research Type Blocking Surfaces

cruciform plate makes more surrounding air available for entrainment into the ground jets, which then requires less air to be entrained away from the fountain, resulting in a stronger fountain (Reference Figure 2). Changing the nozzle turbulence in the presence of the cruciform plate results in a very significant change in the net induced force (Figure 26). This is probably due to a combination of effects. The increased turbulence increases the entrainment of the free and ground jets, which in turn decreases the fountain strength, both of which contribute to a more negative net induced force.

The amount of lift or thrust loss is very configuration dependent as seen in Table 3-4. In all cases, increasing turbulence increases the net lift loss, but the magnitude of the loss is dependent on how turbulence is changed, whether by screen, nozzle pressure ratio, or pressure distribution. Knowing the turbulent intensity alone is not enough to predict an airplane's performance, the nozzle pressure ratio and pressure distribution are also important because they affect the manner in which the turbulence is developed.

The most significant result observed from the net induced force testing is that, when one goes to a smaller planform more characteristic of a realistic airplane configuration, one still sees a 10% thrust loss (which was observed with the large blocking surface), which is on the order of the airplane payload.

As an aid in determining the relative importance of the nozzle exit variables, the variations of net induced force with turbulent intensity, NPR, and model altitude are plotted for the two-, three- and four-nozzle configurations with the large blocking surfaces in Figures 25 through 28. In Figures 25 and 27 the variations produced with the two-nozzle configuration by the screens and pressure profile plates are shown. For a given altitude, $\Delta L/F_j$ is affected more by the changes in I than in NPR, but both parameters are important. Altitude variations for h/D_s from 2.5 to 5.5 also have an effect on the variations in $\Delta L/F_j$ due to I or NPR. For the same turbulent intensity, the screens produce a greater suckdown than the pressure plates at a given NPR.

The effects of turbulent intensity variation on the three- and four-nozzle configurations are compared in Figure 28 at an NPR of 2.0 only. For the four-nozzle configuration,

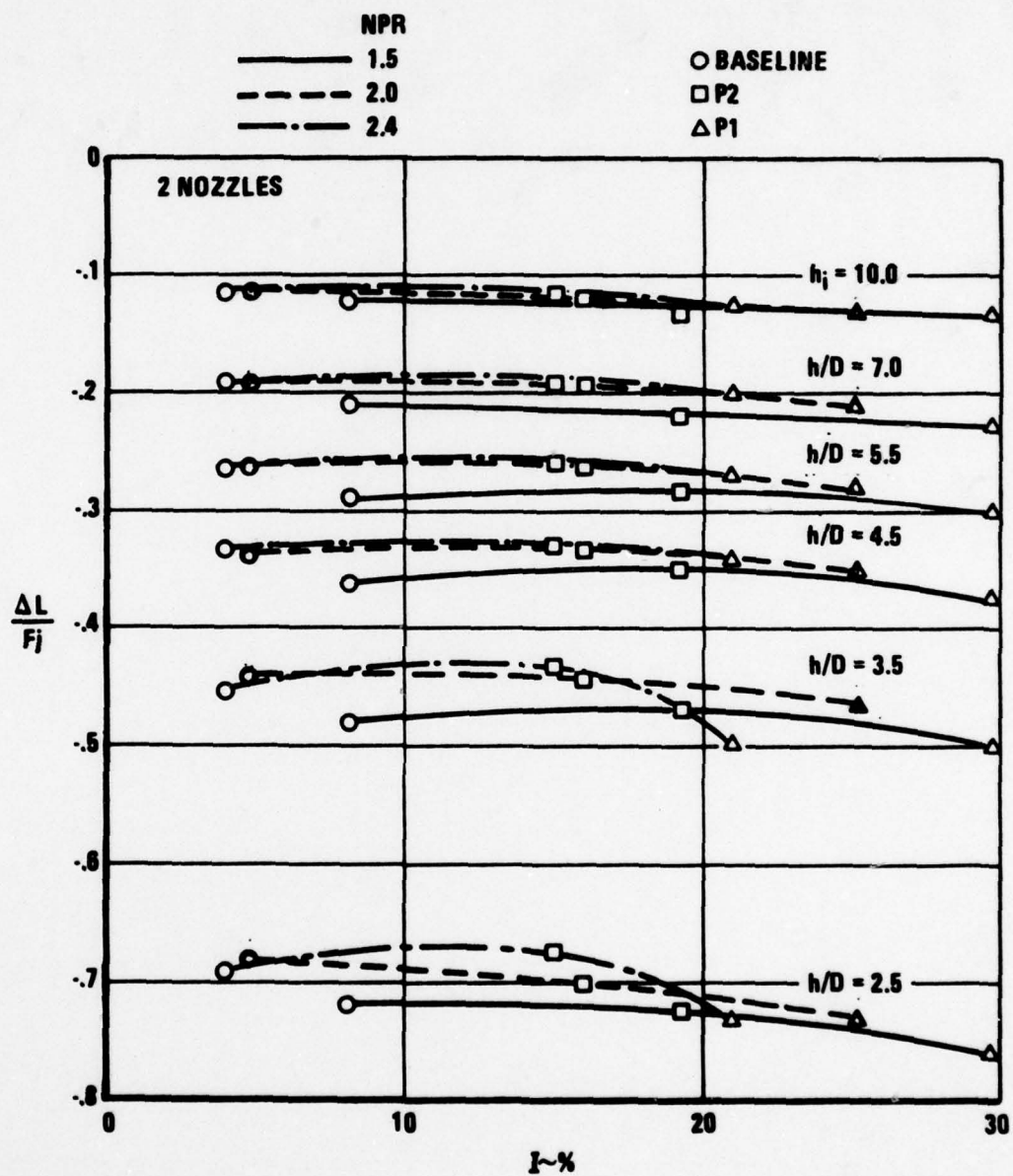


Figure 27 Effects of Pressure Profile Plates on Net-Induced Force, $\Delta L/F_j$, for Two-Nozzle Configuration — Referenced to Turbulent Intensity

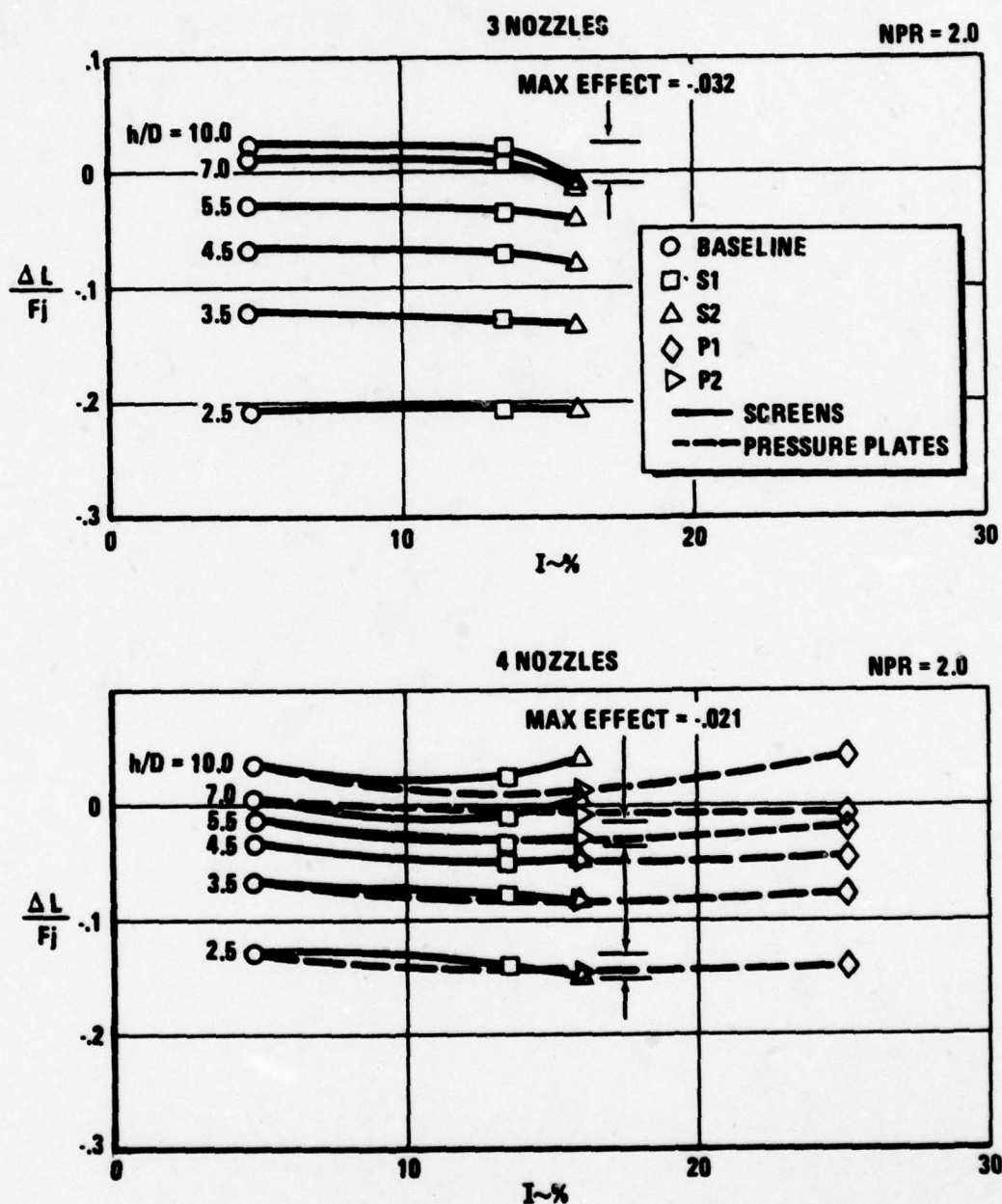


Figure 28 Effects of Turbulence Screens and Pressure Profile Plates on Net Induced Force, $\Delta L/F_j$, for Three-Nozzle and Four-Nozzle Configurations – Referenced to Turbulent Intensity

at the same turbulent intensity the P_2 pressure profile plate and S_2 screens produce the same $\Delta L/F_j$. The screens and pressure profile plates at the same NPR, probably create different types of turbulent flows; this might be expected considering the differences in their total-pressure distributions and the types of shear flows they represent. For this reason, turbulent intensity alone may be an unsuitable correlating parameter for the pressure-profile-plate cases. A more suitable parameter for characterizing the pressure-profile-plate flows may be the maximum total pressure (gage) required with each device to achieve the thrust of the baseline nozzle at a given NPR; the data in Figure 29 provides an illustrative example of the variation of $\Delta L/F_j$ with $P_{T_{\max}}$ (required) for the pressure profile plates P_1 and P_2 with the two-nozzle configuration.

Another parameter of interest for gaining some insight into the flow mechanism associated with the screens is the turbulence characteristic length, the large-scale eddy size, ϵ_e . Foley (Reference 18), in an effort to correlate some of the results of this study into an overall VSTOL prediction methodology, has shown that screen grid size, ϵ , which is directly related to ϵ_e (see Section 3.2), may be

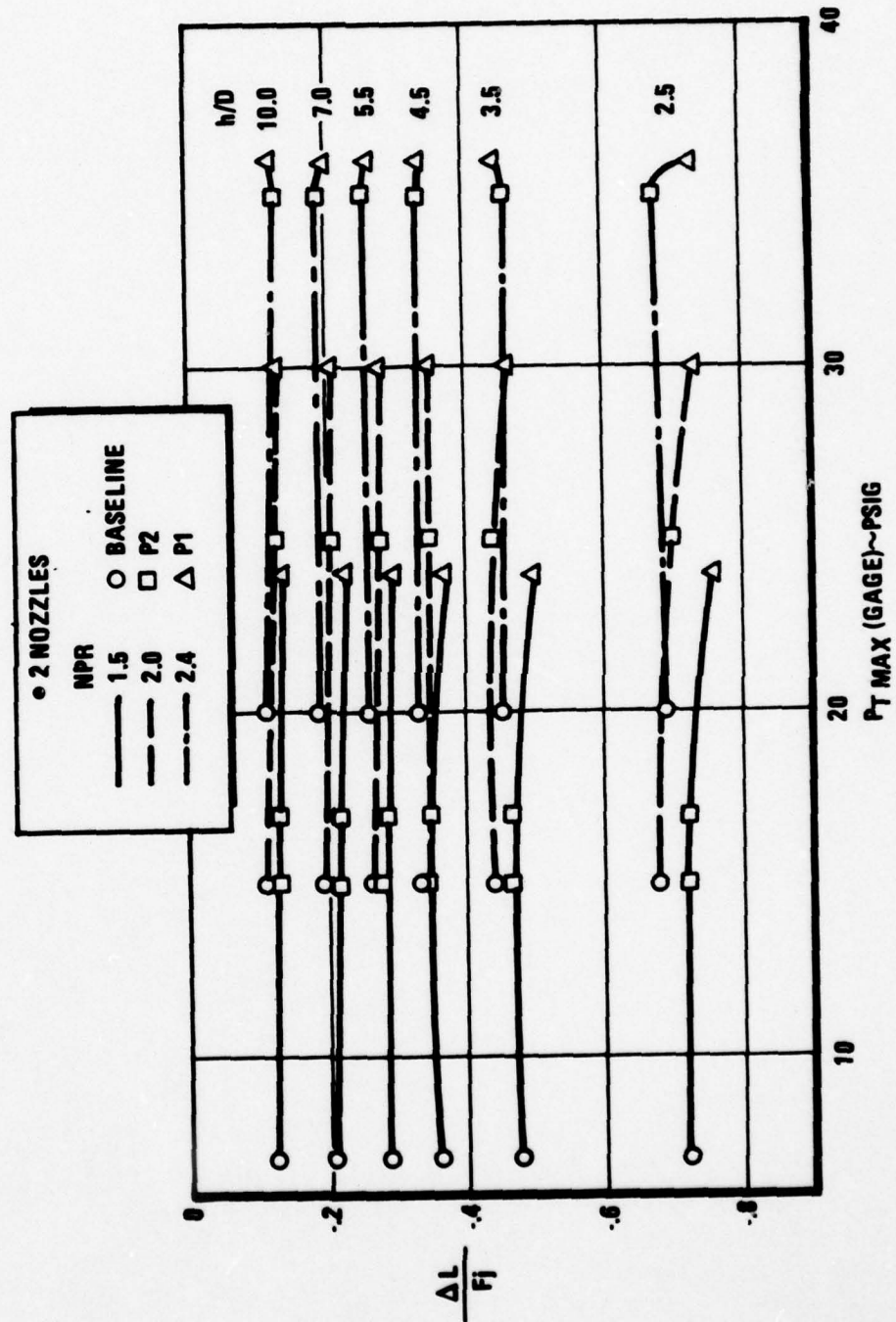


Figure 29 Variation of $\Delta L/F_j$ with $P_{T \text{ MAX}}$ (Required) for the Two-Nozzle Configuration

the parameter to use for correlating purposes. In fact, he has successfully shown that the effects of changing screens and varying NPR on the pure suckdown component, $\frac{\Delta L_j}{F_j}$, may be separated (see Section 3.2, Effects of Component Forces, below).

Similar curves for the two-nozzle configuration have been developed to show the independent effects on the net induced forces of varying turbulence by changing the base level with the screen grid size or by changing the NPR (Figures 30 and 31). The magnitudes of these effects, averaged over h/D_s of from 2.5 to 10.0, are referenced to the net induced force with the baseline nozzle choking plate at an NPR of 2.0. Increasing the screen grid or eddy size produces an increased suckdown (the ratio of $\Delta L/F_j$ to $\Delta L/F_{j_{REF}}$ is positive because a negative force is being divided by another negative force); increasing NPR produces a substantial reduction in suckdown. The maximum deviations due to altitude-averaging are indicated.

Plots of the net induced force variations with altitude for the two- and four-nozzle configurations are presented in Figures 31 and 32 as a function of the ratio of the nondimensionalized turbulence-producing characteristic length, ϵ/D , to the reference nondimensional length of the choking

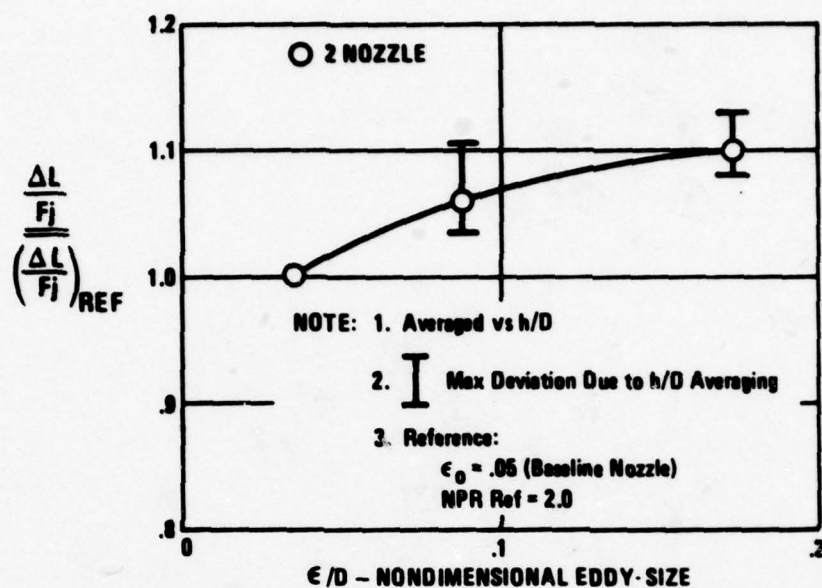


Figure 30 Effect of Varying Nozzle Exit Turbulence with Screens on Net-Induced Force for Two Nozzle Case

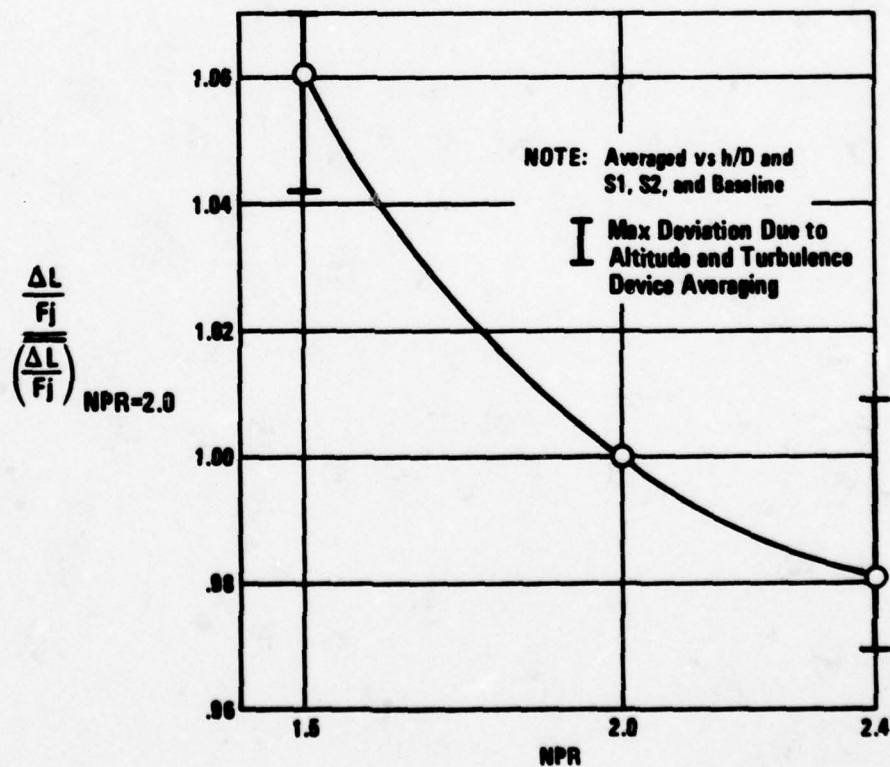


Figure 31 Effect of Varying NPR on Net-Induced Force for Two-Nozzle Case

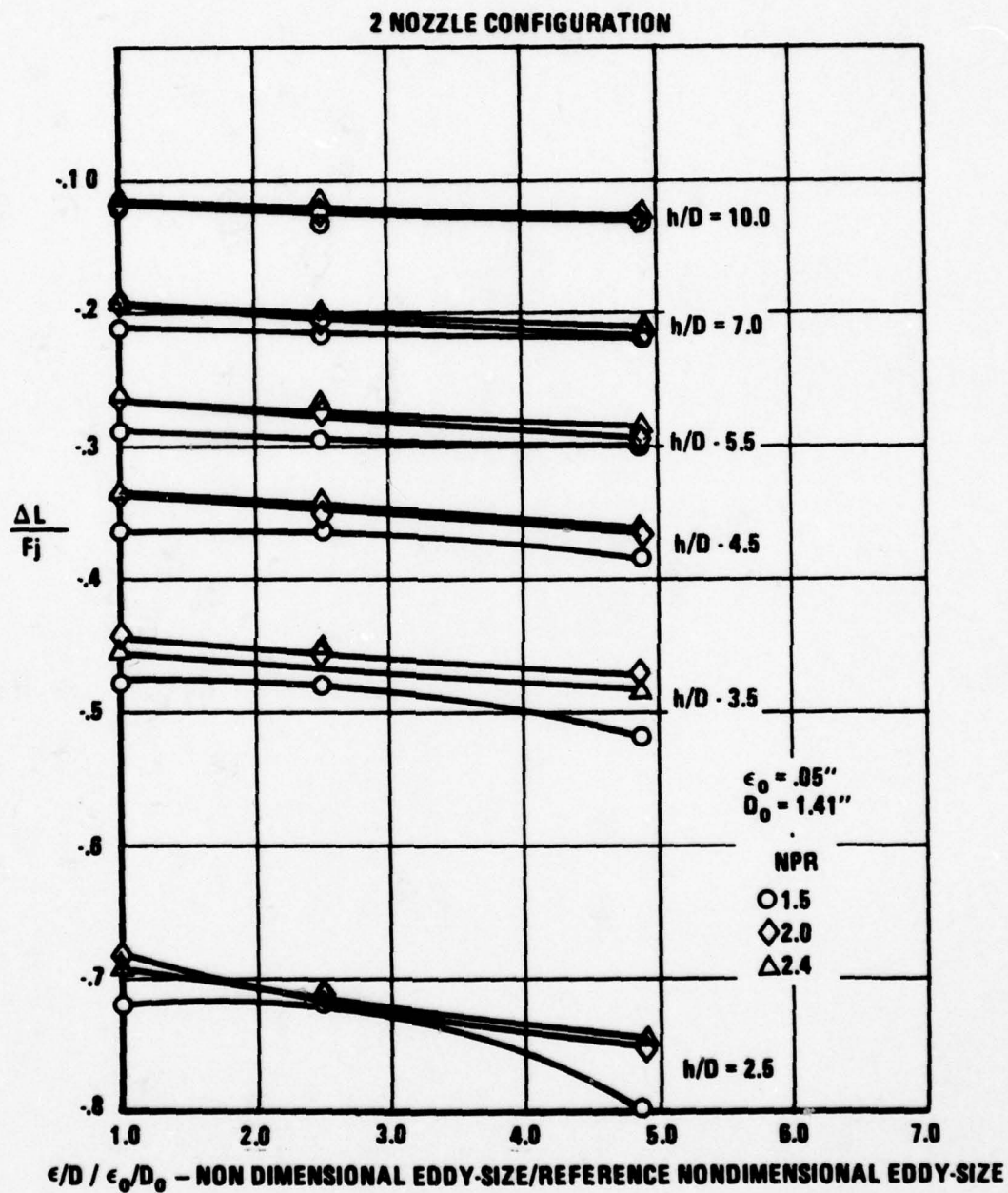


Figure 32 Effect of Varying Turbulence with Screens on Net-Induced Forces, $\Delta L/F_j$, for Two-Nozzle Configuration - Referenced to Turbulent Eddy Size

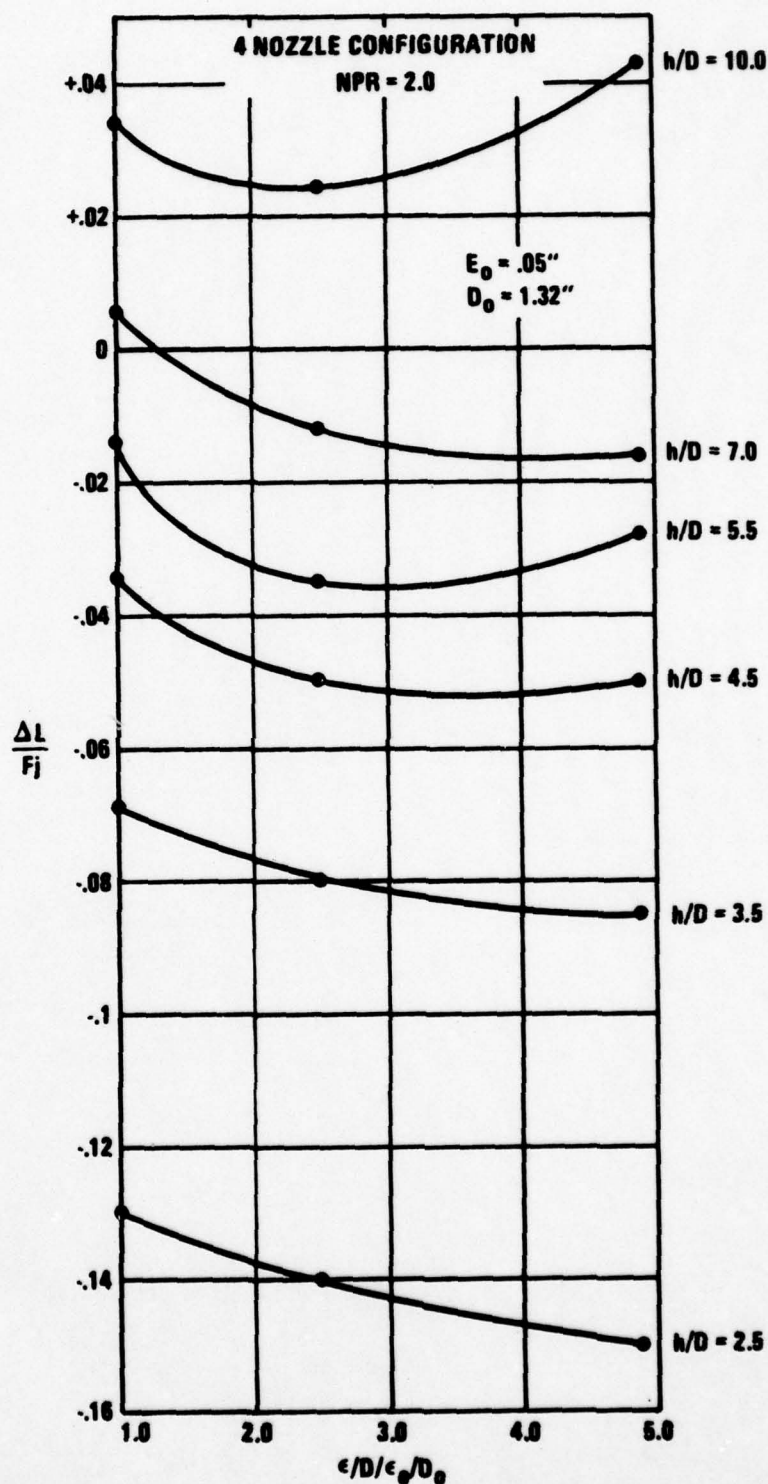


Figure 33 Effect of Varying Turbulence with Screens on Net-Induced Forces, $\Delta L/F_j$, for Four-Nozzle Configuration - Referenced to Turbulent Eddy Size

plate screen, ϵ_0/D . These curves could be used for determining the effects of changing the characteristic turbulence producing length and/or nozzle diameter (i.e., a quasi-"scaling") provided the blocking surface and nozzle spacing relationships remain constant.

The concept of the turbulent eddy size to explain the increased suckdown obtained with the screens and NPR variations is useful. The Kolmogorof energy dissipation rate (ϵ) for turbulence scaled by eddy size is related to $\frac{U^3}{\epsilon}$ (Reference 15). Foley postulates (Reference 19) that, ϵ^e for a given NPR, as eddy size is increased, turbulent intensity increases and the energy dissipation rate decreases, providing higher energy large eddies for entraining surrounding air and therefore increasing suckdown. For a given eddy size, as NPR (which is proportional to U^2 up to $NPR_{CRITICAL}$) is increased, the dissipation rate increases, reducing the energy in the large eddies for entrainment and thereby reducing suckdown. At choked and super-choked conditions, NPR is not proportional to U^2 , and the effect of varying NPR on eddy size is much degraded, as noted in Figure 24.

However, replacing turbulent intensity with eddy size (or the characteristic length producing the eddy size) as

the key variable presupposes that the effective eddy size of the full scale engine can be estimated by knowing the size of the turbulence-producing parts of the engine (say turbine blade size). This remains to be determined. It may be easier to continue to measure the model and full-scale engine turbulent-intensity levels and apply appropriate corrections to the model-scale ground effects data or simply correctly simulate the full-scale nozzle exit conditions in the model ground effects test.

3.2.2 Effects on Component Forces

In order that the flow mechanisms producing the changes described above on the net induced force could be understood, the effects of varying the nozzle-exit conditions on the individual components of the net induced force had to be determined.

Table 3-5 summarizes the maximum effects observed on the component forces due to varying the nozzle exit conditions. The effects on the pure suckdown components are discussed below; the effects relating to the fountain core force and fountain interference components are discussed in the next section (Section 3.3).

As part of an ongoing methodology development program, the data from this experiment have been correlated with the

Table 3-5 MAXIMUM EFFECT OF VARYING NOZZLE EXIT CONDITIONS ON COMPONENT FORCES

CHANGE IN COMPONENT			
$\Delta L/F_j$ NET INDUCED = FORCE	$\Delta L_i/F_j$ PURE SUCKDOWN	$\Delta L_{FC}/F_j$ + FOUNTAIN CORE	$\Delta L_{FI}/F_j$ + FOUNTAIN INTERFERENCE
TURBULENCE (with Screens S1 & S2)	-07	Two Nozzle 0 (0) Four Nozzle -.01	Two Nozzle -.015 Four Nozzle -.024
NOZZLE PRESSURE RATIO (from 1.5 to 2.4)	+04 Assumed Same As for $\Delta L/F_j$	—	—
NOZZLE TOTAL PRESSURE DISTRIBUTION (with Plates P1 & P2)	-.04	Four Nozzle -.007	Two Nozzle -.03

work of several previous experimenters (Reference 20, 21, and 22) by Foley (Reference 18). This correlation shows that there is "a fine structure" to suckdown that is a function of the implied area ratio, \bar{D}/d , where \bar{D} is the angular mean diameter as defined by Wyatt in Reference 20. Foley, Reference 18, has refined Wyatt's results; empirical relations have been developed allowing the prediction of pure suckdown as a function of altitude, \bar{D}/d , and planform shape for a reference NPR of 2.0 and a turbulent intensity level equal to that measured for the baseline nozzle case in this experiment. This value was then corrected for variations from baseline NPR and nozzle-exit conditions.

Corrections for turbulence level and NPR have been derived from the test data of this experiment for a uniform total-pressure distribution (screens). The data in Figure B-12 show the effect on the pure suckdown component force of varying the nozzle exit conditions with the screens and pressure profile plates. This variation was determined with the single jet exiting through one half of the two-nozzle blocking surface (the other half being removed), as described in Section 2.2. The corrections for NPR effects on pure suckdown are the same as those noted for the two-nozzle-configuration net induced force

averaged over h/D_s from 2.5 to 5.5 with only the screens installed (since an NPR of 2.0 only was run with the pure-suckdown-component measurements). This correction due to NPR is considered reasonably accurate because, as will be shown in Section 3.3, the two-nozzle case has a very weak fountain that fails to reach the blocking surface at most altitudes and is therefore primarily suckdown dominated.

With a uniform pressure distribution (baseline nozzle and screens), changing the NPR causes different (independent) changes in turbulent intensity and suckdown than are obtained by changing the turbulence screens; these changes are each independent of altitude. Therefore, the pure suckdown that results from turbulent entrainment rate is proportional to turbulence, which can be characterized by the large eddy size, ϵ_e , associated with the turbulence and NPR. As noted above, the large-scale eddy size (ϵ_e) is proportional to the largest physical dimension causing the turbulence, ϵ . If ϵ is taken as the grid size of the screens, the pure suckdown variation with eddy size (normalized by the NPR = 2.0 baseline nozzle case) is not a function of altitude or NPR; conversely, the change in nondimensionalized suckdown with NPR is not a function of altitude or eddy size (Figure 34). Therefore, corrections

to pure suckdown for NPR and turbulence with uniform profile distribution were formulated by Foley as

$$\frac{\Delta L_j}{F_j} = C_{j1} \cdot C_{j2} \left(\frac{\Delta L_j}{F_j} \right) \quad \left| \begin{array}{l} \text{NPR} = 2.0 \\ \epsilon_0 = .05'' \end{array} \right. \quad (7)$$

where C_{j1} and C_{j2} are empirically derived functions from Figure 31 for the effects of eddy size and NPR, respectively; they are presented in Figures 35 and 36.

3.3 Fountain Survey Testing

The net fountain force exerted on the blocking surfaces is composed of a fountain core force and a fountain interference force. Under certain conditions the fountain core force, $\frac{\Delta L_{FC}}{F_j}$, impacts the blocking surface, produces lift, and may counteract the induced life losses caused by the entrainment action of the radial ground jet. Pressure fields are often produced as a result of fountain blocking-surface interference, leading to additional lift losses or gains, $\frac{\Delta L_{FI}}{F_j}$.

3.3.1 Fountain Core Force

An estimate of the fountain core force $\frac{\Delta L_{FC}}{F_j}$, is determined by integrating the vertical component of the fountain dynamic pressure with the methods developed in Reference 5.

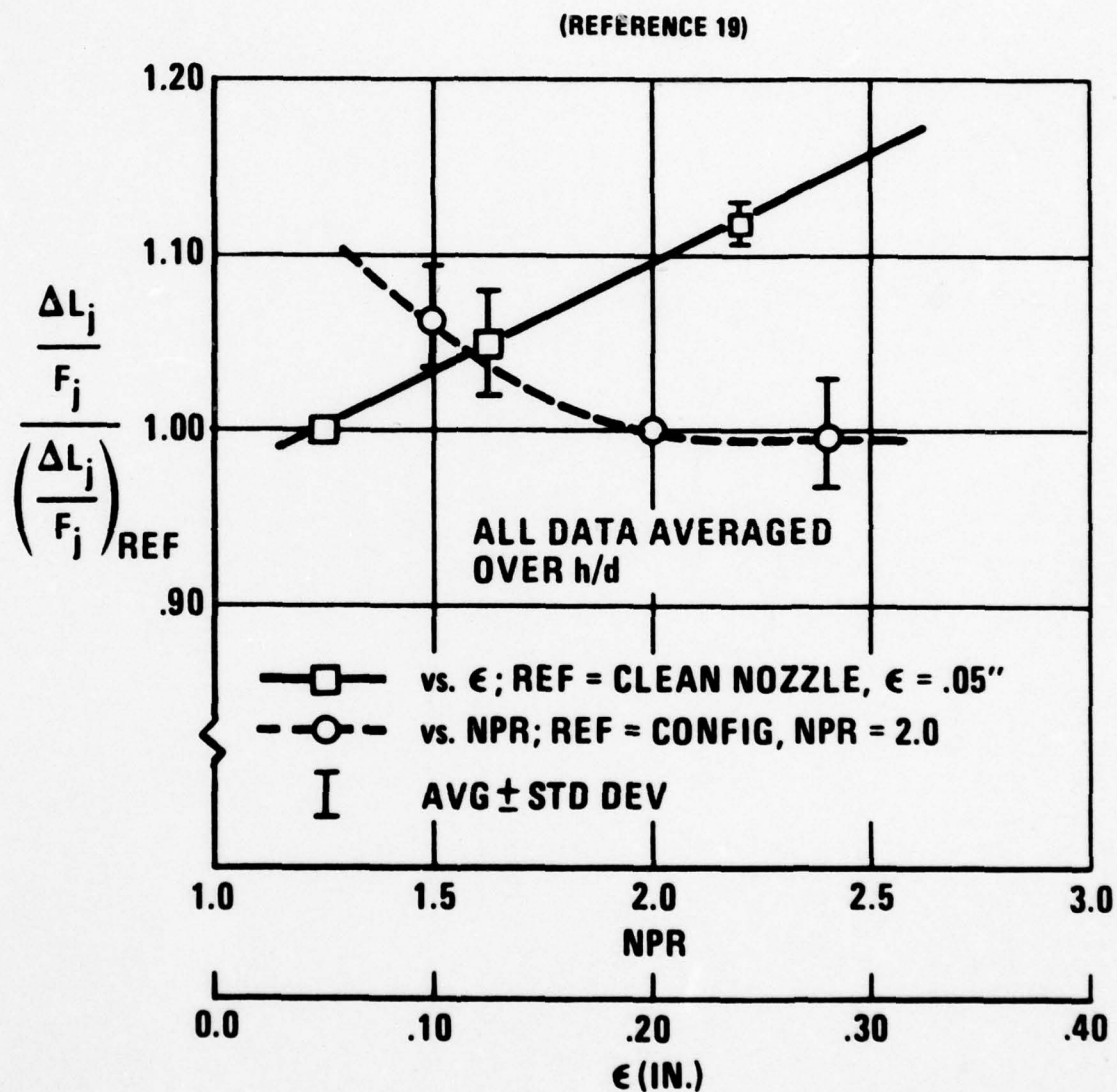


Figure 34 Effect of Nozzle Exit Pressure Ratio and Turbulence Scale on Pure Suckdown

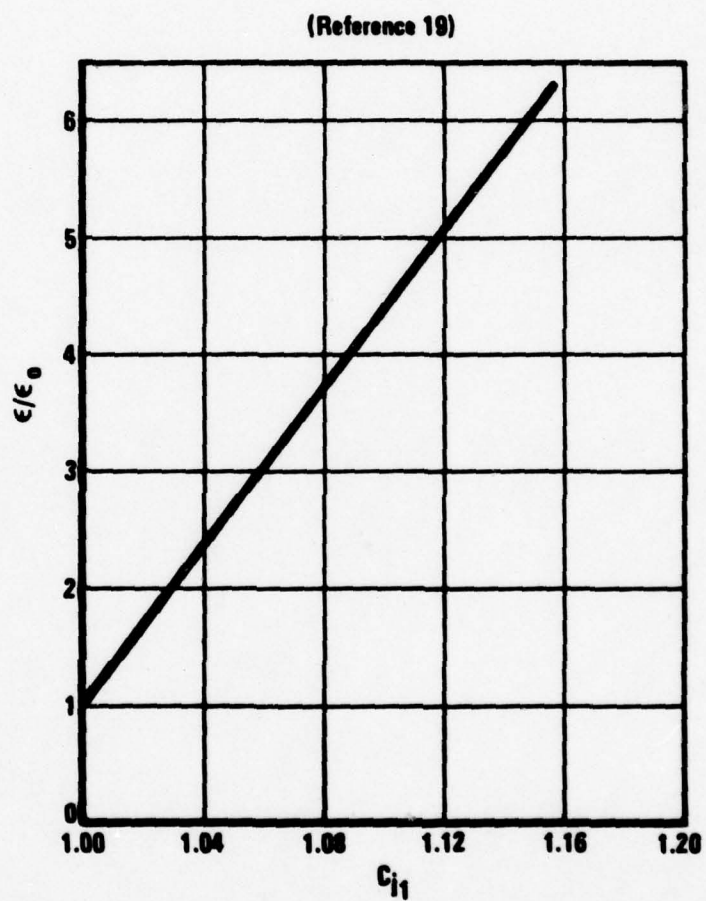


Figure 35 Effect of Eddy Size on Pure Suckdown

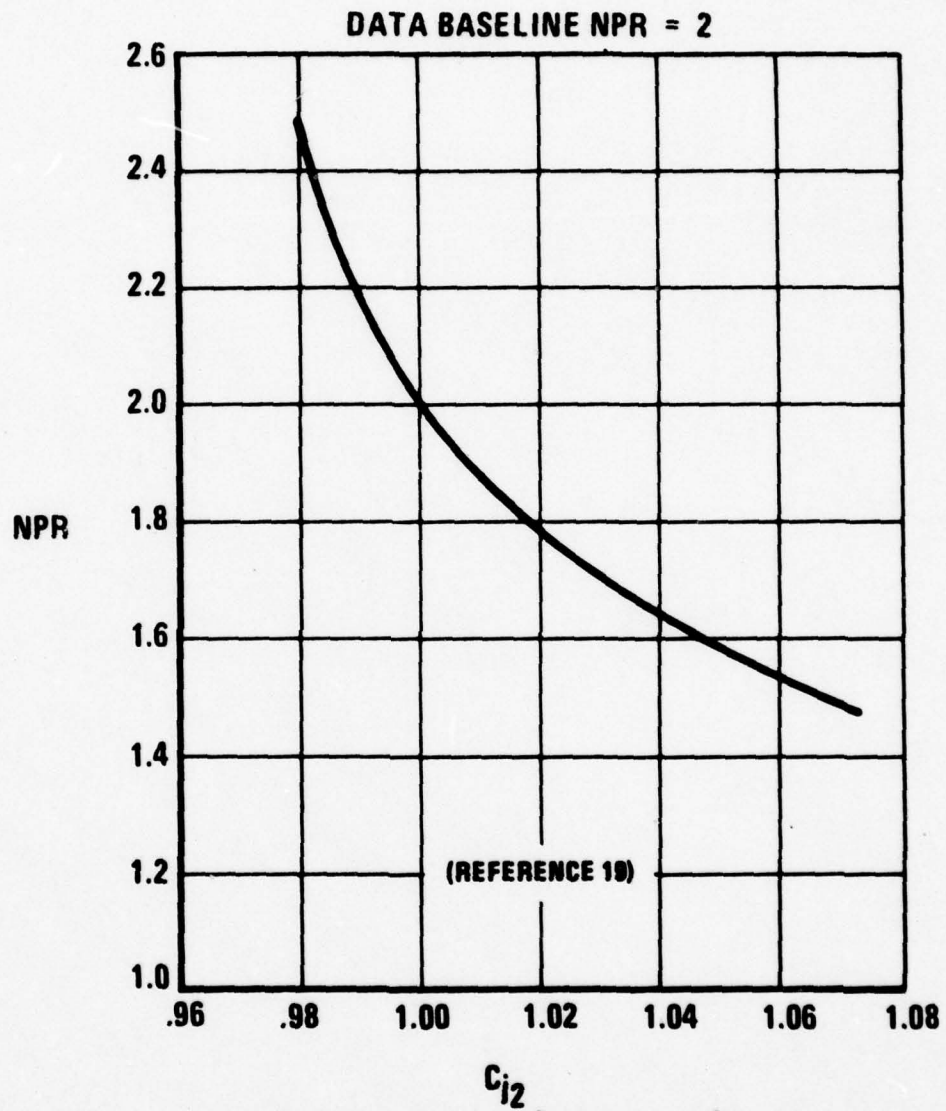


Figure 36 Effect of Nozzle Pressure Ratio on Pure Suckdown

A discussion of the integration process and the resulting effects of varying the nozzle exit conditions on the fountain-core-force-characteristics follows.

The fountain momentum flux passing through a plane parallel to the ground at any height can be determined from the rake pressure data. For steady flow and negligible body forces, the momentum flux equation can be expressed as

$$F = \iint \bar{U} (\rho \bar{U} \cdot dA). \quad (8)$$

An estimate of the effective fountain core force at any height can be found by assuming that, if a solid surface could be placed in the flow at that height without altering the flow, all of the momentum would be converted to a force on the plate with no losses. Integrating in the X-Y plane for the vertical component of this force, this equation becomes

$$\Delta L_{FC} = \frac{1}{144} \iint \rho U^2 \cos^2 \theta_F \cos^2 \gamma_F dx dy \quad (9)$$

where ΔL_{FC} = vertical component of the fountain core force -

$$\begin{array}{l} \text{lb}_f \\ \rho = \text{density} - \text{slugs/ft}^3 \end{array}$$

θ_F, γ_F = Euler angles of the flow inclination from
vertical - degs

U = Velocity, fps

In terms of dynamic pressure in the fountain, Q_F , psi:

$$\Delta L_{FC} = \iint 2Q_F \cos^2 \theta_F \cos^2 \gamma_F dx dy \quad (10)$$

In dealing with large amounts of pressure data that require mechanized integration, it is necessary to review the data to eliminate the few erroneous data points that are inevitably present. To this end, an interactive computer procedure was developed (during the effort reported in Reference 5) that plots the rake dynamic pressures and allows the data to be edited. It then fairs the edited data with an interactive capability for the user to smooth the fairing; it then integrates the results. Edited and faired data for all of the fountain rake surveys are presented in Appendix C in the form of profiles of the vertical component of the dynamic pressure at the tested locations along the fountain.

Fountain rake surveys obtained with the two- and four-nozzle cases have been integrated to determine the changes in fountain core force acting on the blocking surface experienced with varying nozzle-exit conditions (Figure 37). The two-nozzle configuration produces a weak fountain that fails to reach the blocking surface, even at very low model altitudes, and therefore produces no net fountain force. The entrainment of air away from the fountain by the free and radial ground jets

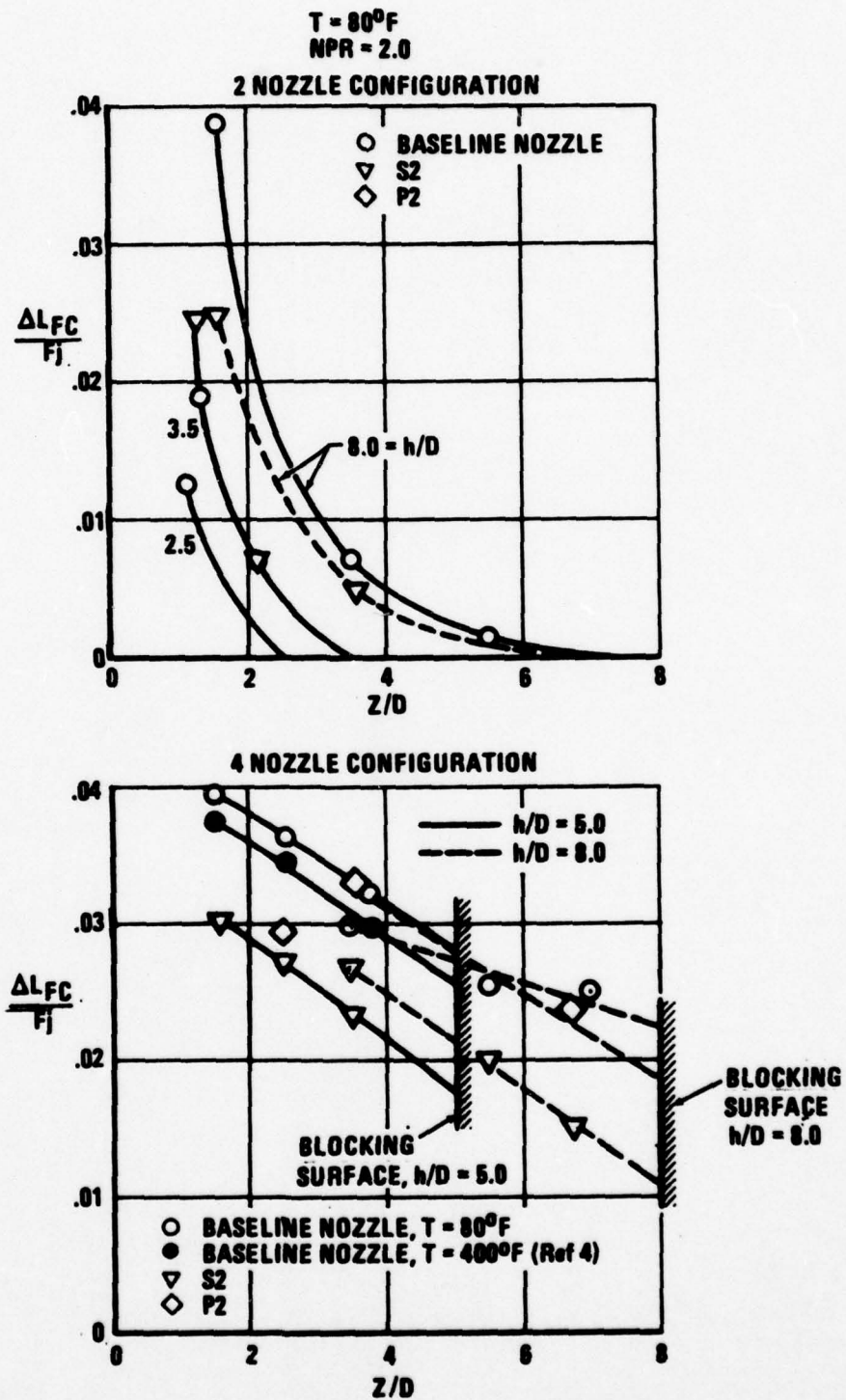


Figure 37 Effect of Varying Nozzle Turbulence (Screens) and Pressure Distribution on Fountain Core Force

reduces its momentum to zero by the time it reaches the blocking surface. This agrees with the results of Reference 5. It is shown in Figure 37 that increasing the nozzle turbulence (and thereby increasing free jet and ground jet entrainment) does reduce the fountain core force, implying that before it reaches the blocking surfaces even more air has been entrained away from the fountain. However, varying the nozzle turbulence has no effect on the fountain core lift at the blocking surface, $\frac{\Delta L_{FC}}{F_j}$, since the weak fountain does not reach the blocking surface. Although not run, varying the pressure distribution is also expected to have no effect on $\frac{\Delta L_{FC}}{F_j}$ for this weak-fountain case for the same reason.

The baseline four-nozzle case at a temperature of 80°F and an h/D of 5.0 shows very good agreement with the data taken in the previous experiments reported in Reference 5 at a temperature of 400°F. The fountain is much stronger than for the two-nozzle case and has not dissipated when it reaches the blocking surface at an h/D of 5.0 or 8.0. Increasing the nozzle turbulence causes a reduction in $\frac{\Delta L_{FC}}{F_j}$ at the blocking surface ($\Delta\left[\frac{\Delta L_{FC}}{F_j}\right] = -.01$ at h/D = 5.0). It appears that varying the total pressure distribution may have about the same magnitude effect on $\frac{\Delta L_{FC}}{F_j}$ (Figure 37). Increasing the blocking surface height yields a stronger fountain for the same degree of nozzle

turbulence (or pressure distribution). For a given blocking surface height, the fountain dissipates at increasing altitudes and apparently at a rate that is virtually independent of nozzle turbulence.

3.3.2 Fountain Interference

The effect on fountain interference, $\frac{\Delta L_{FI}}{F_j}$, of varying the nozzle exit conditions has been determined for the two- and four-nozzle configuration at an NPR of 2.0 (Figure 38) by subtracting the pure suckdown and fountain core increments from the net induced forces.

In the case of the two-nozzle configuration, the pure suckdown force variations with the screens and plates were measured directly, as shown in Figure B-11; the fountain core force was zero for nozzle exit variations. This allowed the direct determination of the fountain interference variation with nozzle exit conditions and model altitude, plotted in Figure 38.

For the four-nozzle case, at an NPR of 2.0, the fountain core force variation due to the S_2 screen was estimated for h/D_s of 5 and 8 from Figure 37. The net induced force variation was determined from Figure B-9. The variation in pure suckdown force due to turbulence screen S_2 (at $h/D = 5.0$ and

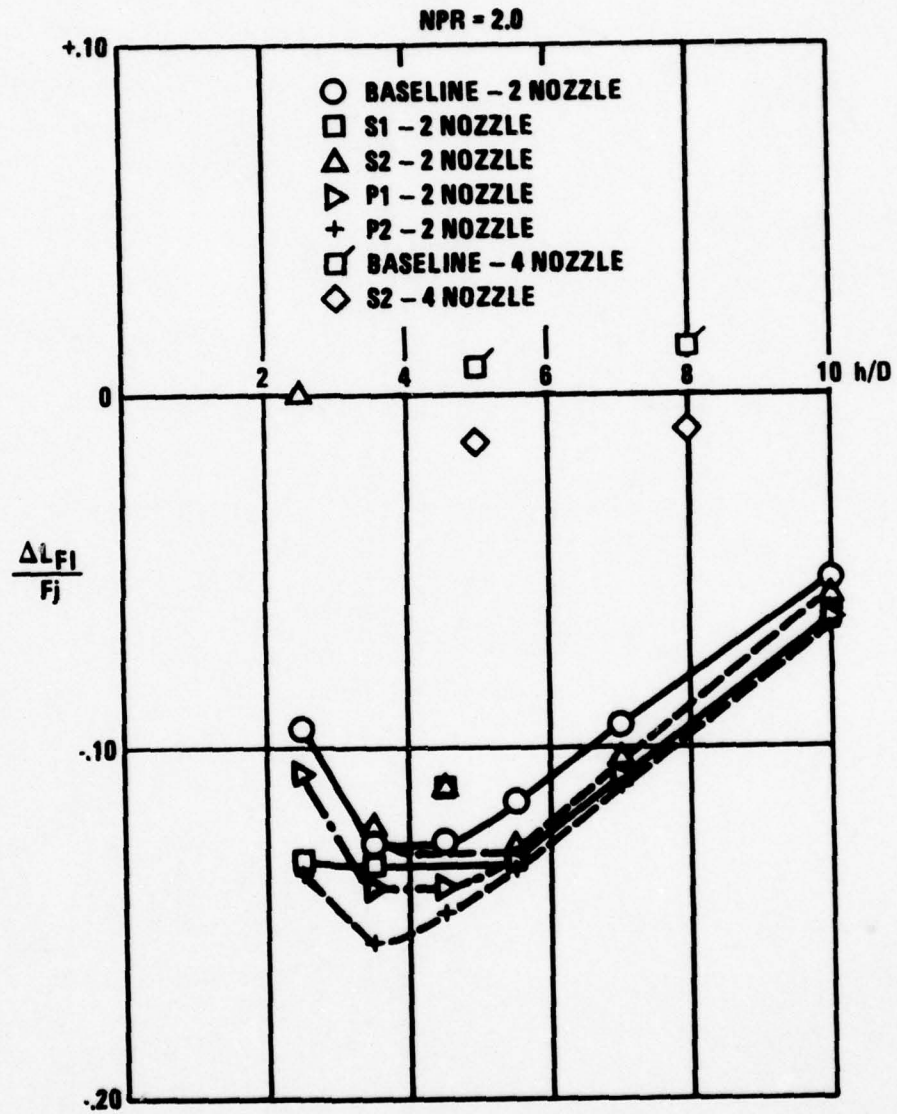


Figure 38 Increasing Nozzle Turbulence or Varying the Nozzle Pressure Distribution Degrades Fountain Interference, $\frac{\Delta LFI}{F_j}$

8) was determined for the four-nozzle case by applying the percentage variation in pure suckdown due to S_2 observed with the two-nozzle case (Figure 34 or 35) to the baseline four-nozzle pure-suckdown case run in the Reference 5 test. Varying the nozzle exit conditions with the screens produces a maximum change in $\frac{\Delta L_{FI}}{F_j} = -0.015$ in the two-nozzle case and a change in $\frac{\Delta L_{FI}}{F_j} = -0.024$ in the four-nozzle fountain interference component (Table 3-5). Using the pressure profile plates to vary the nozzle total pressure distributions results in a change in $\frac{\Delta L_{FI}}{F_j} = -0.03$ in the fountain interference force for the two-nozzle case. At almost all altitudes (Figure 38), varying the nozzle exit conditions at a constant NPR causes a suckdown-increasing fountain-interference effect.

4. CONCLUSIONS

This investigation has successfully demonstrated the criticality of engine exhaust simulations on model-measured ground effects. The results have formed the basis of prediction techniques to account for these effects and have provided some understanding of the associated flow phenomena.

(1) The results of this investigation support the conclusions of Reference 5. With the baseline nozzles and large planforms tested, weak fountains that usually dissipate before reaching the blocking surfaces are formed between two jets. Consequently, little or no positive lift is contributed to the hovering system. Conversely multiple-nozzle arrangements (three and four) contribute stronger fountains that impact the blocking surface over a wide range of heights. However, the positive ground effect experienced derives as much or more of its lift from fountain interference as from the core of the fountain itself.

(2) Variations in nozzle exit turbulence, total-pressure distribution, and nozzle pressure ratio have been experimentally demonstrated over the ranges expected for full-scale VSTOL aircraft turbojet and turbofan engines.

(3) Increasing nozzle turbulence increases net lift or thrust loss, but the magnitude of the loss is de-

pendent on the configuration and how the turbulence is changed, whether by screen, nozzle pressure ratio, or pressure distribution.

Turbulence may be increased by increasing the large-scale eddy size with screens while maintaining a virtually uniform total-pressure distribution, by varying the total pressure distribution from that of a turbojet to a turbofan engine or by decreasing NPR.

(4) Variations in nozzle-exit turbulence, total-pressure distribution, and pressure ratio over ranges expected for full-scale engines cause significant changes with the large planform blocking surfaces not only in the total net-induced force measured by the usual ground effects model, but also in the pure suckdown, fountain core, and fountain interference components. Changes of up to 10% of the nozzle thrust for each component are observed.

(5) Because the net induced force is often the sum of two relatively large-valued forces of opposite sign (suckdown and fountain lift), changes on the order of 10% in the suckdown and fountain force could potentially result in first-order changes in aircraft sizing and performance and must therefore be accounted for in any prediction methodologies.

(6) The effect of the nozzle exit variables on the net induced force is highly configuration dependent. When the large research-type blocking surface is changed to a smaller, cruciform planform more characteristic of a realistic airplane configuration, varying the nozzle exit conditions still produces a 10% thrust loss, which is on the order of the airplane payload. Therefore, if the effects of the nozzle exit conditions of the engines expected for use on VSTOL airplanes are not considered, costly errors in airplane sizing will result.

(7) All three full-scale engine nozzle-exit variables - turbulence (measured in terms of an intensity or, a characteristic eddy-size-producing length), NPR, and nozzle total-pressure distribution - should be modeled in small-scale ground effects testing or more experimental research should be conducted to develop a detailed empirical prediction methodology to account for the interdependency of configuration and nozzle-exit variable effects. It may be simpler to correctly simulate the full-scale nozzle exit conditions in model ground effects tests. This would still necessitate knowing the full-scale nozzle exit conditions. A suitable means of measuring and relating the the model nozzle exit conditions may be the technique of using a

Kulite transducer and the total-pressure rakes developed in this study (or other suitable turbulent intensity measurement devices).

It is still not known if the effects of the nozzle exit conditions on the net and component induced forces determined in this study are subject to any "scaling" modifications (i.e., Reynolds number) when going from model to full scale. It is recommended that research be conducted to determine whether any such "scaling" effects exist.

(8) The induced loads and fountain survey measurements have led to the following explanation of the flow phenomena observed with changing nozzle-exit conditions. A free jet existing under a blocking surface (Figure 2) impacts the ground and forms a radial ground jet. The radial ground jet has a strong appetite for entrained air, which can be supplied from any direction (Sketch A in Figure 2). When two or more jets are present, the intersecting ground jets often form an upflow or fountain region which blocks one path for gas entrainment by the ground jets (Sketch B). Gas is entrained away from the fountain (Sketch C) by the radial ground jet, reducing fountain core strength and inducing pressure fields on the bottom of the blocking surface that would not be present if the fountain were not

there - hence the fountain interference term. The net result is the development of a complex flow circulation and exchange pattern (Sketch D). Therefore, the induced forces for a configuration are largely a function of the entrainment by the free and radial ground jets.

Entrainment may be increased by increasing the turbulent eddy size or by decreasing the NPR, possibly resulting in slower energy dissipation by the eddies and higher energy eddies for entrainment.

When turbulence levels like those measured for real engines are introduced, the entrainment rate of the free and radial ground jets is increased, which results in more air being entrained away from the fountain, in higher suckdown pressures, and in reduced fountain core strength.

REFERENCES

1. Kotansky, D. R., Durando, N. A., & Bristow, D. R., "Jet-Induced Forces and Moments In and Out of Ground Effect," McDonnell Aircraft Company Report No. July 1977.
2. Siclari, M. J., Barche, J., & Migdal, D., "V/STOL Aircraft Prediction Technique Development for Jet-Induced Lift in Hover," Grumman Aerospace Corporation Report PDR 623-18, April 1975.
3. Karemaa, A., & Ramsey, J. C., "Aerodynamic Methodology for the Prediction of Jet-Induced Lift in Hover," Convair Report CADS-ERR-73-013, December 1973.
4. Karemaa, A., "Abbreviated Methodology for the Prediction of Jet-Induced Lift in Hover," Convair Report CASD-ERR-74-024, December 1974.
5. Karemaa, A., Smith, C. W., Weber, H. A., and Garner, J. E., "The Aerodynamics and Thermodynamic Characteristics of Fountains and Some Far-Field Temperature Distributions," Office of Naval Research Report Number ONR-CR-212-237-1, May 1978.
6. Karemaa, A., Weber, H. A., and Smith, C. W., "Aerodynamic and Thermodynamic Characteristics of Flow Fields Below VTOL Vehicles in Ground Proximity," AIAA Paper No. 79-0338-January 1979.
7. Bradbury, L. J. S., "The Impact of an Axisymmetric Jet Onto a Normal Ground," Aeronautical Quarterly, May 1972.
8. Kuhlman, J. M., & Warcup, R. W., "Effect of Jet Decay Rate on Jet-Induced Loads on a Flat Plate," AIAA/NASA Ames VSTOL Conference Collection of Technical Papers, p. 194, June 1977.
9. Gentry, G. L., & Margason, R. J., "Jet-Induced Lift Losses on VTOL Configuration Hovering In and Out of Ground Effects," NASA TN D-3166, February 1966.

REFERENCES (Continued)

10. Wyganski, I., & Fielder, H., "Some Measurements in the Self-Preserving Jet," *Journal of Fluid Mechanics*, Vol. 38, Pt. 3, 1969.
11. Krenz, G., Haftmann, R., Brennan, T., & Fortenbaugh, R., "USN/FMOD FRG VAK-191B Joint Flight Test Program, Vol. 8," *Naval/Air Systems Command Rept. NAVAIR-8R-76*, August 1976.
12. Kind, R. J., Suthanthiran, K., "The Interaction of Two Opposing Plane Turbulent Wall Jets," *AIAA Paper No. 72-211*, January 1972.
13. Smart, A. E. and Moore, C. J., "Aero-Engineer Applications of Laser Anemometry," *AIAA Journal*, Vol. 14, No. 3, March 1976, pp 363-370.
14. Zalay, A. D., et al, "Investigation of a Laser Doppler Velocimeter System to Measure the Flow Field of a Large Scale V/STOL Aircraft in Ground Effect," unpublished, *AIAA Paper to be presented at Las Vegas Propulsion Conference*, June 1979.
15. Landau, L. D. and Lifshitz, G. M., *Fluid Mechanics*, ch. III, Pergamon Press, London, 1966.
16. Schlichting, Dr. Herman, *Boundary-Layer Theory*, ch. II, McGraw Hill, New York, 1968.
17. Hoerner, S. F., *Fluid Dynamic Drag*, ch. III, Hoerner, Midland Park, New Jersey, 1965.
18. Foley, W. H., "Development of an Experimental Basis for a V/STOL Handbook," *Proceedings of the Workshop on V/STOL Aerodynamics Workshop*, Monterrey, May 1979.

REFERENCES (Continued)

19. Foley, W. H., "Methodology for Prediction of Propulsion Induced V/STOL Forces in Ground Effect," AIAA Paper 79-1281, June 1979.
20. Wyatt, L. A., "Static Tests of Ground Effect on Planform Fitted with a Centrally Located Round Lifting Jet," Ministry of Aviation CP. 749, 1962.
21. Spreeman, K. P. and Sherman, I. R., "Effects of Ground Proximity on the Thrust of a Simple Downward Directed Jet Beneath a Flat Surface," NACA TN 4407, 1958.

APPENDIX A

NOZZLE CALIBRATION SURVEYS

This appendix contains the nozzle-exit RMS fluctuating-pressure and total-pressure surveys conducted with the Kulite transducer and total-pressure probes as described in Sections 2.2, 2.3 and 3.1. Tables 2-1 and 3-1 (in the main body) summarize the nozzle-exit surveys and their results. Figures A-1 through A-6 describe the baseline nozzle configuration characteristics; Figures A-7 through A-18 show the effects of turbulence screens S_1 and S_2 , and Figures A-19 through A-22 show the effects of pressure profile plates P_1 and P_2 , all with the N_3^2 nozzle configuration. Figure A-23 shows the surveys for the baseline nozzle N_{13}^2 (aft plenum), and Figures A-24 and A-25 show the surveys for the N_{11}^1 and N_9^1 nozzles with screen S_2 installed. Both X and Y traverses are shown where available.

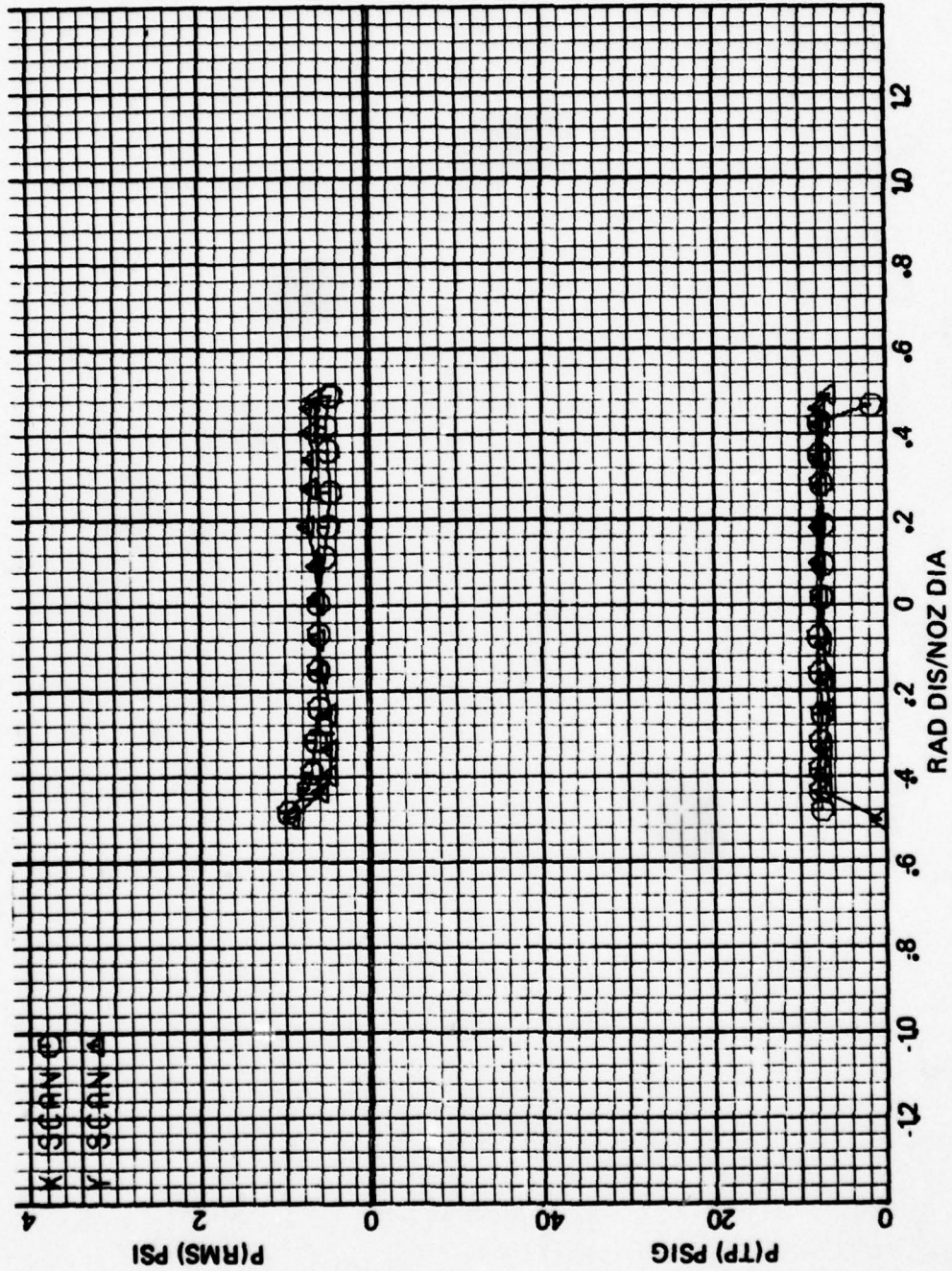


Figure A-1 Exit Pressure Surveys for the N₃₂ Baseline Nozzle at NPR = 1.503

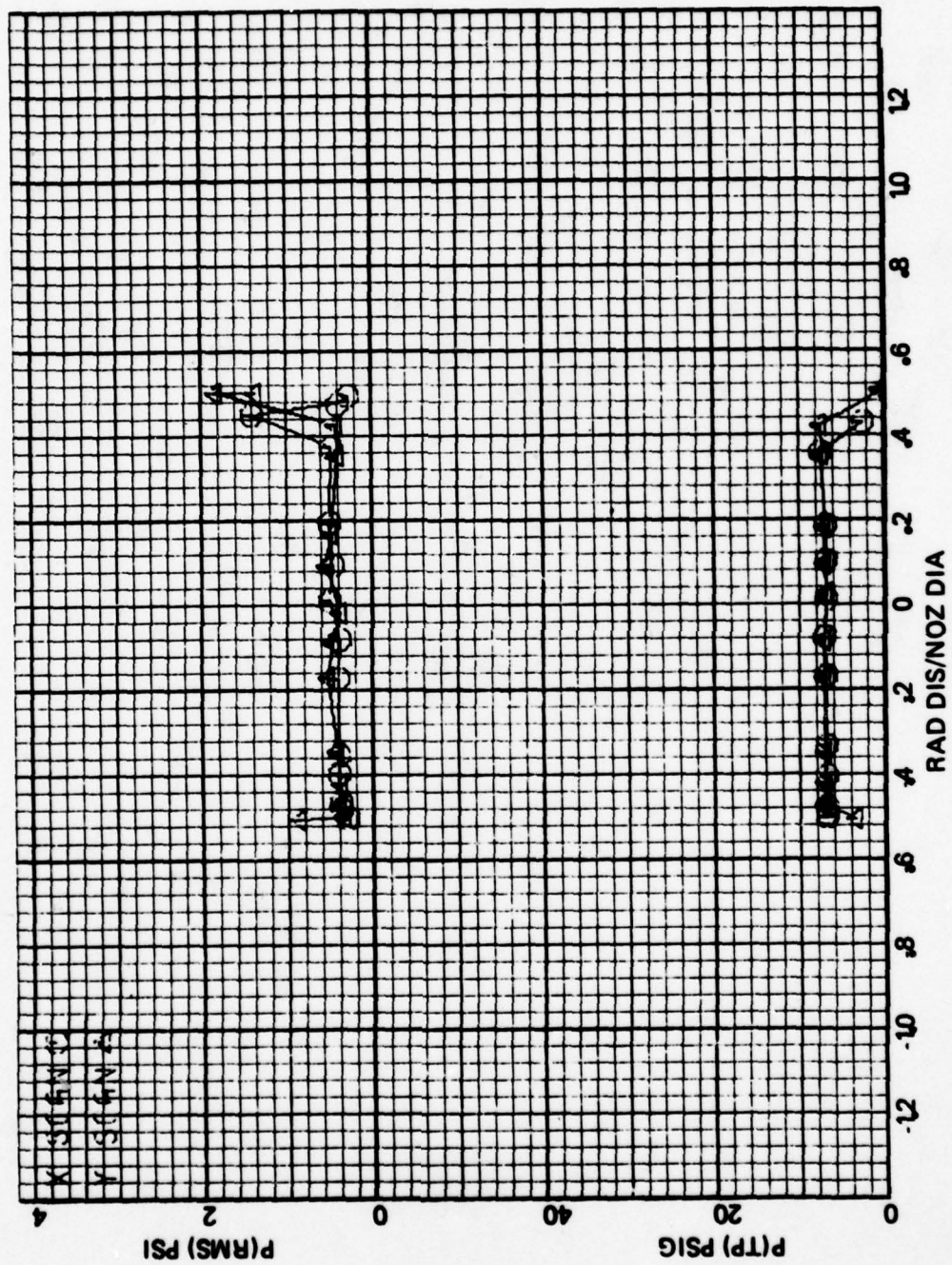


Figure A-2 Exit Pressure Surveys for the N₂ Baseline Nozzle at NPR = 1.551

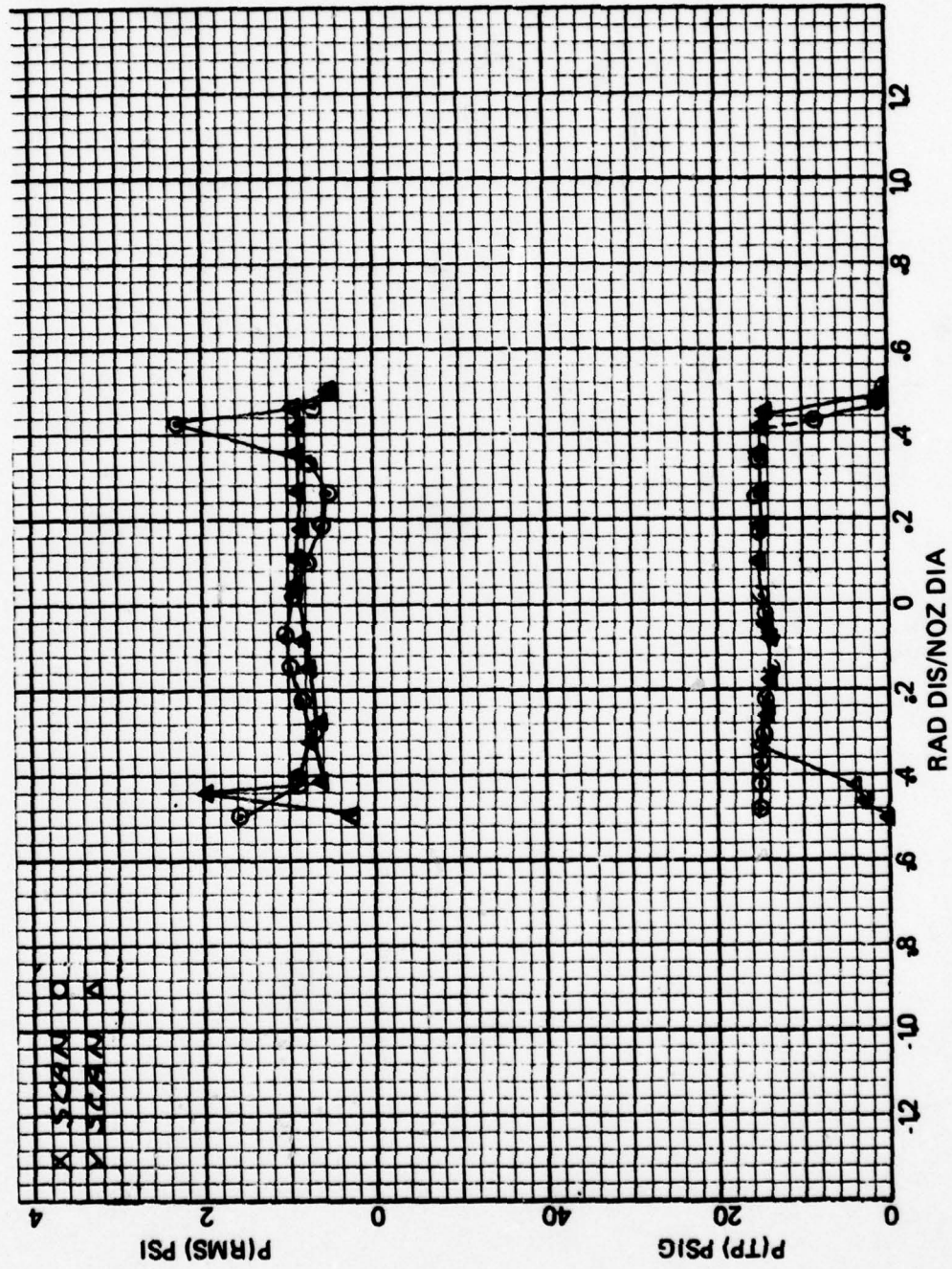


Figure A-3 Exit Pressure Surveys for the N₃₂ Baseline Nozzle at NPR = 1.924

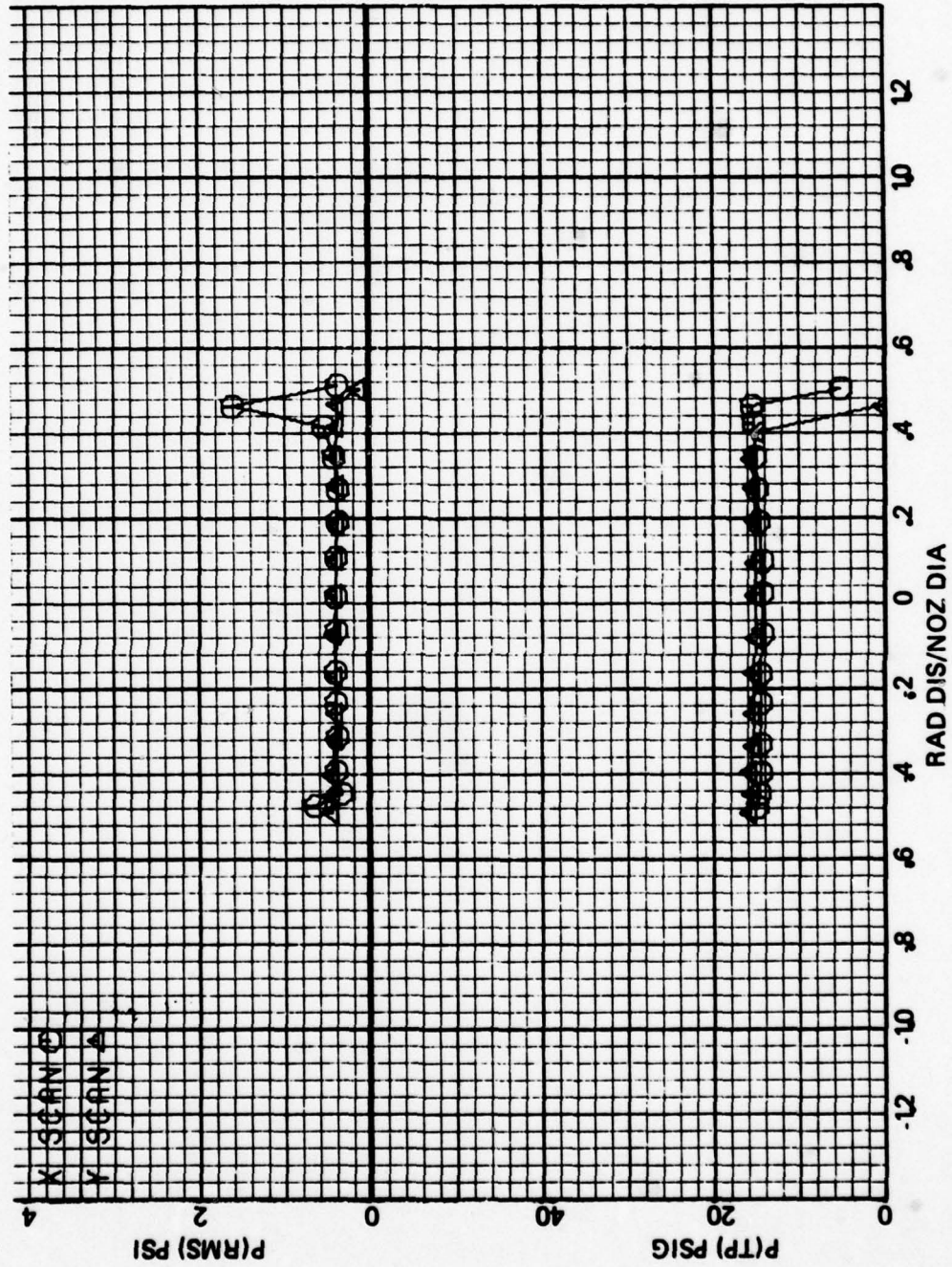


Figure A-4 Exit Pressure Surveys for the N_3^2 Baseline Nozzle at $NPR = 1.958$

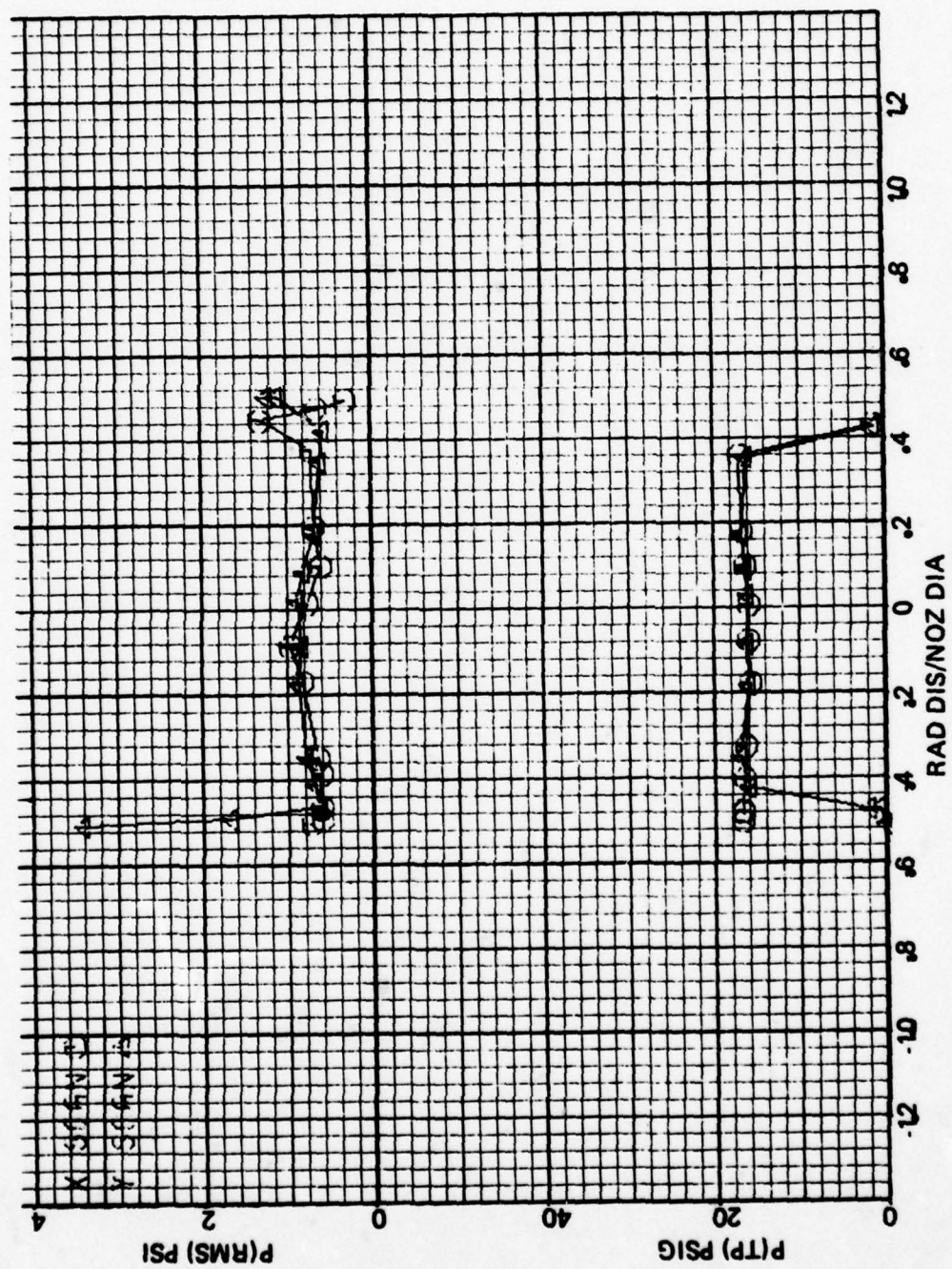


Figure A-5 Exit Pressure Surveys for the N₃₂ Baseline Nozzle at NPR = 2.096

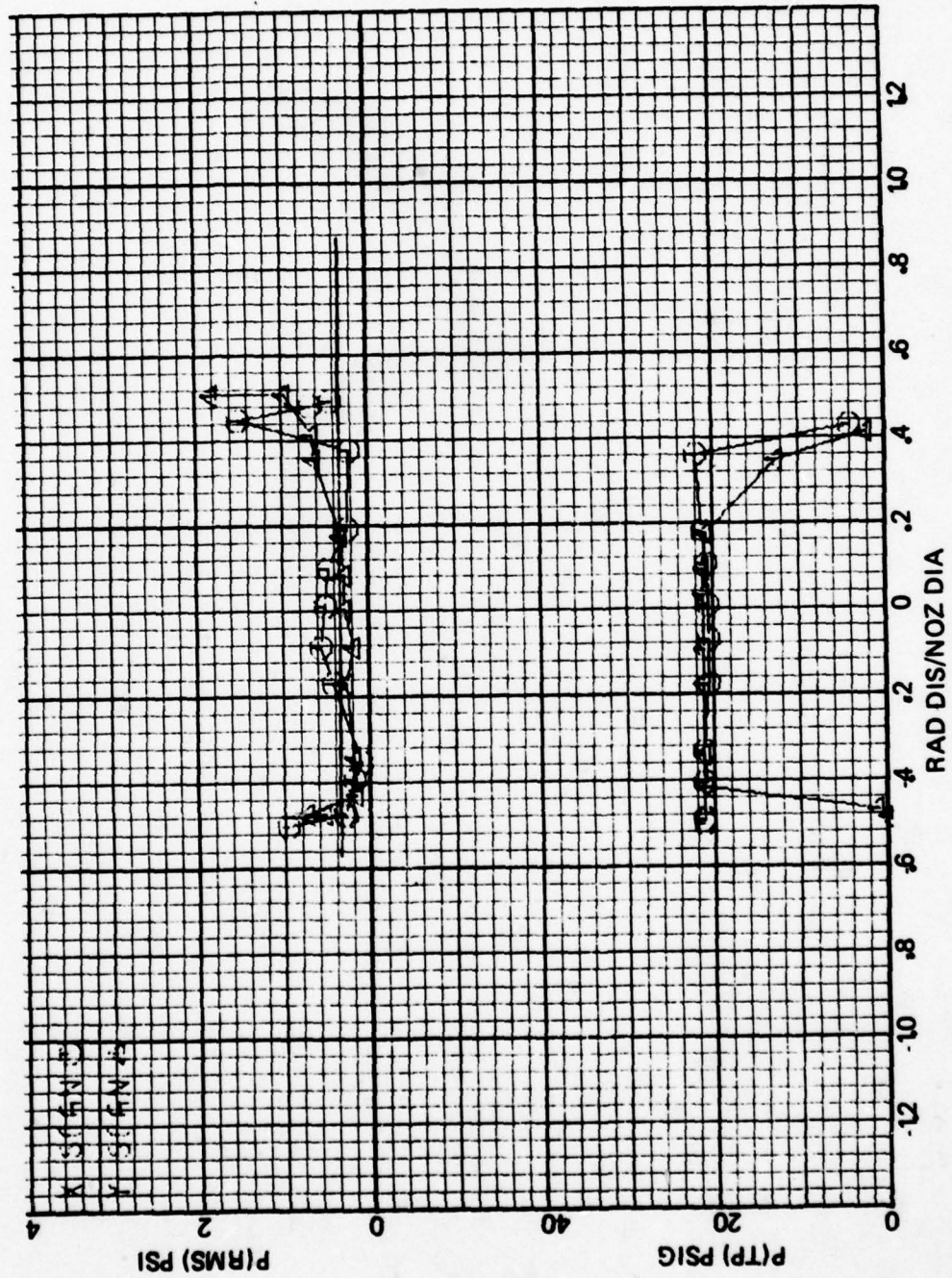


Figure A-6 Exit Pressure Surveys for the N₃₂ Baseline Nozzle at NPR = 2.276

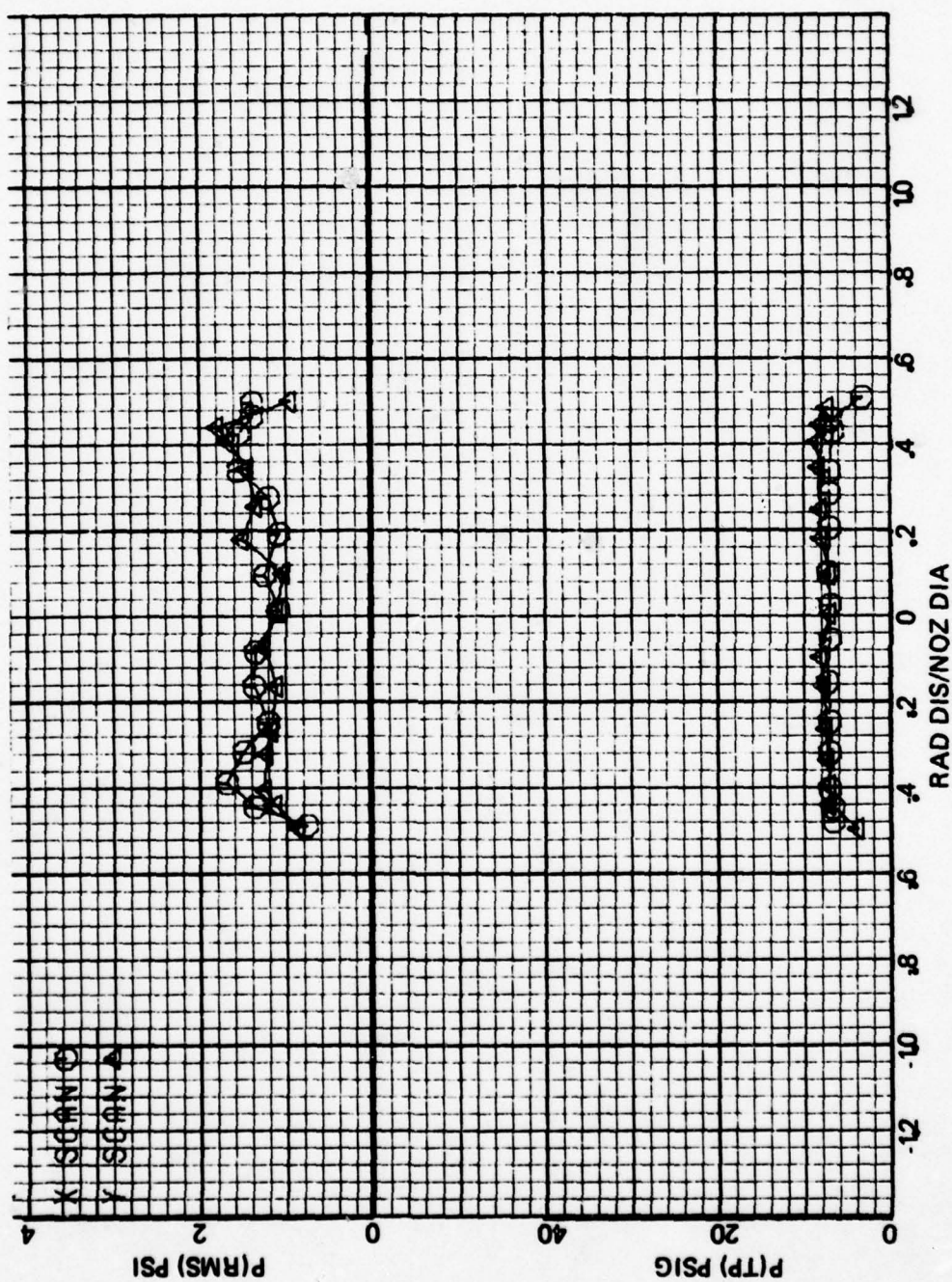


Figure A-7 Exit Pressure Surveys for the N_2 Nozzle with Screen S1 at $NPR = 1.517$

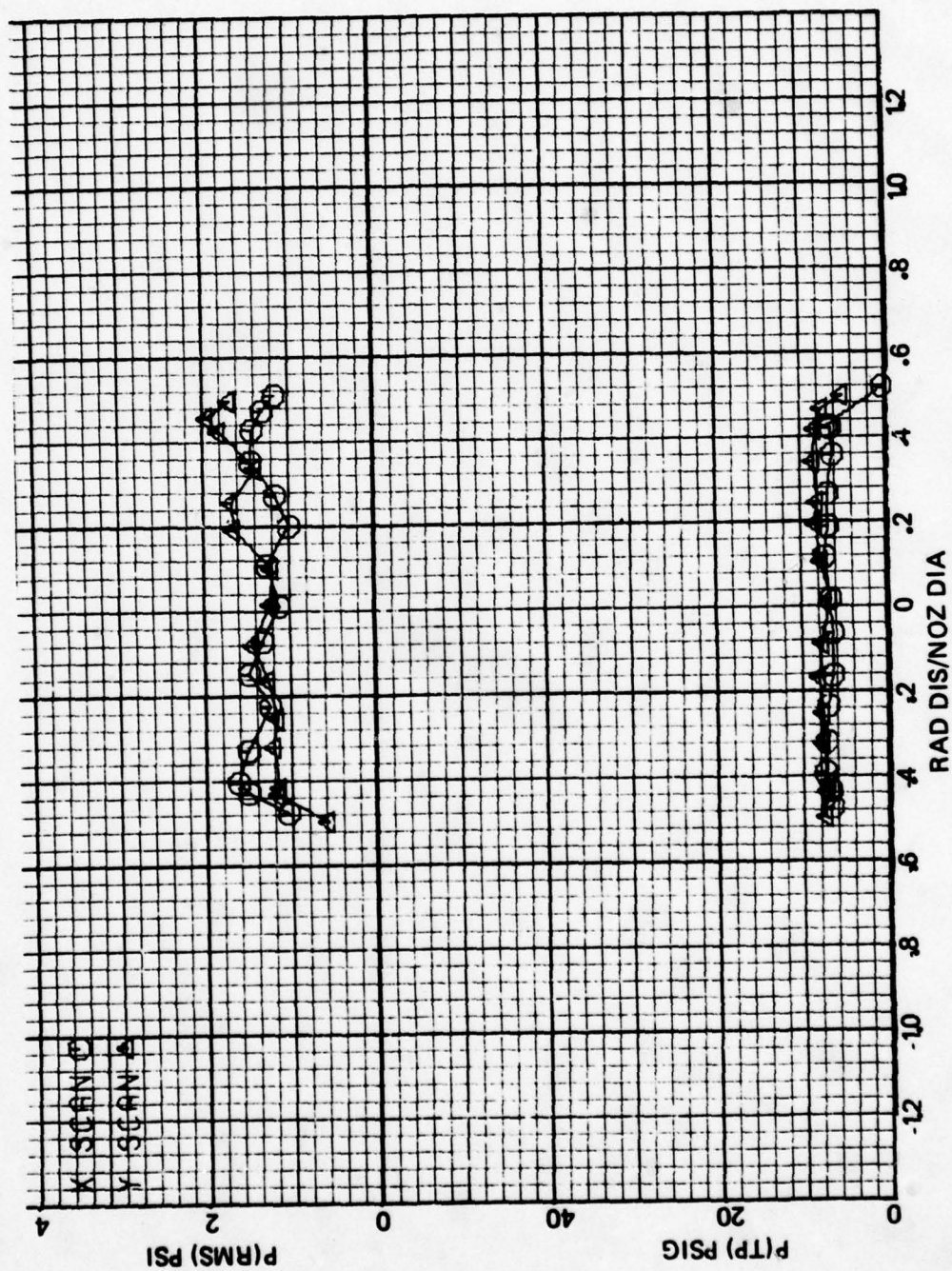


Figure A-8 Exit Pressure Surveys for the N₃₂ Nozzle with Screen S₁ at NPR = 1.531

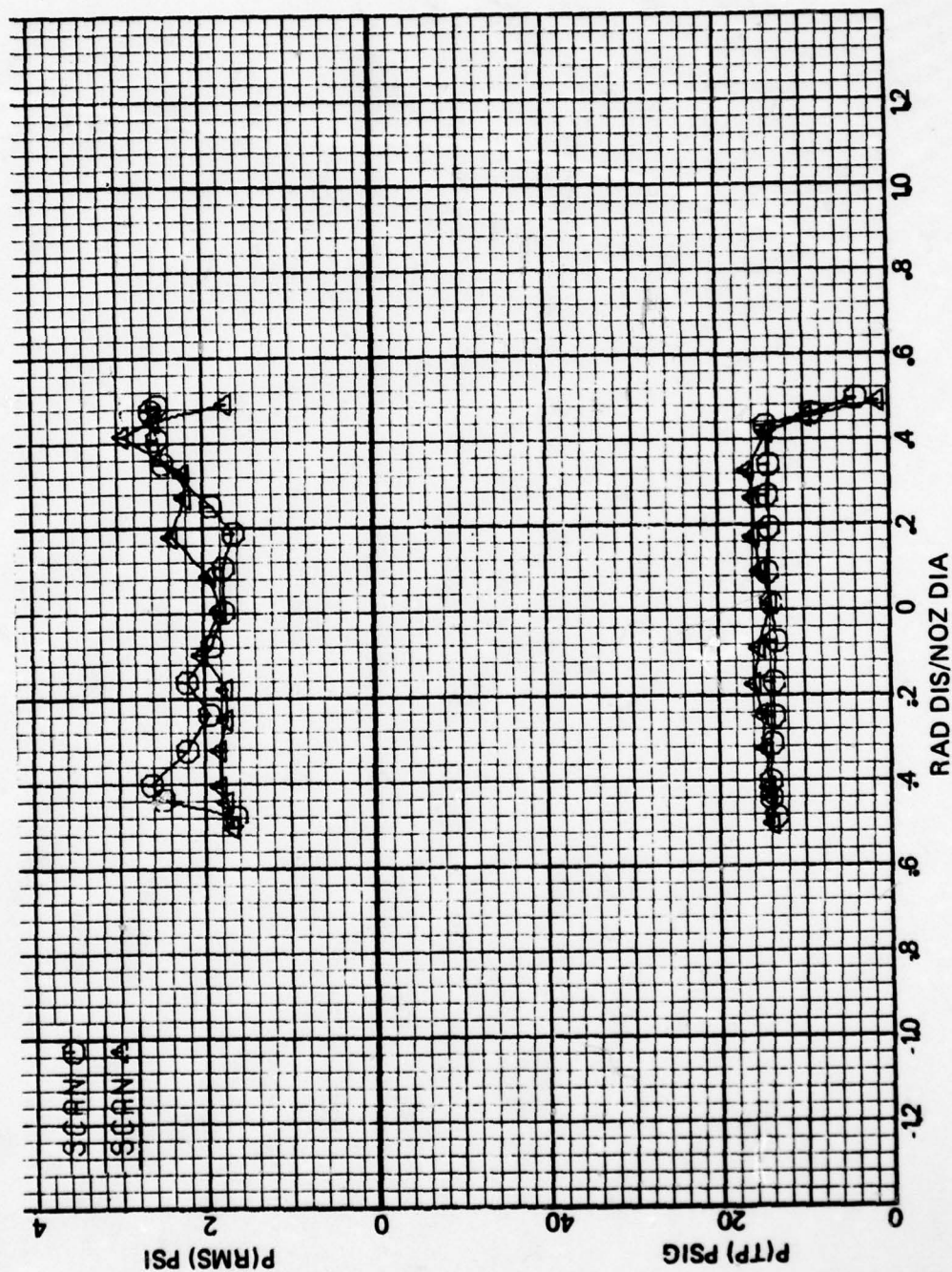


Figure A-9 Exit Pressure Surveys for the N₃₂ Nozzle with Screen S₁ at NPR = 1.931

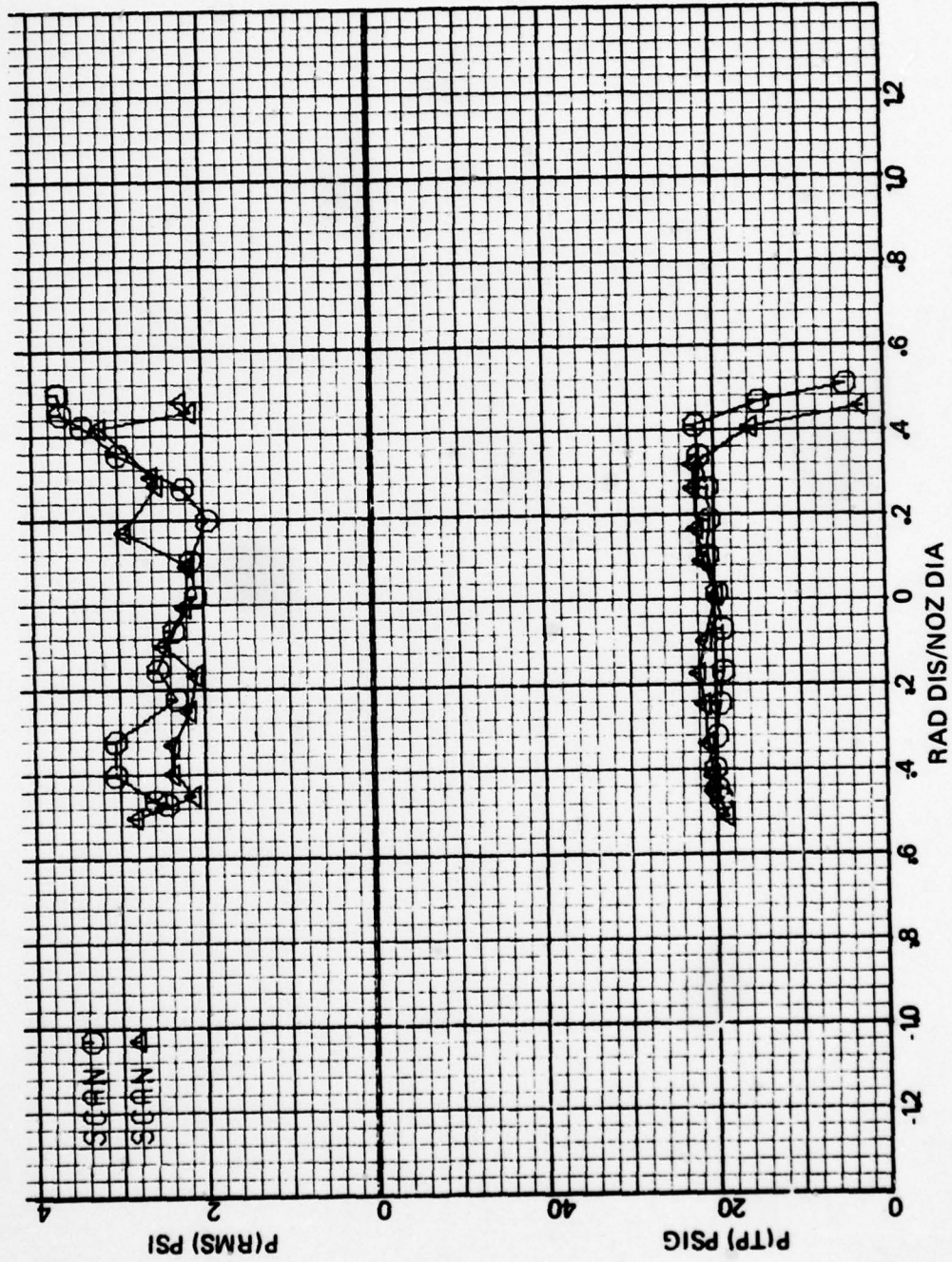


Figure A-10 Exit Pressure Surveys for the N₃² Nozzle with Screen S₁ at NPR = 2.317

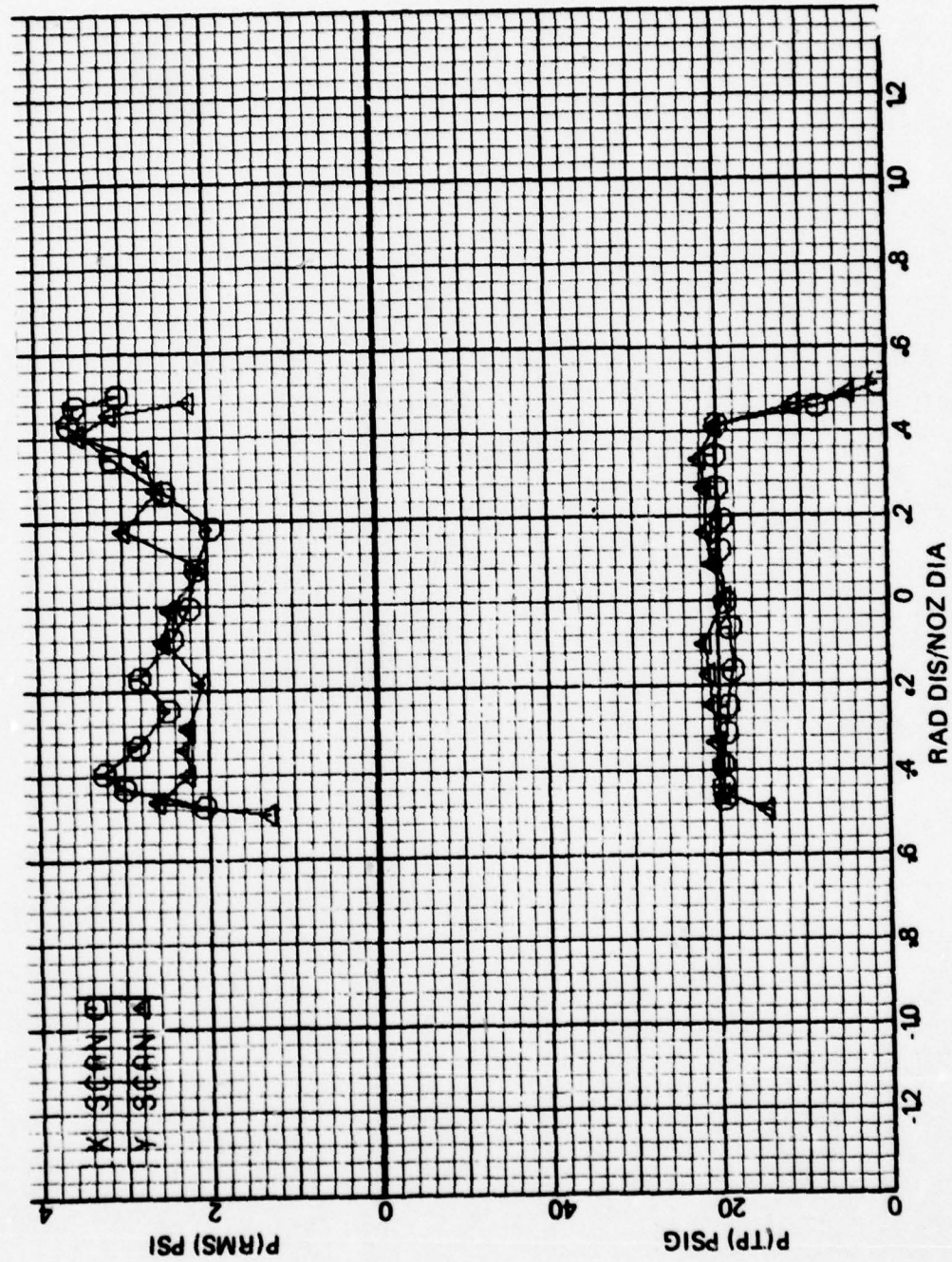


Figure A-11 Exit Pressure Surveys for the N_3^2 Nozzle with Screen S_1 at $NPR = 2.321$

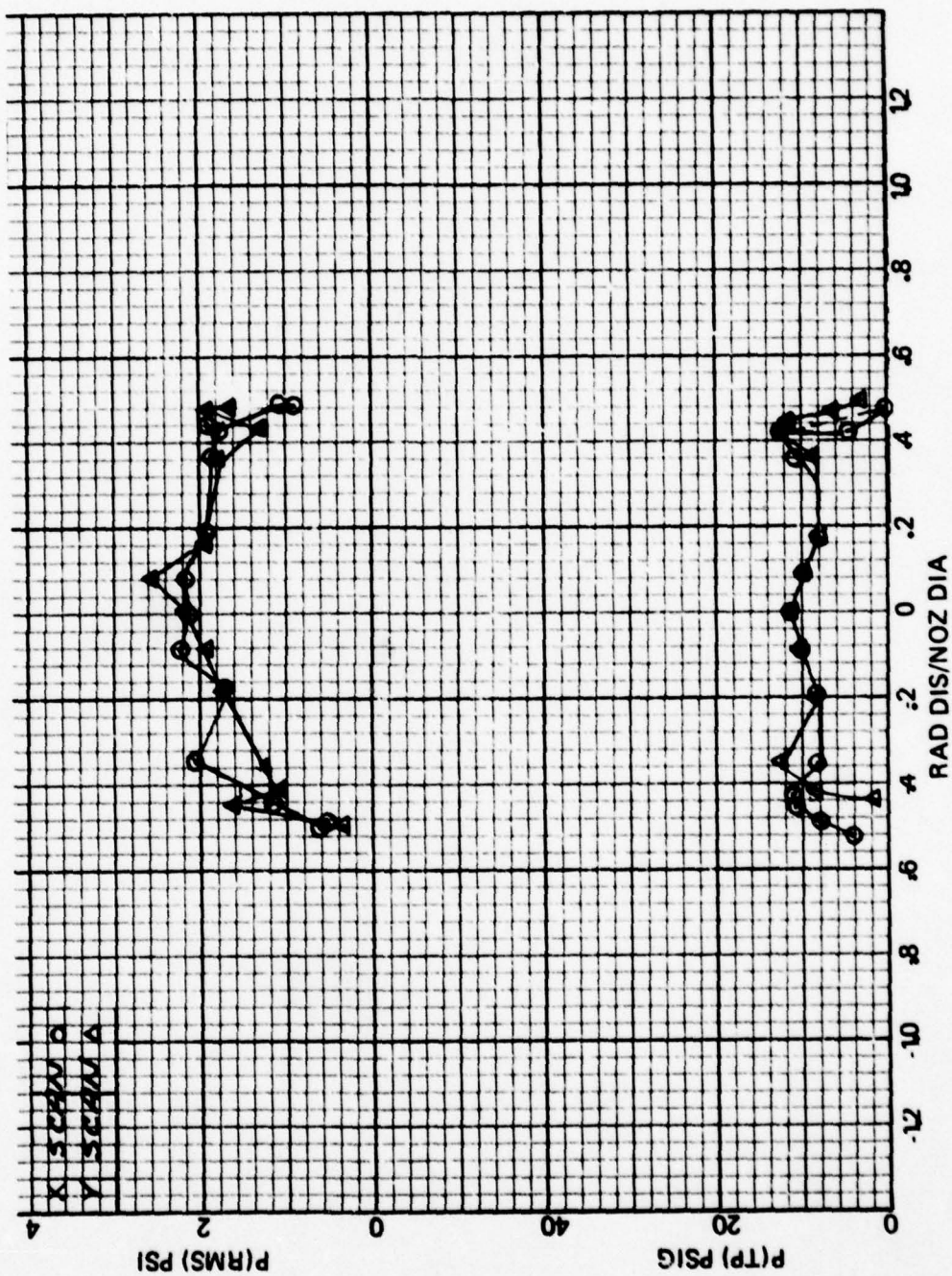


Figure A-12 Exit Pressure Surveys for the N₃-2 Nozzle with Screen S₂ at NPR = 1.552

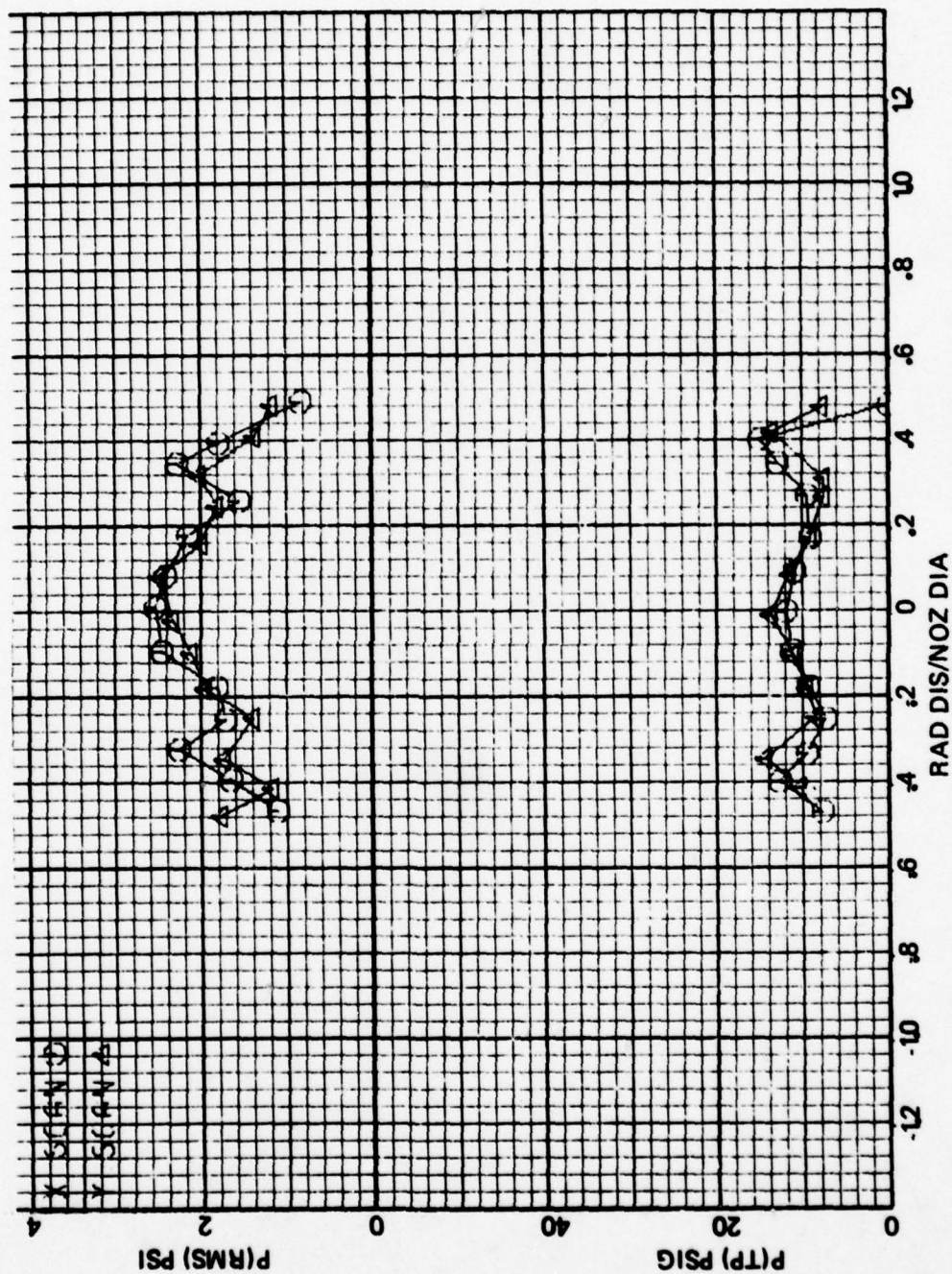


Figure A-13 Exit Pressure Surveys for the N_{32} Nozzle with Screen S_2 at $NPR = 1.655$

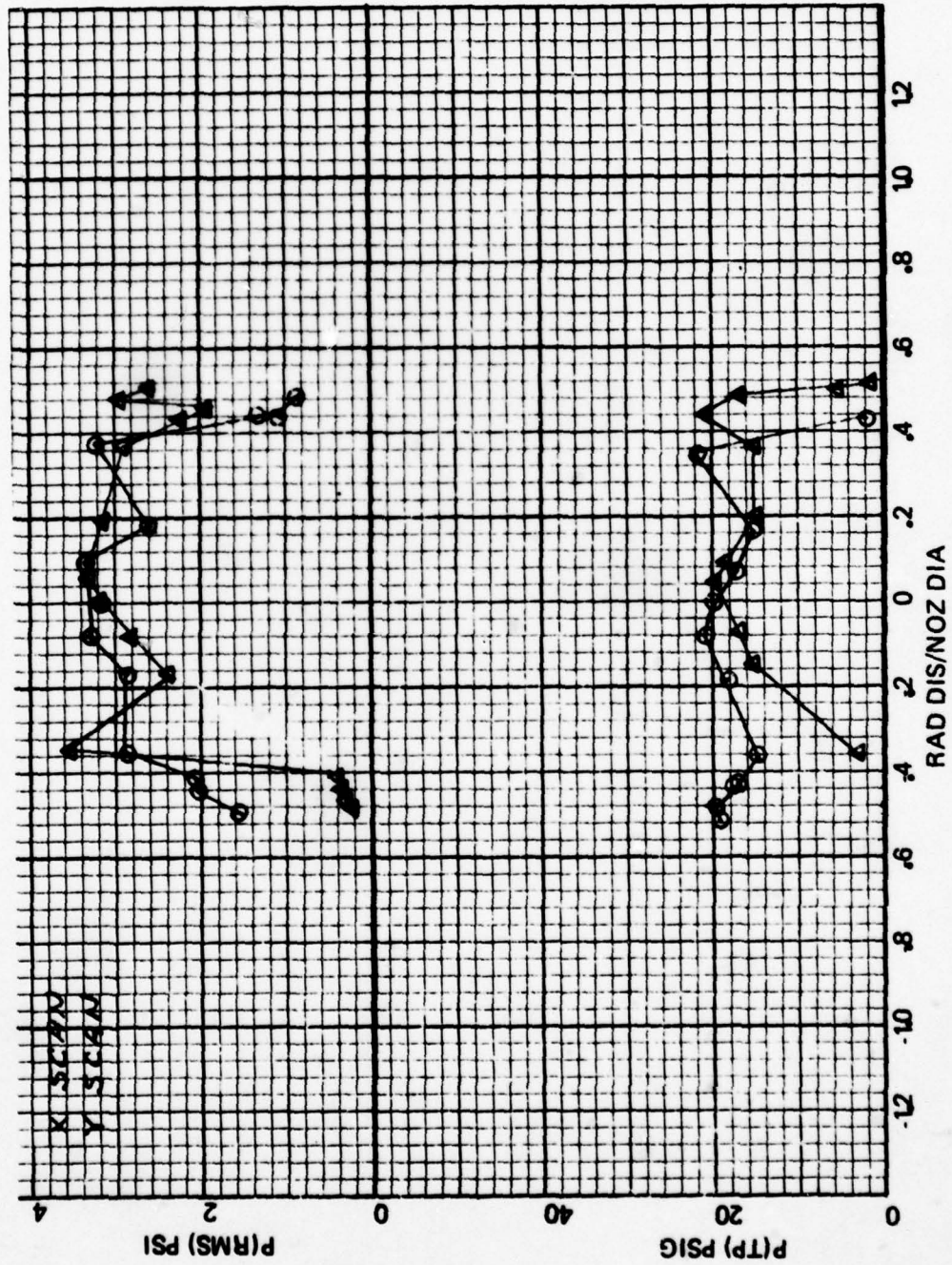


Figure A-14 Exit Pressure Surveys for the N_{32} Nozzle with Screen S_2 at $NPR = 1.958$

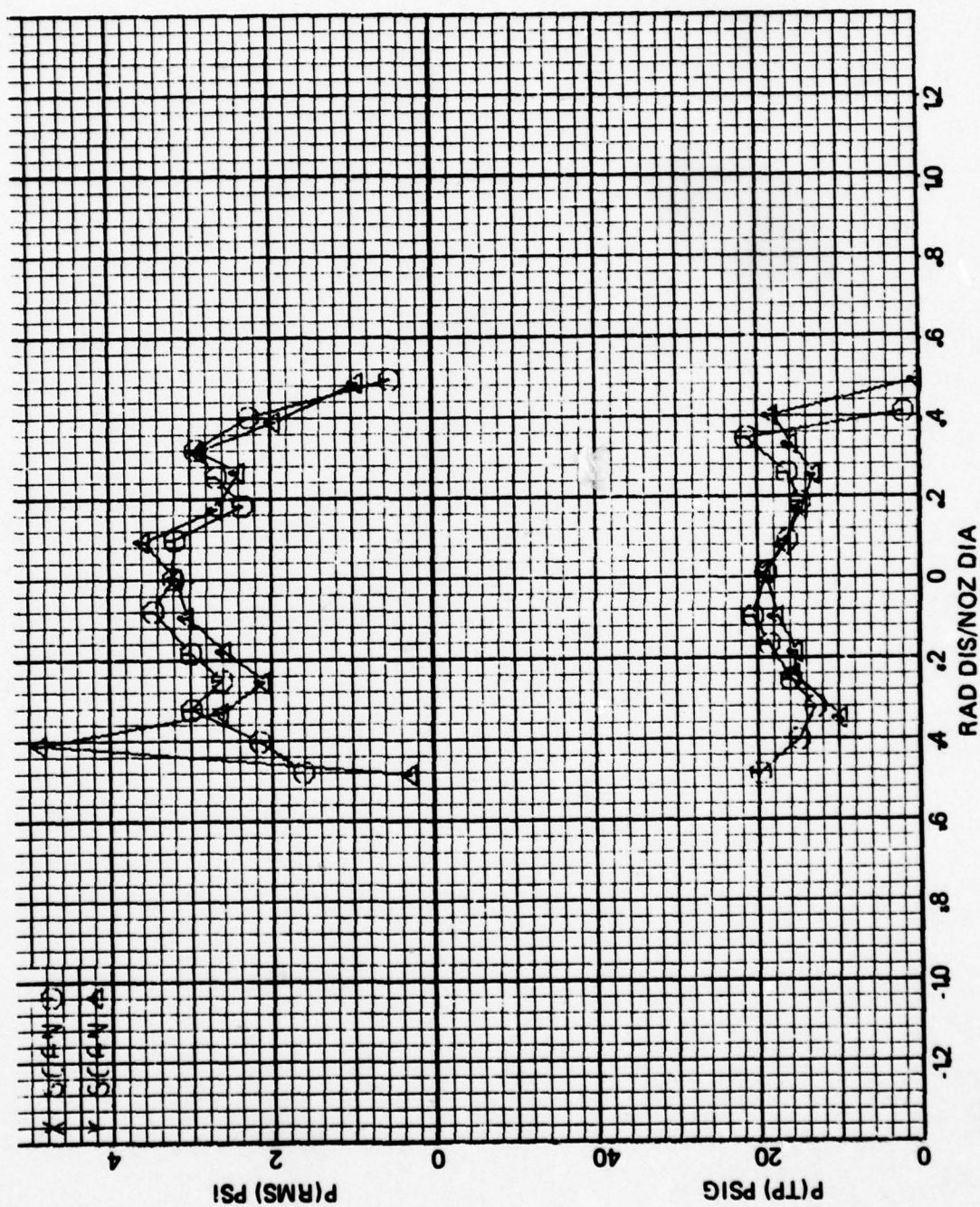


Figure A-15 Exit Pressure Surveys for the N₃₂ Nozzle with Screen S₂ at NPR = 1.986

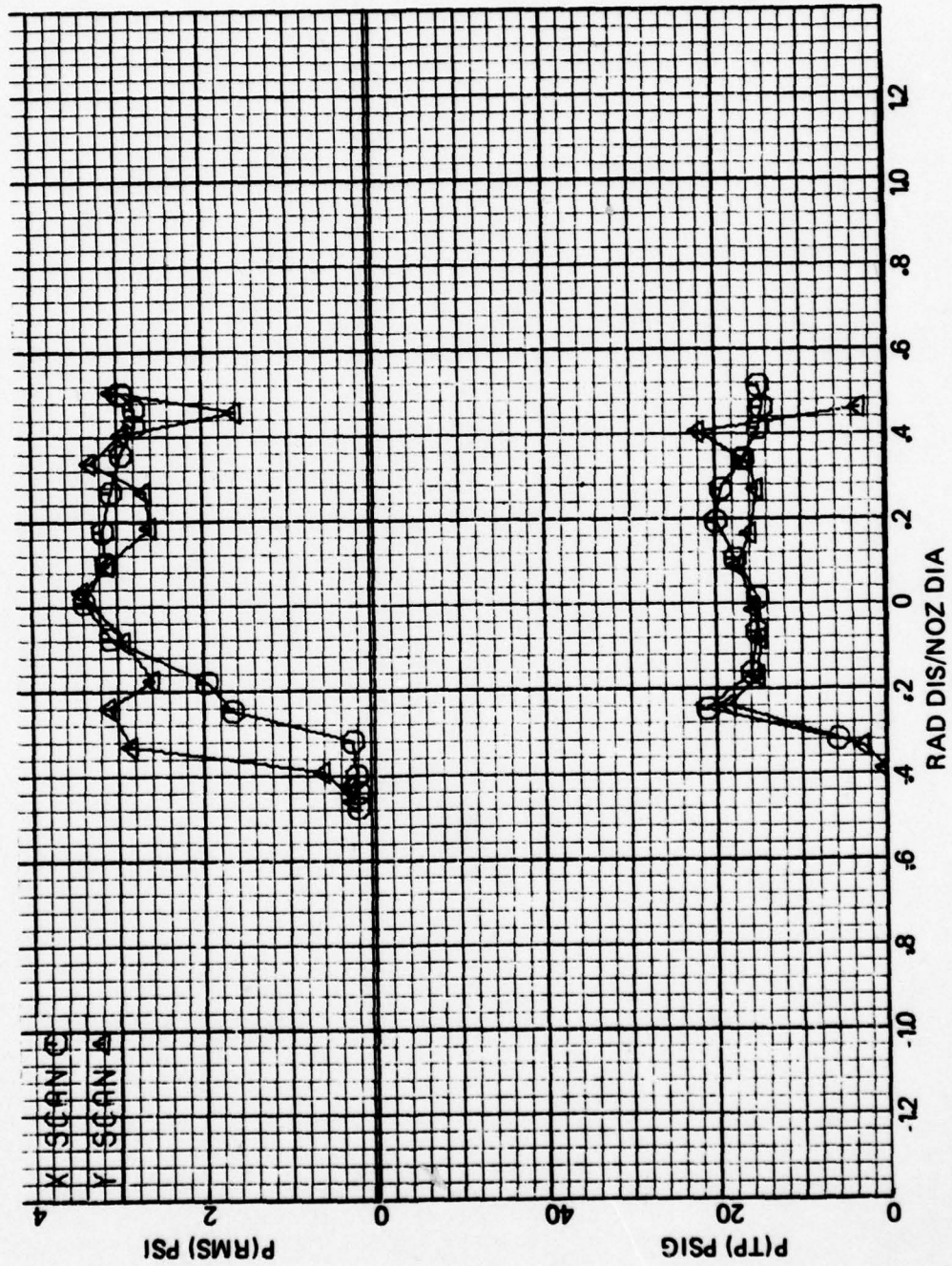


Figure A-16 Exit Pressure Surveys for the N₃₂ Nozzle with Screen S₂ at NPR = 2.041

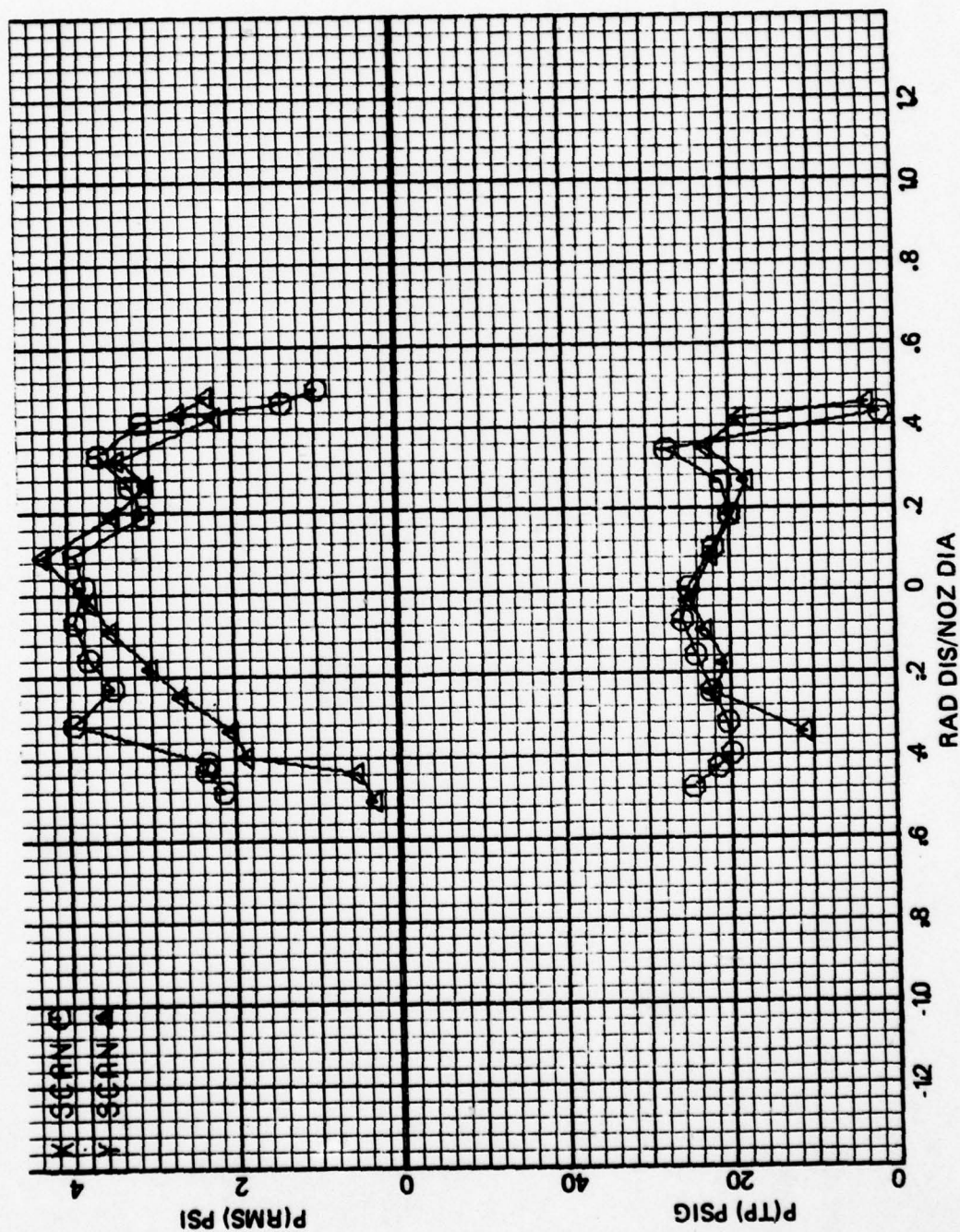


Figure A-17 Exit Pressure Surveys for the N₃₂ Nozzle with Screen S₂ at NPR = 2.317

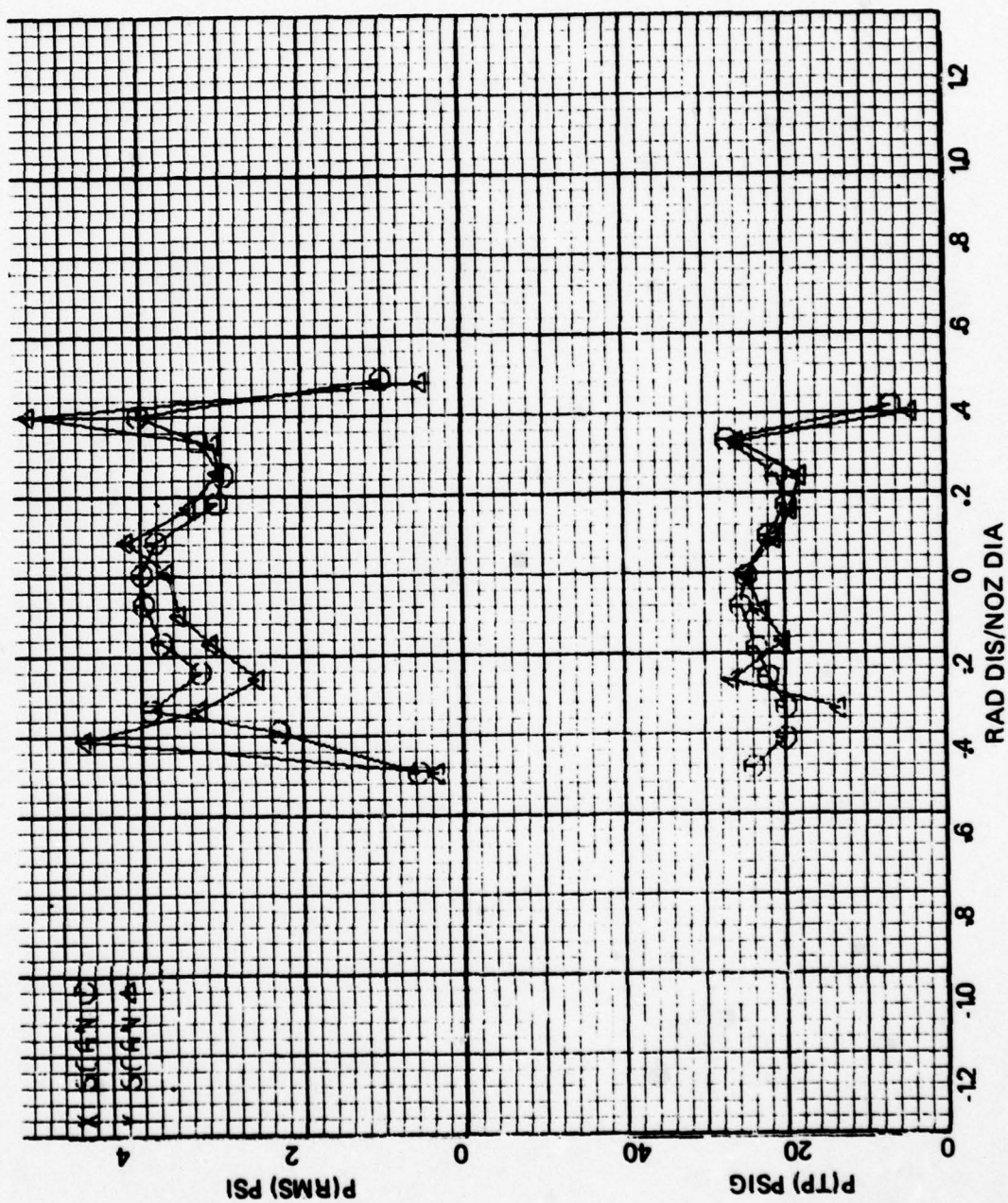


Figure A-18 Exit Pressure Surveys for the N₃₂ Nozzle with Screen S₂ at NPR = 2.372

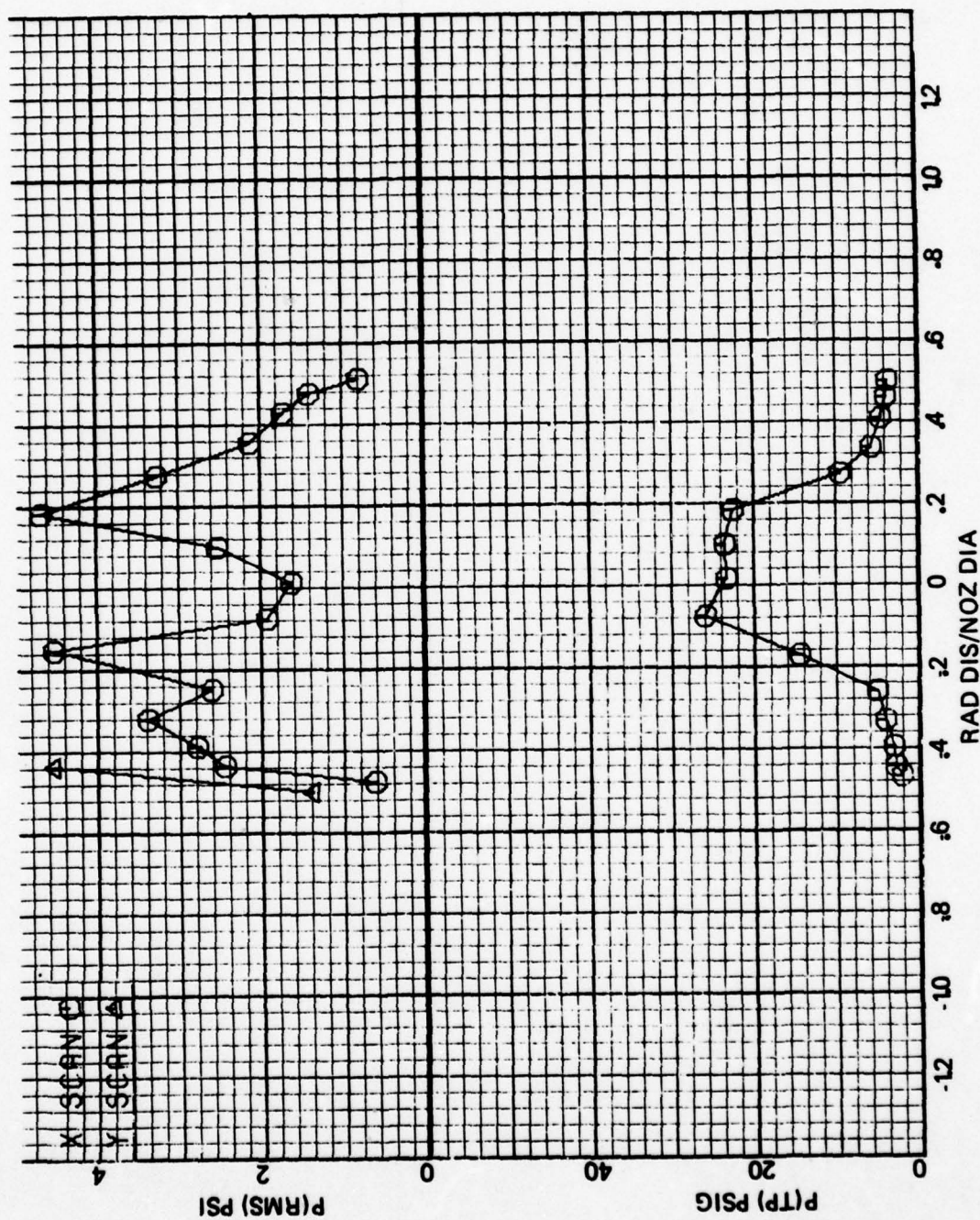


Figure A-19 Exit Pressure Surveys for the N_3^2 Nozzle with Pressure Plate P_1 at $NPR = 1.551$

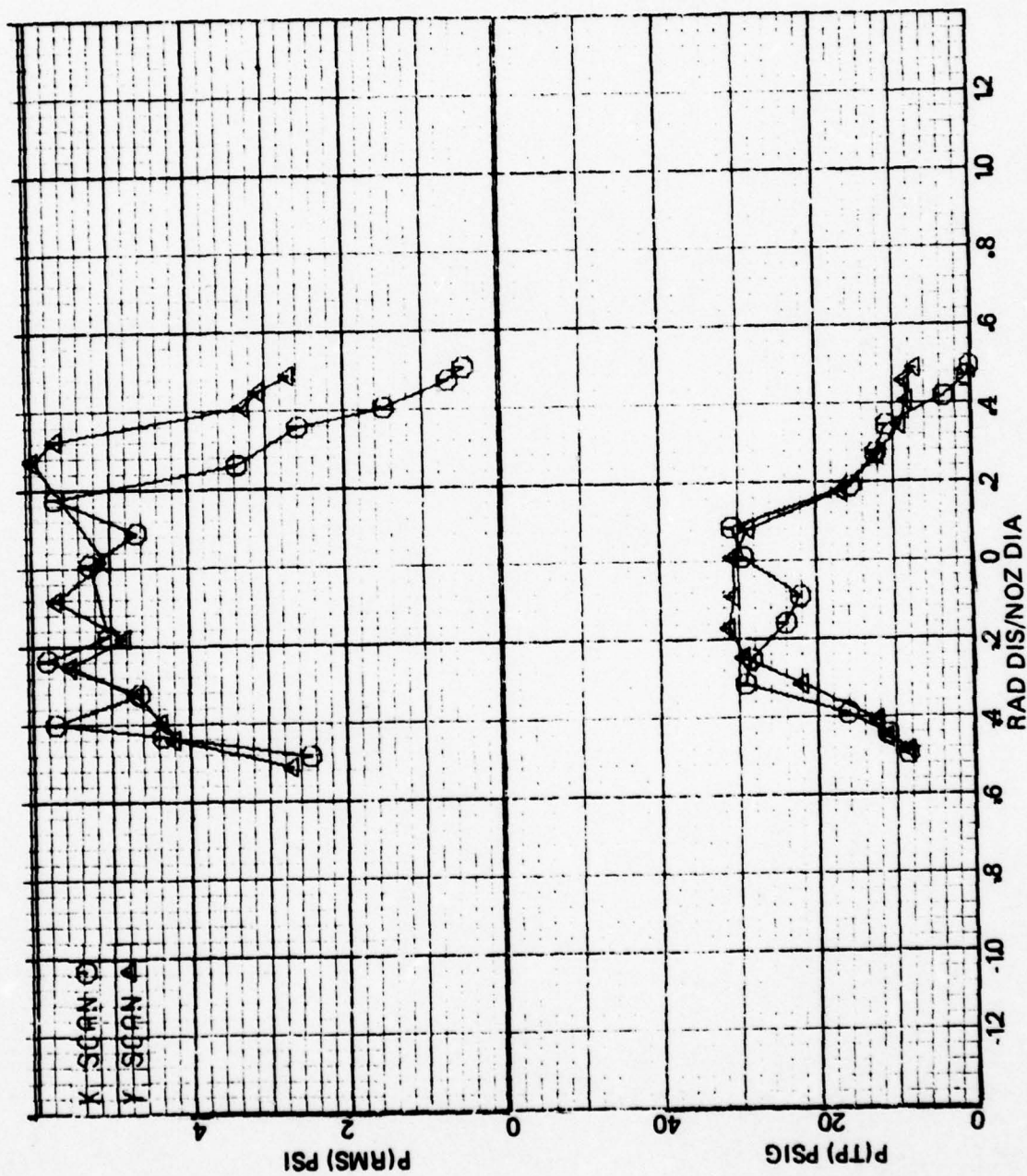


Figure A-20 Exit Pressure Surveys for the N₃₂ Nozzle with Pressure Plate P₁ at NPR = 1.972

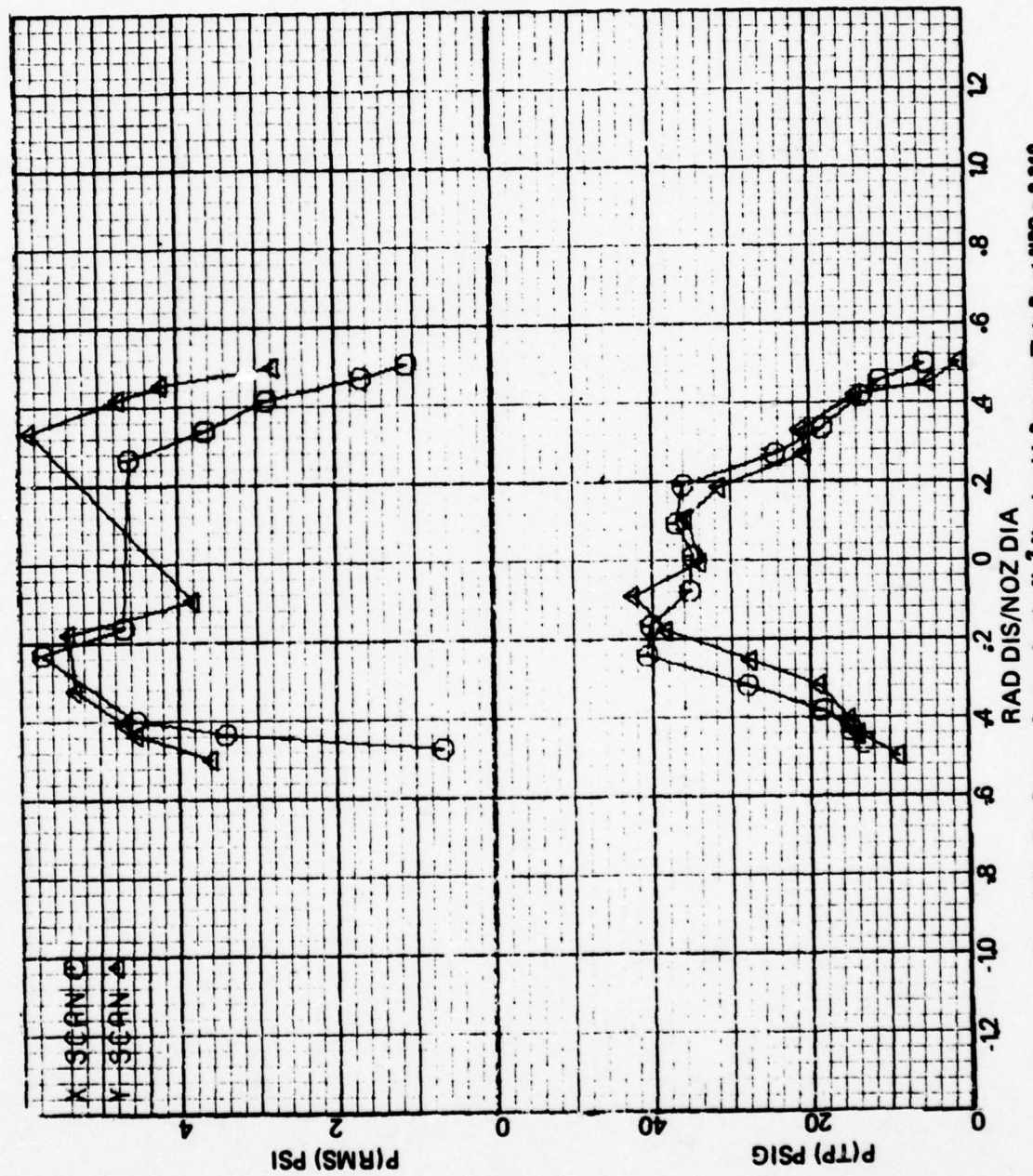


Figure A-21 Exit Pressure Surveys for the N₃-2 Nozzle with Pressure Plate P₁ at NPR = 2.310

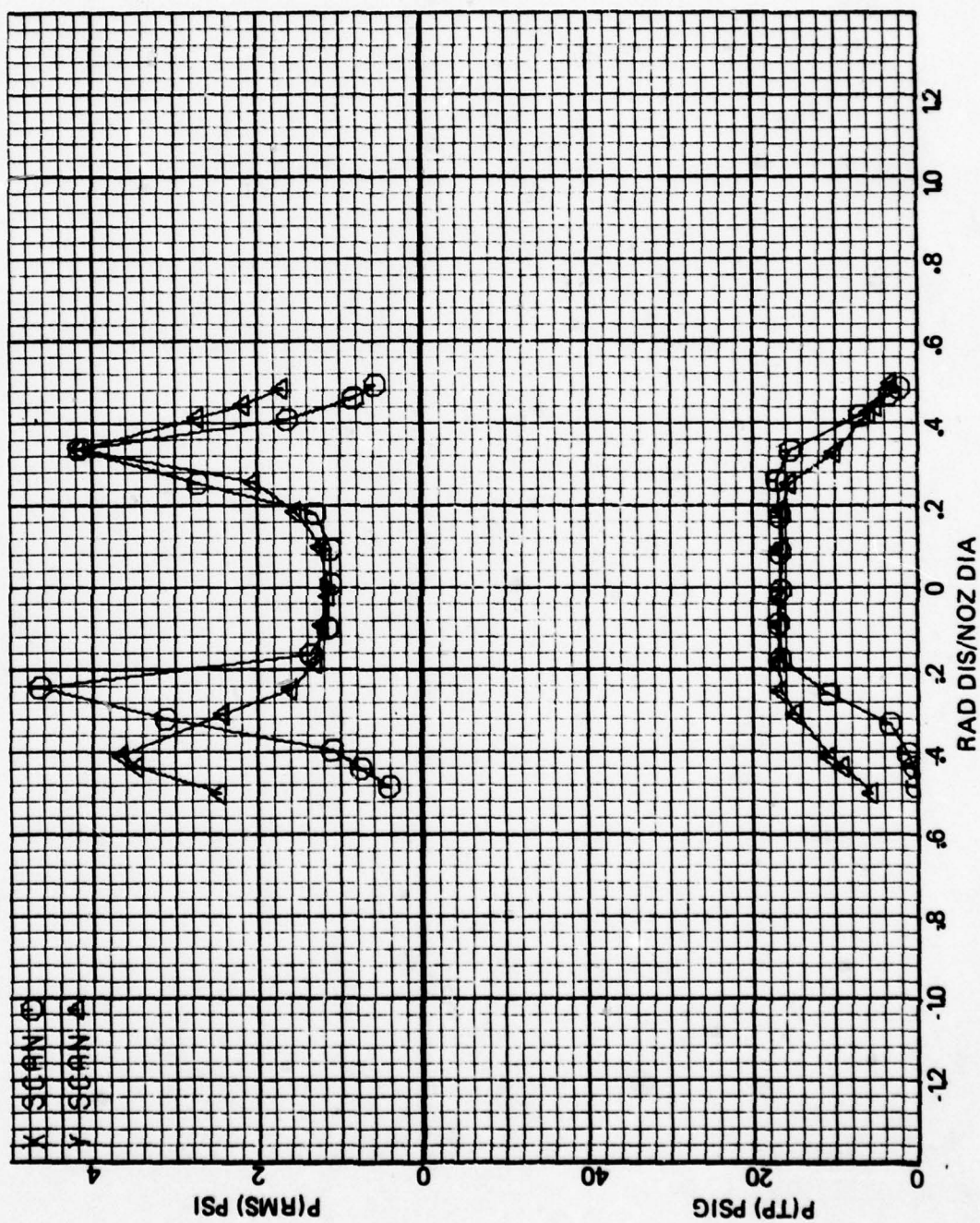


Figure A-22 Exit Pressure Surveys for the N₃₂ Nozzle with Pressure Plate P₂ at NPR = 1.520

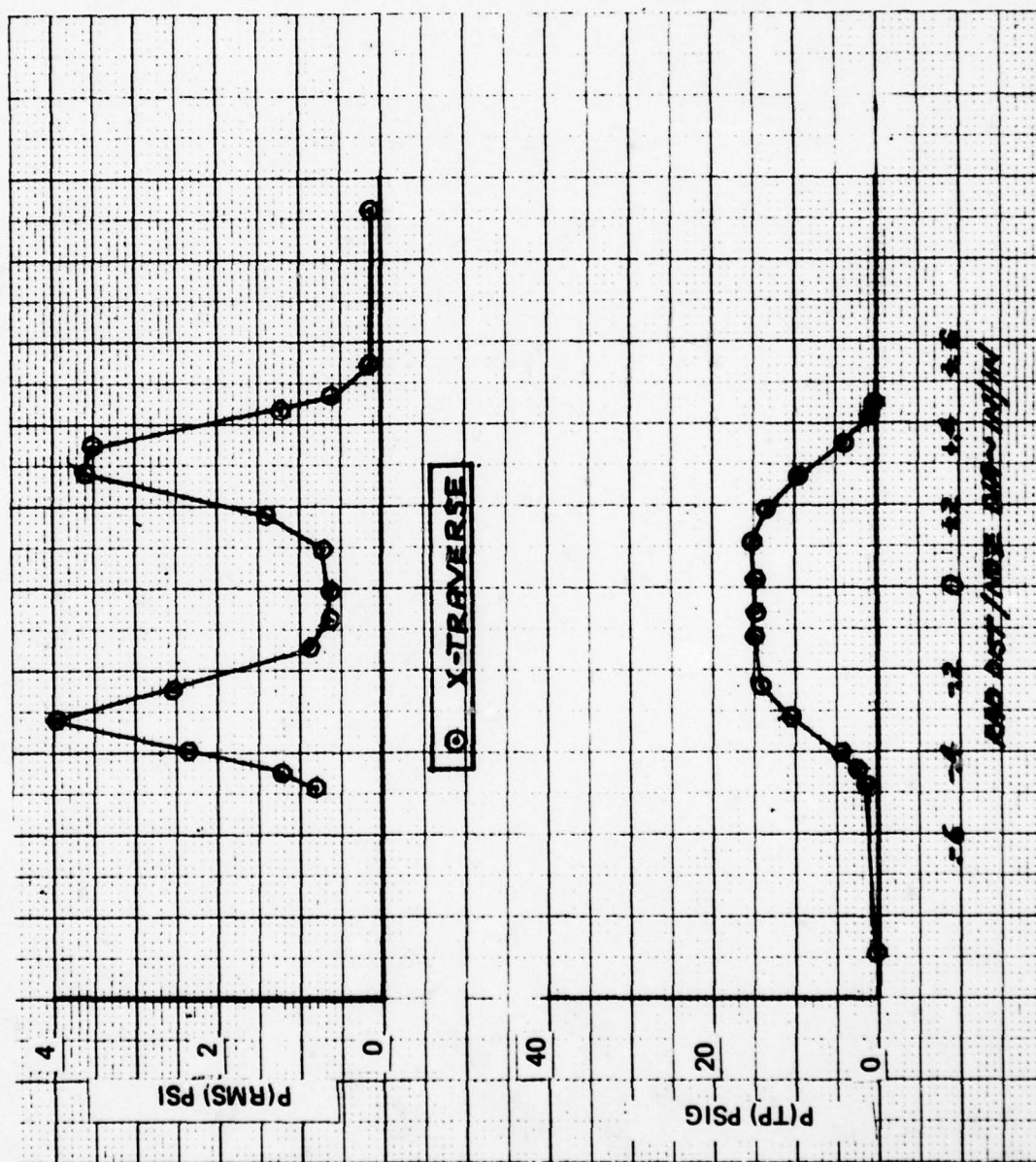


Figure A-23 Exit Pressure Surveys for the N_2 Nozzle with Pressure Plate P_2 at NPR = 1.510

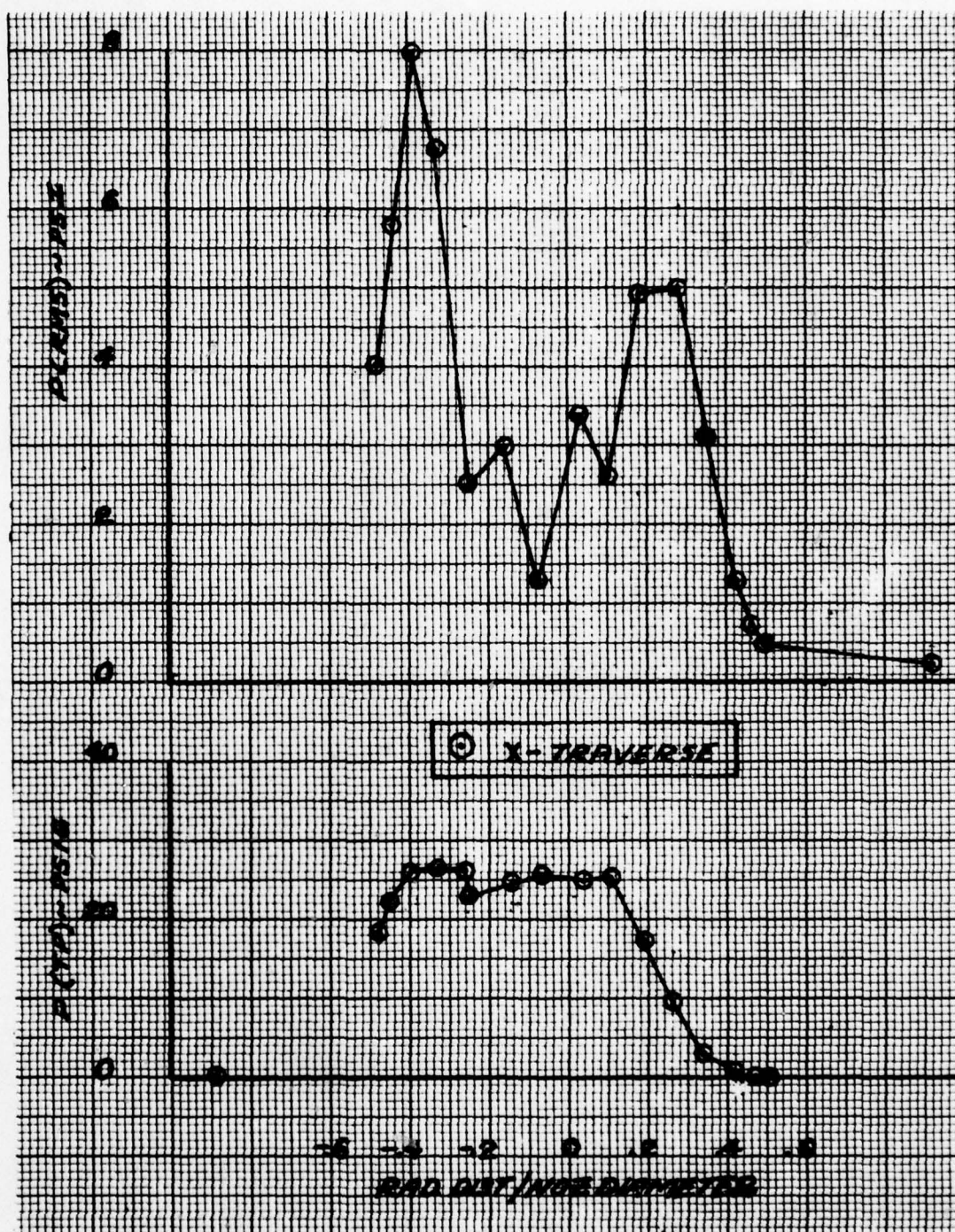


Figure A-24 Exit Pressure Surveys for the N_3^2 Nozzle with Pressure Plate P_2 at NPR = 1.990

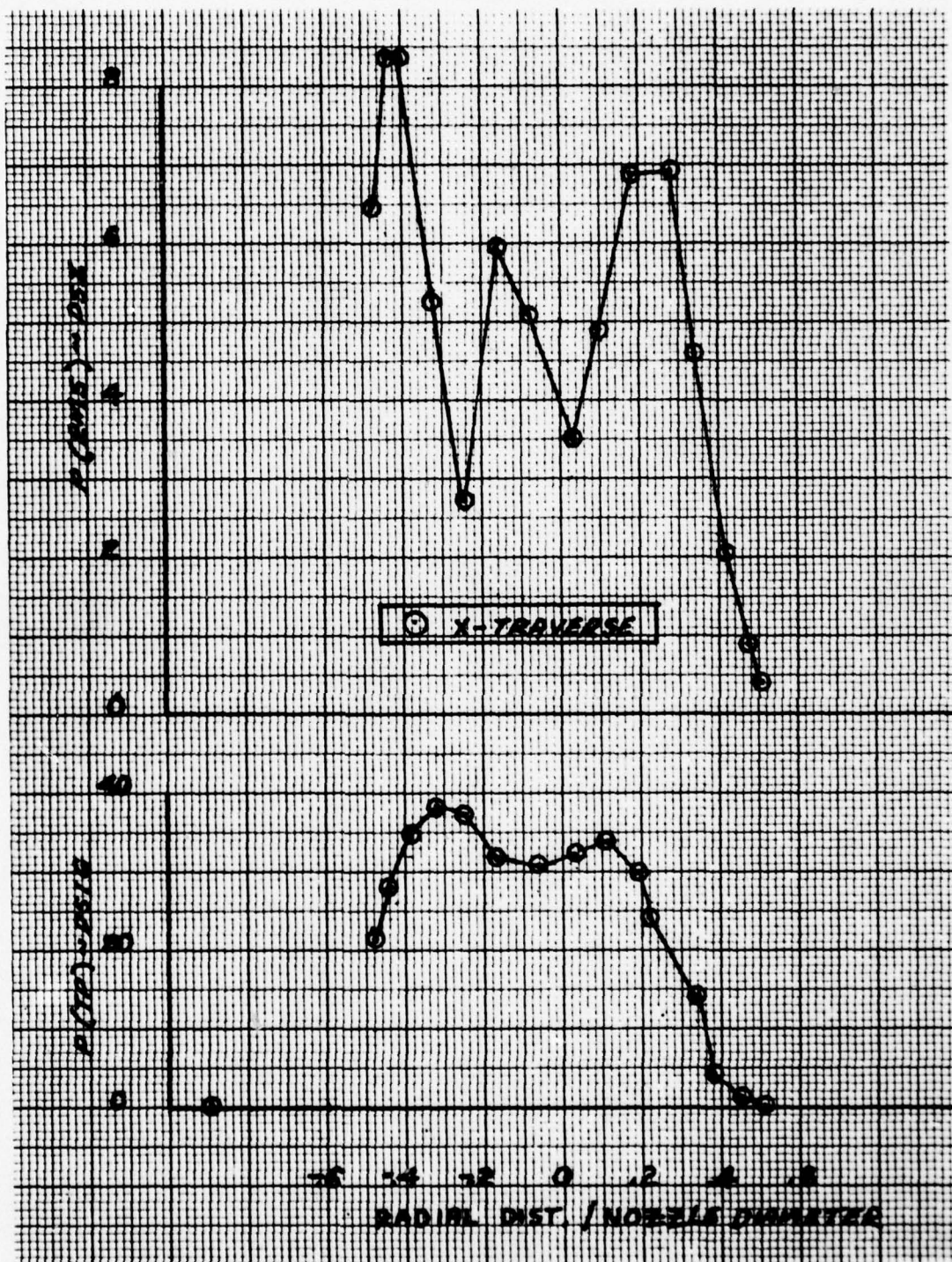


Figure A-25 Exit Pressure Surveys for the N_3^2 Nozzle with Pressure Plate P_2 at NPR = 2.420

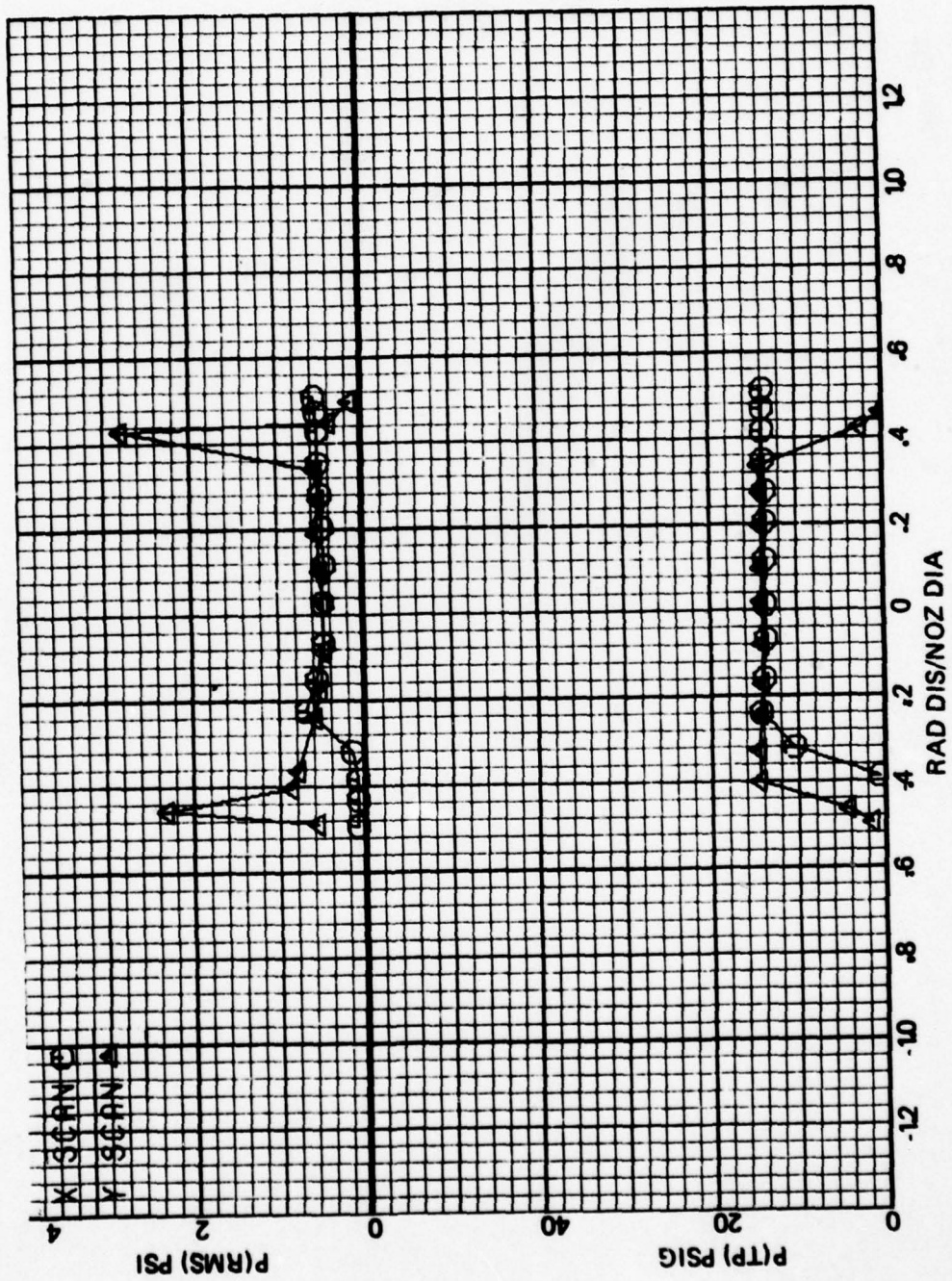


Figure A-26 Exit Pressure Surveys for the N₁₃² Baseline Nozzle at NPR = 1.897

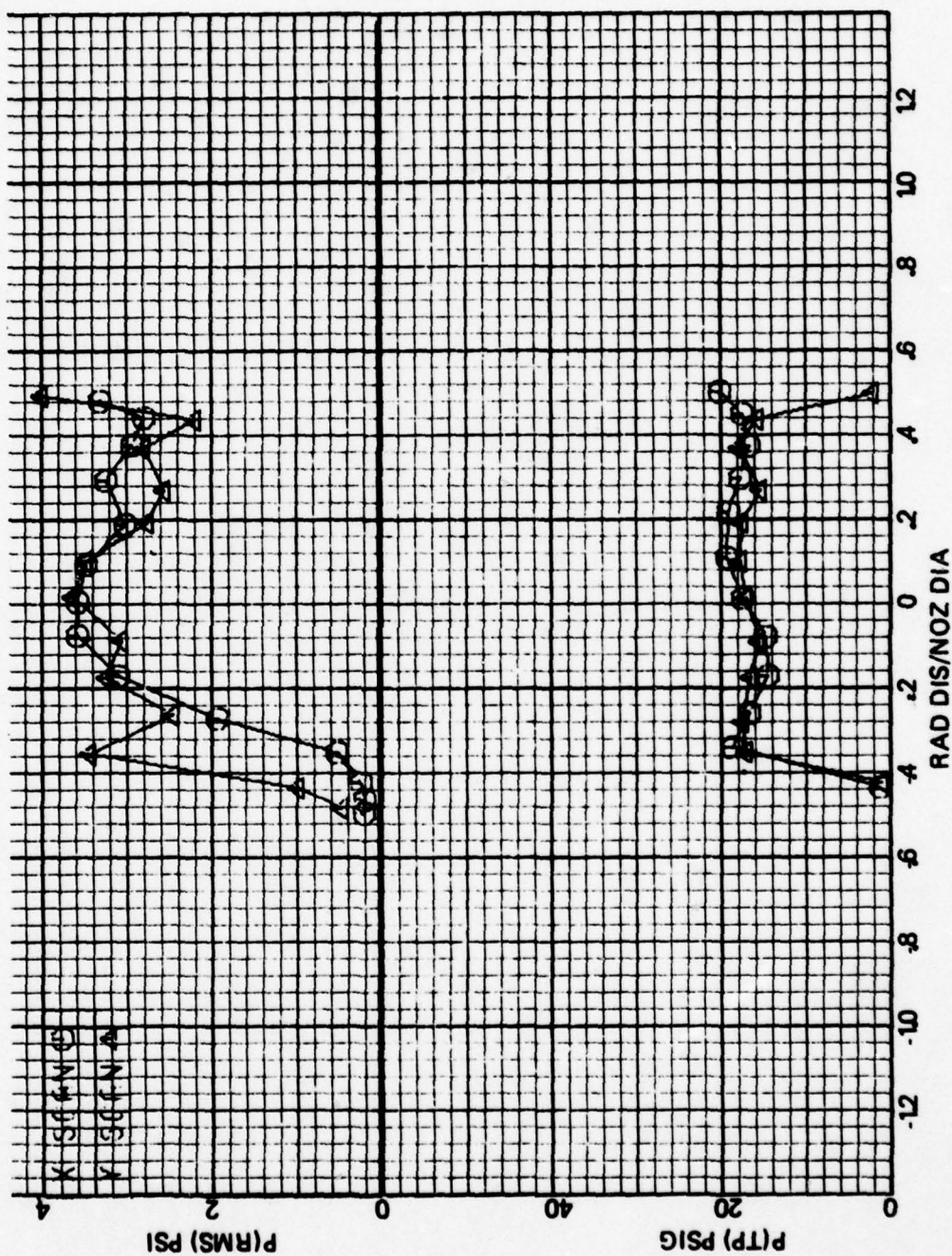


Figure A-27 Exit Pressure Surveys for the N_{11} Nozzle with Screen S_2 at $NPR = 2.062$

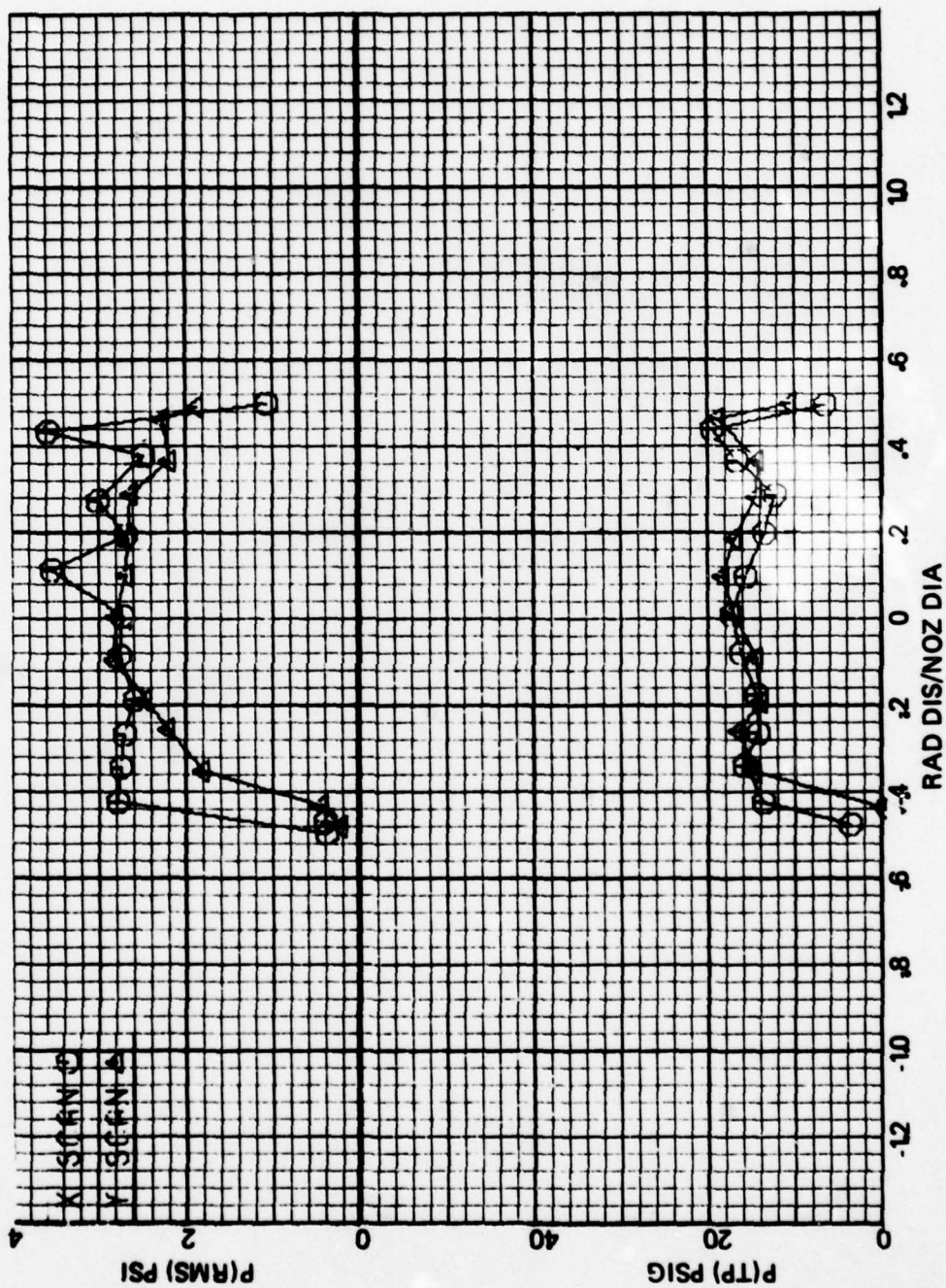


Figure A-28 Exit Pressure Surveys for the Ng^1 Nozzle with Screen S_2 at $\text{NPR} = 2.010$

APPENDIX B

INDUCED-FORCE MEASUREMENTS

This appendix contains the variation of net-induced forces with altitude for the configurations tested. Figure B-1 shows the effect of varying NPR on the baseline 2-nozzle configuration, and Figures B-2 through B-7 show the effects of varying NPR, screens S_1 and S_2 , and pressure profile plates P_1 and P_2 . Figure B-8 shows the effect of adding screens S_1 and S_2 to the three-nozzle configuration at a constant NPR of 2.0, and Figures B-9 and B-10 show the effects of adding these screens and plates P_1 and P_2 to the four-nozzle configuration. Figure B-11 compares the cruciform and large rectangular two-nozzle plate results. Figure B-12 shows the pure suckdown forces measured with the half-plate model, as described in Section 2.2.2

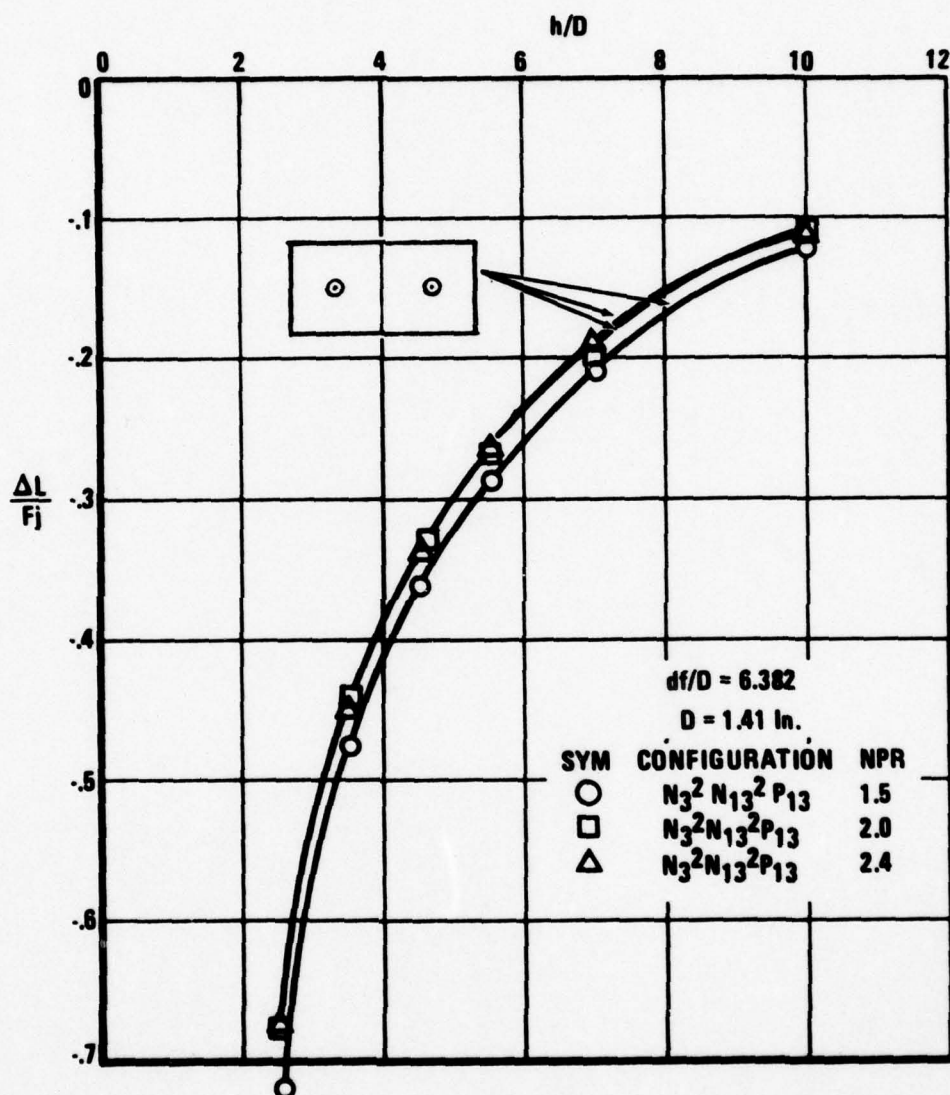


Figure B-1 Effect of Varying NPR and Model Altitude on $\Delta L/F_j$ for Baseline Two Nozzle Configuration

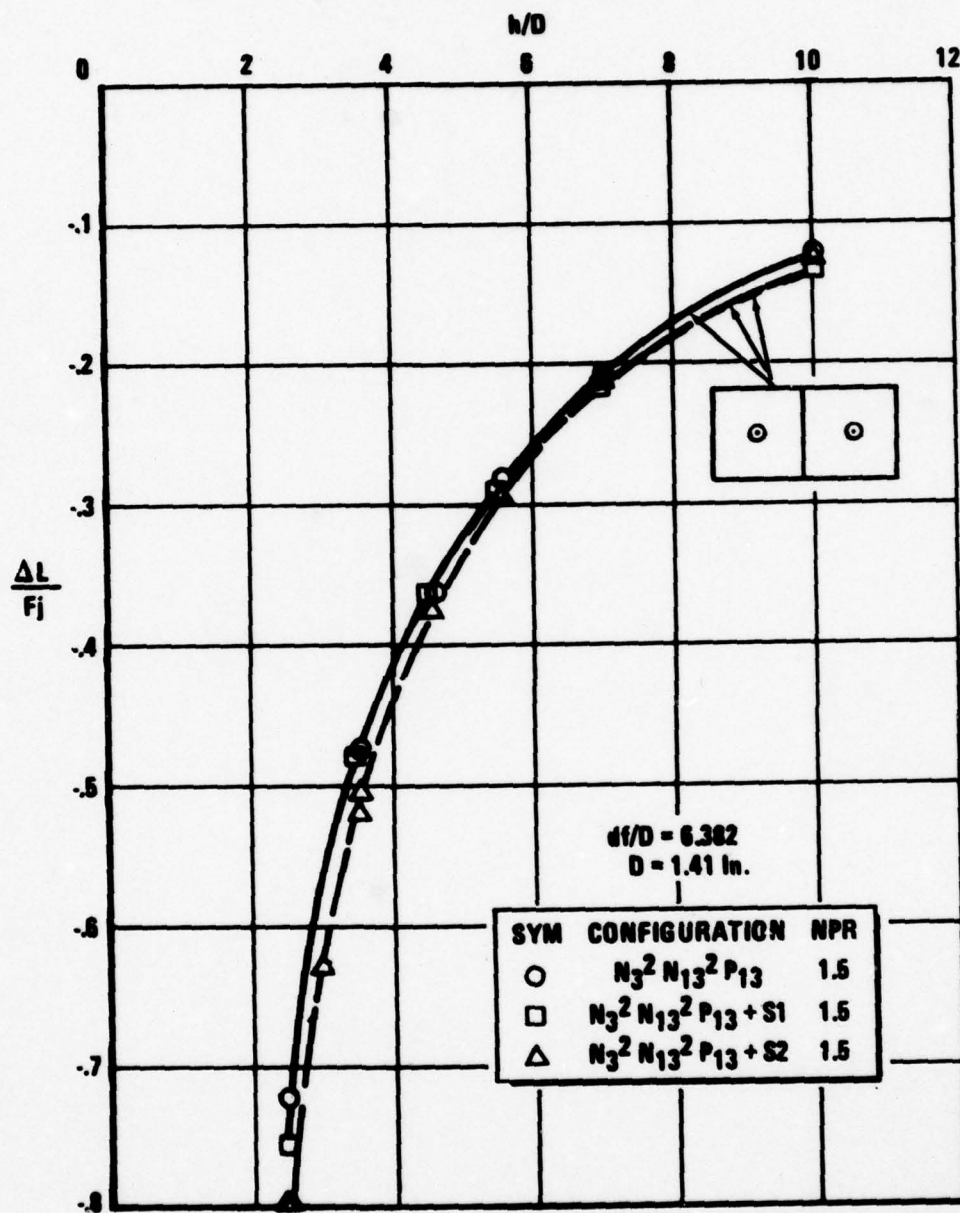


Figure B-2 Effect of Turbulence Screens on $\Delta L/F_j$ for Two Nozzle Configuration, $N_3^2 N_{13}^2 P_{13}$, at $NPR=1.5$

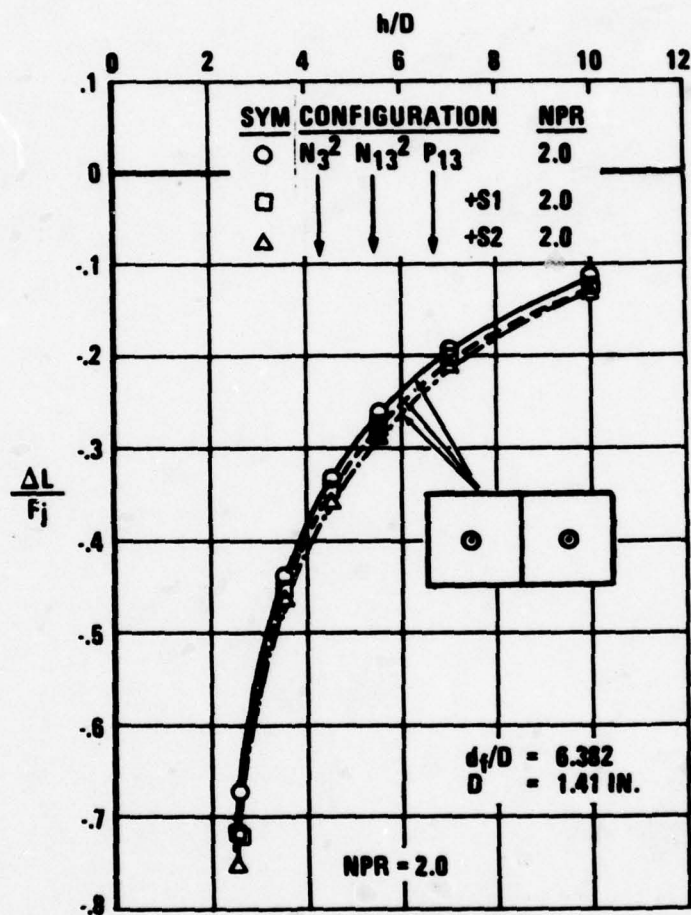


Figure B-3 Effect of Turbulence Screens on $\Delta L/F_j$ for Two Nozzle Configuration, $N_3^2 N_{13}^2 P_{13}$, at NPR = 2.0

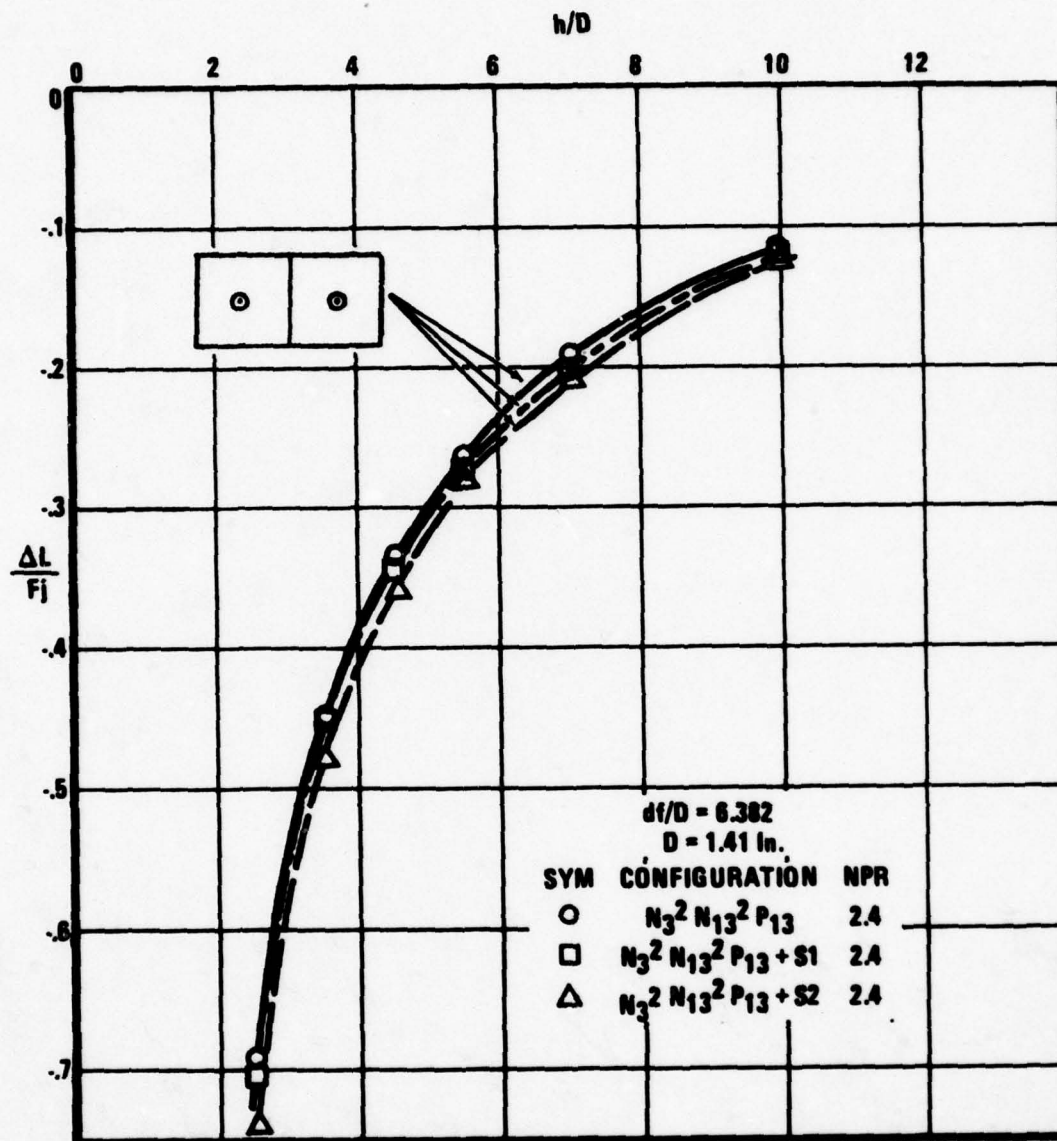


Figure B-4 Effect of Turbulence Screens on $\Delta L/F_j$ for Two Nozzle Configuration, $N_3^2 N_{13}^2 P_{13}$, at $NPR = 2.4$

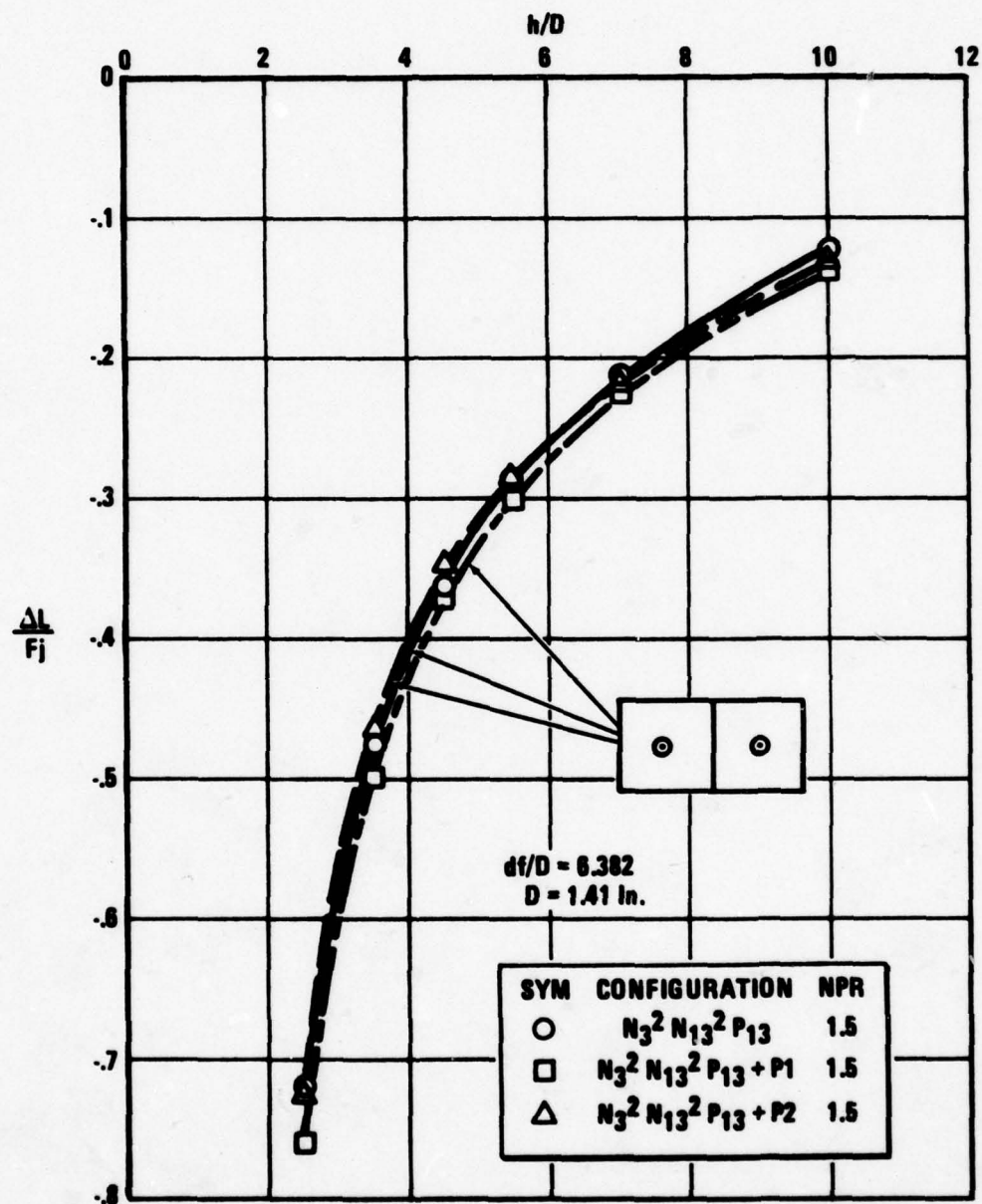


Figure B-5 Effect of Pressure Profile Plates on $\Delta L/F_j$ for Two Nozzle Configuration, $N_3^2 N_{13}^2 P_{13}$, at $NPR = 1.5$

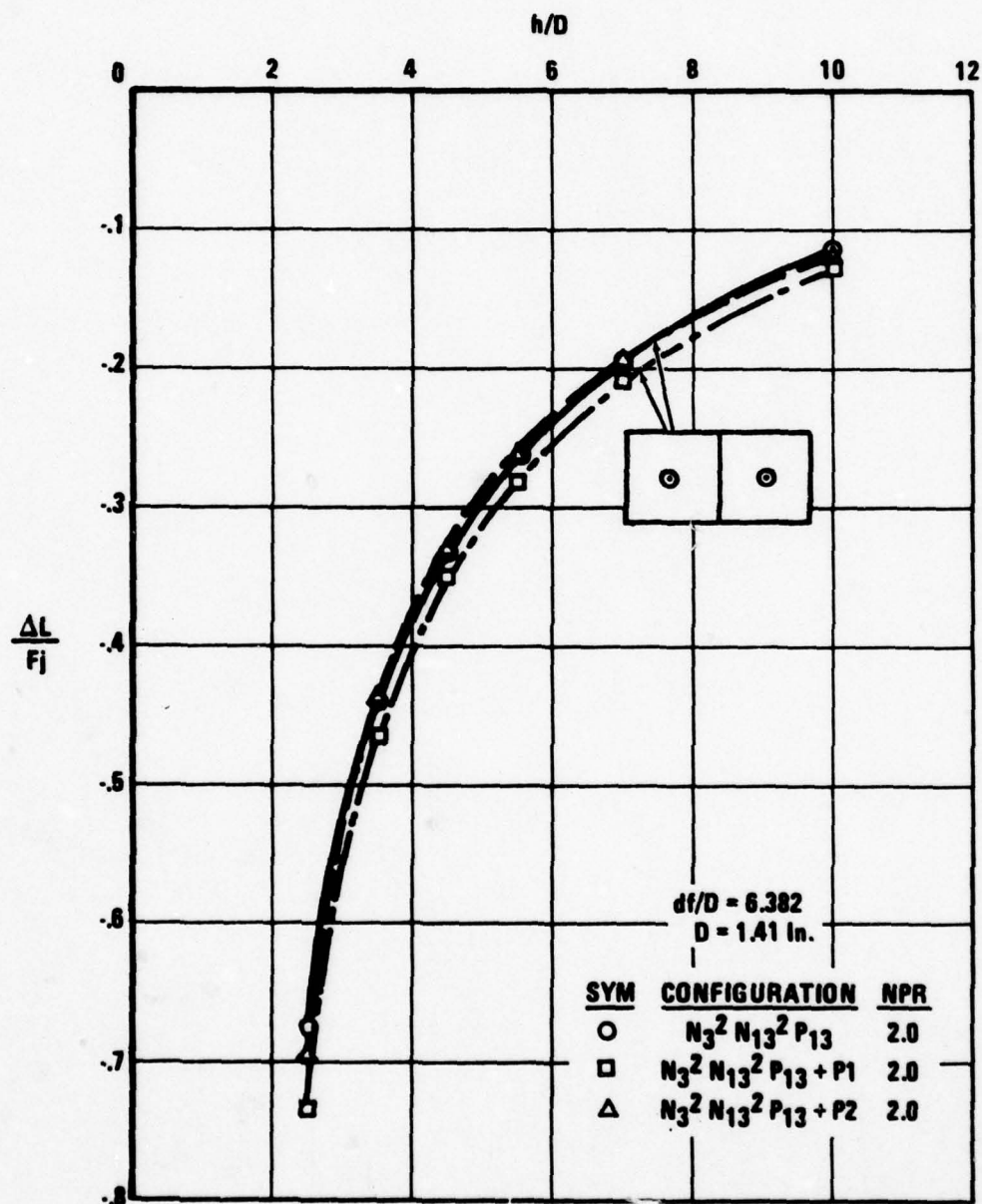


Figure B-6 Effect of Pressure Profile Plates on $\Delta L/Fj$ for Two Nozzle Configuration, $N_3^2 N_{13}^2 P_{13}$, at $NPR = 2.0$

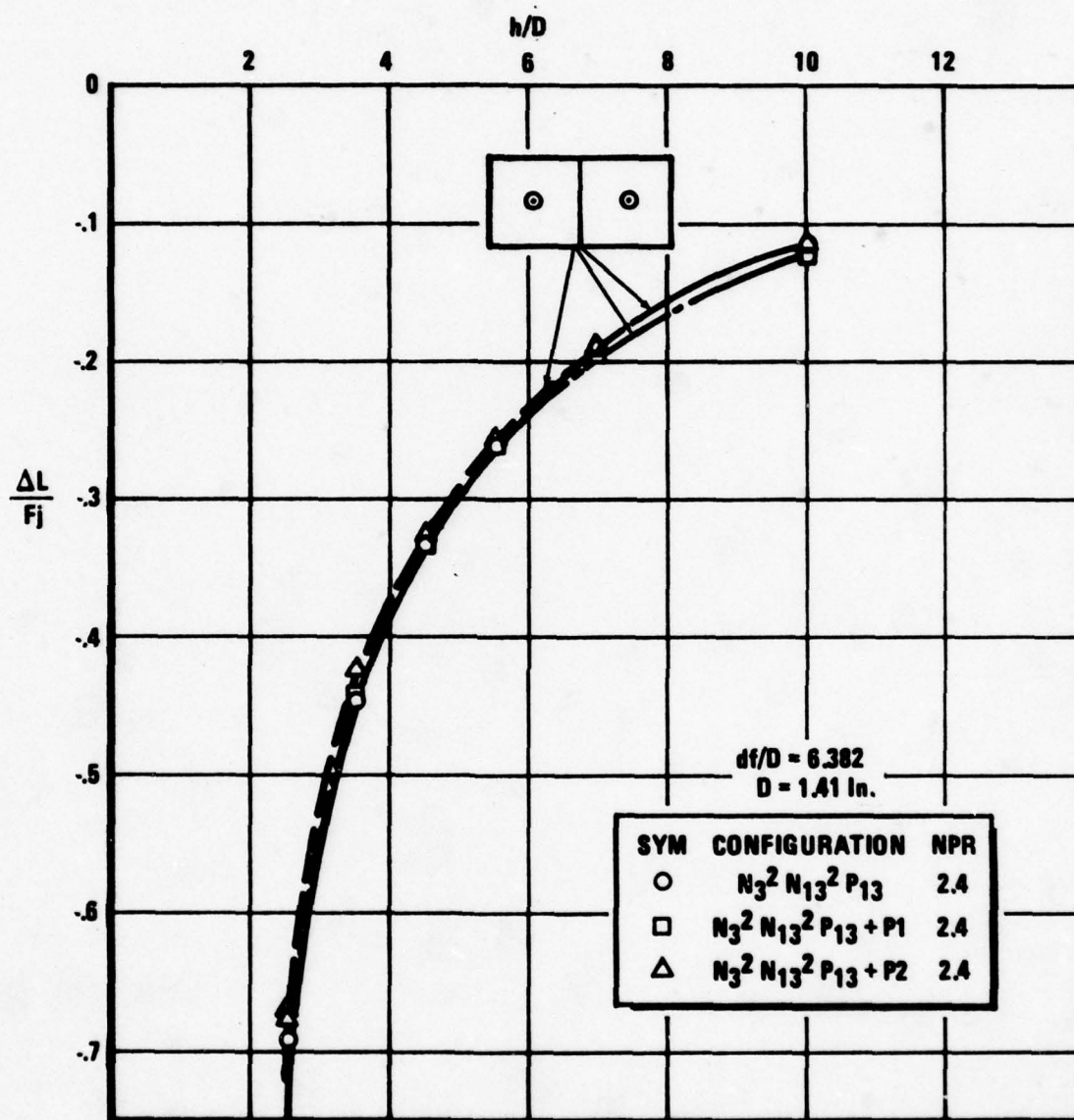


Figure B-7 Effect of Pressure Profile Plates on $\Delta L/F_j$ for Two Nozzle Configuration, $N_3^2 N_{13}^2 P_{13}$, at $NPR = 2.4$

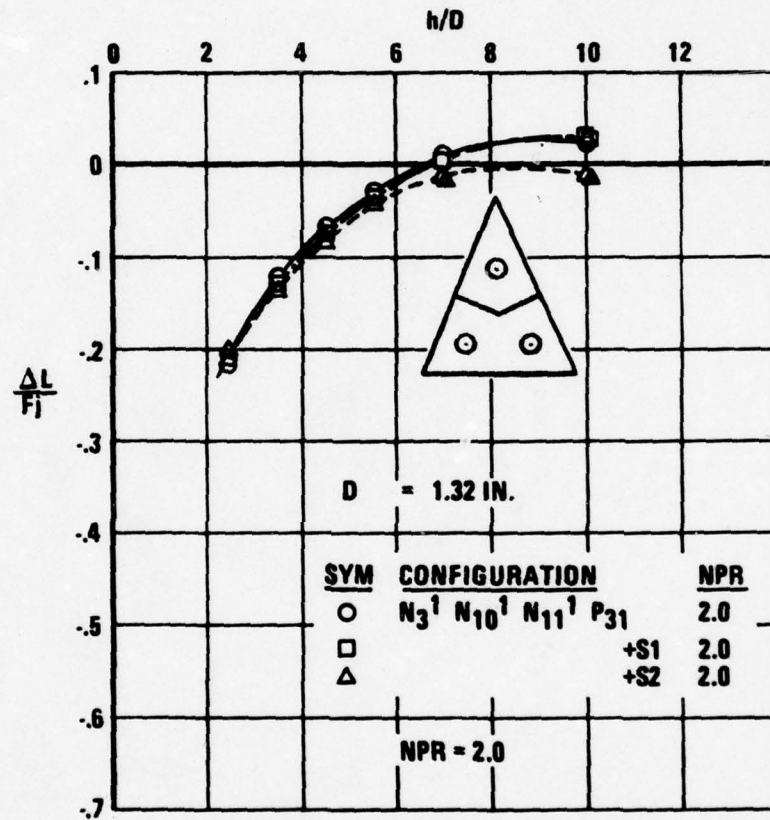


Figure B-8 Effect of Turbulence Screens on $\Delta L/Fj$ for Three Nozzle Configuration, $N_3^1 N_{10}^1 N_{11}^1 P_{31}$, at NPR = 2.0

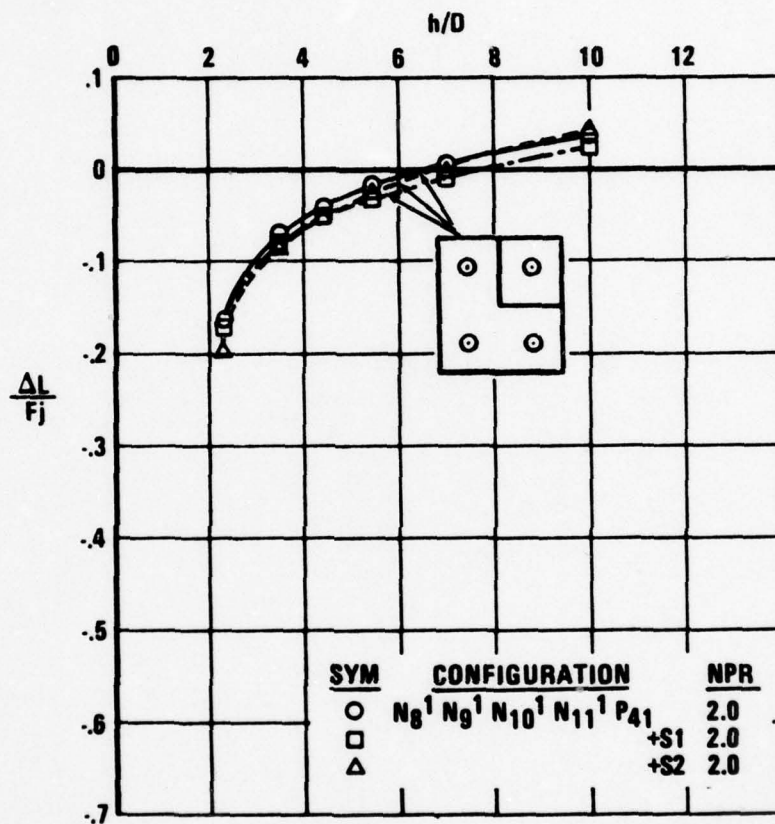


Figure B-9 Effect of Turbulence Screens on $\Delta L/Fj$ for Four Nozzle Configuration, $N_8^1 N_9^1 N_{10}^1 N_{11}^1 P_{41}$, at NPR = 2.0

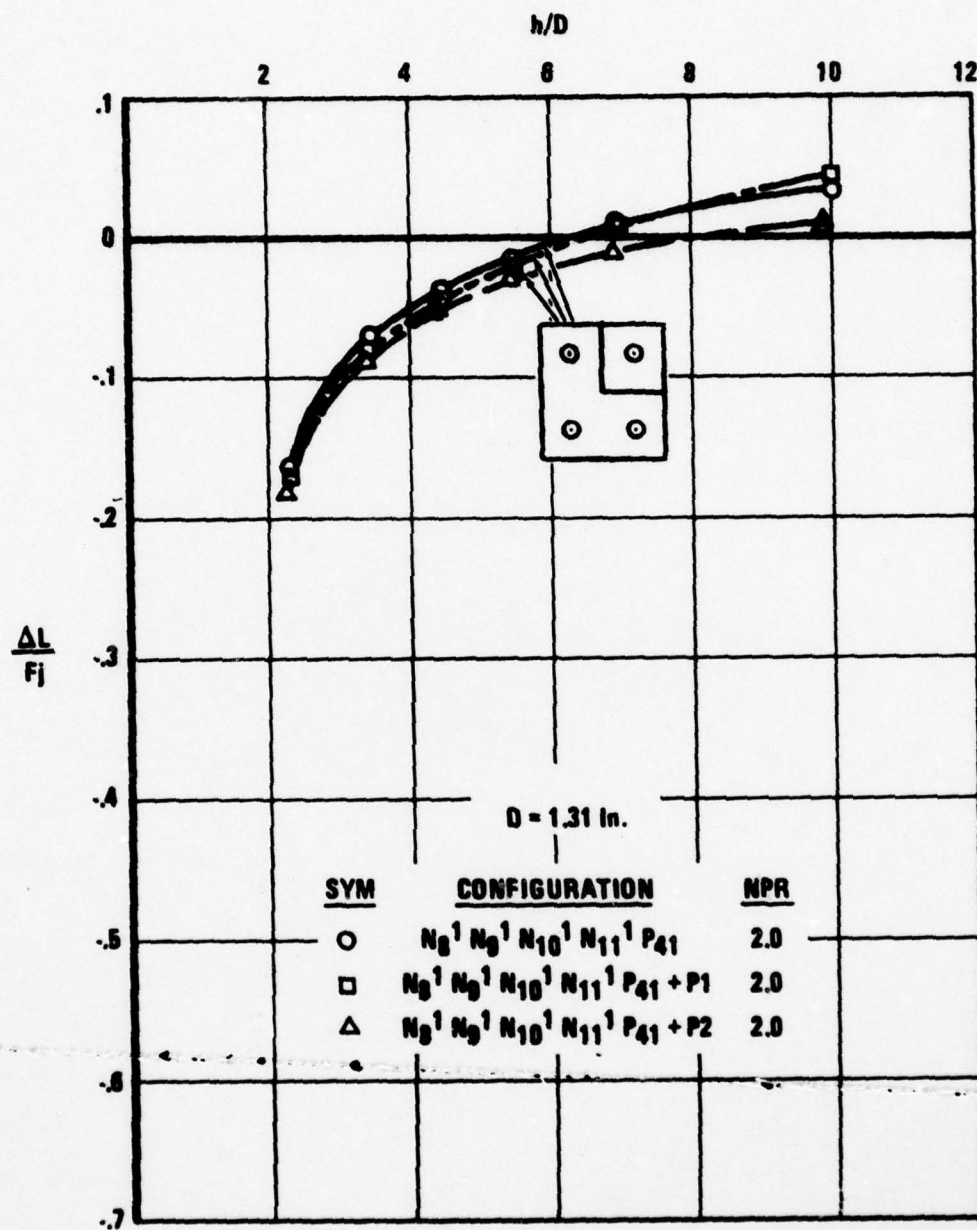


Figure B-10 Effect of Pressure Profile Plates on $\Delta L/F_j$ for Four Nozzle Configuration, $N_8^1 N_9^1 N_{10}^1 N_{11}^1 P_{41}$, at $NPR = 2.0$

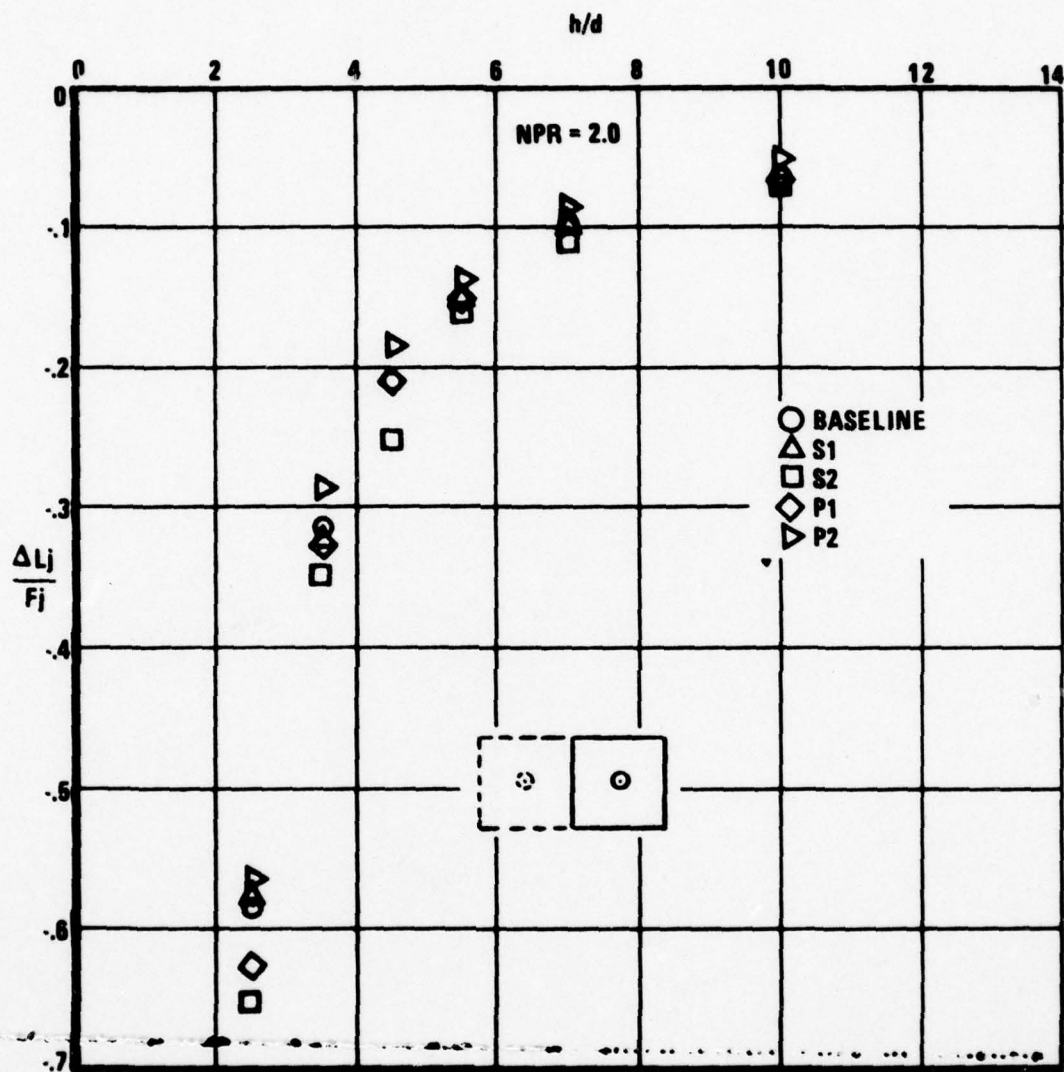


Figure B-11 Effect of Turbulence Screens and Pressure Profile Plates on Pure Suckdown

APPENDIX C

FOUNTAIN DYNAMIC PRESSURE CHARACTERISTICS

The methods employed to integrate the fountain dynamic pressure data to obtain the fountain core force characteristics are discussed in Section 3.3. The data were edited and faired before integration by use of an interactive graphics procedure at the Fort Worth Division. The faired data are included in this appendix for each configuration for which rake surveys indicated the presence of a fountain. These data are presented in the form of dynamic pressure profiles across the fountain (X-direction) at various locations along the fountain (Y-direction) for each model height, h/D , and rake height, Z/D (see Figure 16 for axis system definition).

Table 2-3 summarizes the fountain survey cases. Figures C-1 through C-16 contain the data for the four-nozzle baseline and the S_2 and P_2 configurations. Figures C-17 through C-28 contain the two-nozzle-baseline and S_2 data.

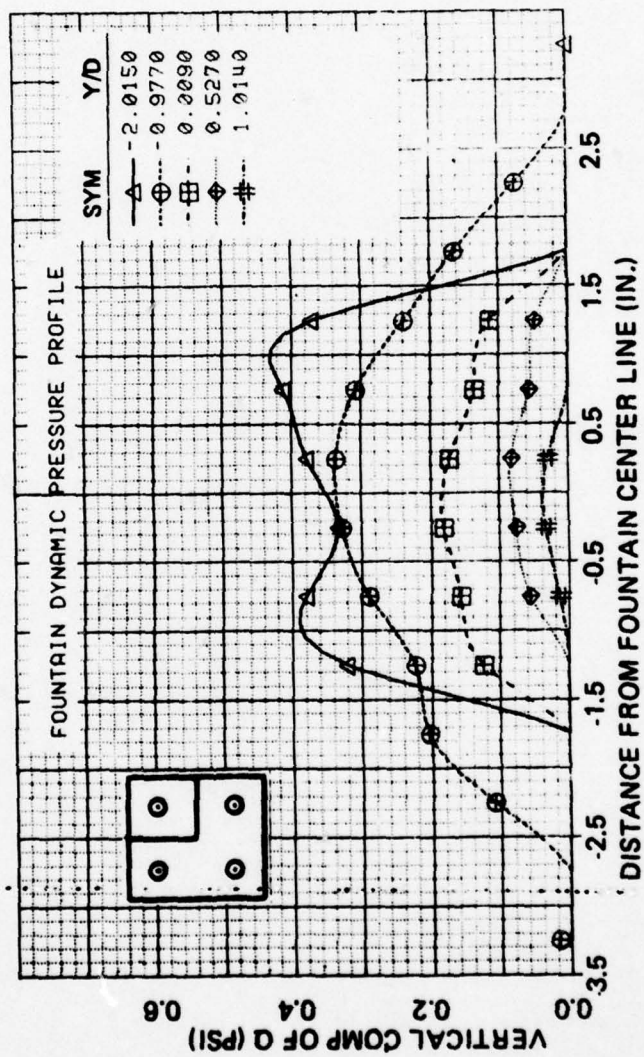


Figure C-1 Dynamic Pressure Profiles for Baseline Four Nozzle Configuration at NPR = 2.0,
 $D = 1.31$ in., $h/D = 8.0$, $z/D = 7.0$

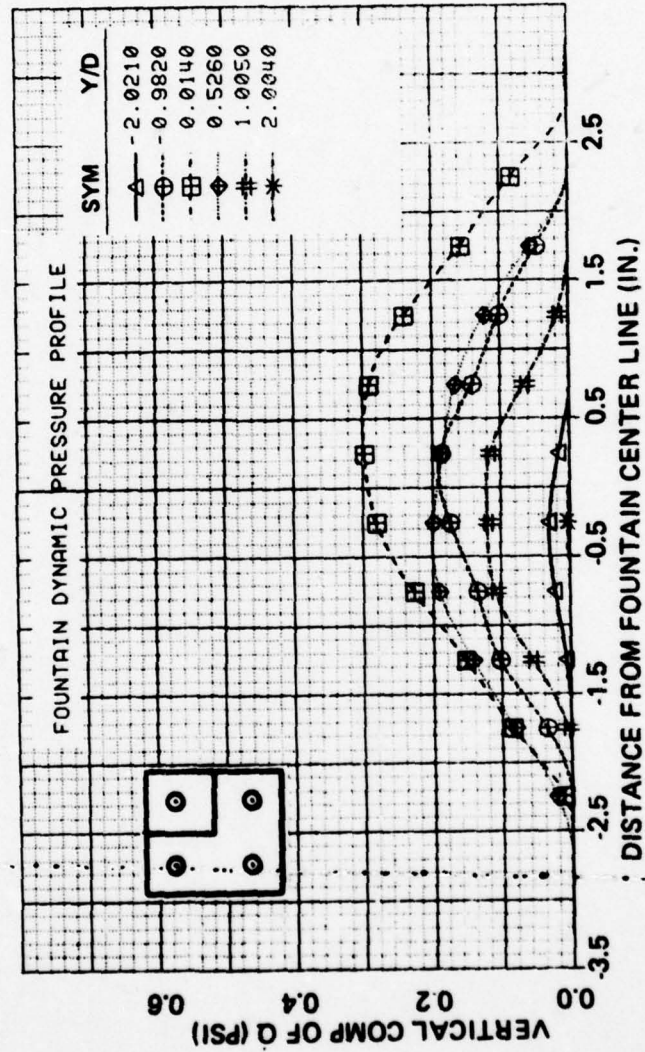


Figure C-2 Dynamic Pressure Profiles for Baseline Four Nozzle Configuration at $NPR = 2.0$,
 $D = 1.31$ in., $h/D = 8.0$, $z/D = 5.5$

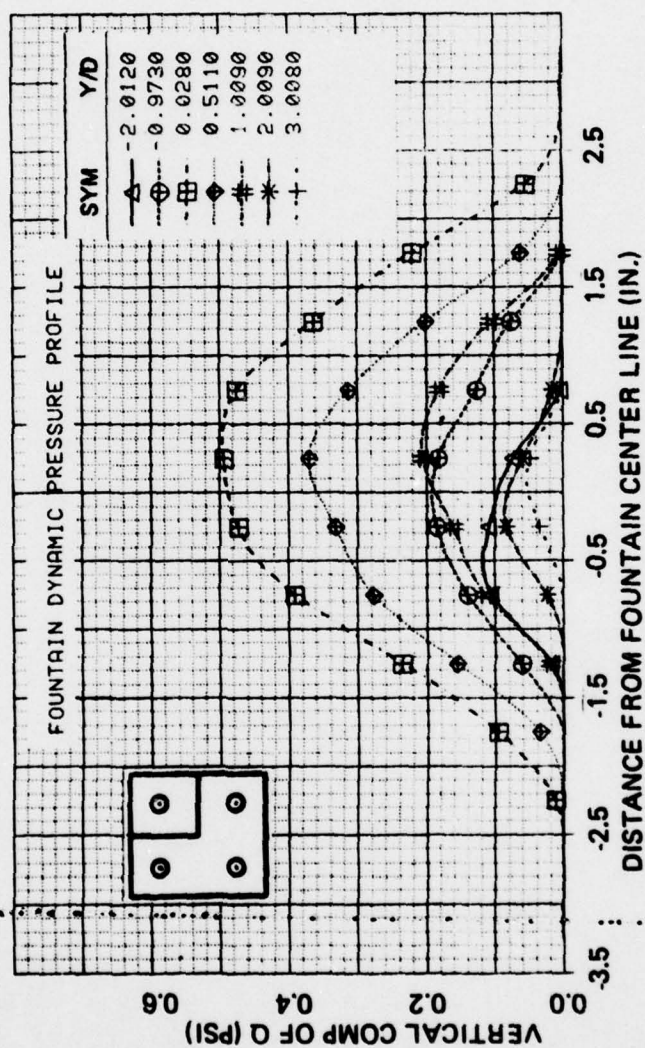


Figure C-3 Dynamic Pressure Profiles for Baseline Four Nozzle Configuration at $NPR = 2.0$,
 $D = 1.31$ in., $h/D = 8.0$, $z/D = 3.5$

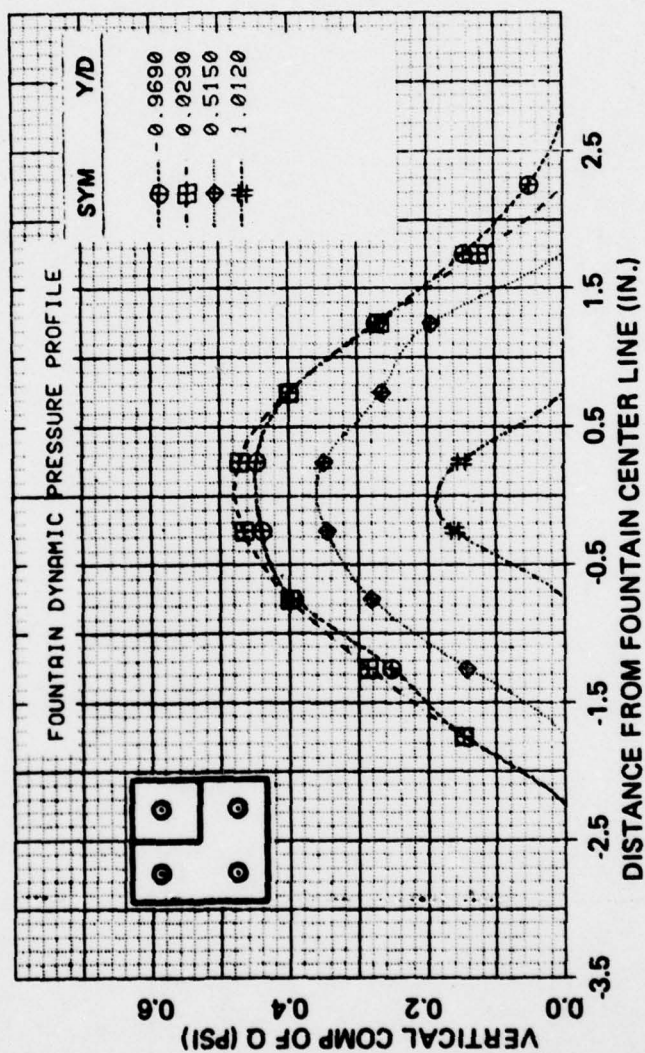


Figure C-4 Dynamic Pressure Profiles for Baseline Four Nozzle Configuration at NPR = 2.0,
 $D = 1.31$ in., $h/D = 5.0$, $z/D = 3.7$

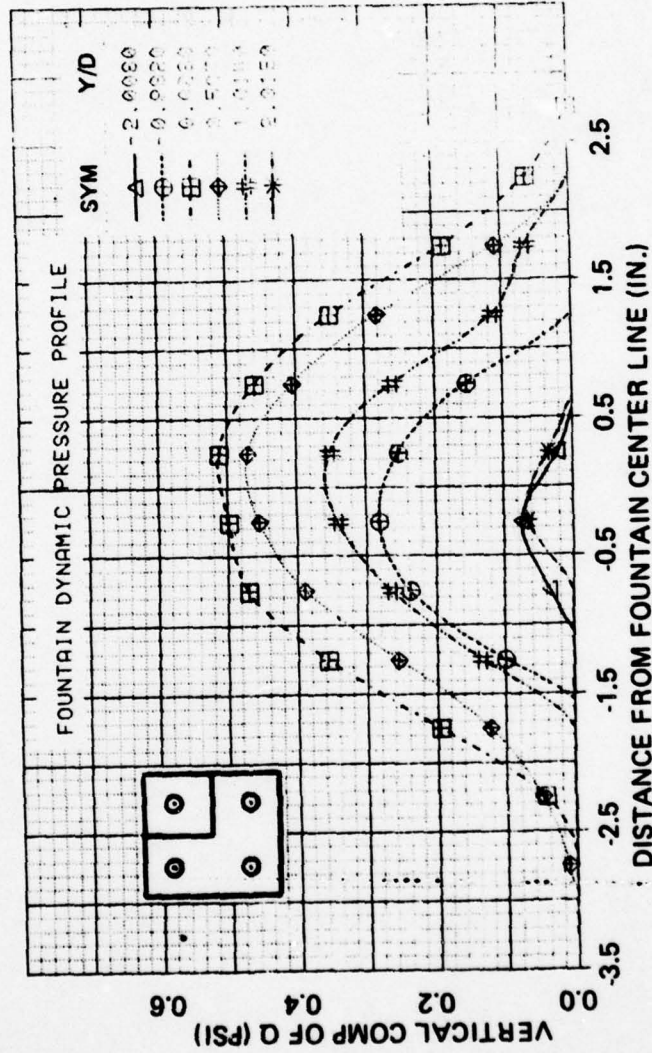


Figure C5 Dynamic Pressure Profiles for Baseline Four Nozzle Configuration at NPR = 2.0.
 $D = 1.31$ in., $h/D = 5.0$, $z/D = 2.5$

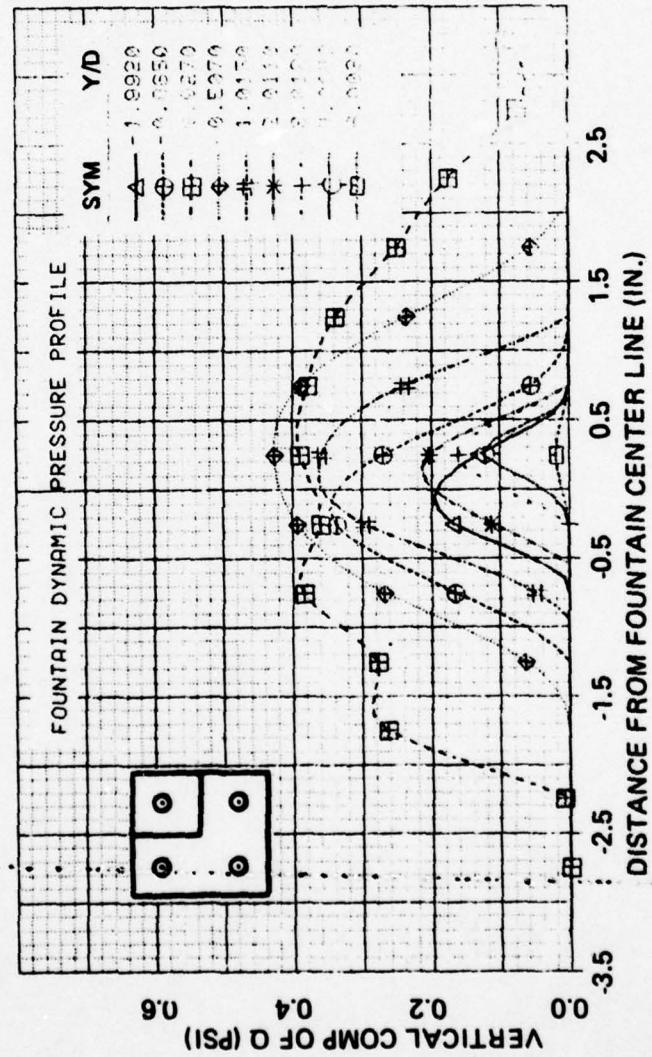


Figure C-6 Dynamic Pressure Profiles for Baseline Four Nozzle Configuration at $NPR = 2.0$, $D = 1.31$ in., $h/D = 5.0$, $z/D = 1.5$

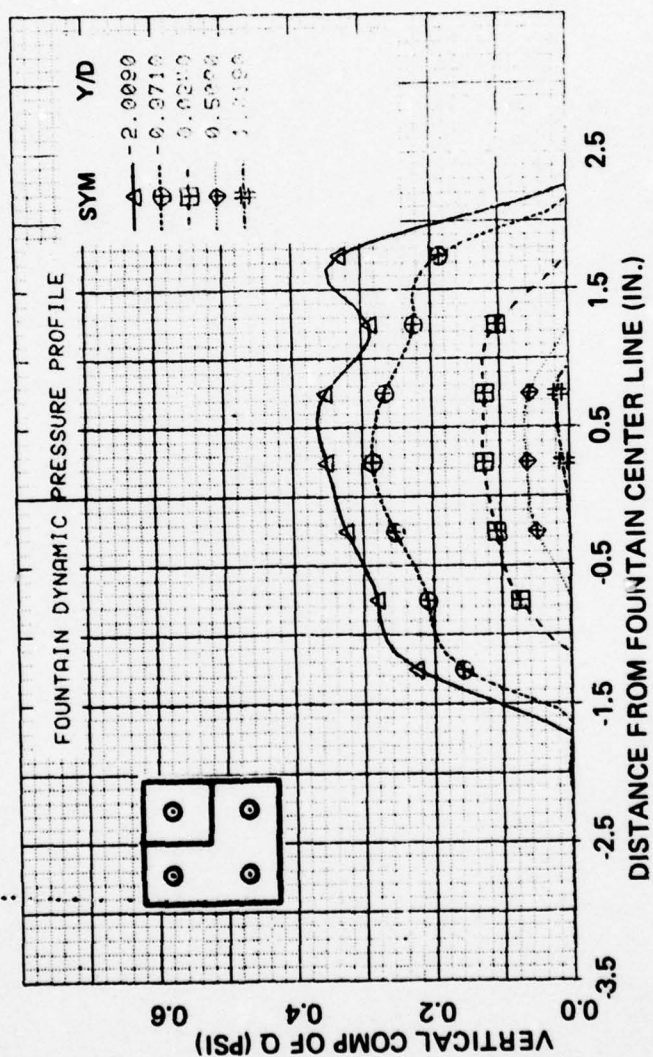


Figure C-7 Dynamic Pressure Profiles for Baseline Four Nozzle Configuration at NPR = 2.0, $D = 1.31$ in., $h/D = 5.0$, $z/D = 6.7$

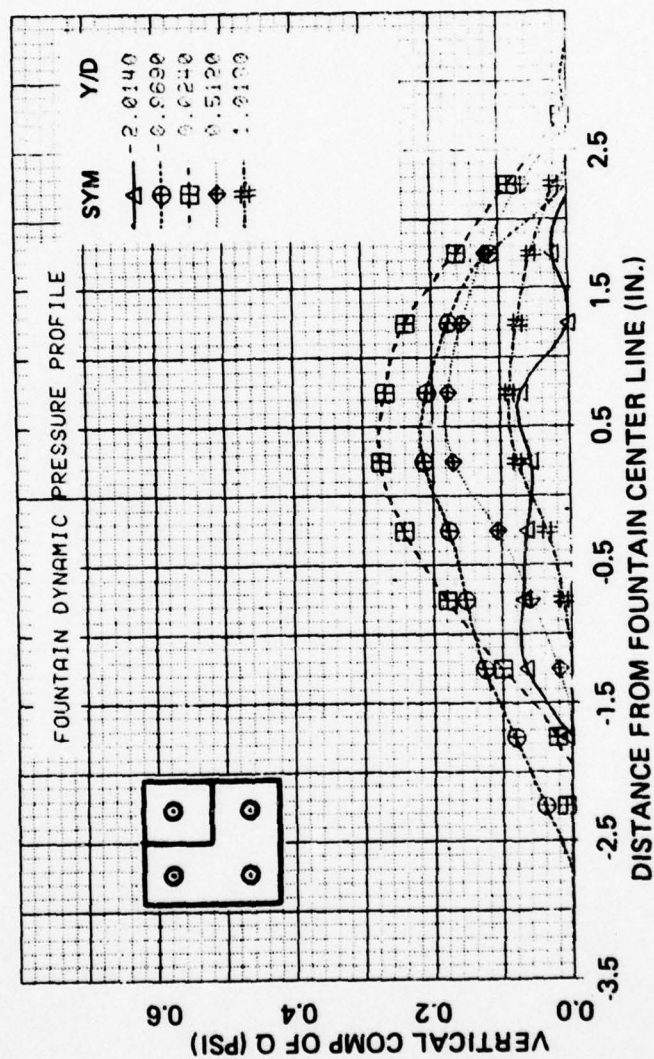


Figure C-8 Dynamic Pressure Profiles for Four Nozzle Configuration with S2 Screens at $NPR = 2.0$, $h/D = 8.0$, $z/D = 3.5$

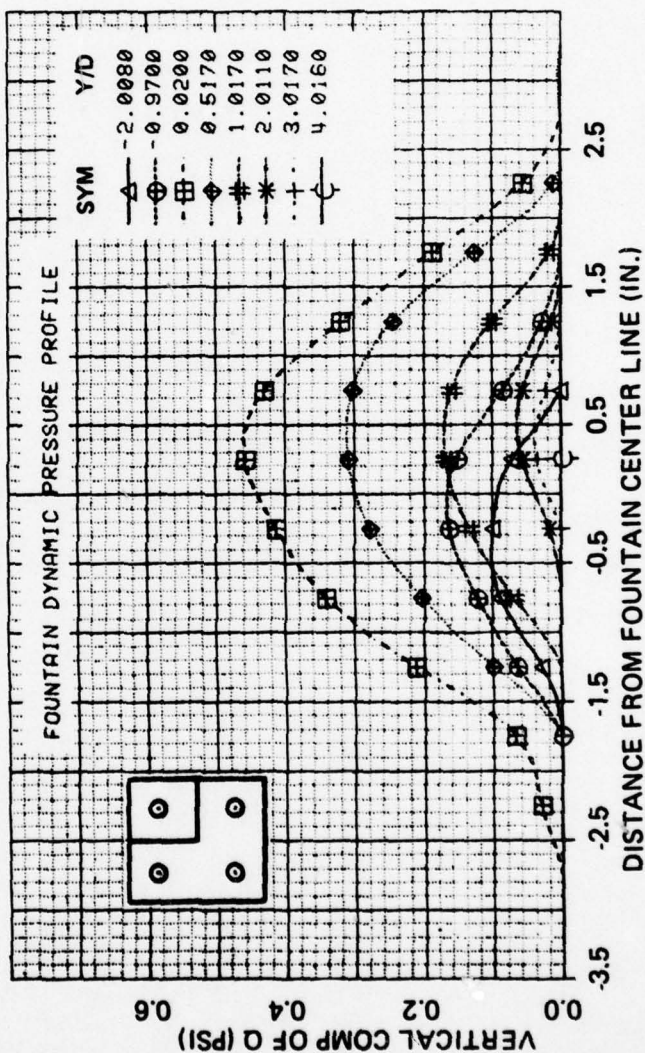


Figure C-9 Dynamic Pressure Profiles for Four Nozzle Configuration with S2 Screens at NPR = 2.0,
 $h/D = 8.0$, $z/D = 5.5$

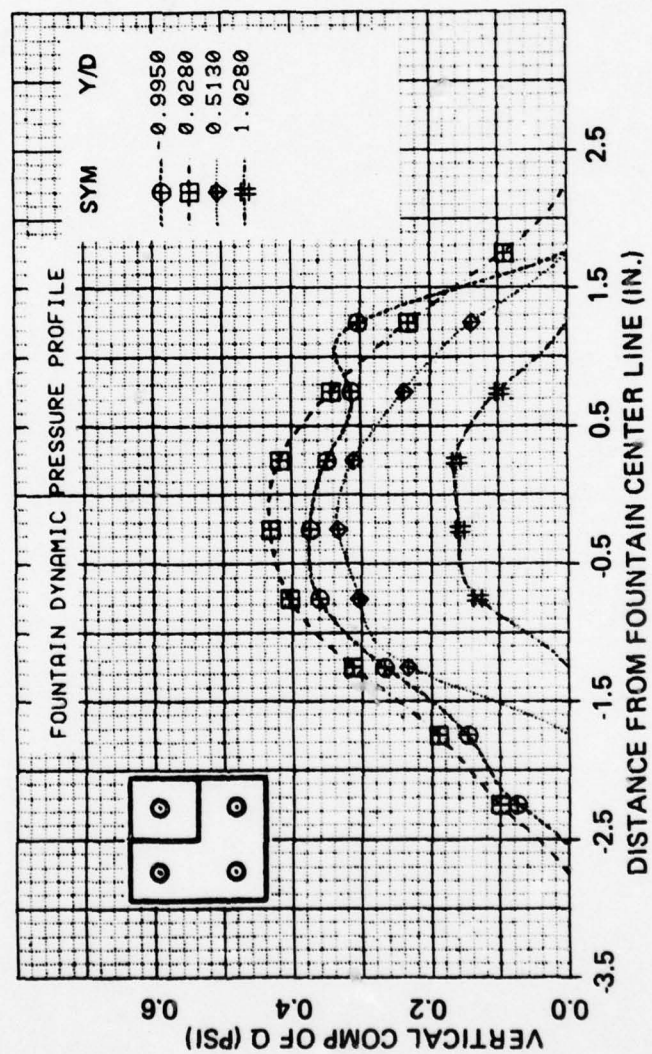


Figure C-10 Dynamic Pressure Profiles for Four Nozzle Configuration with S2 Screens at $NPR = 2.0$, $h/D = 5.0$, $z/D = 3.5$

AD-A073 114

GENERAL DYNAMICS CORP FORT WORTH TX FORT WORTH DIV
THE CRITICALITY OF ENGINE EXHAUST SIMULATIONS ON VSTOL MODEL-ME--ETC(U)
JUL 79 J R LUMMUS

F/G 20/4

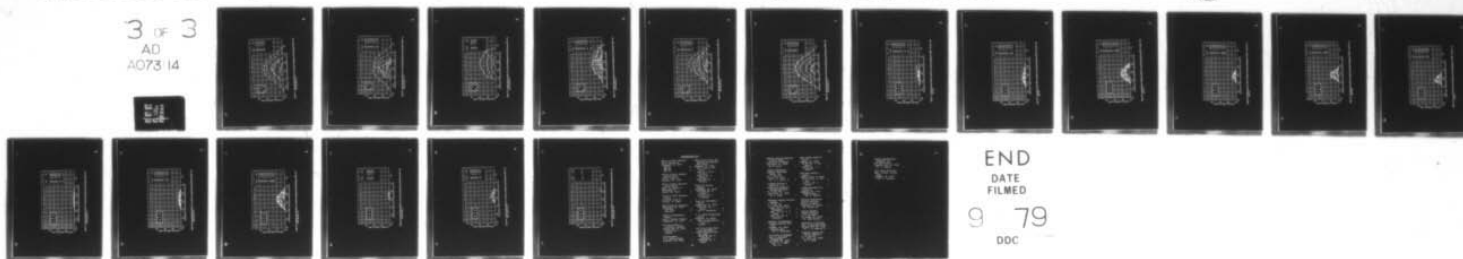
N00014-78-C-0384

NL

UNCLASSIFIED

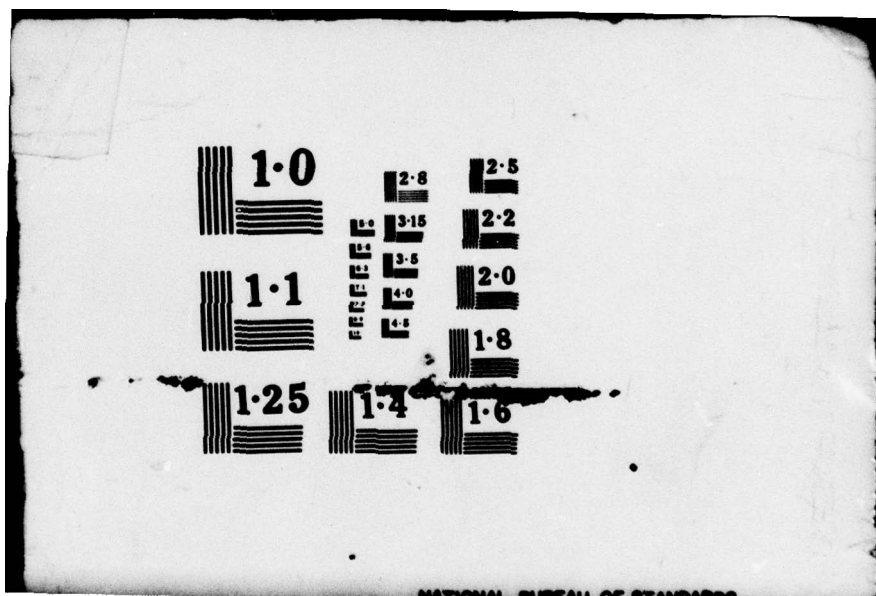
ONR-CR212-255-1F

3 OF 3
AD
A073 14



END
DATE
FILMED

9 79
DOC



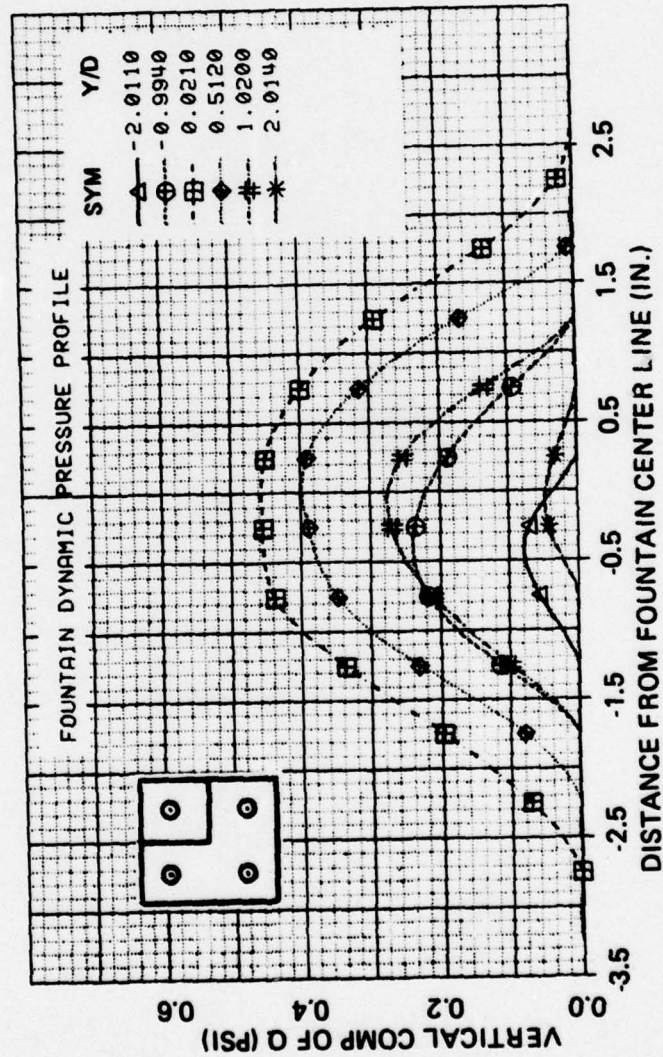


Figure C-11 Dynamic Pressure Profiles for Four Nozzle Configuration with S2 Screens at NPR = 2.0,
 $h/D = 5.0$, $z/D = 2.5$

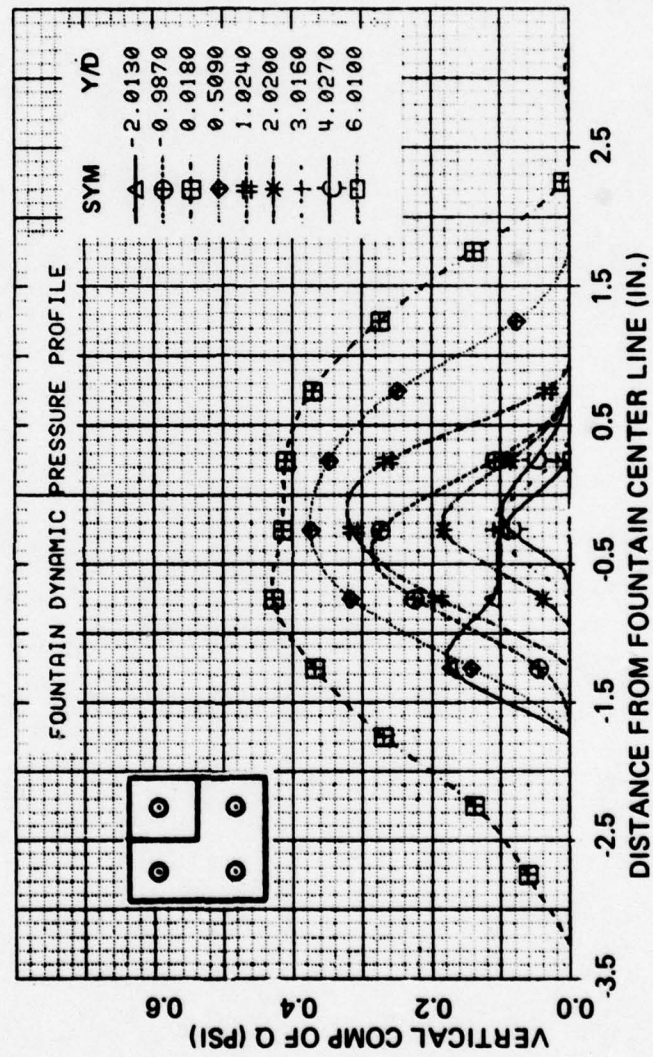


Figure C-12 Dynamic Pressure Profiles for Four Nozzle Configuration with S2 Screens at NPR = 2.0,
 $h/D = 5.0$, $z/D = 1.5$

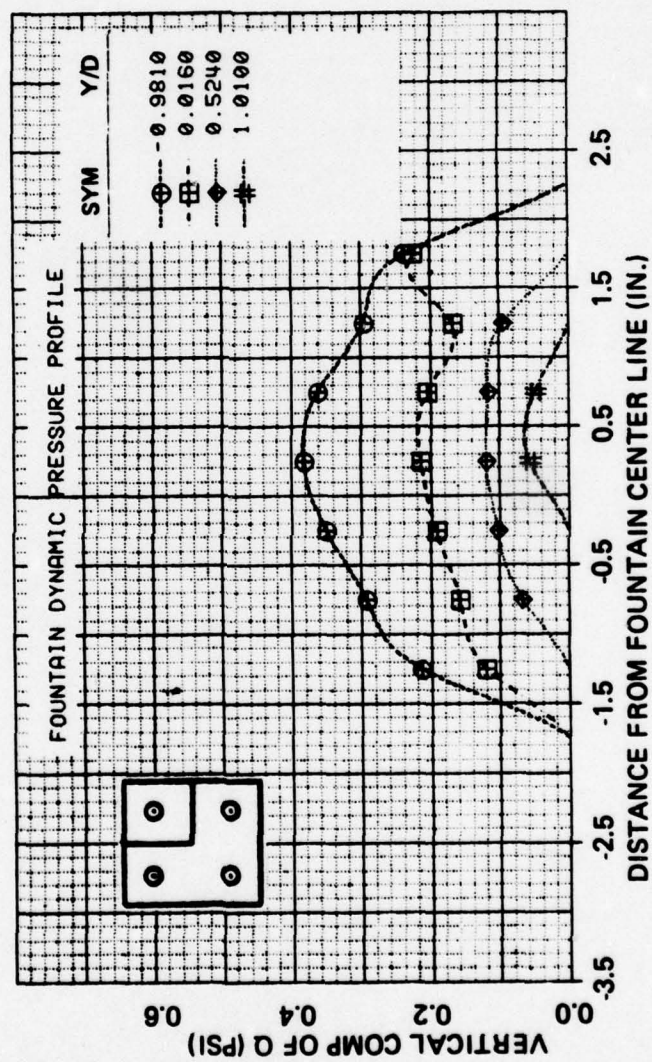


Figure C-13 Dynamic Pressure Profiles for Four Nozzle Configuration with P2 Screens at NPR = 2.0, $h/D = 8.0$, $z/D = 6.7$

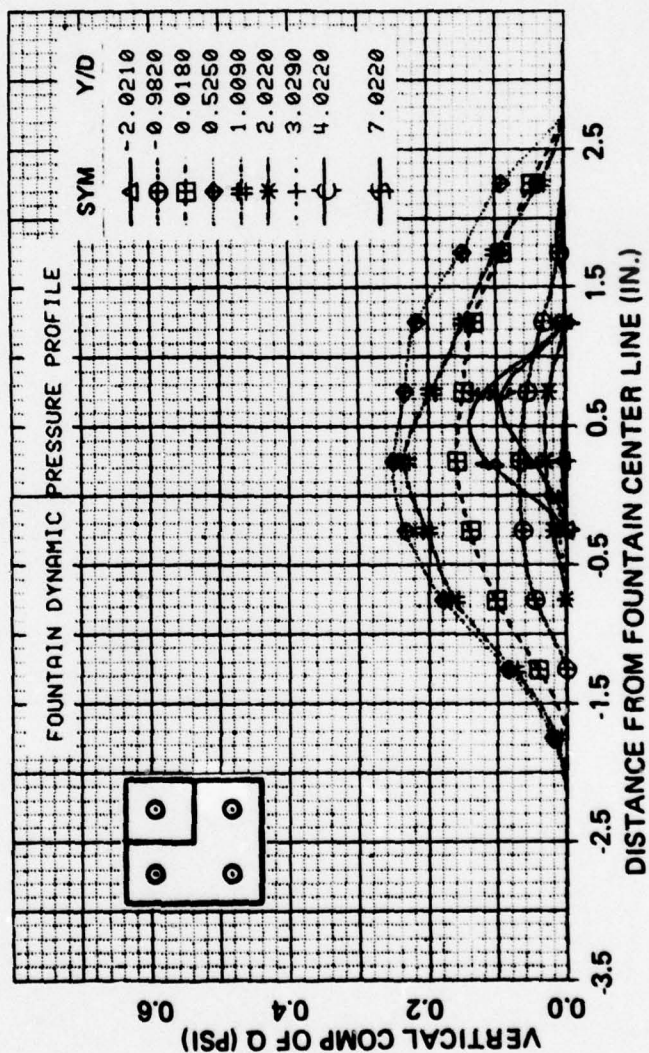


Figure C-14 Dynamic Pressure Profiles for Four Nozzle Configuration with P2 Screens at NPR = 2.0,
 $h/D = 8.0$, $z/D = 5.5$

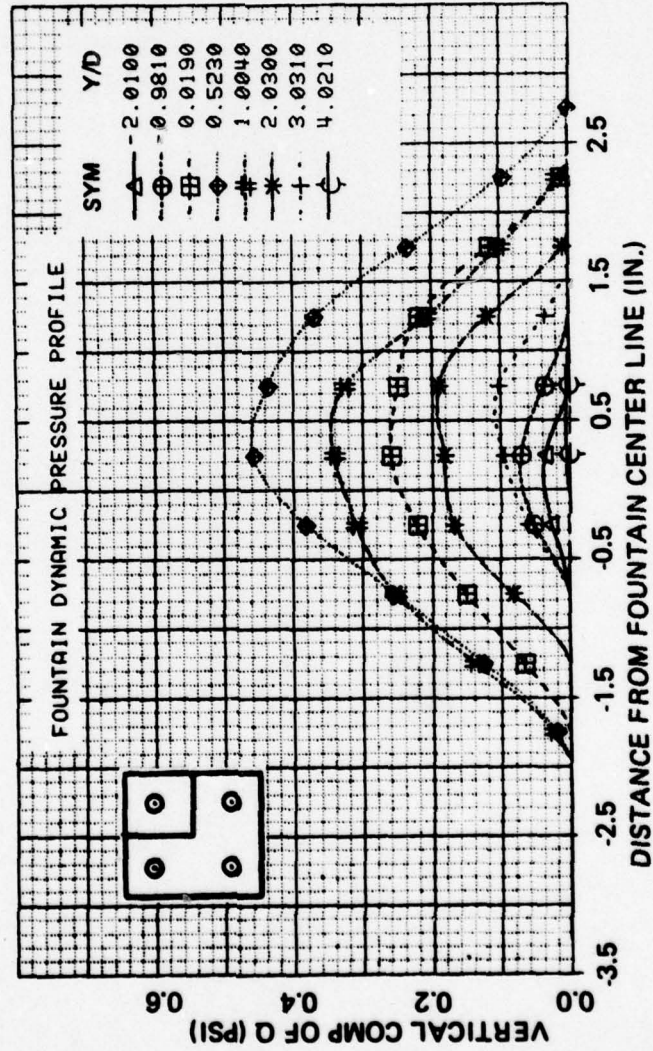


Figure C-15 Dynamic Pressure Profiles for Four Nozzle Configuration with P2 Screens at NPR = 2.0,
 $h/D = 8.0$, $z/D = 3.5$

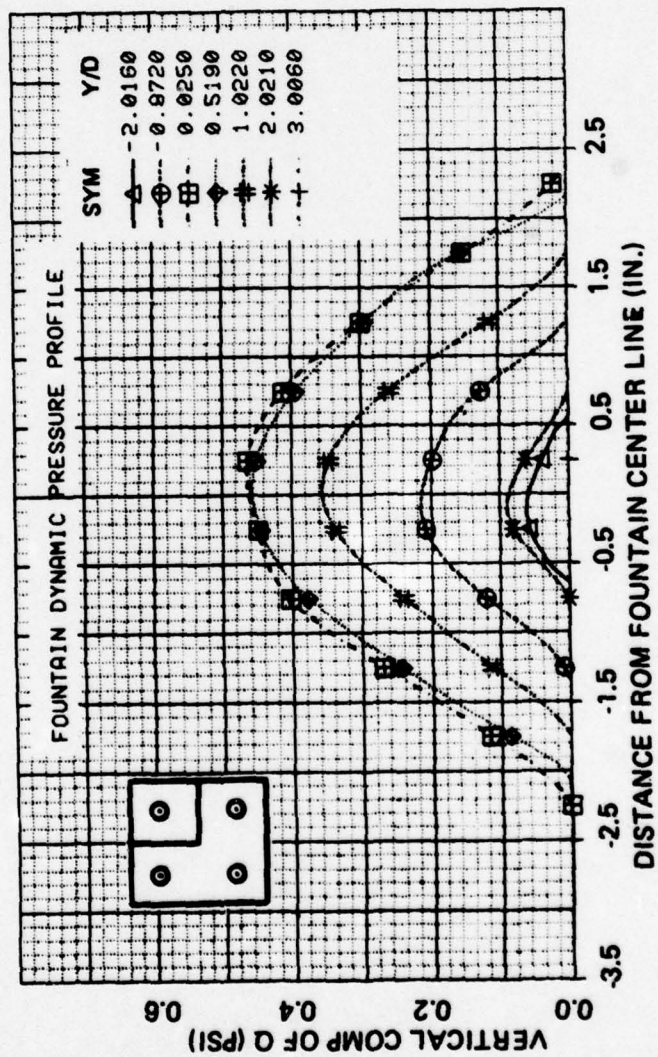


Figure C-16 Dynamic Pressure Profiles for Four Nozzle Configuration with P2 Screens at NPR = 2.0,
 $h/D = 5.0$, $z/D = 2.5$

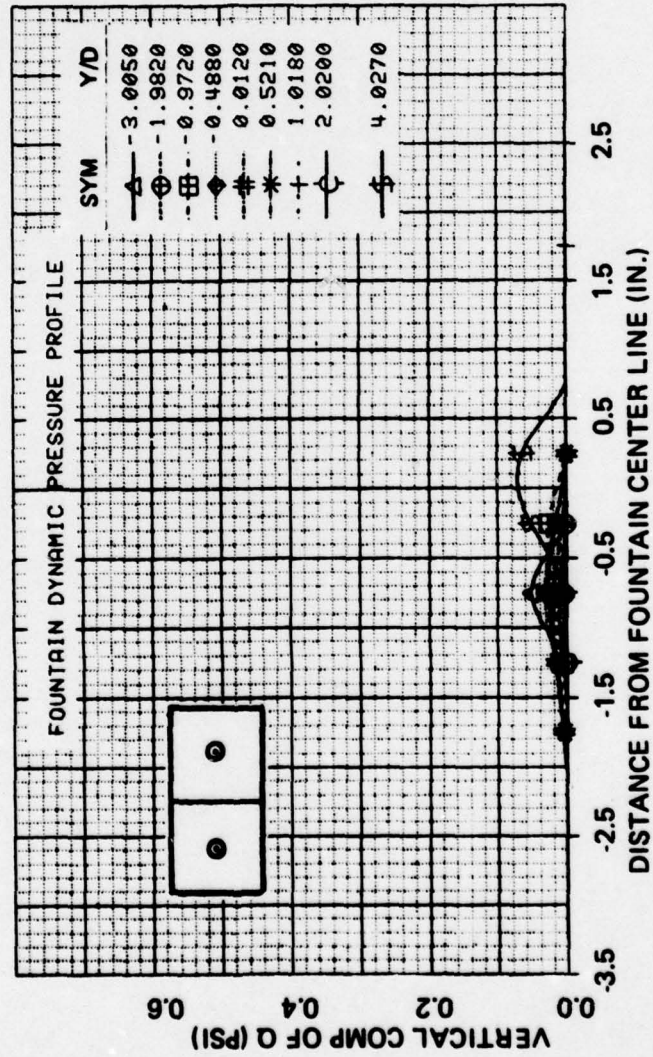


Figure C-17 Dynamic Pressure Profiles for Baseline Two Nozzle Configuration at $NPR = 2.0$, $h/D = 8.0$, $z/D = 5.5$

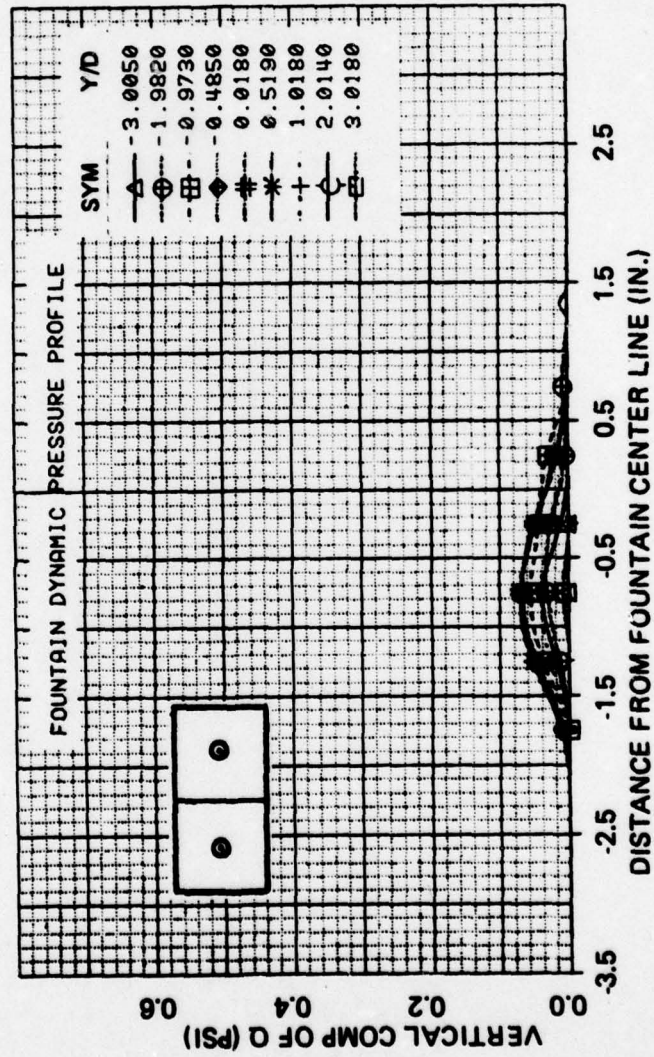


Figure C-18 Dynamic Pressure Profiles for Baseline Two Nozzle Configuration at NPR = 2.0, $h/D = 8.0$, $z/D = 3.5$

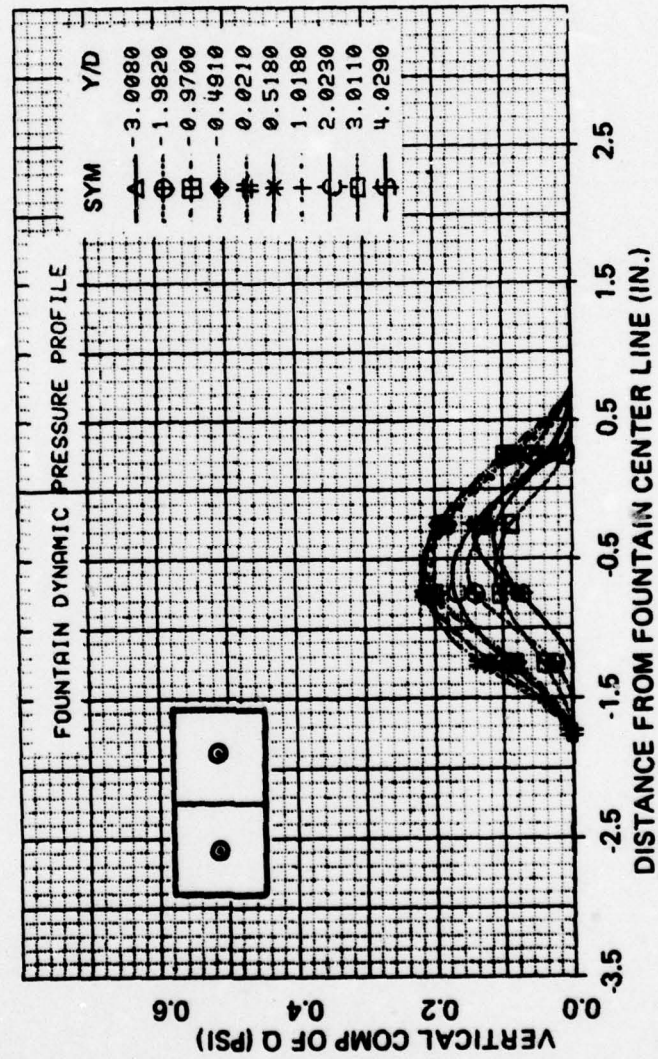


Figure C-19 Dynamic Pressure Profiles for Baseline Two Nozzle Configuration at $NPR = 2.0$, $h/D = 0.0$, $z/D = 1.5$

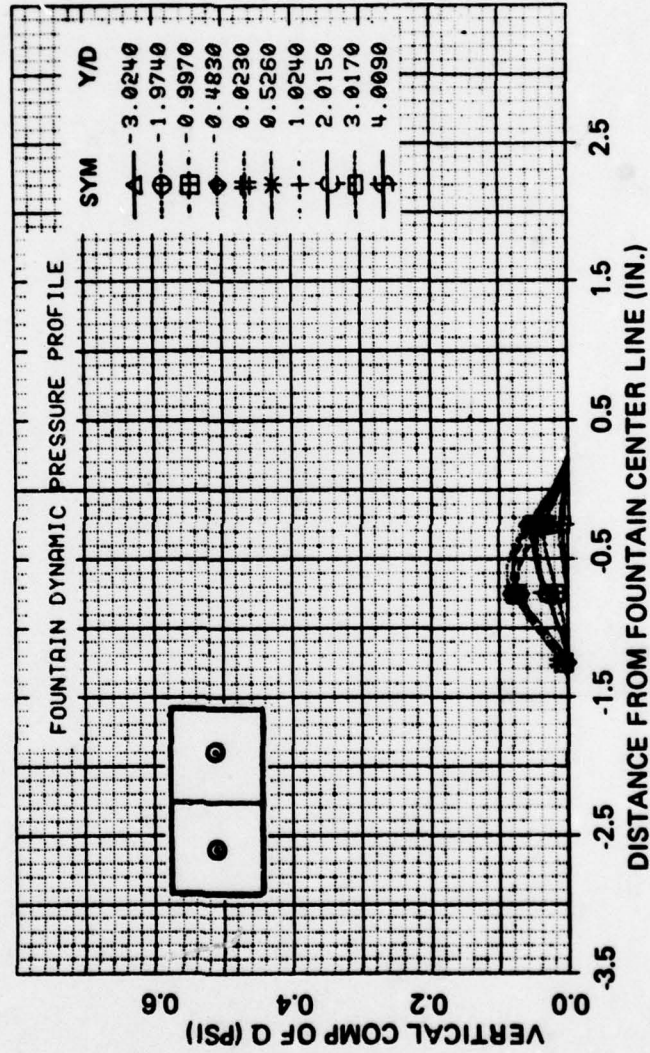


Figure C-20 Dynamic Pressure Profiles for Baseline Two Nozzle Configuration at NPR = 2.0, $h/D = 3.5$, $z/D = 2.1$

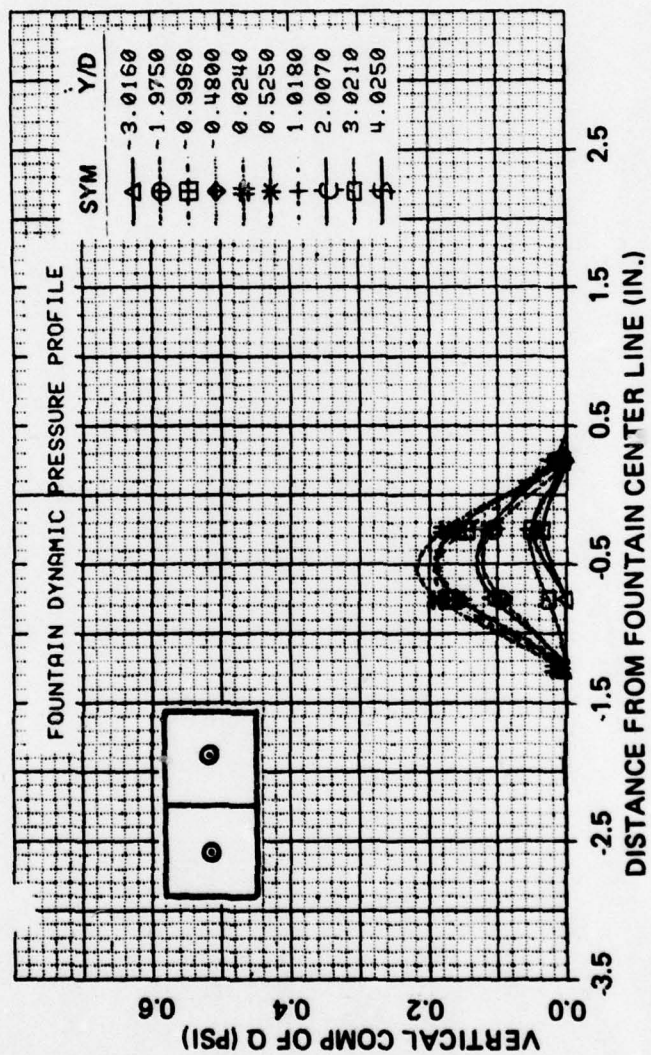


Figure C-21 Dynamic Pressure Profiles for Baseline Two Nozzle Configuration at NPR = 2.0, $h/D = 3.5$, $z/D = 1.25$

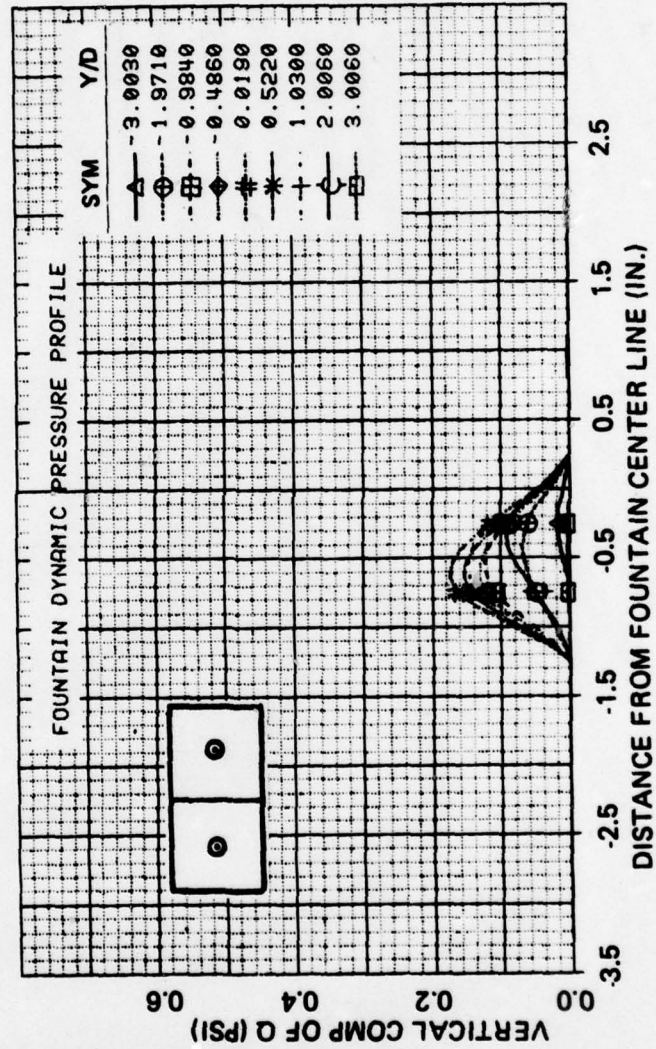


Figure C-22 Dynamic Pressure Profiles for Baseline Two Nozzle Configuration at NPR = 2.0, $h/D = 2.5$, $z/D = 1.1$

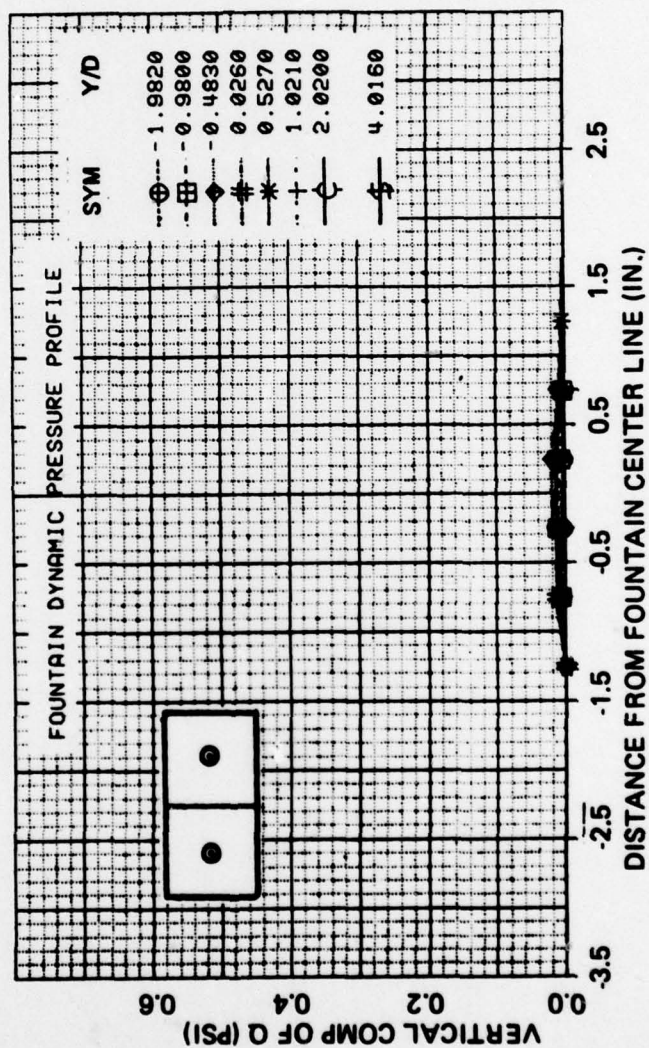


Figure C-23 Dynamic Pressure Profiles for Two Nozzle Configuration with S2 Screens at NPR = 2.0,
 $h/D = 8.0$, $z/D = 5.5$

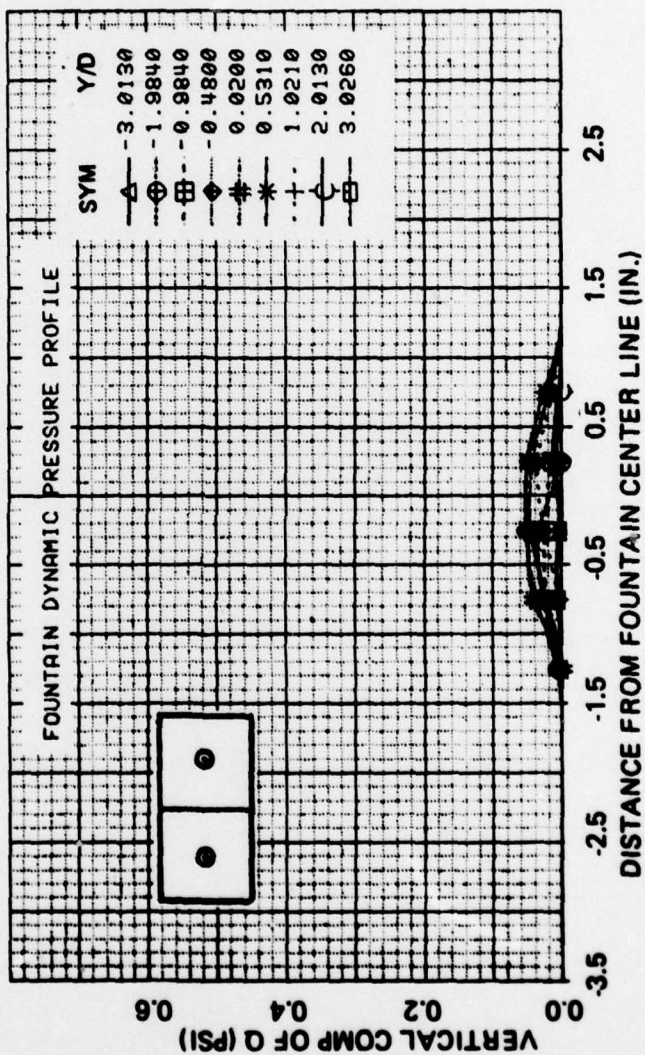


Figure C-24 Dynamic Pressure Profiles for Two Nozzle Configuration with S2 Screens at $NPR = 2.0$,
 $h/D = 8.8$, $z/D = 3.5$

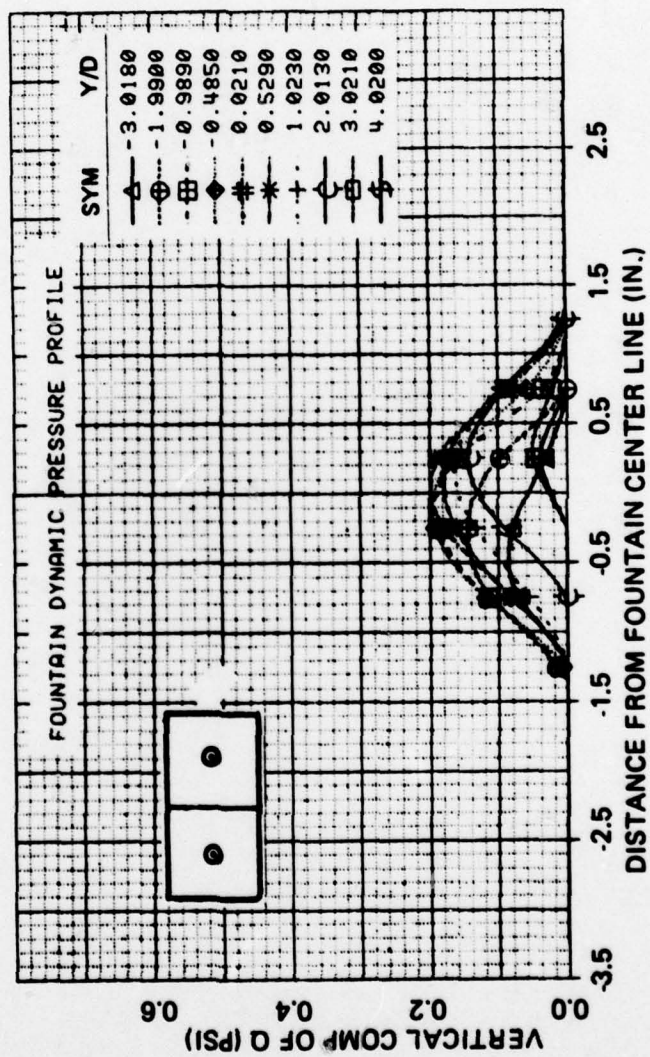


Figure C-25 Dynamic Pressure Profiles for Two Nozzle Configuration with S2 Screens at NPR = 2.0,
 $h/D = 8.0$, $z/D = 1.5$

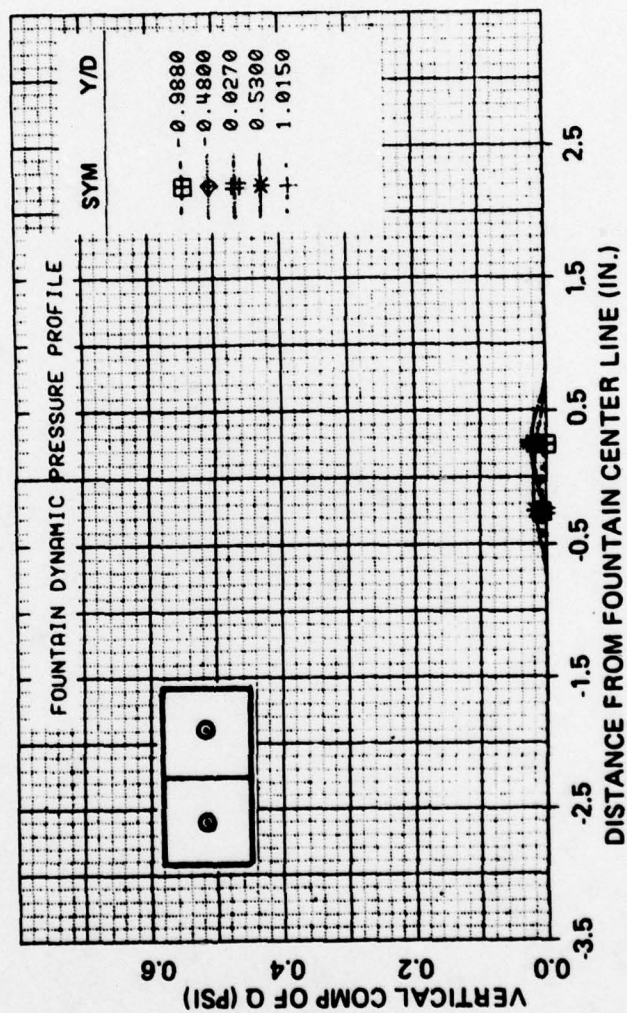


Figure C-26 Dynamic Pressure Profiles for Two Nozzle Configuration with S2 Screens at NPR = 2.0,
 $h/D = 3.5$, $z/D = 2.1$

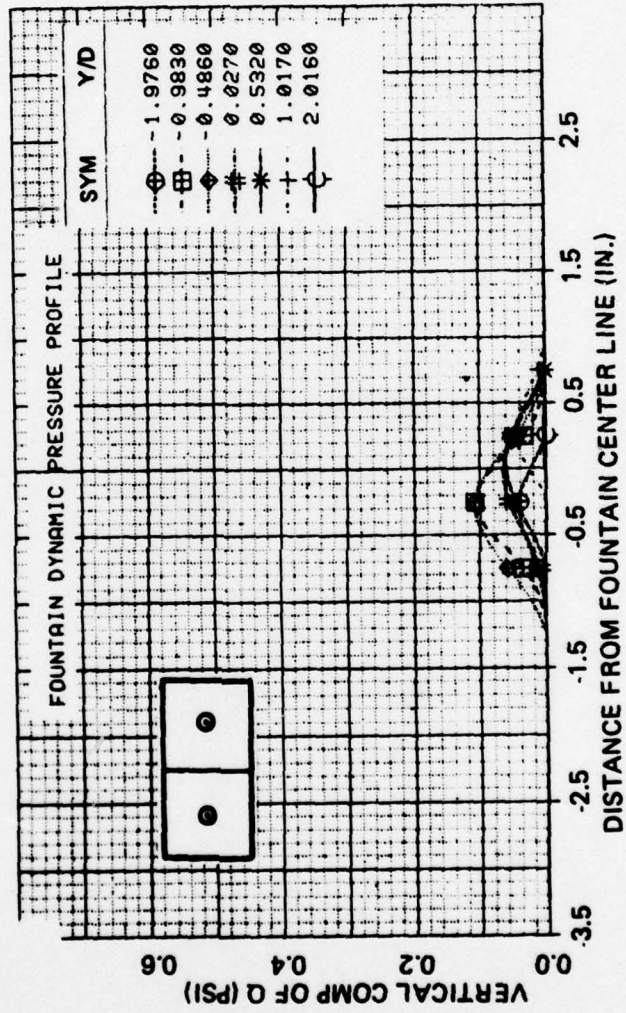


Figure C-27 Dynamic Pressure Profiles for Two Nozzle Configuration with S2 Screens at $NPR = 2.0$,
 $h/D = 3.5$, $z/D = 1.25$

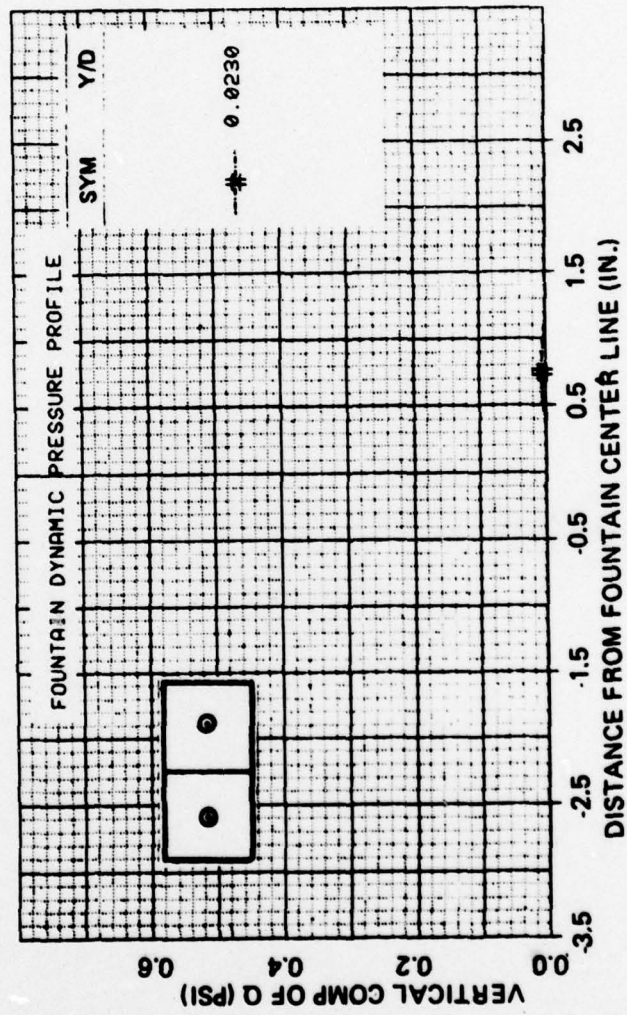


Figure C-28 Dynamic Pressure Profiles for Two Nozzle Configuration with S2 Screens at NPR = 2.0, $h/D = 3.5$, $z/D = 1.10$

DISTRIBUTION LIST

Office of Naval Research		David Taylor Naval Ship	
800 N. Quincy St.		Research and Develop-	
Arlington, VA 22217		ment Center	
ONR 211	4	Bethesda, MD 20084	
ONR 222	1	Main Library, Code	
ONR 438	1	522.1	1
		Code 522.3 (Aero	
Office of Naval Research		Library)	1
Branch Office		Code 16 (Dr. H.	
1030 E. Green St.		Chaplin)	1
Pasadena, CA 91106	1	Code 1669 (Mr. J.	
		Nichols)	1
Office of Naval Research		Naval Air Systems	
Branch Office		Command	
Bldg. 114 Section D		Washington, DC 20361	
866 Summer St.		AIR 320D (Mr. R.	
Boston, MA 02210	1	Siewert)	1
		AIR 5301 (Mr. L.	
Office of Naval Research		Trobaugh)	1
Branch			
536 South Clark St.		Naval Air Development	
Chicago, IL 60605	1	Center	
		Warminster, PA 18974	
Naval Research Laboratory		Code 6053 (Mr. C.	
Washington, DC 20375		Mazza)	1
Code 2627	1	(Mr. C. Henderson)	1
Code 2629	1		
Defense Documentation		U. S. Naval Postgraduate	
Center		School	
Bldg. 5 Cameron Station		Monterey, CA 93940	
Alexandria, VA 22314	12	Dept. of Aeronautics	
		(Code 57)	1
Air Force Office of		Library	1
Scientific Research			
Bolling AFB, DC 20332		Air Force Flight Dyna-	
Code NA (Dr. J.		mics Laboratory	
Wilson)	1	Wright Patterson AFB,	
		OH 45433	
Superintendent		AFFDL/FXM (Mr. R.	
U. S. Naval Academy		Jeffries)	1
Annapolis, MD 21402	1	AFFDL/FGC (Dr. T.	
		Weeks)	1

Defense Advanced Research Projects Agency 1400 Wilson Boulevard Arlington, VA 22209 Mr. R. Moore	1	NASA Langley Research Center Hampton, VA 23365 MS 286 (Mr. R. Mar- gasson)	1
Vought Corporation Advanced Technology Center, Inc. P. O. Box 6144 Dallas, TX 75222 Dr. C. S. Wells, Jr.	1	MS 287 (Dr. J. F. Campbell)	1
Lockheed Missiles & Space Co., Inc. Huntsville Research & Engineering Center P. O. Box 1103 Huntsville, AL 35807 Mr. A. Zalay	1	NASA Ames Research Center Moffett Field, CA 94035 MS 227-8 (Mr. G. Mal- com)	1
		MS 227-2 (Mr. D. Bencze)	1
		Grumman Aerospace Cor- poration Bethpage, NY 11714 Research Dept. (Dr. R. Melnik)	1
McDonnell Douglas Aircraft Company P. O. Box 516 St. Louis, MO 63166 Dept. 230 (Mr. R. W. McDonald)	1	Northrop Corporation Aircraft Division 3901 W. Broadway Hawthorne, CA 90250 Mr. Gordon Hall	1
Dept. 241 (Mr. R. B. Jenny)	1	General Dynamics Convair Division P. O. Box 80847 San Diego, CA 92138 Mr. Aadu Karemaa	1
Dept. 241 (Mr. D. Kotansky)	1		
Rockwell International Columbus Aircraft Divi- sion Columbus, OH 43216 Research Dept. (Dr. P. Bevilaqua)	1	University of Maryland Dept. of Aerospace Engr. College Park, MD 20742 Dr. J. D. Anderson, Jr.	1
University of Michigan Dept. of Aerospace Engineering Ann Arbor, MI 48109 Prof. T. C. Adam- son, Jr.	1	McDonnell Douglas Re- search Laboratory P. O. Box 516 St. Louis, MO 63166 Dr. W. Bower	1

Nielsen Engineering &
Research, Inc.
510 Clyde Avenue
Mountain View, CA 94043
Dr. J. Nielsen 1

Ohio State University
Dept. of Aero. & Astro.
Engr.
Columbus, OH 43210
Prof. G. Gregorek 1